MINISTRY OF EDUCATION AND TRAINING

HO CHI MINH CITY UNIVERSITY OF TECHNOLOGY AND EDUCATION

VO NGOC YEN PHUONG

"STUDY ON THE QUASI-ZERO STIFFNESS VIBRATION ISOLATION SYSTEM"

MAJOR: MECHANICAL ENGINEERING

MAJOR CODES: 9520103

THE DOCTORAL THESIS

Ho Chi Minh City, Oct./ 2022

MINISTRY OF EDUCATION AND TRAINING

HO CHI MINH CITY UNIVERSITY OF TECHNOLOGY AND EDUCATION

VO NGOC YEN PHUONG

“STUDY ON THE QUASI-ZERO STIFFNESS VIBRATION ISOLATION SYSTEM”

MAJOR: MECHANICAL ENGINEERING

MAJOR CODES: 9520103

SCIENTIFIC SUPERVISORS:

1. Assoc. Prof. Dr. Le Thanh Danh

2. Dr. Nguyen Minh Ky

1. Reviewer 1:

2. Reviewer 2:

3. Reviewer 3:

Ho Chi Minh City, Oct./ 2022

Số: 1882a/QĐ-ĐHSPKT Tp. Hồ Chí Minh, ngày 01 tháng 10 năm 2018

QUYẾT ĐỊNH

V.v giao đề tài luận án và người hướng dẫn NCS khóa 2018 - 2021

HIỆU TRƯỞNG TRƯỜNG ĐẠI HỌC SƯ PHẠM KỸ THUẬT TP. HỒ CHÍ MINH

Căn cứ Quyết định số 426/TTg ngày 27 tháng 10 năm 1976 của Thủ tướng Chính phủ về một số vấn đề cấp bách trong mạng lưới các trường đại học và Quyết định số 118/2000/QĐ-TTg ngày 10 tháng 10 năm 2000 của Thủ tướng Chính phủ về việc tổ chức lại Đại học Quốc gia Thành Phố Hồ Chí Minh, tách Trường Đại học Sư phạm Kỹ thuật Thành phố Hồ Chí Minh trực thuộc Bộ Giáo dục và Đào tạo;

Căn cứ Quyết định số 70/2014/QĐ-TTg ngày 10 tháng 12 năm 2014 của Thủ tướng Chính phủ về việc ban hành Điều lệ trường Đại học;

Căn cứ Quyết định số 937/QĐ-TTg ngày 30 tháng 6 năm 2017 về việc phê duyệt đề án thí điểm đổi mới cơ chế hoạt động của Trường Đại học Sư phạm Kỹ thuật TP. Hồ Chí Minh;

Căn cứ Thông tư số 08/2017/TT-BGDĐT ngày 04 tháng 4 năm 2017 của Bộ Giáo dục và Đào tạo về việc Ban hành Qui chế tuyển sinh và đào tạo trình độ tiến sĩ;

Xét nhu cầu công tác và khả năng cán bộ;

Xét đề nghị của Trưởng phòng Đào tạo,

QUYẾT ĐỊNH:

Điều 1. Giao đề tài luận án tiến sĩ và người hướng dẫn cho:

Nghiên cứu sinh : ***Võ Ngọc Yến Phương***

Ngành : ***Kỹ thuật cơ khí*** Khoá: ***2018 – 2021***

Tên luận án : ***Nghiên cứu thiết kế và điều khiển hệ thống cách ly dao động tần số thấp với đặc tính độ cứng gần bằng không***

Người HD thứ nhất (HD chính): ***TS. Lê Thanh Danh***

Người HD thứ hai : ***TS. Nguyễn Minh Kỳ***

Thời gian thực hiện : ***01/10/2018 đến 01/10/2021***

Điều 2. Giao cho Phòng Đào tạo quản lý, thực hiện theo đúng Qui chế đào tạo trình độ tiến sĩ của Bộ Giáo dục & Đào tạo đã ban hành.

Điều 3. Trưởng các đơn vị, phòng Đào tạo, các Khoa quản ngành tiến sĩ và các Ông (Bà) có tên tại Điều 1 chịu trách nhiệm thi hành quyết định này.

Quyết định có hiệu lực kể từ ngày ký./.

Nơi nhận :
- BGH (để biết);
- Như điều 2, 3;
- Lưu: VT, SĐH (4b).

HIỆU TRƯỞNG
PHÓ HIỆU TRƯỞNG

PGS. TS Lê Hiếu Giang

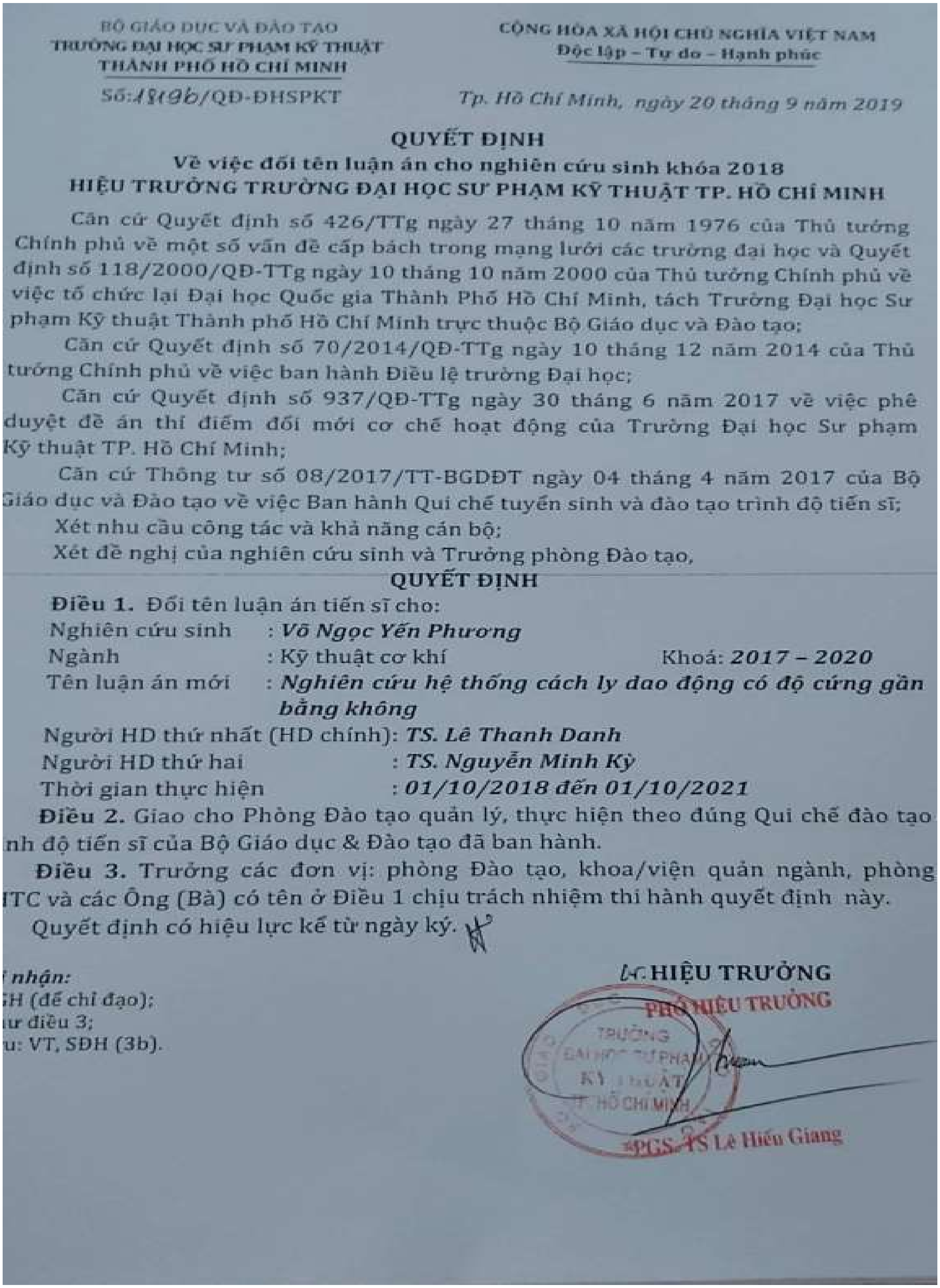

BỘ GIÁO DỤC VÀ ĐÀO TẠO
TRƯỜNG ĐẠI HỌC SƯ PHẠM KỸ THUẬT
THÀNH PHỐ HỒ CHÍ MINH

Số: 1896/QĐ-ĐHSPKT

CỘNG HÒA XÃ HỘI CHỦ NGHĨA VIỆT NAM
Độc lập – Tự do – Hạnh phúc

Tp. Hồ Chí Minh, ngày 20 tháng 9 năm 2019

QUYẾT ĐỊNH

Về việc đổi tên luận án cho nghiên cứu sinh khóa 2018

HIỆU TRƯỞNG TRƯỜNG ĐẠI HỌC SƯ PHẠM KỸ THUẬT TP. HỒ CHÍ MINH

Căn cứ Quyết định số 426/TTg ngày 27 tháng 10 năm 1976 của Thủ tướng Chính phủ về một số vấn đề cấp bách trong mạng lưới các trường đại học và Quyết định số 118/2000/QĐ-TTg ngày 10 tháng 10 năm 2000 của Thủ tướng Chính phủ về việc tổ chức lại Đại học Quốc gia Thành Phố Hồ Chí Minh, tách Trường Đại học Sư phạm Kỹ thuật Thành phố Hồ Chí Minh trực thuộc Bộ Giáo dục và Đào tạo;

Căn cứ Quyết định số 70/2014/QĐ-TTg ngày 10 tháng 12 năm 2014 của Thủ tướng Chính phủ về việc ban hành Điều lệ trường Đại học;

Căn cứ Quyết định số 937/QĐ-TTg ngày 30 tháng 6 năm 2017 về việc phê duyệt đề án thí điểm đổi mới cơ chế hoạt động của Trường Đại học Sư phạm Kỹ thuật TP. Hồ Chí Minh;

Căn cứ Thông tư số 08/2017/TT-BGDĐT ngày 04 tháng 4 năm 2017 của Bộ Giáo dục và Đào tạo về việc Ban hành Qui chế tuyển sinh và đào tạo trình độ tiến sĩ;

Xét nhu cầu công tác và khả năng cán bộ;

Xét đề nghị của nghiên cứu sinh và Trưởng phòng Đào tạo,

QUYẾT ĐỊNH

Điều 1. Đổi tên luận án tiến sĩ cho:

Nghiên cứu sinh : *Võ Ngọc Yến Phương*
Ngành : Kỹ thuật cơ khí Khoá: ***2017 – 2020***
Tên luận án mới : ***Nghiên cứu hệ thống cách ly dao động có độ cứng gần bằng không***
Người HD thứ nhất (HD chính): ***TS. Lê Thanh Danh***
Người HD thứ hai : ***TS. Nguyễn Minh Kỳ***
Thời gian thực hiện : ***01/10/2018 đến 01/10/2021***

Điều 2. Giao cho Phòng Đào tạo quản lý, thực hiện theo đúng Qui chế đào tạo nh độ tiến sĩ của Bộ Giáo dục & Đào tạo đã ban hành.

Điều 3. Trưởng các đơn vị: phòng Đào tạo, khoa/viện quản ngành, phòng ITC và các Ông (Bà) có tên ở Điều 1 chịu trách nhiệm thi hành quyết định này.

Quyết định có hiệu lực kể từ ngày ký.

nhận:
H (để chỉ đạo);
ư điều 3;
u: VT, SĐH (3b).

kt HIỆU TRƯỞNG
PHÓ HIỆU TRƯỞNG

PGS. TS Lê Hiếu Giang

ORIGINALITY STATEMENT

"I hereby declare that this submission is my own work, done under the supervision of Assoc. Prof. Dr. Le Thanh Danh and Dr. Nguyen Minh Ky and all the best of my knowledge, it contains no illegal materials previously published or written by another person."

Ho Chi Minh City, Oct. 10th 2022

Vo Ngoc Yen Phuong

ACKNOWLEDGEMENT

This dissertation was put down in writing from 2018 to 2021 during my time as a Doctor of Philosophy Candidate at the Mechanical Engineering Faculty at Ho Chi Minh City University of Technology and Education. I would like to express my deep gratitude to Assoc. Prof. Dr. Le Thanh Danh for bestowing me the opportunity to take part in his research group as well as for his conscientious instruction as my principal doctoral mentor. Simultaneously, he let me experience my independent study and he always supervised carefully during my research schedule.

Besides, I also want to thank Dr. Nguyen Minh Ky from the Faculty of Mechanical Engineering of HCMC University of Technology and Education for his devotion as a co-supervisor for my PhD thesis.

I would like also to acknowledge the National Foundation for Science and Technology Development (NAFOSTED, Vietnam) and Ho Chi Minh City University of Technology and Education for their financial assistance throughout my research project. Thanks to their interest, this thesis has been accomplished on time.

I am really grateful to my colleagues at Mechanical Engineering Faculty at Industrial University of Ho Chi Minh City for their friendly supports. In addition, I would like to appreciate the lecturers at Mechanical Engineering Faculty at University of Technology and Education for their meaningful assistance.

Finally, I express my thanks to my family, especially my mother, my husband and my two daughters for their emotional encouragement throughout my study.

Ho Chi Minh City, Oct. / 2022

Vo Ngoc Yen Phuong

ABSTRACT

The thesis of “Study on the quasi-zero stiffness vibration isolation system” is presented in six chapters.

The thesis introduces an innovation quasi-zero stiffness adaptive vibration isolation model (QSAVIM) composed by semicircular CAM-wedge-pneumatic spring mechanism. One with the positive stiffness including the wedges, the rollers and the two rubber air springs, is used to support the load. The other comprising the semi-circular cams, the rollers and other air springs, whose stiffness is negative, is employed to adjust the system stiffness. In this model, a component which is non-steel elastic element is the pneumatic spring including rubber air spring and pneumatic cylinder are employed respectively in the proposal model.

The restoring model of a commercial rubber air spring is analyzed and developed, which is contributed by three factors including compressed air, friction and viscoelasticity of the rubber bellow. Herein, the nonlinear hysteresis model of the rubber tube is also considered. Then, an experimental rig is set up to identify and verify the parameters of the rubber air spring model. In addition, the friction force of the pneumatic cylinder is also investigated through using virtual prototyping technology.

The complex nonlinear dynamic response of the quasi-zero stiffness adaptive vibration isolation model which is a parallel connection between a load bearing mechanism and a stiffness corrected one is realized. The important feature of the proposed model is that it is easy not only to adjust the stiffness to adapt according to the change of the isolated mass but to improve the isolation effectiveness in low frequency region that is useful in practical application. The studied results show that the effectiveness of the proposed model is much better than the equivalent traditional model.

CONTENTS OF THESIS

NOMENCLATURE

Latin letters

A	Area of the cylinder in m^2
A_e	Effective area of the rubber air spring in m^2
A_{wh}	Effective area of the rubber air spring at the working height in m^2
C_d	Damping coefficient in Ns/m
c_p	Specific heat capacity at constant pressure
c_v	Specific heat capacity at constant volume
D	Dissipation function
d	Distance between the base and the DSEP in mm
E_k	Kinetic Energy in Joule
E_p	Potential Energy in Joule
F	Force in N
F_{air}	Air compressed force in N
F_{ap}	Approximate force in N
F_c	Coulomb friction force in N
F_{fri}	Frictional force inside rubber material in N
F_{st}	Static friction force in N
F_g	Gravity force in N
F_{ras}	Force of rubber air spring in N
F_s	Restoring force in N
F_{sf}	Sliding frictional force between piston and cylinder in N
F_{vie}	Viscoelastic force in N
F_{LMB}	Restoring force of load bearing mechanism in N

F_{SCM}	Restoring force of stiffness corrected mechanism in N
F_s	Restoring force of the QSAVIM in N
f_e	External force in N
G_{in}	Mass low rates at inlet in kg/s
G_{out}	Mass low rates at outlet in kg/s
g	Acceleration of gravity in $\mathrm{m/s^2}$
H_{o}	Static vertical deformation of the QSAVIM in mm
h	Height of the cylinder in mm
J	Cost function
K_{air}	Compressed air stiffness in N/m
K_{DSEP}	Stiffness at the DSEP in N/m
K_{SCM}	Stiffness of the SCM in N/m
K_{LBM}	Stiffness of the LBM in N/m
m_{air}	Mass of the air in the pneumatic working chamber in kg
M	Mass of the isolated object in kg
n	Ratio of specific heat capacity.
n_{s}	Exponent of the Stribeck curve
P	Pressure in $\mathrm{N/m^2}$
P_{atm}	Atmosphere pressure in $\mathrm{N/m^2}$
P_{wh}	Pressure of the rubber air spring at the working height in $\mathrm{N/m^2}$
P_{ac}	Pressure of air in the auxiliary chamber
P_{cy}	Pressure in pneumatic cylinder
P_{so}	Pressure in the cylinder at the initial position

Q	Generalized force
R	Radius of the semicircular cam in mm
R_{air}	Gas constant in J/Kg.K
r	Radius of the roller in mm
T	Temperature of the air in the pneumatic working chamber in K
T_a	Displacement transmissibility
T_F	Force Transmissibility
u	Relative displacement between then center of the cam and DSEP in mm
V_r	Relative velocity between two contacting surfaces in m/s
v_s	Stribeck velocity in m/s
V	Volume in m^3
V_e	Effective volume in m^3
V_ac	Volume of auxiliary chamber
V_cy	Volume of cylinder
V_wh	Effective volume of the rubber air spring at the working height in m^3
V_d	Volume of the cylinder at the working height in m^3
x	Displacement of one end of the rubber air spring or cylinder in mm
x_{wh}	Deformation of the rubber air spring at the working height in mm
z_e	Excitation in mm
z	Absolute displacement of the isolated object in mm
Z	Absolute vibration amplitude of the isolated object in mm
Greek letters	
α	Angle of the wedge in degree
φ, γ	Phase angle between u and z_e

Φ	Phase angle between z and z_e
μ	Pressure ratio
ω	Excitation frequency in rad/s
ω_n	Natural frequency in rad/s
$\alpha_{\mathbf{ht}}$	Heat transfer coefficient
$\boldsymbol{a}$	the heat transfer surface area
σ	the viscous friction coefficient,
ξ	Damping ratio
ΔL	Vertical displacement of the load plate

Subscripts

ac	Auxiliary chamber
atm	Atmosphere
cy	Cylinder
e	Excitation
ef	External force
F	Force
k	Kinetic
LBM	Load bearing mechanism
p	Potential
SCM	Stiffness corrected mechanism
ras	Rubber air spring
s	Spring
sf	Sliding force

r	Relative
vie	Viscoelasticity
wh	Working height
Superscripts	
- *or* $\wedge$	Dimensionless quantity
•	Time derivative
′	Dimensionless time derivative

LIST OF FIGURES

LIST OF TABLES

ABBREVIATION

ABBREVIATION	FULL FORM
QSAVIM	Quasi-zero stiffness adaptive vibration isolation model
QZS	Quasi-zero stiffness
LBM	Load bearing mechanism
SCM	Stiffness corrected mechanism
ETVIM	Equivalent traditional vibration isolator model
GA	The genetic algorithm
HSLDS	High static low dynamic stiffness
NSS	Negative stiffness system
DSEP	Desirable static equilibrium position
RAS	Rubber air spring
PC	Pneumatic cylinder

CHAPTER 1

INTRODUCTION

1.1 The necessity of vibration isolation

In engineering systems, vibration is one of the reasons which can cause damages or unstable to machineries, equipment. etc. Furthermore, it also affects directly on human healthy as well as working effectiveness and reduces comfort when human must work on the systems which exist the unwanted vibrations. For example, when vehicles move on the ground, the floor frame has still vibrated because of the rough road surface and the vibration from the engines, although vehicles are always equipped suspension systems.

Especially, vibrations with low frequencies (<25Hz), these are dangerous for human spine [1-2] in which the authors have carried out the test to investigate and determine the number of reflecting and discomfort. Then, in [3] it has been studied to find out twelve subjects estimated the discomfort caused by low frequency vibration (<5Hz).

Accordingly, in order to eliminate the effects of unwanted vibration, it is necessary to delete this source. However, this method is not always implemented because vibration may be generated during the working process of machineries, equipment and vehicles moving on the roughness of the road. For these reasons, attaching intelligent isolators between the isolated object and the unwanted vibration source is necessary. However, present traditional linear isolators including an elastic element and a damper in parallel is very difficult to prevent the transmission of the low frequency vibrations to other elements of the system. Therefore, the motivation of this thesis is to develop an adaptive low frequency vibration isolator.

1.2 The aim of the research

This research aims to develop an innovated quasi-zero stiffness adaptive vibration isolation model which can broaden the isolation range toward the low frequency, increases the vibration attenuation rate compared with the equivalent conventional isolator but remain the load supporting capacity and low deformation.

1.3 Problems are needed solutions

In order to achieve the overall aim, the specific problems are considered as following:

- Studying comprehensively types of vibration isolation model including passive and active, advantage and limitation of each type.
- Developing an innovated quasi-zero stiffness adaptive vibration isolation model featuring non-steel elastic element
- Studying and identifying the restoring properties of elastic elements without steel material.
- Analyzing the nonlinear dynamic response comprising bifurcation as well as jump frequency phenomenon;
- Simulating, experimenting and evaluating the proposed model.

1.4 Research scope and object:

The scope of this thesis is:

- Non-steel elastic element is the pneumatic spring
- Isolation region is within 32-63 (rad/s) corresponding to 5-10 (Hz)

1.5 Research approach

Inheritability: studying and synthesizing previous works related to vibration isolation methods to develop a vibration isolation model featuring quasi-zero stiffness characteristic.

Analysis: establishing the stiffness model, dynamic equation, vibration transmissibility of the system through using thermodynamic laws, ideal gas equations, mechanism laws, etc.

Simulation: from analysis results, the simulation method is realized to determine nonlinear dynamic response and isolated effectiveness of the system.

Experiment: verifying and comparing the dynamic response and isolation effectiveness of the proposed model compared with that of the equivalent linear model.

1.6 The contents of the thesis:

In order to achieve the objectives above, the thesis" Study on the quasi-zero stiffness vibration isolation system" will solve some problems as following:

Literature reviews:

- Studying on the demand of the vibration isolation especially under low frequency excitation.
- Referring to the previous studies about the vibration isolation methods.
- Presenting the necessary of the thesis, the object, scope and objectives of the thesis. Moreover, the scientific contribution and application of the thesis have also showed.

Fundamental of relative theories: in order to consider the dynamic response, the vibration transmissibility and stability of the proposed model, some relative theories such as thermodynamics, Normal form, Multi-scale and Poincare map are employed. In addition, some model such as Berg model, Kelvin-Voigt are also used to analyzed the suggested system characteristics.

Quasi-zero stiffness adaptive vibration isolation model using a rubber air spring:

- An innovated quasi-zero stiffness adaptive vibration isolation system using rubber air spring is introduced.
- The force models of which such as compressed air, frictional and viscoelastic forces are analyzed.
- An experimental model is set up to identify the restoring characteristic of a rubber air spring.
- The stiffness model and dynamic equation is established and the complex dynamic analysis of the system was conducted.
- The effects of configurative parameters on stiffness curve and equilibrium position are analyzed.
- The vibration transmissibility and stability of the system was examined, the jump and bifurcation phenomena were considered
- An experiment to compare the isolation effectiveness between the QSAVIM and ETVIM are carried out.

Quasi-zero stiffness adaptive vibration isolator using a pneumatic spring:

- Another model of the isolator which is modified by replacing the air spring by a pneumatic cylinder.
- The stiffness of a pneumatic cylinder is analyzed and the frictional model is investigated by using virtual prototyping technology.
- The stiffness of the modified model is found. The stiffness of each mechanism and the equilibrium position of the modified model are also analyzed.
- The effects of the configuration such as the auxiliary tank volume as well as the wedge angle on the system stiffness are considered.
- The frequency-amplitude relation and the stability of the steady state solution are studied. Simultaneously, the amplitude-frequency curves obtained by Multi-scale method and fourth-order Runge-Kutta algorithm are compared.

- To obtain the solution of the dynamic response, the family of the initial conditions named the attractor-basin phase portrait affecting on the dynamic response will be detected in three cases.

1.7 Organization of thesis:

Chapter 1. Introduction

Chapter 2. Literature review

Chapter 3. Fundamental of relative theories

Chapter 4. Quasi-zero stiffness adaptive vibration isolator using rubber air spring

Chapter 5: Quasi-zero stiffness adaptive vibration isolator using pneumatic cylinder

Chapter 6. Conclusions and Future works

Published papers

References

1.8 The obtained results

With the objectives and the content of the thesis, the author gains some following results:

- The physical models of the quasi-zero stiffness adaptive vibration isolation system using rubber air spring and pneumatic cylinder are described.
- The mathematical model of the proposed system is defined.
- The vibration transmissibility equation is found out and analyzed.
- The effects of the configuration on the system stiffness are investigated.
- The test - rig to identify the characteristics of a rubber air spring as well as pneumatic cylinder is set up.
- An experiment to compare the isolation effectiveness between the QSAVIM and ETVIM are carried out.
- A novel QSAVIM design procedure is suggested.

1.9 The scientific and application contribution of the thesis:

The scientific contributions of this thesis

- Study comprehensively quasi-zero stiffness adaptive vibration isolation model using air spring including rubber air spring and pneumatic cylinder adding auxiliary tank to prevent the unwanted effects of low frequency vibrations (≥32 rad/s) to the isolated object. This is frequency region in which it can be a challenge for currently traditional isolation method.
- The stiffness model of the air spring as well as hysteresis model and sliding frictional model was analyzed and identified to contribute for analyzing dynamic response of the proposed isolation model.
- The effects of the configurative and working parameters on the stiffness curve and the nonlinear dynamic response of the system evaluated.
- The effect of the damping coefficient on the vibration transmissibility of the quasi-zero stiffness model is analyzed and simulated.
- Design procedure of the proposed system is offered
- Especially, another important contribution is to establish the equations of vibration transmission of the proposed system for purpose of prediction of the isolation effectiveness

The practical contributions of this thesis

- The proposed model has an applied potential in vibration isolation fields such as: suspension for vehicle, isolation seat for driver as well as passengers, isolation table for measurement instrument, vibration sensitive equipment, etc.
- Especially, the proposed model can fabricate and apply easily in Viet Nam. It is completely able to implement technology transfer.

SUMMARY OF CHAPTER 1

In this chapter, the necessary of the vibration isolation is presented. Next, the works in the vibration isolation field will be studied and synthesized. From that, an innovated the quasi-zero stiffness vibration isolation model is developed which meets mentioned objectives

CHAPTER 2

LITTERATURE REVIEW

The theoretical methods such as vibration isolation as well as some particular works in the quasi-zero stiffness vibration isolation field have been researched. From these results, the gap is found out by the author to propose a quasi-zero stiffness vibration isolator system using air springs thanks to taking the merits of these two objects. It is said that the proposed model can guarantee both the desired low stiffness and the load bearing ability.

2.1. Vibration Isolation

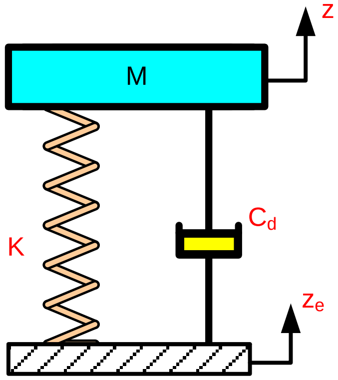

Fig. 2.1. A conventional vibration isolation system [4]

Fig. 2.1 illustrates a conventional linear vibration isolation system comprising a spring (K) connected in parallel with a damper (C) to bear a load mass (M). The vibration transmissibility is given in [4] as below:

$$T=\frac{|z|}{|z_e|}=\sqrt{\frac{1+\left(2\gamma\omega/\omega_n\right)^2}{\left(1-\left(\omega/\omega_n\right)^2\right)^2+\left(2\gamma\omega/\omega_n\right)^2}} \qquad (2.1)$$

in which

z is the displacement of the mass in mm

z_e is the excitation in mm

ω is the excited frequency in rad/s

$\omega_n = \sqrt{K/M}$ is the natural frequency in rad/s

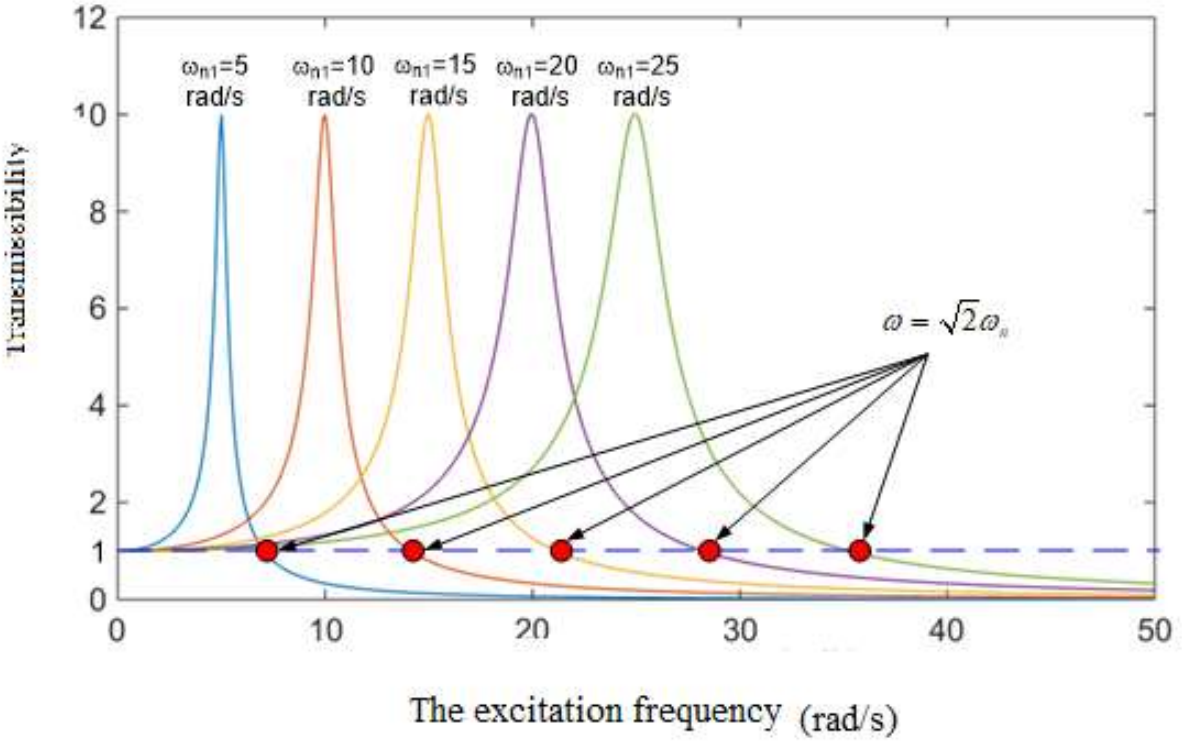

Fig. 2.2 The transmissibility curve of the conventional vibration isolation system

As shown in Fig. 2.2, if the excited frequency is smaller than $\sqrt{2}\omega_n$, the vibration level of the mass is higher than the excitation whereas the linear isolator starts to suppress the vibration transmissibility when the excitation frequency is larger than $\sqrt{2}\omega_n$. Besides, it is worthy to see that the lower the natural frequency, the higher the isolation effectiveness is and the more the isolation region is enlarged.

2.2. Models of proposed vibration isolation.

From above analysis, it may be revealed that one of the meaningful methods to decrease the natural frequency is either to reduce the stiffness of the springs or to increase the weight of the isolated object. However, the latter is difficult to apply in practice.

2.2.1. Isolated model using Euler spring

Decreasing the stiffness to expand the isolation range has been researched by many authors. For example, in the model of N. Virgin et al. [5] as plotted in Fig. 2.3, a thin strip is bent such that the two ends are brought together and clamped to form a teardrop shape, which is considered as a spring to bear a load, its stiffness depends on the length of the strip. When the length is increased, the stiffness is reduced.

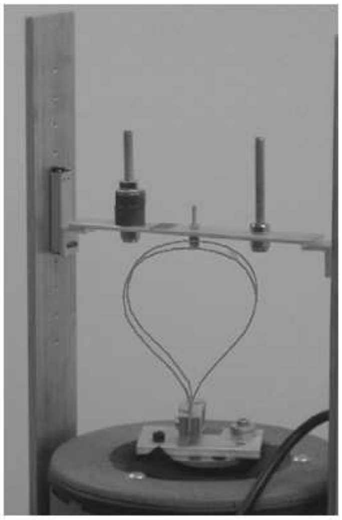

Fig. 2.3 A model of low frequency vibration isolation [5]

Next, a vibration isolator using a Euler spring is suggested by E.J. Chin et al. [6] as in Fig. 2.4 in which by implementing anti-spring technique, the resonance frequency is significant improved.

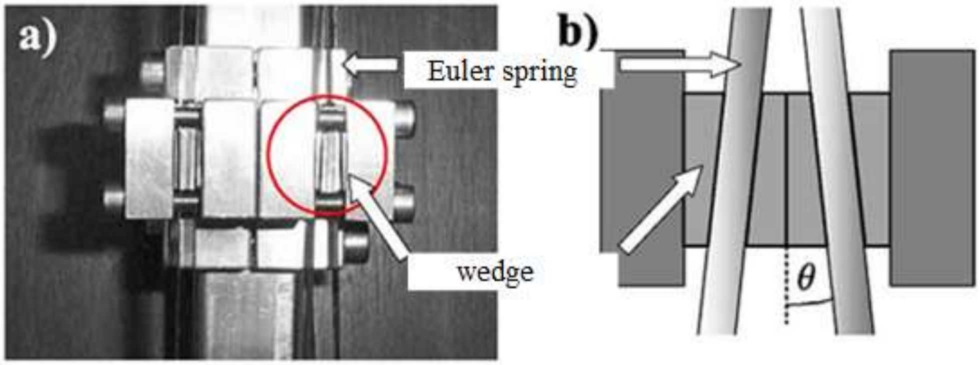

Fig.2.4 A QZS vibration isolation model for low frequency in vertical direction [6]

J. Winterflood et al. [7] proposed a novel vertical suspension technique using the column spring in Euler bucking mode which can achieve the spring rate reduction. Because the Euler spring is constrained within pivoted as well as the higher internal modes thanks to the reduction of the working range of the spring.

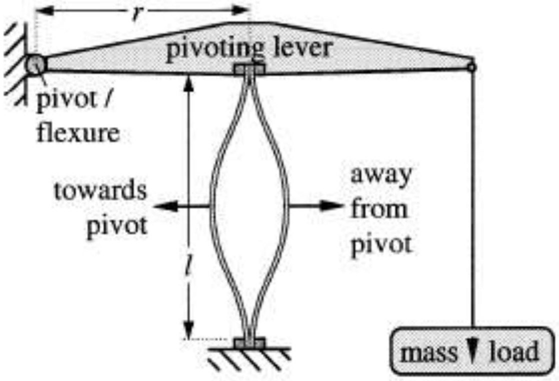

Fig.2.5 A simple structure for mounting and constraining Euler springs [7]

As known, the function of the springs is not only to absorb the energy but also to carry load. The lower the stiffness, the lower the load supporting ability as well as the larger the deflection is. This is one of the limitations for applying these springs to vibration isolation models to attenuate vibration in low frequency range. This dichotomy is also the challenge for scientists, scholars how to find the solutions which overcome the obstacles on upgrading the isolation effectiveness, and reducing the static deformation but remaining the load bearing capacity.

2.2.2. Isolated model featuring quasi-zero stiffness characteristic

In general, isolators, which used the mechanical springs as mentioned above, is able to isolate vibration. However, their disadvantage is that it cannot ensure both the low stiffness and the load bearing ability at the same time.

In order to overcome these weaknesses, QZS vibration isolation models have been attracted by scientific and engineering community. For example, A. Carrella et al. [8] designed a model concluded vertical springs with positive stiffness connected to a pair of oblique springs with negative stiffness. The main feature of this study is to use the negative element as shown in Fig.2.6 without large deformation, this study shows that in order to obtain the large deformation from the equilibrium position, for example, the authors find out the geometrical relationship between the parameters and stiffness such as the optimized inclination from 48 to 57 degree.

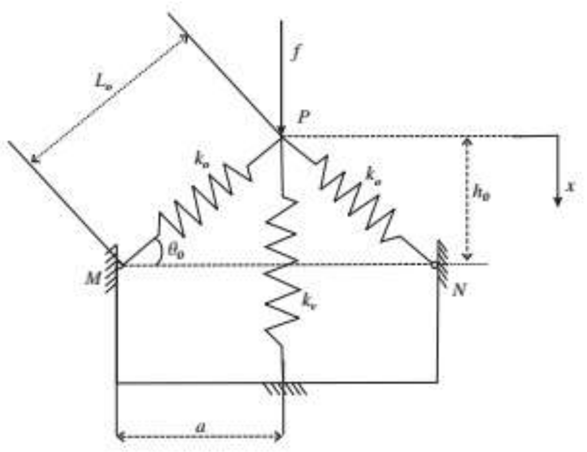

Fig.2.6 A QZS vibration isolation model for low frequency [8]

Besides, another novel dynamic model of QZS isolator constructed by a positive stiffness component and a pair of inclined linear spring providing negative stiffness was also suggested Z. Hao et al. [9] as in Fig. 2.7. Besides, in order to expand previous studies of HSLDS isolator, a passive isolator combining the HSLDS spatial pendulum is developed by G. Dong et al. [10].

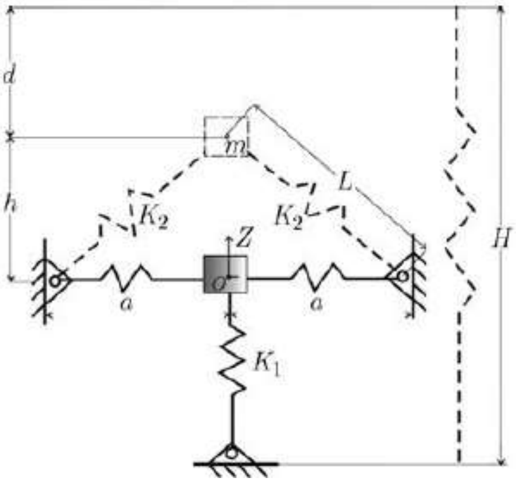

Fig. 2.7 Dynamical model with low frequency comprising a vertical and a pair of oblique springs [9]

A Carrella et al. introduced another vibration isolator including two horizontal springs in parallel with a vertical spring **[11]** as in Fig. 2.8. This system indicates that the more the stiffness decreases, the more the nonlinearity characteristic slows down.

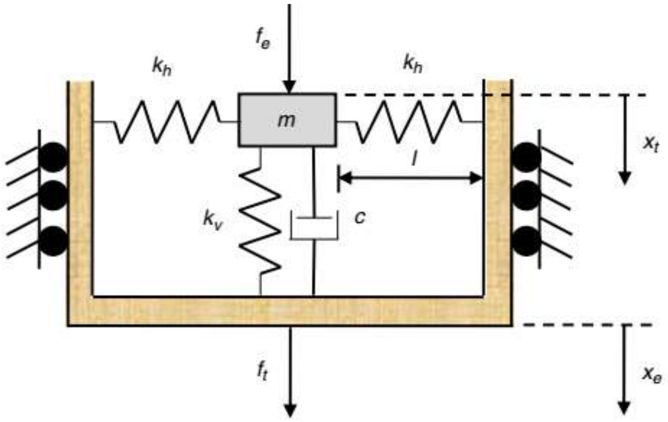

Fig. 2.8 Simple model of a nonlinear isolator that behaves as a Duffing oscillator at low amplitudes of excitation [11].

X. Wang et al. [12] which shown in Fig. 2.9 analyzed the parameters effects on the isolation response of a HSLDS isolator. Theoretical analysis and experimental investigation of this model was carried out by Z. Hu et al. [13], indicating the isolated model is very effectiveness in low excitation frequency region.

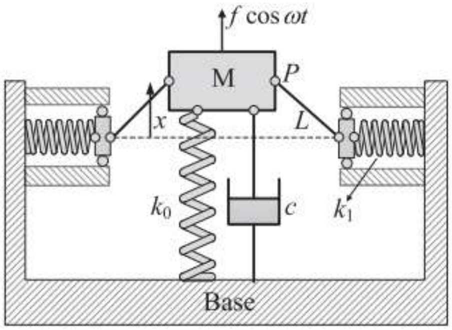

Fig. 2.9 Scheme of HSLDS isolator [12]

Besides, A. O. Oyelade [14], which is indicated in Fig.2.10, proposed a vibration isolator by combining a bar and a Euler beam to obtain low dynamic stiffness, some geometric imperfection of the Euler beam is identified, hence, the isolation range of operation can be widened.

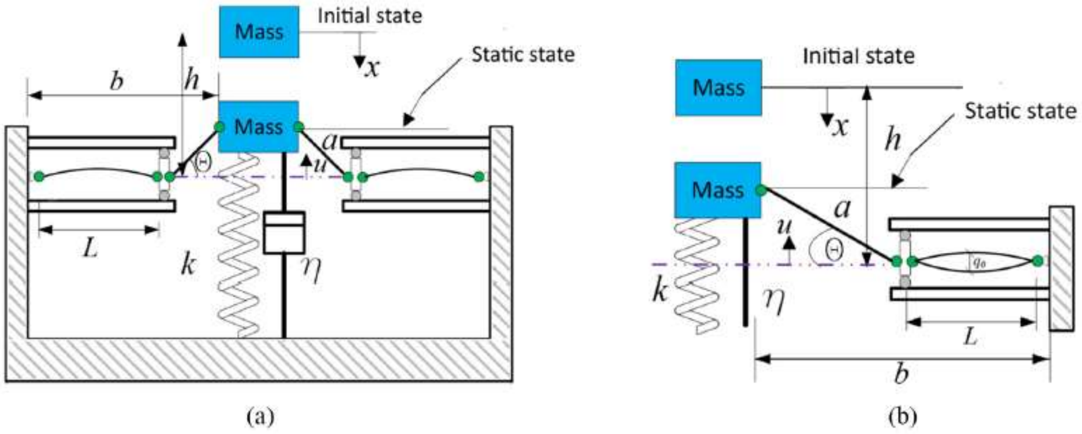

Fig.2.10 Proposed isolation system using Euler buckled beams with bar connected to the seat and (b) detailed part of the seat. [14]

Based on this, X. Liu et al. **[15]** investigated a QZS vibration isolator consisting of a Euler bucked strut and a linear damper-spring. Through adding Coulomb friction by a linear transmissibility at the resonance frequency and decrease the effect of the excitation performance as known in Fig.2.11.

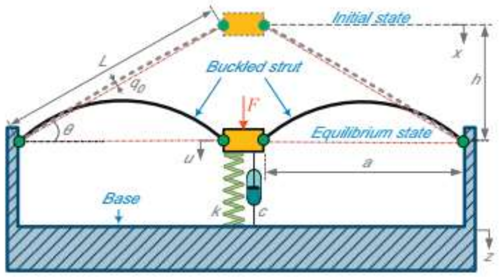

Fig.2.11. Schematic model of Quasi-zero stiffness isolator with Coulomb Damping.[15]

Moreover, in order to enrich the vibration effectiveness, it is necessary to supplement the executive structure like cylinder or motor which makes the isolation system more complex and expensive. Based on these, employing the HSLDS to develop the isolator.

C. Liu et al. [16] experimented a QZS vibration isolator with five transverse groove springs as shown in Fig.2.12. The results show the good isolation performance, the wide frequency range and low peak transmissibility.

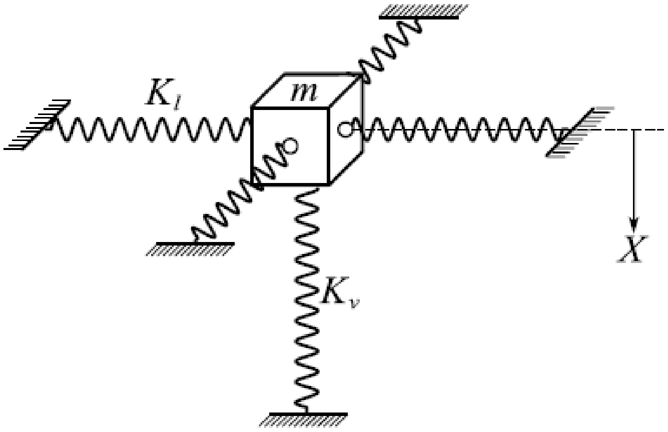

Fig 2.12 Simplified mechanical analysis model of the five-spring QZS vibration isolator (this position is just the static equilibrium position) [16]

K. Ye et al. [17] proposed a coupled translational-rotational QZS vibration isolator in Fig.2.13, which uses the cam-roller mechanism to integrate the two motions above and isolate the vibrations in two directions simultaneously, can exhibit the better isolation performance in the band of low frequency than that of the linear system. Through simulation, the relation between the amplitude and frequency can be investigated.

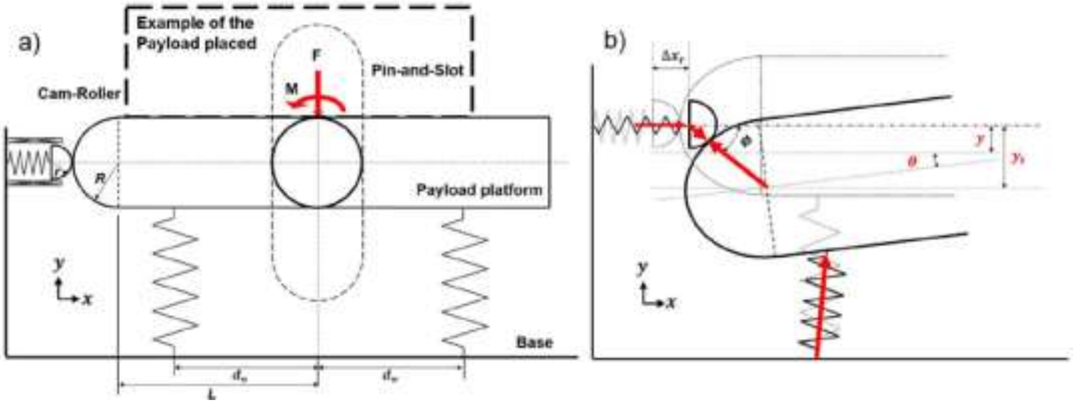

Fig.2.13 Mechanism of the proposed translational-rotational QZS structure: (a) the initial condition, (b) with force and moment applied [17]

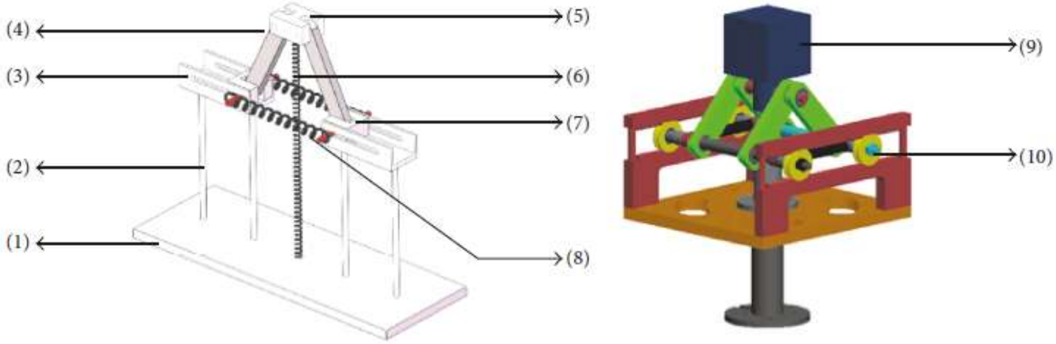

Fig.2.14 Three-dimensional vibration isolation diagram: (1) base, (2) support column, (3) a skateboard, (4) a connecting rod, (5) stage, (6) vertical springs, (7) slider, and (8) tension spring

(b) 3D-modeling of the vibration isolator: (9) isolated objects and (10) rollers [18]

Another QZS vibration isolator combining a tension spring with a vertical linear spring is studied by Q. Meng et al. [18] as in Fig.2.14. This investigation is useful for rehabilitation application because of the low stiffness and transmissibility. The vibration isolator includes the two horizontal springs with the vertical spring, in which the stiffness of these springs can be adjusted leads to the system natural frequency reduce, in consequence, widen the frequency band towards the low frequency.

For example, T.D. Le et al. [19-20] analyzed theoretically and simulated a low frequency vibration isolator as presented in Fig.2.15, showing a resonant peak including the amplitude and frequency lower than that of equivalent linear isolator, the characteristic of this system is a symmetric negative structure both to reduce the dynamic stiffness and to remain the load supporting capacity through adjusting the system geometry parameters to regulate the system stiffness. The simulation results show that the load is remained at equilibrium position by the balance of the compressed force of vertical spring and gravity force. Therefore, the load bearing ability is only dependent on the vertical spring stiffness and its initial deformation.

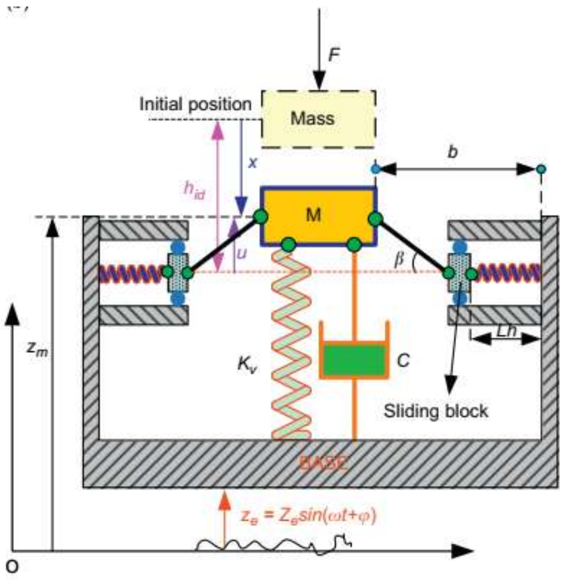

Fig.2.15. A QZS vibration isolation model for low frequency as designed in [19-20]

X. Sun et al. [21] designed a time-delayed active control to improve the QZS vibration isolator the spring and time-delayed (hình 2.16) which can be able to control the results (a) the controller is not to change the static characteristic, for example, static equilibrium state but the dynamic state delayed-time is shown. In a switch which is active control;(b) controlled spring can change the natural frequency of the isolator to enlarge the dynamic stiffness to obtain the control objective; (c) for external excitation load choosing the proper delayed controller to decrease the transitional time and increase the response speed; (d) For external harmonic load, the controller effect on vibration isolation in the resonant region. Thus, active time-delayed control to expand the isolation band without adjusting the structure.

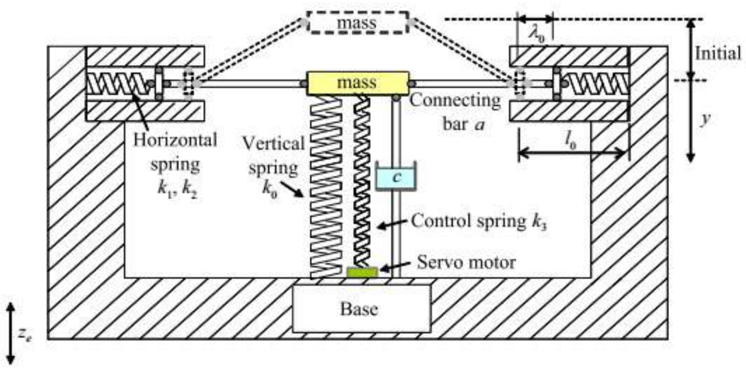

Hình 2.16. Vibration isolator with time delayed active control strategy [21]

A concept of sandwich plate-type elastic metastructures is suggested by D. Cheng [22] shown in Fig. 2.17 in which the grid sandwich plate structure has excellent vibration isolation effectiveness characteristic. the geometrical parameters modulate the subwavelength flexural wave band-gap effectively.

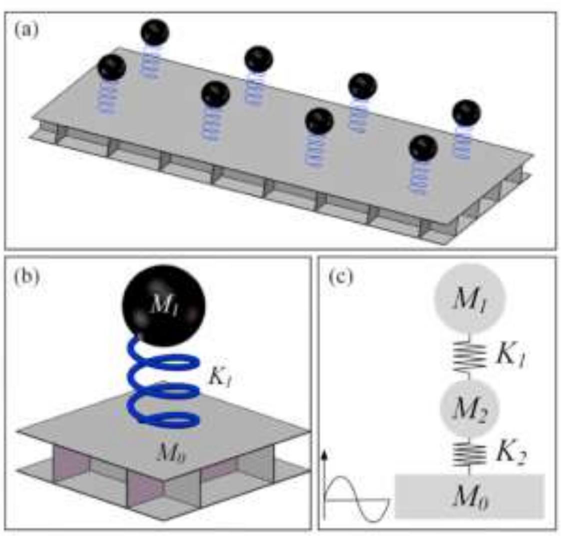

Fig. 2.17 (a) Schematic diagram of local resonant sandwich plate; (b) The unit cell of the spring mass system; (c) Two degrees of freedom 'spring-mass' model of the plate-type elastic metamaterial. [22]

An innovation bio-inspired toe-like structure was introduced by G. Yan et al. [23] in Fig.2.18 which was composed of two rods and a linear spring. The isolation effectiveness towards the low frequency was tested to verify. The isolation vibration range is broadened.

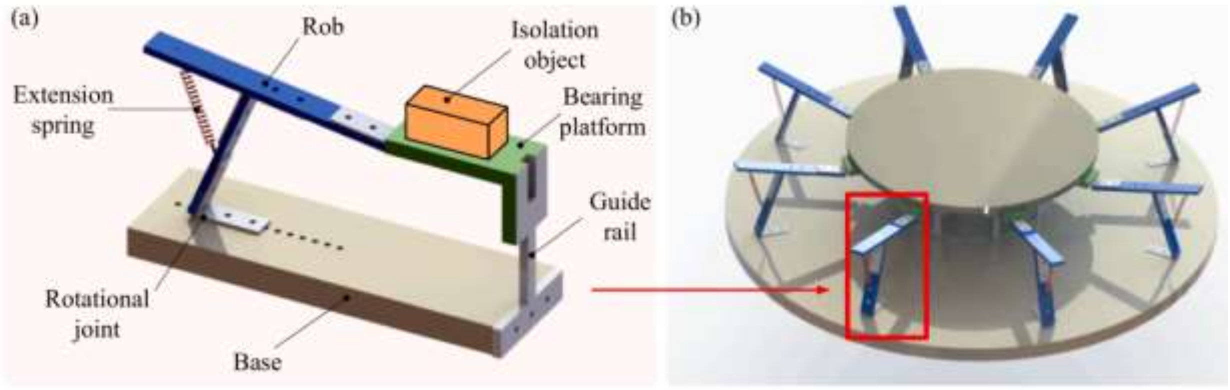

Fig. 2.18 Design of toe-like vibration isolator for vibration isolation in vertical direction inspired by the toe. (a) single TLS for vibration isolation; (b) combination of multiple TLS [23]

Another bionic model of a variable stiffness vibration isolated joint based on human structure, the author of this paper suggested an isolator, which is composed by leaf spring and connecting rod by a universal joint, is suggested by R. Chen [24] illustrated in Fig. 2.19. This model has compact structure, the system stiffness is easy to adjust through regulating the parameters of leaf spring, this maybe vary application in practice.

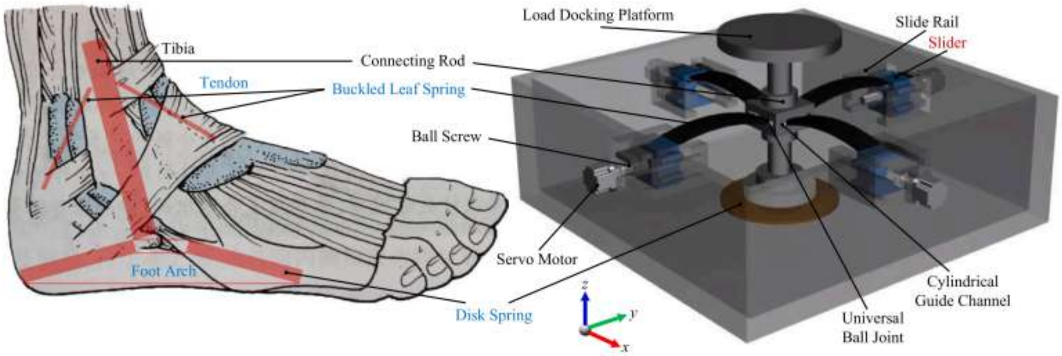

Fig. 2.19. Bionic model of a variable stiffness vibration isolated joint [24]

A geometric anti-spring isolator as in Fig. 2.20 is investigated by L. Yan et al. [25] which consists of several quasi-trapezoidal blade spring which are built flat and bent under the load. The numerical and experimental results show that the effective isolation performance, the relation between changing the payload and vibration isolation performance.

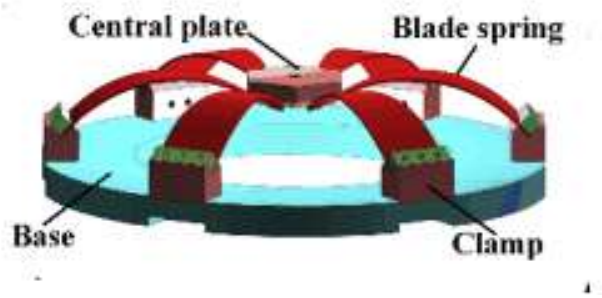

Fig. 2.20. The model of the GAS isolator. (a) Schematic diagram of the GAS isolator.[25]

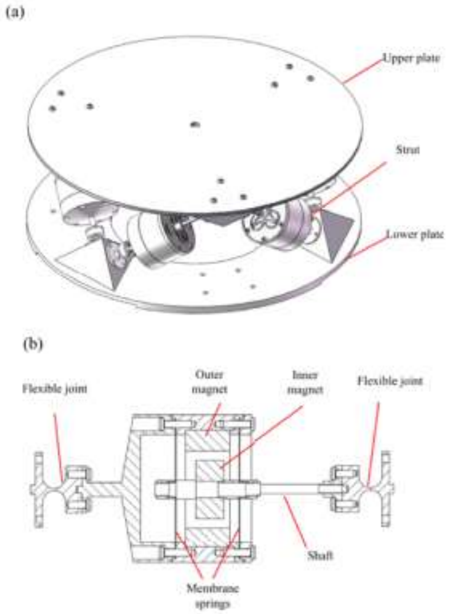

Fig.2.21. Stewart vibration isolator **[26]**

Besides, magnetic springs have been used to study the low frequency vibration isolator. For instance, a compact QZS Stewart isolator which can be applied widely to isolate vibration for 1-6 degrees of freedom systems has been studied to use. Y. Zheng et al. [26] improved the effectiveness of suspension as shown in Fig. 2.21 in which negative magnetic stiffness spring is connected to six trusses. The resonant frequency of the system can be reduced in 6 degrees of freedom, extending the low frequency but remaining the load bearing ability combining the merits of active vibration isolation and high static low dynamic stiffness method.

Y. Zheng et al. **[27]** analyzed and experimented the negative stiffness magnetic spring consisting of a pair of coaxing ring permanent magnetics in parallel with the mechanical spring (hình 2.22) to reduce the resonance frequency and achieve the desired isolation effectiveness. The experimental result conformed the resonance frequency of the isolator which can be reduced to 5.8 Hz.

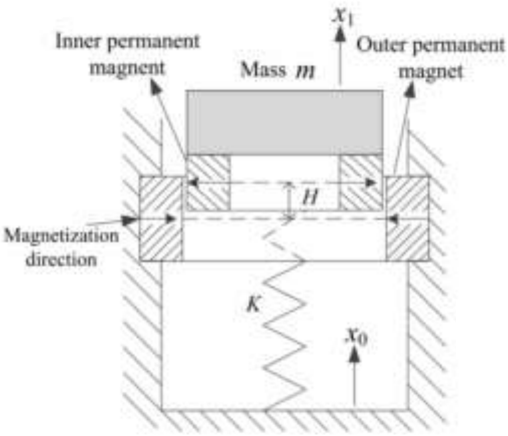

Fig. 2.22. Isolated mode proposed by Y. Zheng et al. **[27]**

Based on Maxwell normal stress, F. Zhang et al. [28] designed and validated experimented an innovative magnetic negative stiffness isolation system for enhancing isolation effectiveness in the low frequency range which is presented in Fig. 2.23.

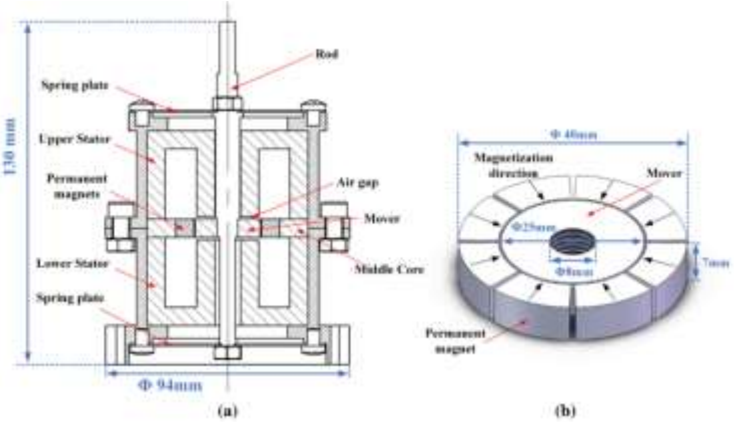

Fig. 2.23. Configuration of MNSI based on Maxwell magnetic normal stress. (a) Cross-section view of isolator; (b) Configuration of excitation mechanism.[28]

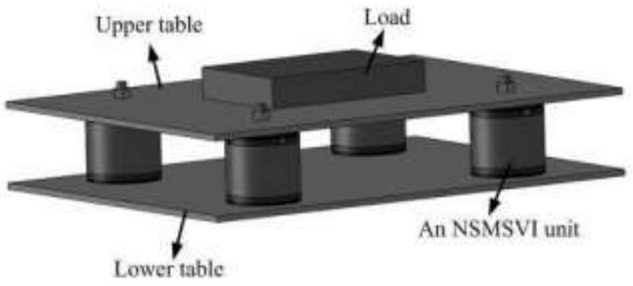

Fig. 2.24. Configuration of isolator designed by [29]

For purpose of the decreasing of the peak frequency and expanding of the isolation frequency towards the low frequency band, an alternative model of QZS isolator as shown in Fig. 2.24 in which the magnetic spring is with combined rubber membrane is proposed by Q. Li et al. [29]. Besides, a mount design of the low frequency multi-direction isolator is presented by G. Dong et al. [30] which is constructed by three ring magnets magnetized axially shown in Fig.2.25. The isolation range was expanded. The stiffness of the system may be decreased until zero in two horizontal directions. This a one of the low frequency multi- direction vibration isolators.

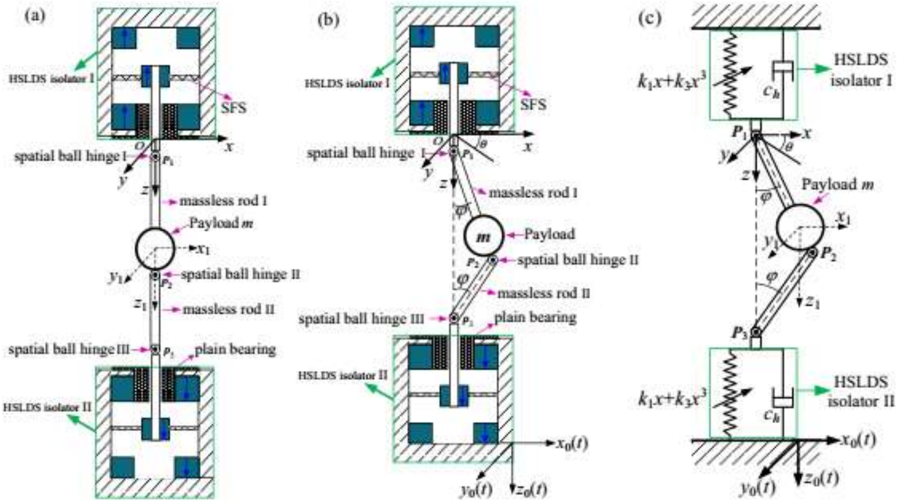

Fig. 2.25. Schematic diagram of the multi-direction isolator. (a) Static equilibrium position; (b) the base excitations applied to the isolator; (c) mechanical model [30]

A new kind of QZS system as in Fig. 2.26 including magnetic springs and cables was studied by C. Liu et al. [31]. This model, which includes two magnetic springs having radial magnetization and eight cables, is designed to improve the vibration isolation ability in different direction in horizontal plane. The stiffness of the magnetic, which is prototyped experimentally, can be regulated to improve the range of zero stiffness region, the vibration effectiveness reaches lower than the excitation.

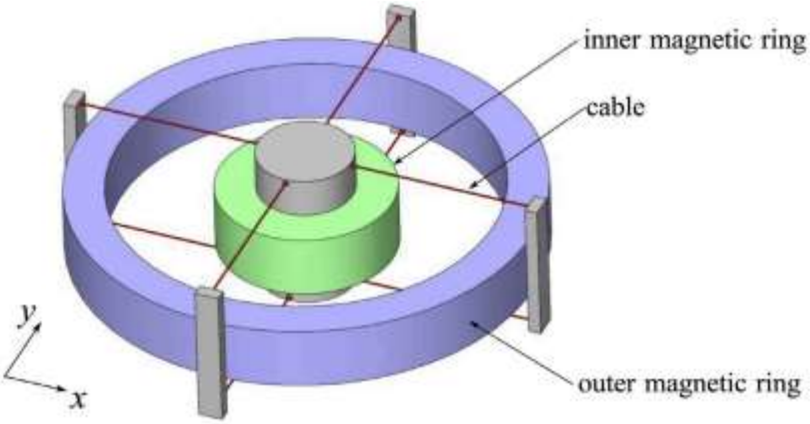

Fig.2.26. Schematic diagram the conceptual model of IP-QZS vibration isolator [31]

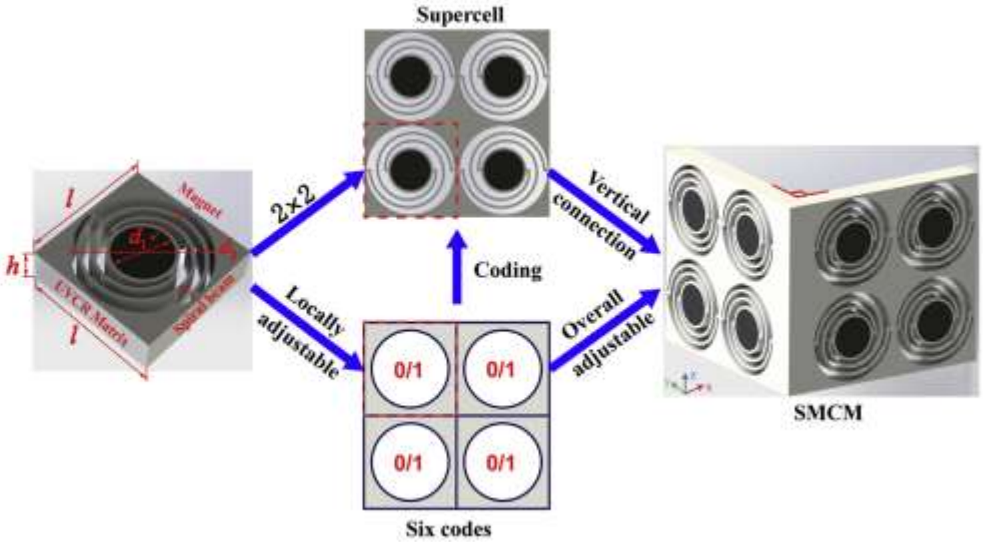

Fig. 2.27. Design of the SMCM with the supercells connected vertically [32]

A stiffness-mass-coding metamaterial vibration isolation model was designed by C. Li et al. **[32]** indicated in Fig.2.27 which is composed of four local resonators. This isolator may be integrated with the controller, which makes it become an active isolator, is widely practical application. Through regulating the distance between two magnets the nonlinear magnetic force is adjusted, ang a new concept on the low-frequency broadband tunability is provided in this work.

Besides, S. Yuan et al. [33] developed an isolator containing three coils with a ring magnet (hình 2.28) by controlling the current to the coils to improve the isolation performance under violent vibration conditions. The experimental results proved that this isolator is suitable for large excitation and can be tuned online. Because of stiffness, the isolation performance of the magnetic spring isolator can be improved. But the drawback of magnetic spring is that only when it has low load. Accordingly, application limitation of the magnetic spring is inevitable.

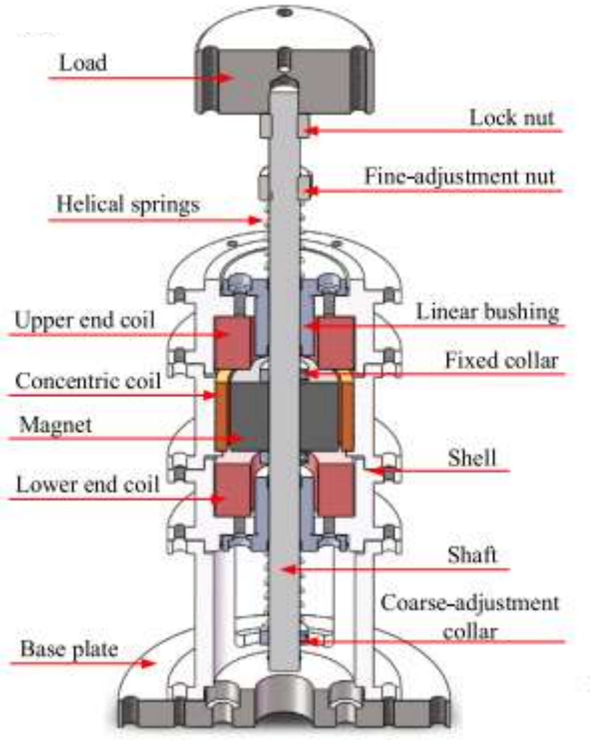

Fig. 2.28. Configuration of isolator designed by [33]

Although present QZS vibration isolation models can offer premising effectiveness for low frequency vibration isolation, there exist disadvantages such as: QZS vibration isolation model only offers the best effectiveness under an optimal isolated load. To remain the isolated effectiveness, the dynamic stiffness of the model must be adjusted properly as there is an increase or reduction in the weight of the isolated object requires, indicating that the restoring properties of springs must be regulated even the elastic element must be replaced. This requirement is very difficult for QZS vibration isolation models using mechanical or permanent magnetic springs.

Another type of elastic element, which can overcome issues mentioned above, is air spring due to easy control of the spring coefficient and high bearing capacity. Thus, in recent years, this type has been applied widely in vehicle suspension field [34-38], vibration isolation platform [39-41], etc. Researching the characteristic of rubber air spring has been motivated by many scholars, engineers [42-44].

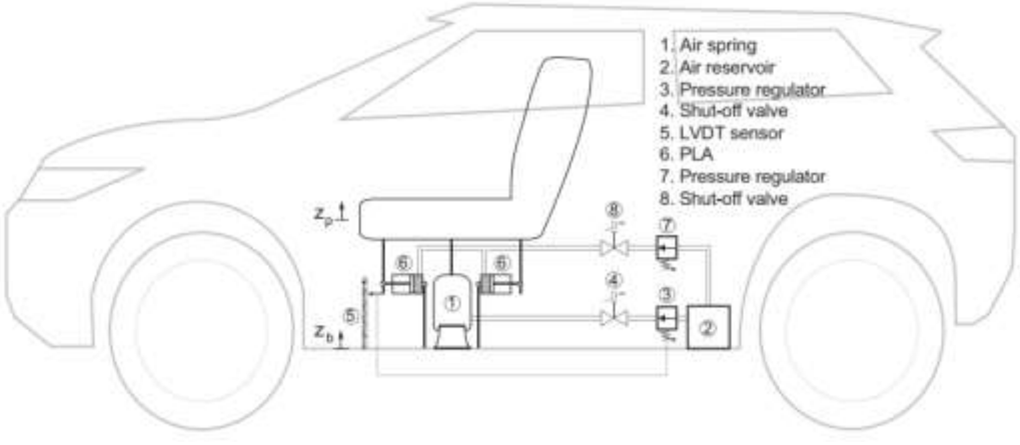

Fig. 2.29. Schematics of the NSS on a vehicle.[45]

Particularly, a set of two Pneumatic Linear Actuators (PLAs) [45] in Fig. 2.29 added to a seat supported by a pneumatic spring which makes the seat more comfortable. In this work shows the advantages of using pneumatic spring in a driver seat by adjusting the pressure of the pneumatic spring.

Therefore, it is interesting to combine the mechanical and pneumatic system to develop a quasi-zero stiffness vibration isolation model which can the isolation region toward low frequency. Adjusting the dynamic stiffness of the proposed model can be carried out simply and easily to remain the isolation effectiveness as the isolated load is changed simultaneously, the load bearing capacity of the proposed model is still ensured.

Nguyen et al. [46] introduces a new vibration isolator as in Fig.2.30 which is composed by two air bellow elements in horizontal direction in perpendicular to a sleeve -type air spring element. This system can create a high static and low dynamic stiffness even achieve zero through controlling the pressure in the air spring. This work can improve the vehicle seat because the decreasing in seat displacement and the vibration isolation performance under low excitation frequency is excellent.

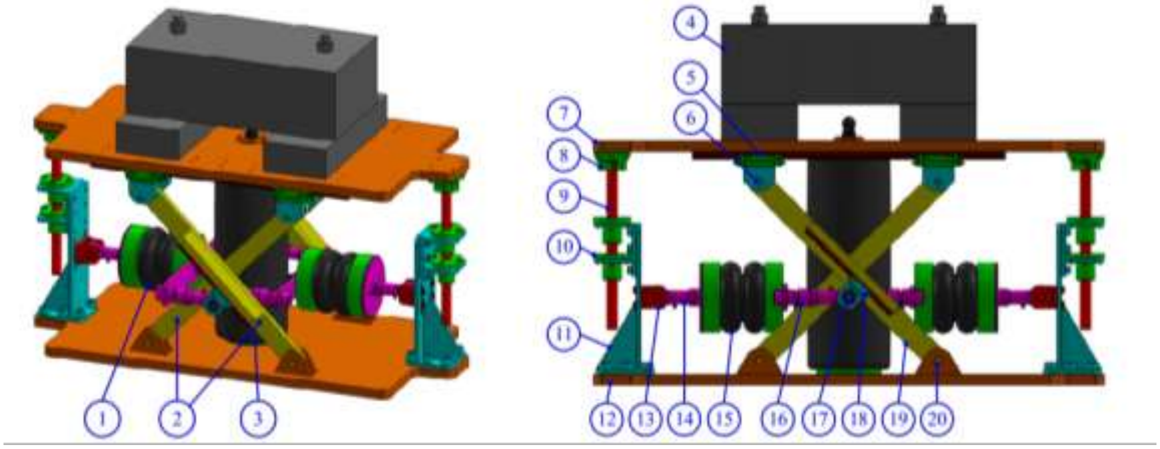

Fig. 2.30. (**a**) Model of ASVIS with NSS, (**b**) schematic diagram of ASVIS at the static equilibration position [46]

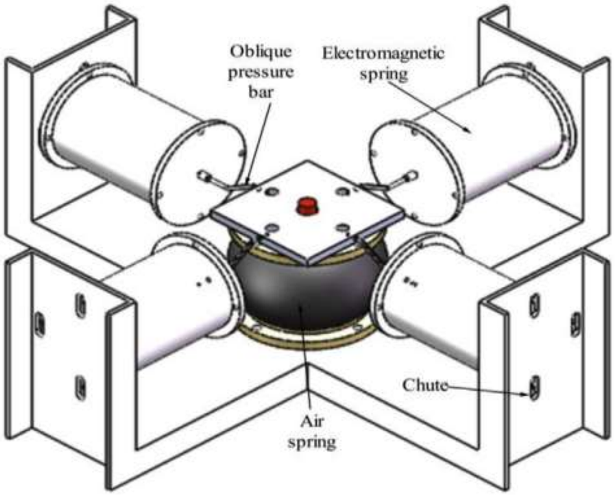

Fig. 2.31. Structure of magnetic-air hybrid quasi-zero stiffness vibration isolation system [47]

In previous studies, the QZS isolator is usually constructed by the two springs or magnet spring. In this study, a magnetic-air hybrid quasi-zero stiffness vibration isolation system is proposed by Y. Jiang et al. [4], which is composed by an air spring in the vertical direction in parallel with an electromagnetic springs in the horizontal direction, indicated in Fig.2.31. This magnetic-air hybrid QZS vibration isolation system obtains both the isolation performance and meet with variable support load.

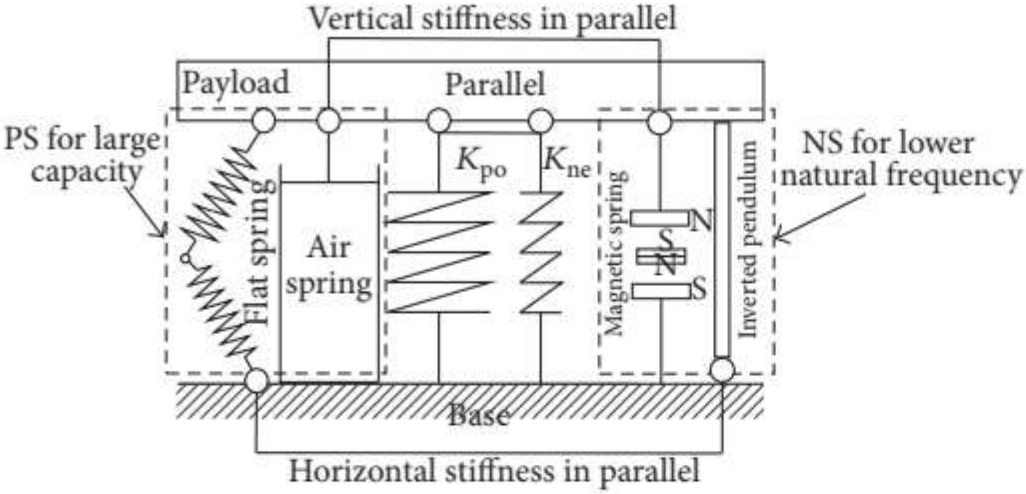

Fig. 2.32. The structure sketch of passive isolator using PNSP [48]

Another isolation system, which is the composing of two opposite mechanisms, is the study of M. Wang et al. by using magnetic spring [48] plotted in Fig.2.32. The mentioned structure is verified the validity as well as superiority through the experiment. This system also solves the problem about both the low stiffness and load bearing ability.

Y. Zhao et al. [49] proposed an electromagnetic active-negative-stiffness generator which is illustrated in Fig. 2.33. In which the micro-vibration of an optical platform was examined by nano-resolution laser interference sensors. The experimental results proved the meaningful effectiveness of the low-frequency vibration isolator of the proposed model which is constructed by precision electromagnetic actuators counteracted the positive pneumatic.

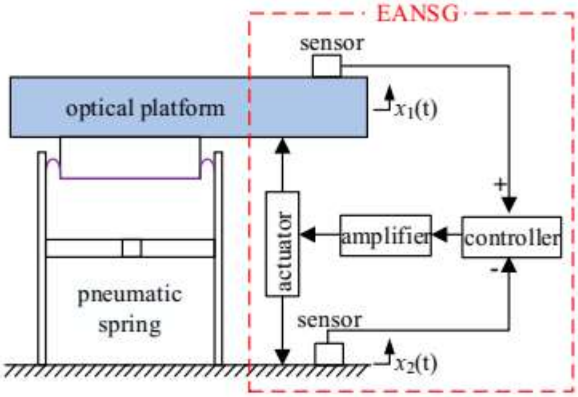

Fig. 2.33. Scheme of electromagnetic active-negative stiffness generator (EANSG) [49]

SUMMARY OF CHAPTER 2

The advantage of the vibration isolation model using air springs is to possess the load supporting capacity and low static deformation. Specially, the stiffness of the spring is able to be adjusted. Nevertheless, the drawback of the air springs is its hysteresis and complex dynamic response. Hence, when it is applied for the quasi-zero stiffness vibration isolation system (QSVIS) causing the dynamic response complex. It brings the same results for applying into the QSVIS resulted in the dynamic response of the system to be more complicated including the bifurcation and frequency jump phenomena. This I sone of the significant effects on the isolation performance which has not been discovered completely in previous studies.

Taking the strong points of the quasi-zero stiffness vibration isolation method as well as air springs, this thesis will design an innovative quasi-zero stiffness vibration isolation system using air springs. The dynamic response of the system will be analyzed comprehensively. Since then, a method for designing a vibration isolation will be proposed to meet the practical application.

CHAPTER 3

FUNDAMENTAL OF RELATIVE THEORIES

In order to realize contents in this thesis, some fundamental theories have been used to discover the dynamic response as well as vibration transmissibility of the system such as thermodynamics, frictional model, viscoelastic model. Additionally, the mathematical methods including Normal form, Multi-scale, Runge-kutta, Poincare section along with Genetic Algorithm are employed to find solutions for the proposed system.

3.1. Air spring:

3.1.1 Introduction

A system which uses compressed air as its elastic element is considered as an air spring. It can be classified into two categories including rubber bellow and pneumatic cylinder. The load bearing capacity of an air spring depends on the effective area and internal air pressure. The air spring offers a lot of superior merits such as low static deformation, large and various load supporting ability, adjustable elasticity thorough changing the pressure within spring, meaning that the spring rate is variable and controllable. Additionally, another advantage is that the energy-storage capacity of the air spring is greater than that of mechanical one. Generally, air springs have not only low resonance frequencies and static deformation but also smaller overall length than the mechanical spring. Especially, along with elastic function, the air spring can work as a damper. That is the reason why air spring systems gain more and more popularity in practice. Hence, in order to broaden the isolation region toward low frequency, studying the use of the air spring for vibration isolation systems is necessary.

3.1.2 General structure of rubber bellow

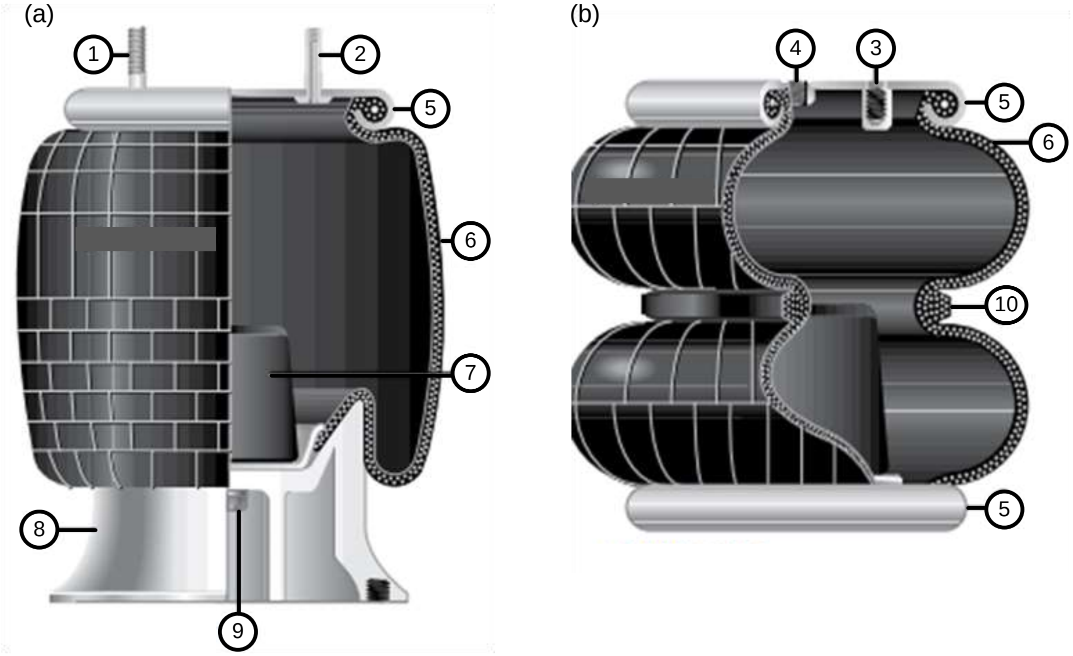

Fig.3.1 Configuration of a rubber air spring: (a) Reversible sleeve, (b) Convoluted [50]

There are basic types of rubber bellow such as reversible sleeve, convoluted as shown in Fig. 3.1. It comprises some following parts:

- **Mounting stud** (1), which is a part, is fixed on the bead plate used to connect the air spring to the suspension.
- **Combination stud** (2) is to combine the mounting stud and the air fitting.
- **Blind nut** (3) which provides an alternative mounting system to the stud is a fixed part of the bead plate. Air fitting hole which is tapped for air to enter the part.
- **Air fitting hole** (4) is a hole allows air entrancing which is tapped.
- **Bead plate** (5) which is made of steel for corrosion resistance closes the top end of the flexible member. It is permanently crimped on to the bellows to form an airtight assembly. It is assembled attachment to the vehicle structure through studs, blind nuts, brackets, or pins.

- **Rubber bellows** (6) is the main part of an air spring. Its main function is to contain a column of compressed air. It is constructed from layers including the inner, middle and outer layer as shown in Fig. 3.2.
    - Inner liner is made of a rubber.
    - First ply is a layer of fabric-reinforced rubber with the cords at a specific bias angle.
    - Second ply is a second layer of fabric reinforced rubber with the same bias angle which is laid opposite of the first ply.
    - Outer cover is a rubber outer cover.
- **Internal bumper** (7) is an internal device to prevent damage to the air spring during times when there is no air in the system.
- **Piston** (8) which may be made of aluminum, steel, or engineered composites. The pistons with the thread holes are used to ensure the assembly to the mounting surface.
- **Piston bolt which** (9) attached the piston to the bellows assembly
- **Girdle hoop (optional)** (10) is a ring between the convolutions of the convoluted-type air spring.

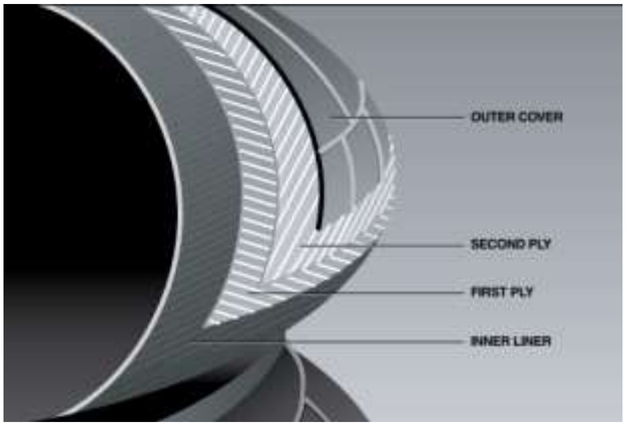

Fig. 3.2 Structure of the rubber bellow

3.2. Mathematical model of the compressed air

Supposing a working chamber as shown in Fig. 3.3, according to the first law of thermodynamics [51], the energy balance in the working chamber volume is expressed by Eq. (3.1)

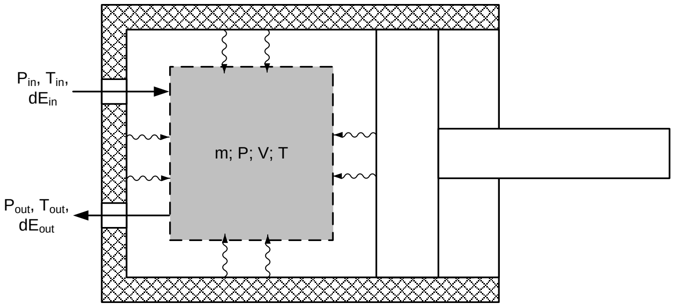

Fig. 3.3. Schematic diagram of the pneumatic working chamber

$$dE_{ch} = dE_{in} - dE_{out} - dE_{ae} - Q \tag{3.1}$$

in which dE_{in} and dE_{out} are the air energies of input and output lines, dE_{ch} is the air energy in spring, dE_{ae} is the work of air expansion and Q is the heat exchange with environment. These energies are given as following:

$$\begin{aligned} dE_{in} &= C_p T_{in} G_{in} \\ dE_{out} &= C_p T\, G_{out} \\ dE_{ch} &= C_v m\, dT + C_v T dm \\ dE_{ae} &= PdV \\ Q &= \alpha a \Delta T \end{aligned} \tag{3.2}$$

where

C_{p} and C_{v} are specific heat capacities at constant pressure and volume, respectively,

T_{in} is the temperature of air at the inlet,

m_{air}, *P, V and T* are the mass, pressure, volume and temperature of the air in the pneumatic working chamber,

G_{in} and G_{out} are mass low rates at inlet and outlet, α is the heat transfer coefficient,

a is the heat transfer surface area,

ΔT is the temperature difference between the air inside working chamber and environment.

It is assumed that the heat transfer between the air inside working chamber of the air spring and environment is ignored and the air is considered as ideal gas, we have:

$$\begin{aligned} & C_v T dm = nT_{in}G_{in} - nT\,G_{out} - \frac{P}{C_v}dV \\ & PV = mR_{air}T \end{aligned} \tag{3.3}$$

herein: $n=C_p/C_v$ is the ratio of specific heat capacity,

R_{air} is the gas constant (R_{air}=287J/kg.K).

3.3. Frictional model of pneumatic cylinder and rubber material

3.3.1. Frictional model of pneumatic cylinder

The friction is generated from relative motion between rod and cylinder. According to [52] the friction model (F_f) is a combination between Coulomb friction, viscous friction and static friction. The characteristic of this model is presented by a Stribeck curve in both the extending and retracting strokes of a pneumatic cylinder as shown in Fig. 3.4.

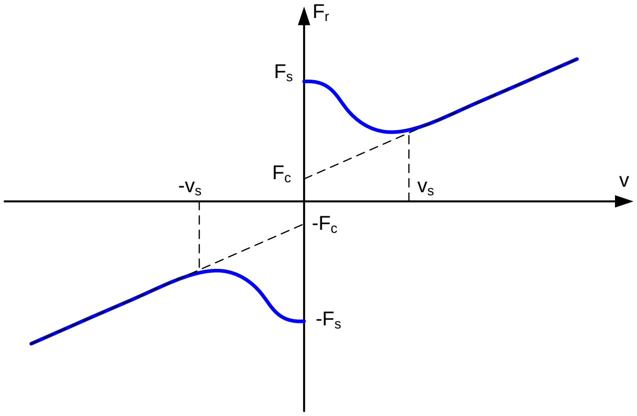

Fig. 3.4. Stribeck curve

The frictional force model is calculated as below:

$$F_f = F_c + (F_{st} - F_c)e^{-(v_r/v_s)^{n_s}} + \sigma v_r \tag{3.4}$$

in which

F_c is Coulomb friction force,

F_{st} is the static friction force,

v_s is the Stribeck velocity,

v_r is the relative velocity between two contacting surfaces,

σ is the viscous friction coefficient,

n_s is the exponent of the Stribeck curve.

3.3.2. Frictional model of rubber material

The friction is generated between filled and cord fabric. The frictional model of the rubber material is expressed through Berg's rubber model [53] which enables a good fit to the hysteresis loop as the inflated bellow is compressed. The friction force depends on the relationship between the displacement x and reference displacement (x_{ref}), given by:

$$\begin{aligned} &F_{fri} = F_{ref} && \text{for } x = x_{ref} \\ &F_{fri} = F_{ref} + \frac{x - x_{ref}}{x_2(1-a) + (x - x_{ref})}\left(F_{fri\max} - F_{ref}\right) && \text{for } x > x_{ref} \\ &F_{fri} = F_{ref} + \frac{x - x_{ref}}{x_2(1-a) - (x - x_{ref})}\left(F_{fri\max} + F_{ref}\right) && \text{for } x < x_{ref} \end{aligned} \tag{3.5}$$

in which F_{ref} is the reference force along with the displacement x_{ref} called the reference state (x_{ref}, F_{ref}). F_{frimax} is the maximum friction force. x_2 is the displacement at which the friction force is developed to the value of $F_{\text{frimax}}/2$ when it starts from $x=0$, $F_{\text{fri}}=0$. An auxiliary quantity a is equal to $F_{\text{fri}}/\ F_{\text{frimax}}$ ranging from -1 to 1. In the case, the air spring is excited by a harmonic signal with the amplitude x_{o} and frequency ω, the steady-state amplitude of the frictional force is expressed as below:

$$F_{frio} = \frac{F_{fri\max}}{2x_2}\left(\sqrt{x_2^2 + x_o^2 + 6x_2x_o} - x_2 - x_o\right) / \, 2x_2x_o \tag{3.6}$$

As shown in Fig. 3.5 K_{max} is the maximum tangent stiffness as the displacement is close to x_{o}. The dot lines are representative for the linear stiffness K_{e}, the vertical distance between these lines approximately equals $2F_{\text{frimax}}$. The displacement x_2 is obtained as below:

$$x_2 = \frac{F_{fri\max}}{K_{\max} - K_e} \tag{3.7}$$

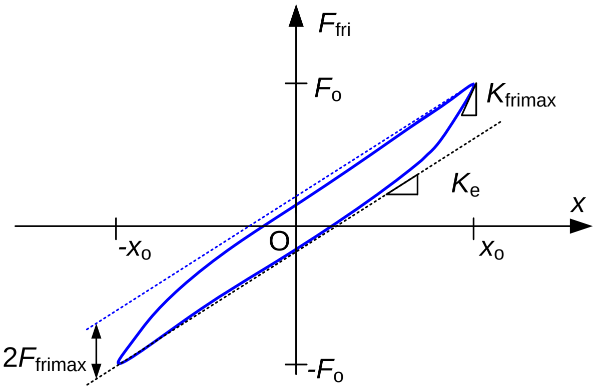

Fig. 3.5 Friction force with respect to displacement

3.4. Viscoelastic model of the rubber material

The viscoelasticity of the rubber bellow is one of the properties causing the hysteresis phenomenon in the dynamic behavior of the rubber air spring. Fraction Kelvin-Voigt model is one of the powerful methods for describing the characteristic of the rubber-like parts [54]. It consists of the spring and springpot in parallel as shown in Fig. 3.6 where K_{vie} is the stiffness and b, $0<c<1$ are the springpot parameters. The motion equation of the fractional Kelvin-Voigt model is obtained as following:

$$F_{ve}(t) = K_{vie}x(t) + bD_t^c x(t) \tag{3.8}$$

in which $D_t^c x(t)$ is the fractional derivation of the displacement x(t) versus the time. By applying the definition of Grünwald fraction derivative [**55**], we have:

$$D_t^c x(t) = \lim_{\Delta t \to 0}\left(\Delta t^{-c}\sum_{i=0}^{N} B_{i+1} f(t - i\Delta t)\right) \tag{3.9}$$

where $B_{i+1} = (-1)^i \begin{pmatrix} c \\ i \end{pmatrix} = \dfrac{\Gamma(i-c)}{\Gamma(-c)\Gamma(i+1)} = \dfrac{-c+i-1}{i} B_i$ and N is integer

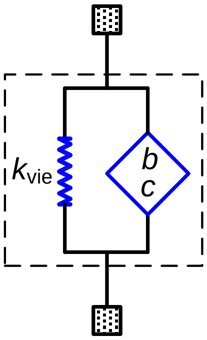

Fig. 3.6. Diagram of Fraction Kelvin-Voigt model

3.5. Normal form method

Normal Form method [56] is used to find the fundamental solution of the dynamic equation, the equation of motion may be written as following:

$$\ddot{v}+\Lambda v+\mathcal{N}_v(v,\dot{v},r)=P_v r \tag{3.10}$$

with *x* is the *n* x *1* vector, Λ the *n* x *n* matrix, n is the degree of freedom in the system. *P*$_{\mathrm{v}}$ is the *n* x *2* forcing amplitude matrix, r=$\{r_p, r_m\}^T$ is a forcing vector with $r_p = e^{i\Omega t}$ and $r_p = e^{-i\Omega t}$, where Ω is the forcing frequency. $\mathcal{N}_v(v,\dot{v},r)$ is a *n* x *1* vector of nonlinear terms given by:

$$\mathcal{N}_v(v,\dot{v},r)=\varepsilon\,\mathrm{n}_1(v,\dot{v},r)+\varepsilon^2\,\mathrm{n}_2(v,\dot{v},r)+\varepsilon^3\,\mathrm{n}_3(v,\dot{v},r)+\ldots \tag{3.11}$$

In which: ε is a small parameter, the near-identity transform can be applied follow:

$$v=u+h(u,\dot{u},r) \text{ where } h(u,\dot{u},r)=\varepsilon\,\mathrm{h}_1(u,\dot{u},r)+\varepsilon^2 h_2(u,\dot{u},r)+\ldots. \tag{3.12}$$

The post-transformed equation of motion:

$$\ddot{u}+\Lambda u+\mathcal{N}_u(\mathrm{u},\dot{u},r)=P_u r \tag{3.13}$$

herein: $\mathcal{N}_u(\mathrm{u},\dot{u},r)=\varepsilon n_{u1}(\mathrm{u},\dot{u},r)+\varepsilon^2 n_{u1}(\mathrm{u},\dot{u},r)+\varepsilon^3 n_{u3}(\mathrm{u},\dot{u},r)+\ldots$ (3.14)

Combining Eq. (3.8) into Eq. (3.11), then the balance of ε^0 and ε^1 term, we have:

$$\begin{aligned}
&\varepsilon^0:\ P_u r = P_v r\\
&\varepsilon^1:\ n_{u1}(\mathrm{u},\dot{u},r)-\frac{d^2}{dt^2}\left(h_1(\mathrm{u},\dot{u},r)\right)=\Lambda h_1(\mathrm{u},\dot{u},r)+n_{u1}(\mathrm{u},\dot{u},r)
\end{aligned} \tag{3.15}$$

The state vector *u* can be split into components

$$u = u_p + u_m \tag{3.16}$$

With $u_{np} = \left(\dfrac{U_n e^{-i\theta_n}}{2}\right) e^{i\omega_{rn} t}; u_{mp} = \left(\dfrac{U_n e^{-i\theta_n}}{2}\right) e^{-i\omega_{rn} t}$

The vector n_1, h_1, $n_{\mathrm{u}1}$ are expressed as below:

$$\begin{aligned} n_1(u,\dot{u},r) &= [f]u^*(u_p,u_m,\mathrm{r}), \\ h_1(u,\dot{u},r) &= [\mathrm{b}]u^*(u_p,u_m,\mathrm{r}), \\ n_{u1}(u,\dot{u},r) &= [a]u^*(u_p,u_m,\mathrm{r}), \end{aligned} \tag{3.17}$$

where u^* is a column vector (of size L x 1) containing all the combinations of u_p, u_m and r

From Eq. (3.17), Eq. (3.15) can be rewritten as following:

$$[a]u^*(u_p,u_m,\mathrm{r}) - b\frac{d^2}{dt^2}\Big(u^*(u_p,u_m,\mathrm{r})\Big) = \Upsilon\Upsilon u^*(u_p,u_m,\mathrm{r}) + [f]u^*(u_p,u_m,\mathrm{r}) \tag{3.18}$$

where: $\Lambda = -\Upsilon\Upsilon$

in which u^* is a column vector having size of L x 1, $n^*, h^*,$ and n_u^* are the n x L containing coefficient terms. The *ℓth* element in u^* is expressed as following:

$$u_\ell^* = r_p^{m_{\ell p}} r_m^{m_{\ell m}} \prod_{k=1}^{n}\Big(u_{pk}^{s_{pk\ell}} u_{mk}^{s_{mk\ell}}\Big) \tag{3.19}$$

where $\mathrm{m}_{p\ell}$ and $\mathrm{m}_{m\ell}$ are power indicates.

The time derivative of the ***ℓth*** element of vector u^* is obtained as:

$$\frac{d}{dt}\Big(u_\ell^*\Big) = \frac{\partial u_\ell^*}{\partial r_p}\Big(i\Omega\Big)r_p + \frac{\partial u_\ell^*}{\partial r_m}\Big(-i\Omega\Big)r_m + \sum_{i=1}^{n}\left(\frac{\partial u_\ell^*}{\partial u_{np}}\Big(i\omega_{rn}\Big)u_{np} + \frac{\partial u_\ell^*}{\partial u_{nm}}\Big(-i\omega_{rn}\Big)u_{nm}\right) \tag{3.20}$$

The second derivative of u^* is:

$$\frac{d^2}{dt^2}\Big(u^*(u_p,u_m,\mathrm{r})\Big) = \tilde{\Upsilon}\tilde{\Upsilon}u^*(u_p,u_m,\mathrm{r}) \tag{3.21}$$

herein: $\tilde{\Upsilon}$ is a diagonal matrix of size n x n determined as following:

$$\tilde{\Upsilon}_{\ell} = i\left[\left(m_{\ell p} - m_{\ell m}\right)\Omega + \sum_{i=1}^{n}\left(s_{\ell \mathrm{i}p} - s_{\ell \mathrm{i}m}\right)\omega_{rn}\right] \tag{3.22}$$

From this information, the Eq. (3.16) is rewritten as following:

$$\left([a] - [\mathrm{b}]\tilde{\Upsilon}\tilde{\Upsilon} + \Upsilon\Upsilon[b]\right)u^{*}(u_{p}, u_{m}, \mathrm{r}) = [f]u^{*}(u_{p}, u_{m}, \mathrm{r}) \tag{3.23}$$

Considering non-zero $u^{*}(u_{p}, u_{m}, \mathrm{r})$, letting:

$$[\tilde{b}] = [f] - [a] = -[b]\tilde{\Upsilon}\tilde{\Upsilon} + \tilde{\Upsilon}\tilde{\Upsilon}[b] \tag{3.24}$$

with the (n, ℓ) element in matrix $[\tilde{b}]$ is given by:

$$\tilde{b}_{n,\ell} = \left(\left[\left(m_{\ell p} - m_{\ell m}\right)\Omega + \sum_{i=1}^{n}\left(s_{\ell \mathrm{i}p} - s_{\ell \mathrm{i}m}\right)\omega_{rn}\right]^{2} - \omega_{rn}^{2}\right)b_{n,\ell} \tag{3.25}$$

3.6. Multi scale method [56]

Considering an equation as below

$$\ddot{x} + f(x, \dot{x}, r) = 0 \tag{3.26}$$

By introducing a new independent variable as following:

$$T_{n} = \varepsilon^{n} t$$

where t denotes the time in second, ε is a small constant

It is assumed that the solution of Eq. (3.26) can be represented by an expansion having the form:

$$x(t, \varepsilon) = \varepsilon x_{1}(T_{0}, T_{1}, T_{2}, \ldots) + \varepsilon^{2} x_{2}(T_{0}, T_{1}, T_{2}, \ldots) + \varepsilon^{3} x_{3}(T_{0}, T_{1}, T_{2}, \ldots) + \ldots \tag{3.27}$$

The time derivative becomes expansion in terms of the partial derivatives versus the Tn as following:

$$\begin{aligned} \frac{d}{dt} &= \frac{dT_o}{dt}\frac{\partial}{\partial T_o} + \frac{dT_1}{dt}\frac{\partial}{\partial T_1} + \ldots = D_o + \varepsilon D_1 + \ldots \\ \frac{d^2}{dt^2} &= \frac{d^2T_o}{dt^2}\frac{\partial^2}{\partial T_o^2} + \frac{d^2T_1}{dt^2}\frac{\partial^2}{\partial T_1^2} + \ldots = D_o^2 + 2\varepsilon D_o D_1 + \varepsilon^2\left(D_1^2 + 2D_o D_2\right) + \ldots \end{aligned} \tag{3.28}$$

where $D_n = \partial / \partial T_n$.

3.7. Runge-kutta method [57]

The Runge-Kutta methods is an important family of predictor-corrector methods for approximation of solutions of ordinary differential equations (ODEs) which were developed by German mathematicians C. Runge (1856–1927) and M. W. Kutta (1867–1944)

We shall not derive these methods in fullness but shall give a flavor of how this may be done. In order to solve the system

$$\frac{dy}{dt} = f\,(\mathrm{t}, \mathrm{y}), \tag{3.29}$$

We use Taylor series and as such we write the scheme as

$$y_{n+1} = y_n + ak_1 + bk_2 \tag{3.30}$$

where

$$\begin{aligned} k_1 &= \Delta t f\,(t_n, y_n), \\ k_2 &= \Delta t f\,(t_n + \alpha\Delta \mathrm{t}, y_n + \beta k_1). \end{aligned}$$

In order to derive an equation of this form we start with the Taylor series for

$$y_{n+1} = y(t + \Delta t) \tag{3.31}$$

$$y_{n+1} = y_n + \Delta t f\,(t_n, y_n) + \frac{\Delta t^2}{2} f^{'}(t_n, y_n) + \ldots, \tag{3.32}$$

where the prime denotes a derivative with respect to t. Using the chain rule we can write

$$\frac{df}{dt} = \frac{\partial f}{\partial t} + \frac{\partial f}{\partial y}\frac{\partial y}{\partial t}, \qquad (3.33)$$

but using the original equation

$$(\dot{y} = f)$$

so that

$$y_{n+1} = y_n + a\Delta t f(t_n, y_n) + \frac{\Delta t^2}{2}\left(\frac{\partial f}{\partial t} + \frac{\partial f}{\partial y} f\right).... \qquad (3.34)$$

Let us now substitute the forms for k_1 and k_2 into Equation (3.32), so that

$$y_{n+1} = y_n + a\Delta t f(t_n, y_n) + b\Delta t f(t_n + \alpha\Delta t, y_n + \beta\Delta t f(t_n, y_n)). \qquad (3.35)$$

We now need to expand the last term in this equation, so that

$$f(t_n + \alpha\Delta t, y_n + \beta\Delta t f(t_n, y_n)) \approx f(t_n, y_n) + \alpha\Delta t \left.\frac{\partial f}{\partial t}\right|_{t_n, y_n}. \qquad (3.36)$$

Using this number of points there is no visible difference between the numerical and the exact solution. We can investigate the effect of altering the value of α. This method can be extended to higher orders: for instance, the fourth-order scheme is given by

$$y_{n+1} = y_n + \frac{1}{6}(k_1 + 2k_2 + 2k_3 + k_4) \qquad (3.37)$$

where

$$k_1 = \Delta t f(\mathrm{t}_n, y_n);\ k_2 = \Delta t f(t_n + \frac{\Delta t}{2}, \mathrm{y}_n + \frac{k_1}{2})$$

$$k_3 = \Delta t f(t_n + \frac{\Delta t}{2}, \mathrm{y}_n + \frac{k_2}{2});\ k_2 = \Delta t f(t_n + \Delta t, \mathrm{y}_n + k_3).$$

3.8. Poincaré section [58]

The cross-section Σ that it cuts each phase path transversely in some region of the phase diagram is called a Poincaré section of the phase diagram as shown in Fig. 3.7. Consider A_o (x_o,y_o) on the section Σ, following the phase path through A_o in its direction of flow, it will next cut Σ in the same direction at $A_1(x_1,y_1)$. This point is called first return or Poincaré map of the point A_o. Similarly, $A_2(x_2, y_2)$ is the first return point of $A_1(x_1, y_1)$. This process can be presented as following:

$$(x',y') = p_\Sigma(x,y) \tag{3.38}$$

where (x',y') is the point of first return of the path from (x,y). For successive, first returns starting from A_o is expressed as below:

$$(x_n,y_n) = p_\Sigma^n(x_o,y_o) \tag{3.39}$$

It is worth noting that the time lapse between two successive intersections of a trajectory with a chosen Poincaré section is not a constant.

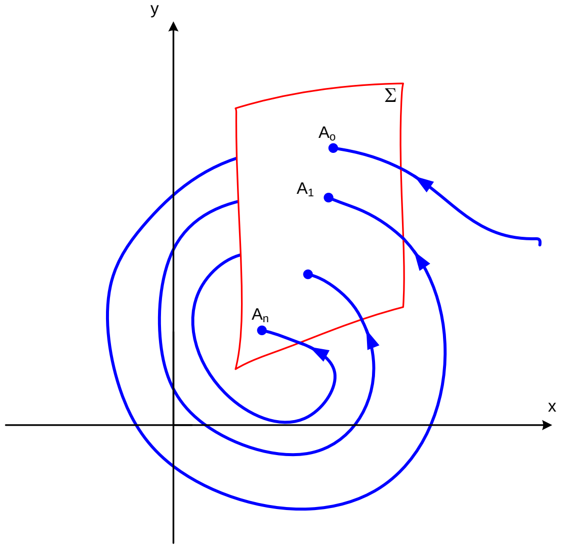

Fig. 3.7. Poincaré section of the phase diagram

The Poincaré map is **used** to analyze the dynamic response of the nonlinear system including bifurcation, resonance, etc. For a steady-state vibration, Poincaré map is formed by sampling the cycle one per forcing period. For instance, if an expected solution having period T, then we plot on the x,y plane a sequence of points determined at time T, 2T, 3T, **etc.** Along the phase paths starting from various states. Result is to obtain the series of data points (x_o,y_o), (x_1,y_1), (x_2, y_2), (x_3, y_3)…for corresponding sampling times as shown in Fig. 3.8.

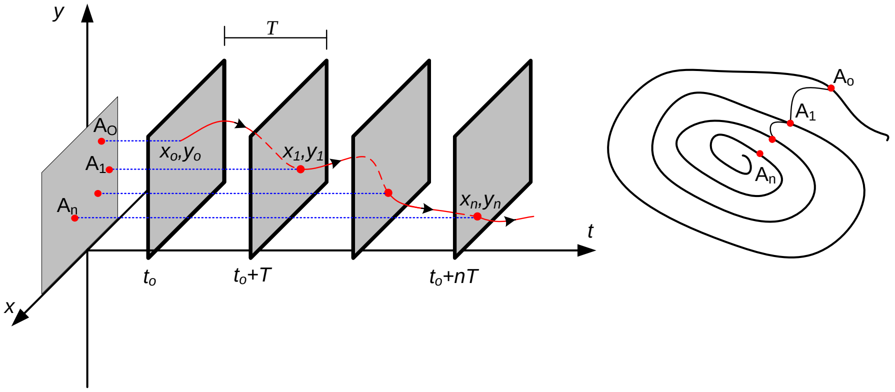

Fig. 3.8 Poincaré map showing the continuous orbit in x, y, t space

3.9. Brief introduction of Genetic Algorithm [59]

The genetic algorithm (GA) involves three main operations: reproduction, crossover and mutation. The GA creates a sequence of chromosomes that correspond to numerical values of a particular variable in order to derive a solution to a near optimal problem. Each chromosome represents a potential solution to the problem in question. Selection or reproduction is the process by which chromosomes in a population contain a better fitness value and thus have a greater probability of reproducing. The roulette wheel selection scheme is used in this thesis. The selected chromosomes that are encoded with better fitness values are chosen for recombination to yield off-spring for successive generations. Subsequently, natural evolution of the population is continued until a desired termination. This results in a final generation composed of highly fitted chromosomes, which represent the optimal solution to the search problem. Fig. 3.9 shows the procedure of GA optimization

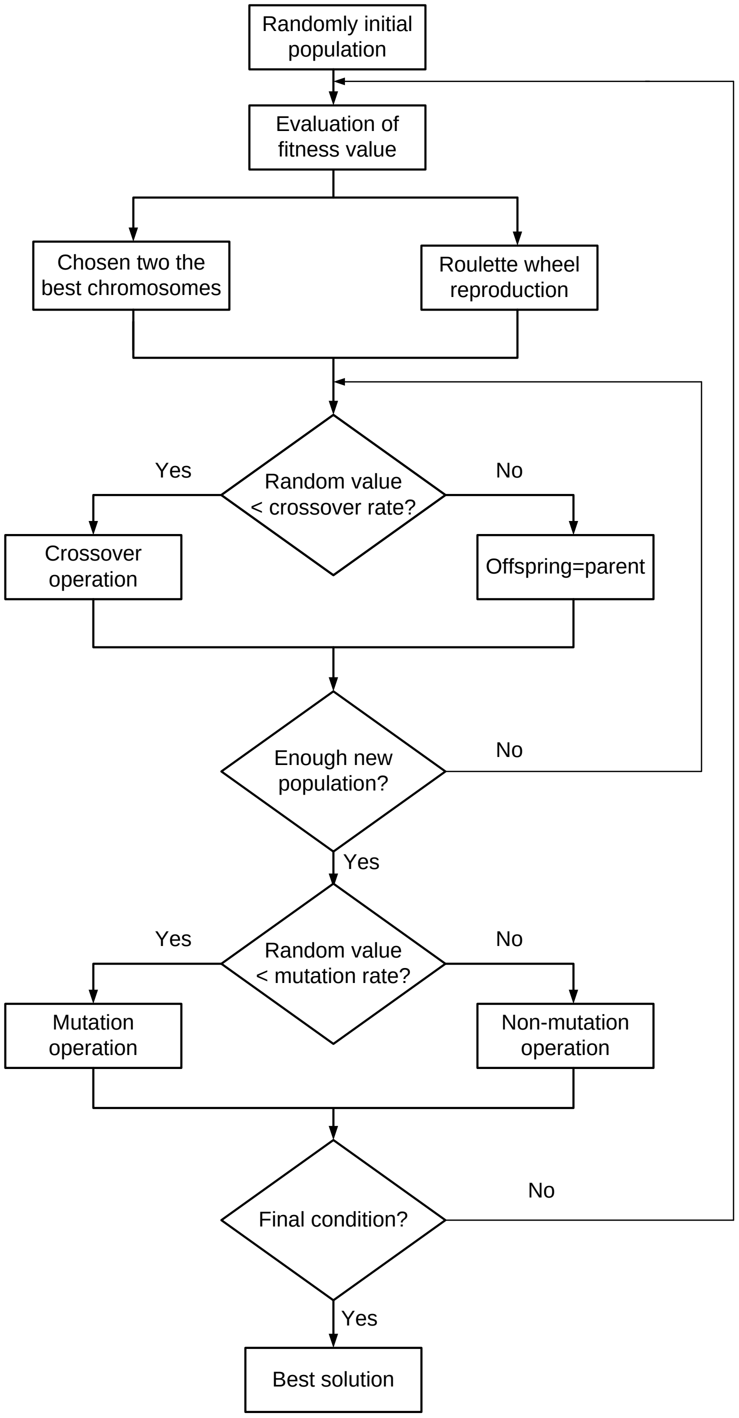

Fig. 3.9. Flow chart of the genetic algorithm

SUMMARY OF CHAPTER 3

This chapter provided brief outlook on theories relating the contents of thesis including air spring, thermodynamic, friction, elastic, numerical methods…etc. Following these relative theories, the dynamic characteristic of the proposed model will be discovered in next chapters. In addition, the static analysis as well as stability of solution will be also studied.

CHAPTER 4

QUASI-ZERO STIFFNESS VIBRATION ISOLATOR USING RUBBER AIR SPRINGS

This chapter will focus on propose and analyze dynamic response as well as vibration transmissibility of the quasi-zero stiffness adaptive vibration isolation model (QSAVIM) using rubber air springs. This proposed model is named “QSAVIM using RAS” in which the restoring force is generated by rubber air springs. First of all, the restoring model of the RAS is analyzed and identified experimentally. The static and dynamic analyses are then performed to find the stiffness model and relation between the amplitude and frequency as well as the transmissibility for vibrated base. Especially, effects of configurative parameters on stiffness curve and equilibrium position are analyzed and the frequency jump and bifurcation phenomena were considered. Finally, an experimental apparatus of the QSAVIM using RAS was established to verify the isolated effectiveness and compared with the equivalent traditional vibration isolation model (ETVIM) which has the same load bearing ability and static deformation as the QSAVIM. The content of this chapter is organized as follows. Section 4.1 displays the mechanical model of the proposed isolator. Section 4.2 shows the restoring model of a RAS. Next, the static analysis of the isolator is presented in section 4.3. Next, the dynamics analysis is indicated in section 4.4. Then, section 4.5 presents the effects of the configurative parameters on vibration transmissibility curve. Section 4.6 reveals the complex dynamic analysis. Section 4.7 exhibits the design procedure for obtaining quasi-zero stiffness isolator. Finally, the experimental apparatus and result were demonstrated in section 4.8.

4.1. Mechanical model of proposed isolator

The prototype of the QSAVIM has been designed comprises two mechanisms as shown in Fig. 4.1. One includes four rollers 3, four wedges 8 with the angular of α and two rubber air springs 1. The other comprises four semicircular cams 6, four rollers 4 and two rubber air springs 2. The former which is above with the positive stiffness is called the load bearing mechanism (LBM), meaning that the isolated object is only supported by this mechanism. The latter is the stiffness corrected mechanism (SCM) with the negative stiffness is below. This model is operated based on the opposite stiffness of two mechanisms, indicating that the proposed model can achieve the desired low stiffness or even the quasi-zero stiffness. It is noted that, the wedge and semicircular cam are fixed on the table leg 7 and the isolated object includes four wedges, four legs, load plate and isolated load 14. During the operation, the rollers 3 and 4 always roll without sliding on the surface of the wedge and cam simultaneously, the centers of these rollers only move in the horizontal direction through the sliding-blocks 5 and guide-bar 11 fixed on the base frame. In order to ignore the effect of the friction, a linear bushing is installed between the sliding-block 5 and guide-bar 11. In addition, the load plate along with the legs only realizes the vertical motion by introducing the sliding bushings 9 and guide-bar 10.

A main merit of the proposed model is that the stiffness of both mechanisms including LBM and SCM can be adjusted through the control of the pressure in the rubber air springs. Hence, the system can adapt to obtain the high-static-low-dynamic stiffness at desired static equilibrium position when there is a change of the weight of the isolated object, meaning that the QSAVIM can achieve the low resonant frequency but remain the load bearing capacity.

After describing the configuration of the proposed isolation model, next sections will have realized works including static and dynamic analyses of the QSAVIM. From these results, the procedure for designing the QSAVIM with quasi-zero stiffness is offered. As introduced, the elastic element of this isolation model is the rubber air spring hence, one of the first works will be carried out to establish the restoring force model generated by the RAS.

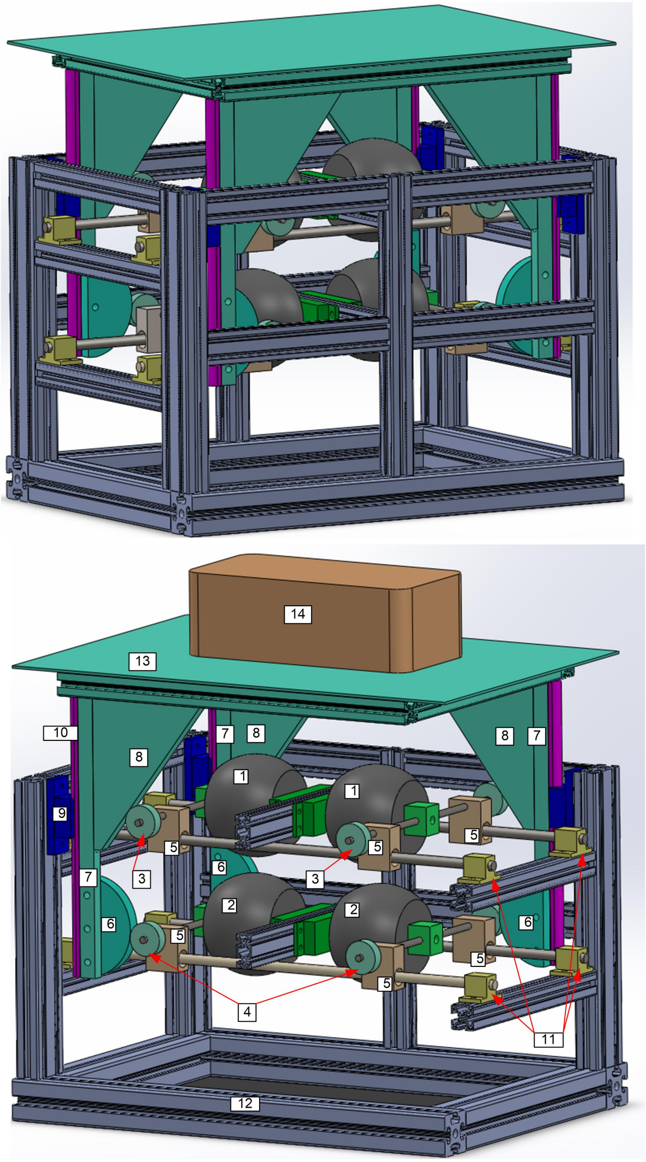

Fig. 4.1. Prototype of the QSAVIM, herein: 1 and 2- rubber air springs, 3 and 4- rollers; 5-sliding blocks; 6- semicircular cams; 7-table legs; 8-wedges; 9-sliding bushing; 10 and 11- guide-bar; 12- base frame and 13-load plate, 14-isolated load (Published by Vo et al. "Adaptive pneumatic vibration isolation platform", Mechanical Systems and Signal processing)

4.2. Restoring model of a RAS.

A RAS composes of the cover plate, bellow and piston as shown in Fig. 4.2. The bellow is made of rubber with the fabric reinforced rubber wall. The piston and cover plate are made of plastic or metal, aiming to seal the ends of the rubber bellow. Additionally, the rubber bellow can also roll on the surface of the piston. During the operation, the effective volume and area of the RAS are changed as a function with respect to the displacement due to the piston shape and the variable contact area between the cover plate and inflated bellow.

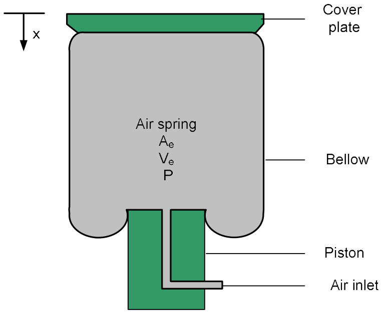

Fig. 4.2. The physical model of a RAS

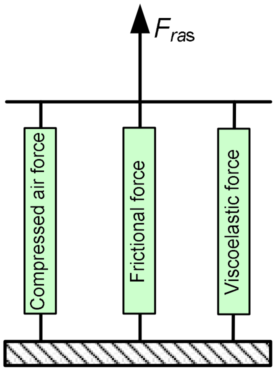

Fig. 4.3. Basic model of the rubber air spring force

The resultant force generated by the rubber air spring is contributed by the thermodynamic force of the compressed air, the frictional force contributed by the relative motion between the rubber and fabric as well as rubber bellow and the surface of the piston, and the viscoelastic force of the rubber material. Through the principle of superposition (Published by Vo et al. “Analysis model of restoring force of a rubber air spring,” Journal of Vibroengineering), the total force (F_{ras}) of the rubber air spring is shown in Fig. 4.3, meaning that it is expressed as following:

$$F_{ras} = F_s + F_{\mathrm{fri}} + F_{\mathrm{vie}} \tag{4.1}$$

where F_{s}, F_{fri} and F_{vie} are forces generated by the compressed air, friction and viscoelastic, respectively.

4.2.1 Compressed air force

Assuming that the heat exchange in the rubber bellow as well as air leakage is ignored, according to the thermodynamic theories and ideal air state equation, the mathematical model of the pressure (P) in the air spring is determined as follows:

$$\frac{dP}{dx} = -\frac{nP}{V_e}\frac{dV_e}{dx} \tag{4.2}$$

where, V_{e} is the effective volume of the inflated bellow, n is the polytropic exponent which depends on the thermodynamic state of the compressed air including n=1 for the isothermal state, n=1.4 for the adiabatic state and $1<n<1.4$ for the polytropic process.

From Eq. (4.2), the pressure inside the inflated bellow at an arbitrary compressed position is obtained as following:

$$PV_e^n = P_o\left(\frac{V_{eo}}{V_e}\right)^n \tag{4.3}$$

where P_{o} and V_{eo} are the initial pressure and effective volume

The compressed air force is determined as following:

$$F_{air} = A_e\left(P - P_{atm}\right) \tag{4.4}$$

in which P_{atm} is the atmosphere pressure, A_{e} is the effective area of the air spring.

The stiffness (K_{air}) of compressed air is defined by differentiating Eq. (4.4) with respect to the displacement x, we have:

$$K_{air} = \frac{dF_{air}}{dx} = -\frac{nPA_e}{V_e}\frac{dV_e}{dx} + \left(P - P_{atm}\right)\frac{dA_e}{dx} \tag{4.5}$$

The stiffness model given in Eq. (4.5) can be linearized around the working height h_{wh} as following:

$$K_{air} = -\frac{nP_{wh}A_{wh}\delta V_{wh}}{V_{wh}} + (P_{wh} - P_{atm})\delta A_{wh} \tag{4.6}$$

in which the volume, effective area and pressure at the working height are denoted by V_{wh}, A_{wh} and P_{wh}. δA_{wh}, δV_{wh} are the change rate of the effective area and volume.

4.2.2. Frictional force

As presented in chapter 3, the frictional force is generated by filled rubber components and relative motion between the rubber bellow and the surface of the piston. The friction is one of the causes creating the hysteresis behavior of the restoring force of a rubber air spring. According to Berg's model, the model of frictional hysteresis is presented as below:

$$F_{fri} = \begin{cases} F_{ref} & \text{for x=x}_{ref} \\ F_{ref} + \dfrac{x - x_{ref}}{x_2\left(1-a\right) + \left(x - x_{ref}\right)}\left(F_{fri\max} - F_{ref}\right) & \text{for x>x}_{ref} \\ F_{ref} + \dfrac{x - x_{ref}}{x_2\left(1-a\right) - \left(x - x_{ref}\right)}\left(F_{fri\max} + F_{ref}\right) & \text{for x<x}_{ref} \end{cases} \tag{4.7}$$

where the displacement x_2 is given in Eq. (3.7) in which K_{e} is replaced by K_{air}. Hence, it becomes: $x_2 = \dfrac{F_{fri\max}}{K_{\max} - K_{air}}$

4.2.3. Viscoelastic force

As mentioned in chapter 3, the fractional Kelvin-Voigt's model is used to describe the hysteresis behavior due to the viscoelasticity of the rubber bellow. The motion equation of the fractional Kelvin-Voigt 's model (F_{vie}) is given as following:

$$F_{vie}(t) = K_{vie}x(t) + bD_t^c x(t) \tag{4.8}$$

Now, supposing an excitation is given by $x=x_o\sin(\omega t)$, according to [54], the fractional derivation with respect to the displacement (x) is expressed as following:

$$D_t^c x(t) = x_o\omega^c \sin(\omega t + \pi c/2) = x_o\omega^c\left(\sin(\omega t)\cos(\pi c/2) + \cos(\omega t)\sin(\pi c/2)\right) \tag{4.9}$$

Using $x=x_o\sin(\omega t)$, Eq. (4.9) can be rearranged, that:

$$D_t^c x(t) = x_o\omega^c \sin(\pi c/2)\cos(\omega t) + \omega^c \cos(\pi c/2)x \tag{4.10}$$

Substituting Eq. (4.10) into Eq. (4.8), the motion equation of the fractional Kelvin-Voigt's model becomes:

$$F_{vie}(t) = \left(K_{vie} + b\omega^c \cos(\pi c/2)\right)x + bx_o\omega^c \sin(\pi c/2)\cos(\omega t) \tag{4.11}$$

From $x=x_o\sin(\omega t)$ and (4.11), we obtain the functions of sine and cosine as below:

$$\begin{cases} \sin(\omega t) = \dfrac{x}{x_o} \\ \cos(\omega t) = \dfrac{F_{vie}(t) - \left(K_{vie} + b\omega^c \cos(\pi c/2)\right)x}{bx_o\omega^c \sin(\pi c/2)} \end{cases} \tag{4.12}$$

Through $\sin^2(\omega t)+\cos^2(\omega t)=1$, the hysteresis loop of the fraction Kelvin-Voigt's model is expressed as below:

$$\left(\frac{F_{vie}(t) - \left(K_{vie} + b\omega^c \cos(\pi c/2)\right)x}{bx_o\omega^c \sin(\pi c/2)}\right)^2 + \left(\frac{x}{x_o}\right)^2 = 1 \tag{4.13}$$

For a given excited signal with the frequency *(ω)*, we obtain a set of data as following:

At time t_1 having $x(t_1)=x_o$ corresponding to $F_{vie}(t_1)= F_{vie1}$

At time t_2 having $x(t_2)=0$ corresponding to $F_{vie}(t_2)= F_{vie2}$

Thus, Eq. (4.13) becomes:

$$\begin{cases} \dfrac{F_{vie1}(t)}{x_0} = K_{vei} + b\omega^c \cos(\pi c/2) \\ \dfrac{F_{vie2}(t)}{x_o} = b\omega^c \sin(\pi c/2) \end{cases} \tag{4.14}$$

It is clear that the parameters of the fractional Kelvin-Voigt's model such as K_{vie}, b and c are unknown whilst F_{vie1} and F_{vie2} and x_o are physical parameters. Indeed, with a given excited frequency and amplitude, the values of forces F_{vie1} and F_{vie2} corresponding to $x(t_1)=x_o$ and $x(t_2)=0$ are measured experimentally, respectively.

Hence, each excited signal having the amplitude x_{io} and frequency ω_1 (i=1,3,…,m), if the values of K_e, b and c are determined properly, meaning:

$$\begin{cases} \dfrac{F_{vie1i}(t)}{x_{i0}} - \left(K_{vie} + b\omega_i^c \cos(\pi c/2)\right) \approx 0 \\ \dfrac{F_{vie2i}(t)}{x_{io}} - bx_o\omega_i^c \sin(\pi c/2) \approx 0 \end{cases} \tag{4.15}$$

From this analysis, the optimal values of K_{vie}, b, and c will be identified through minimizing the following cost function:

$$J = \frac{1}{2}\sum_{i=1}^{m}\left(\left(\frac{F_{vie1i}(t)}{x_{i0}} - \left(K_{vie} + b\omega_i^c \cos(\pi c/2)\right)\right)^2 + \left(\frac{F_{vie2i}(t)}{x_{io}} - b\omega_i^c \sin(\pi c/2)\right)^2\right) \tag{4.16}$$

where m is the number of the harmonically excited signal, F_{vie1i}, F_{vie2i} are the viscoelastic forces at the time having the corresponding displacement equaling 0 and $x_{io.}$ Then, GA is shown in Fig. 3.9, which is employed to determine optimal values of the viscoelastic model given in Eq. (4.8). This work aims to minimize the cost function expressed by Eq. (4.16).

4.2.4. Test rig

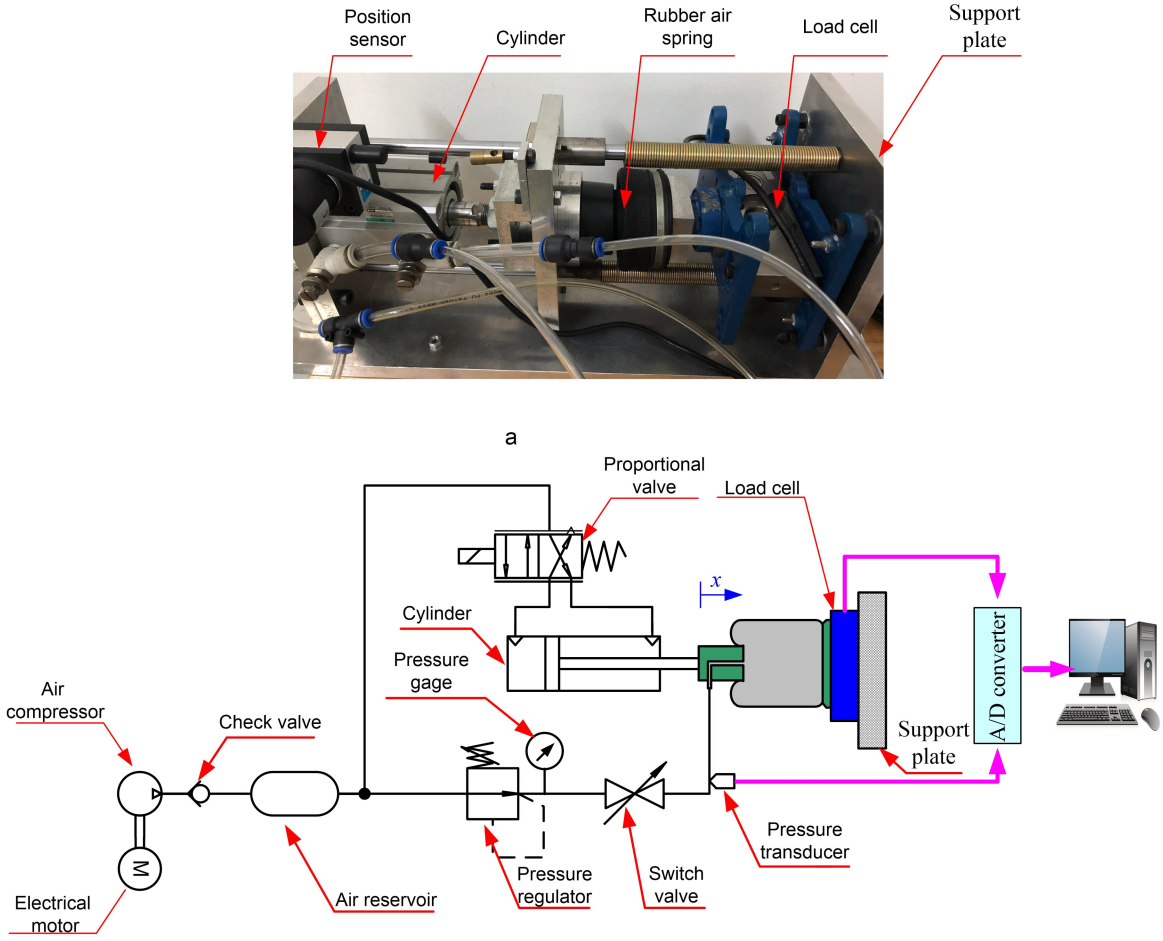

b

Fig. 4.4. Experimental setup: (a) Photograph of test rig; (b) Schematic of test-rig

In order to realize the simulated and experimental verification of the proposed isolation model, the restoring model of RAS must be known. Therefore, one of the first works is that a commercial rubber air spring with model number 1S3-013 having the physical parameters listed in table 4.1 manufactured by Guangzhou Guomat Air spring Co., Ltd is chosen to be identified.

Table 4.1. The physical parameters of the air spring

Parameter	**Value**
Extended Height	91.44 mm
Bumper Height	38.1 mm
Upper Plate	81.28 mm
Lower Plate OD	60.96 mm

The test-rig is set up as shown in Fig. 4.4 in which the rubber bellow is inflated by the air reservoir through the switch valve whilst the internal pressure of the bellow is regulated by the pressure regulator. One end of the air spring is excited by the pneumatic cylinder controlled by the proportional valve while the other is fixed to a support plate where the force can be measured through a load cell with model "HPS". Besides, the pressure inside the rubber bellow is measured by the pressure transducer-EDS.305. A computer in which an NI-card 6221 worked as an A/D converter is installed for communicating between the computer and sensors, is used to monitor as well as collect the data from sensors.

4.2.5. Model identification and verification results

First of all, the effective area and volume will have been predicted, before experimental data collection, the rubber bellow is inflated by the air reservoir to value of 1.5 bar. Then, the free end of the rubber air spring is excited by sinusoidal displacements having amplitude of 15 mm and very low frequency of 0.005Hz, aiming to ignore the effects of viscoelasticity of material. The real force and internal pressure are collected and applying Eq. (4.4) obtains the effective area curve versus the displacement as shown by the dashed line in Fig.4.5 (a). Simultaneously, the effective volume of the rubber air spring is predicted through Eq. (4.3) in which the initial volume of the bellow is 0.243 liter is provided by the company and the polytropic exponent (n) is set at value of 1 due to the low velocity of the cylinder. The result is to attain the predictive curve of the effective volume depicted by the dashed line as shown in Fig. 4.5 (b). It is interesting to confirm that the predictive curve follows well the experimental data as well as data (marked by the filled squares) given by the company.

To simplify restoring force model analysis of the rubber air spring, the predicted effective area (A_e) and volume (V_e) are approximately expressed by polynomial functions as given in Eqs. (4.17) where the Least square method is employed to find the coefficients of the polynomial so that the error between fitting function and predicted result is the minimum. As observed in Fig. 4.5, the fitting curves are in a good agreement with the predicted data.

$$\begin{cases} A_e = \left(0.0002 + 0.0374x - 1.9491x^2 + 68.1424x^3 - 941.3209x^4\right)10^{-3} \\ V_e = \left(0.2077 - 0.0033x - 0.0001x^2\right)10^{-3} \end{cases} \tag{4.17}$$

where x is the displacement of the end of the air spring in mm as shown in Fig. 4.4 (b), A_e and V_e are the effective area in m^2 and effective volume in m^3, respectively.

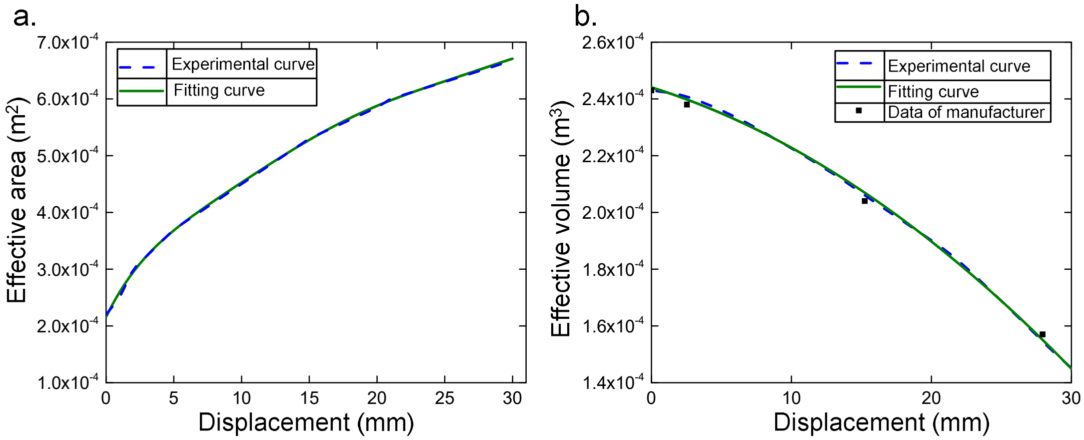

Fig. 4.5 Fitting curve compared with the predicted results: (a) Effective area; (b) Effective volume (Annotation for line types is given on top-corner panel of figure)

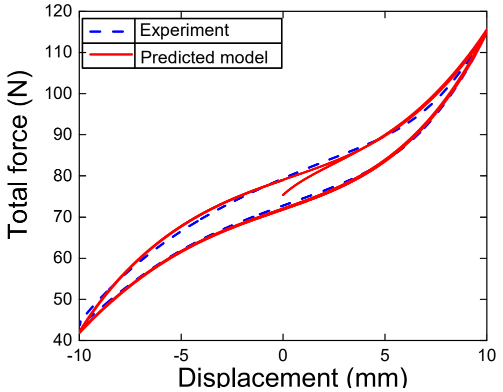

Fig. 4.6 Comparing Berg's model and experiment one

Next, a displacement with amplitude of 10mm and frequency of 0.02Hz is applied on the free end of the rubber air spring to obtain the frictional hysteresis loop as shown in Fig. 4.6 (the detailed notion of the line types is presented in the left-top corner panel of the figure). It can be seen obviously that the sharp corners appear at minimum and maximum displacements of the hysteresis loop. By applying Berg's model, the predicted curves of the frictional hysteresis loops are drawn by the solid line. It confirms that the Berg's model offers (where F_{frimax}=5.7N and x_2=1.95mm) a good fit to the hysteresis loop due to the effects of friction.

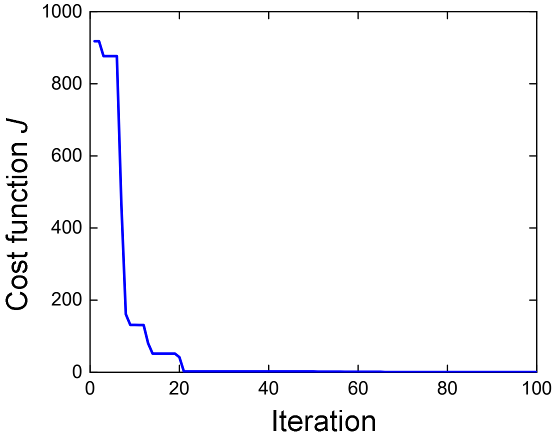

Fig. 4.7. Cost function J versus the iteration

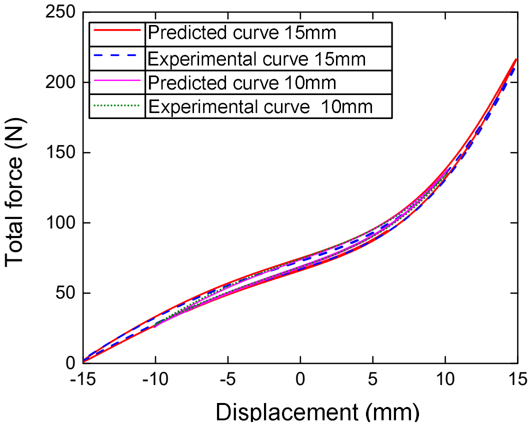

Fig. 4.8. Force-displacement hysteresis loop compared the experiment and identification

Next, the dynamic test with the frequencies of 0.1Hz, 0.2Hz, 0.5Hz, 1Hz, 1.5Hz, 2Hz, 2.5Hz, 3Hz, 4Hz, 5Hz, 6Hz, 7Hz and the amplitude of 8mm are realized to predict the viscoelastic model. By utilizing GA with aiming to minimize the cost function expressed by Eq. (4.16). Clearly, after 20 iterations, the cost function converges to zero as shown in Fig. 4.7, these optimal values are obtained as following $\tilde{K}_{vie} = 1.325, \tilde{b} = 0.909, \text{and } \tilde{c} = 0.859$. Then, the predicted curve of the restoring force model is shown in Fig. 4.8. Obviously, the restoring force model of the rubber air spring and the experiment one match well together. The hysteresis loop generated by a displacement having small amplitude is enclosed in the loop for large amplitude and the sharp corners are appeared at the ends of the displacement. The more the reduction in amplitude is, the more the slope of the hysteresis curve is increased. Especially, comparing with Fig. 4.6, increasing the frequency will lead to reduce the effect of the hysteresis.

4.3. Static analysis of the isolator

In order to carry out the static analysis of the QSAVIM, based on the prototype shown in Fig. 4.1, the schematic diagram of the QSAVIM is drawn in Fig. 4.9 (a). Where, it is interesting to note that the load bearing mechanism is denoted in the dashed-line rectangle meanwhile the stiffness correction mechanism exhibited in the dot-line rectangle. There are two especial states defined as following:

+ One is the undeformed state presented by the dot line in Fig. 4.9 (b) at which both air springs are not compressed.

+ The other is defined as the state at which the center of the semicircular cam 6 and the center of roller 4 are the same on horizontal line as plotted by the red dashed line as shown in Fig. 4.9 (a), which is also called desired static equilibrium position (DSEP).

Considering the load plate moves vertically an amount of *ΔL* from the undeformed state due to the force F_s as shown in Fig. 4.9 (b) whilst the base frame is fixed. This leads to the displacement of the center of the semicircular cam compared with the DSEP being u, simultaneously, the horizontal displacement of centers of rollers 3 and 4 are x_1, x_2, respectively.

The relation of vertical and horizontal displacements is presented as follow:

$$\begin{aligned}
&x_1 = \Delta L \tan\alpha \\
&x_{wh1} = H_o \tan\alpha \\
&\mathrm{x}_2 = \left(\sqrt{(R+r)^2-(H_o-\Delta L)^2}-\sqrt{(R+r)^2-{H_o}^2}\right) \\
&x_{wh2} = R+r-\sqrt{\left(R+r\right)^2-H_o^2}
\end{aligned} \tag{4.18}$$

where the wedge angle is denoted by α and H_o is the static deformation of the system and it is defined as the vertical distance between the DSEP and the center of the semicircular cam. *R* and *r* are radii of the semicircular cam and roller, respectively. It is noted that the subscripts “1” and “2” are representative for the rubber air springs “1” and “2”. To guarantee the contact between the semicircular cam and roller, the static deformation H_o must satisfy following condition:

$$H_o \le \sqrt{\left(R+r\right)^2-r^2} \tag{4.19}$$

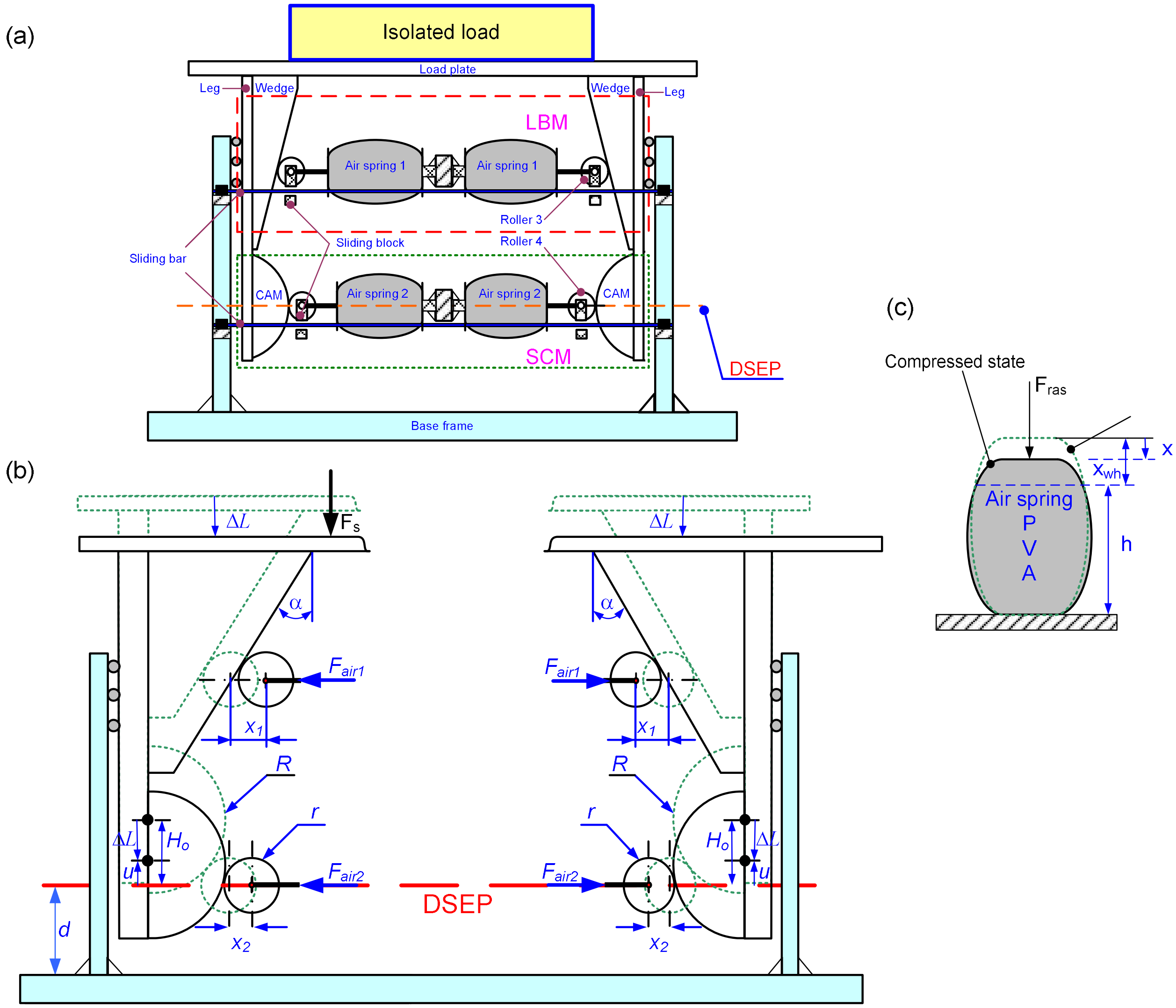

Fig.4.9. (a) Schematic diagram of the QSAVIM including the load bearing mechanism denoted in the dashed-line rectangle meanwhile the stiffness correction mechanism exhibited in the dot-line rectangle. It is noted that the DSEP is presented by the red dashed line. (c) Air spring. (b) Geometric relationship among roller, wedge and semicircular cam

4.3.1. Stiffness model

As mentioned above, as the centers of roller 3 and 4 are displayed x_1 and x_2, indicating the air springs 1 and 2 are compressed by an amount of x_1 and x_2, respectively. This leads to the system be acted by the compressed air forces which are generated by two rubber air springs as shown in Fig. 4.9 (b).

Ignoring the mass of the moving part including the load plate, legs, wedges, semicircular cams and rollers and applying the virtual work principle, the total virtual work acting on the system is equal to zero as given in Eq. (4.20). It is meaningful that the force F_s is also the vertical restoring force acting on the load plate.

$$F_s \delta\Delta L - 2F_{air1}\delta x_1 - 2F_{air2}\delta x_2 = 0 \tag{4.20}$$

where the forces of the rubber air springs 1 (F_{air1}) and 2 (F_{air2}) are expressed as below:

$$F_{air} = -K_{air}\left(x_{wh} - x\right) + (P_{wh} - P_{atm})\,\mathrm{A}_{wh} \tag{4.21}$$

in which K_{air} is the stiffness at the working height as expressed in Eq. (4.6). As presented in Fig. 4.9 (c), x_{wh} and x are the working and arbitrary positions of the rubber air springs. From Eq. (4.18), the virtual displacement δx_1 and δx_2 are obtained as below:

$$\begin{aligned} \delta x_1 &= \tan\left(\alpha\right)\delta\Delta L \\ \delta x_2 &= \frac{(H_o - \Delta L)}{\sqrt{(R+r)^2 - (H_o - \Delta L)^2}}\,\delta\Delta L \end{aligned} \tag{4.22}$$

By substituting Eq. (4.22) int o Eq. (4.20), we obtain:

$$F_s = 2F_{air1}\tan\left(\alpha\right) + 2F_{air2}\frac{(\mathrm{H}_o - \Delta L)}{\sqrt{(\mathrm{R}+\mathrm{r})^2 - (\mathrm{H}_o - \Delta L)^2}} \tag{4.23}$$

Using Eq. (4.18) and (4.21), Eq. (4.23) is expressed as below

$$\begin{aligned} F_s = {} & K_L\Delta L + 2K_{air2}\left(1 - \frac{\sqrt{(\mathrm{R}+\mathrm{r})^2 - H_o^{\,2}}}{\sqrt{(\mathrm{R}+\mathrm{r})^2 - (\mathrm{H}_o - \Delta L)^2}}\right)(\mathrm{H}_o - \Delta L) \\ & + F_{SC}\frac{(\mathrm{H}_o - \Delta L)}{\sqrt{(\mathrm{R}+\mathrm{r})^2 - (\mathrm{H}_o - \Delta L)^2}} + F_{SL}\tan\alpha \end{aligned} \tag{4.24}$$

in which $K_L = 2K_{air1}\tan^2\alpha$ is the equivalent stiffness of the load bearing mechanism, F_{SL} and F_{SC} are the static forces of the LBM and SCM, respectively and expressed by:

$$F_{SL} = 2\left((P_{wh1} - P_{atm})A_{wh1} - K_{air1}x_{wh1}\right)\tan\alpha \tag{4.25}$$

$$F_{SC} = 2\left((P_{wh2} - P_{atm})A_{wh2} - K_{air2}\left(\mathrm{R} + \mathrm{r} - \sqrt{(\mathrm{R}+\mathrm{r})^2 - H_o^{\ 2}}\right)\right) \tag{4.26}$$

Based on Fig. 4.9(b), the distance between the static deformation H_o and the origin of the coordinate u is written by:

$$\Delta L = H_o - u \tag{4.27}$$

Accordingly, Eq. (4.24) is rewritten as:

$$F_s = K_L(H_o - u) + 2K_{air2}\left(1 - \frac{\sqrt{(\mathrm{R}+\mathrm{r})^2 - H_o^{\ 2}}}{\sqrt{(\mathrm{R}+\mathrm{r})^2 - u^2}}\right)u + F_{SC}\frac{u}{\sqrt{(\mathrm{R}+\mathrm{r})^2 - u^2}} + F_{SL}\tan\alpha \tag{4.28}$$

By introducing non-dimension parameters as following:

$$\hat{F}_s = \frac{F_s}{K_L(R+r)};\ \hat{u} = \frac{u}{(R+r)};\ \mu = \frac{P_{wh2}}{P_{wh1}};\ \hat{F}_{SL} = \frac{F_{SL}}{K_L(R+r)};\ \hat{H}_o = \frac{H_o}{(R+r)};$$

$$A = \frac{2P_{atm}\delta A_{wh2}}{K_L};\ B = 2\frac{\dfrac{nA_{wh2}\delta V_{wh2}}{V_{wh2}} - \delta A_{wh2}}{\left[\dfrac{nA_{wh1}\delta V_{wh1}}{V_{wh1}} - \left(1 - \dfrac{P_{atm}}{P_{wh1}}\right)\delta A_{wh1}\right](\tan\alpha)^2};$$

$$C = 2\frac{A_{wh2} - \left(\dfrac{nA_{wh2}\delta V_{wh2}}{V_{wh2}} - \delta A_{wh2}\right)\left(R + r - \sqrt{(R+r)^2 - H_o^2}\right)}{(R+r)\left[\dfrac{nA_{wh1}\delta V_{wh1}}{V_{wh1}} - \left(1 - \dfrac{P_{atm}}{P_{wh1}}\right)\delta A_{wh1}\right](\tan\alpha)^2};$$

$$D = \frac{2P_{atm}A_{wh2} + 2P_{atm}\delta A_{wh2}\left(R + r - \sqrt{(R+r)^2 - H_o^2}\right)}{K_L(R+r)}$$

Then, Eq. (4.28) is rewritten in term of dimensionless form as following:

$$\begin{aligned}\hat{F}_S\left(\hat{u},\mu\right)=(\hat{H}_o-\hat{u})+\hat{F}_{SL}+\mu\left(B\left(1-\frac{\sqrt{1-\hat{H}_o^{\,2}}}{\sqrt{1-\hat{u}^2}}\right)+C\frac{1}{\sqrt{1-\hat{u}^2}}\right)\hat{u}\\+A\left(1-\frac{\sqrt{1-\hat{H}_o^{\,2}}}{\sqrt{1-\hat{u}^2}}\right)\hat{u}-D\frac{\hat{u}}{\sqrt{1-\hat{u}^2}}.\end{aligned}\tag{4.29}$$

Next, by taking differentiation of the dimensionless restoring force given in Eq. (4.29) versus the dimensionless displacement $\hat{u}$, we obtain the dimensionless dynamic stiffness in vertical direction as following:

$$\begin{aligned}\hat{\mathrm{K}}\left(\hat{u},\mu\right)=\mathrm{A}\left[\frac{\hat{u}^2\sqrt{1-\hat{H}_o^{\,2}}}{\sqrt{\left(1-\hat{u}^2\right)^3}}+\frac{\sqrt{1-\hat{H}_o^{\,2}}}{\sqrt{1-\hat{u}^2}}-1\right]+D\left(\frac{\hat{u}^2}{\sqrt{\left(1-\hat{u}^2\right)^3}}+\frac{1}{\sqrt{1-\hat{u}^2}}\right)\\+\mu\left[B\left(\frac{\sqrt{1-\hat{H}_o^{\,2}}}{\sqrt{1-\hat{u}^2}}-1\right)+B\frac{\hat{u}^2\sqrt{1-\hat{H}_o^{\,2}}}{\sqrt{\left(1-\hat{u}^2\right)^3}}-C\frac{1}{\sqrt{1-\hat{u}^2}}-C\frac{\hat{u}^2}{\sqrt{\left(1-\hat{u}^2\right)^3}}\right]+1\end{aligned}\tag{4.30}$$

Then, substituting $\hat{u}=0$ into Eq. (4.30), the dynamic stiffness $\hat{K}_{DSEP}$ at the desirable static equilibrium position is expressed as below:

$$\hat{\mathrm{K}}_{DSEP}\left(\mu\right)=\mathrm{A}\left[\sqrt{1-\hat{H}_o^{\,2}}-1\right]+D+\mu\left[B\left(\sqrt{1-\hat{H}_o^{\,2}}-1\right)-C\right]+1\tag{4.31}$$

This analysis revealed the dependence of the factor (μ) which is defined the ratio of the pressure of the SCM to the LBM named “pressure ratio” on the total vertical dynamic stiffness of the isolation model given in Eq. (4.30). In order to attain quasi-zero stiffness at the desirable static equilibrium position, the pressure ratio is calculated from Eq. (4.31) by setting $\hat{K}_{DSEP}\left(\mu\right)=0$. Based on these analyses, the works including the region of the pressure ratio in which it can exist unstable or stable static equilibrium positions and the stiffness at these equilibrium positions will be determined and analyzed in next section.

4.3.2. Analysis of equilibrium position

The bifurcation and stability of the system without external excitations are discussed and analyzed with the equilibria. The static equilibrium points of the system occur where $\partial E_p / \partial \hat{u} = 0$ in which E_p is the potential energy of the system, $E_p = E_{ps} - E_{pg}$, E_{ps} and E_{pg} are the potential energies of the restoring force and the gravity force, respectively.

$$\partial E_p / \partial \hat{u} = \partial E_{ps} / \partial \hat{u} - \partial E_{pg} / \partial \hat{u} = F_s - F_g = 0 \tag{4.32}$$

where F_g=Mg with M is the weight of the isolated object which is defined above, is calculated by the total weight of the load plate, legs, wedges, semicircular cams and isolated load as shown in Fig. 4.9, g is the gravity acceleration

Combination Eq. (4.32) and (4.29), we have:

$$\hat{f}(\hat{u}, \mu) = \hat{F} + \hat{F}_{es} = 0 \tag{4.33}$$

in which

$$\hat{F} = -\hat{u} + \mu\left(B\left(1 - \frac{\sqrt{1-\hat{H}_o^{\,2}}}{\sqrt{1-\hat{u}^2}} \right) + C\frac{1}{\sqrt{1-\hat{u}^2}} \right)\hat{u} + A\left(1 - \frac{\sqrt{1-\hat{H}_o^{\,2}}}{\sqrt{1-\hat{u}^2}} \right)\hat{u} - D\frac{\hat{u}}{\sqrt{1-\hat{u}^2}}. \tag{4.34}$$

$\hat{F}_{es} = \dfrac{\left(K_L H_o + F_{SL}\right)\tan\alpha - Mg}{K_L (R + r)}$ is the equivalent static force, in the case the system attains the DSEP, the equivalent static force will equal zero, it means that the weight of the isolated object must satisfy the following equation:

$$M = 2\frac{(P_{wh1} - P_{atm})A_{wh1}\tan\alpha}{g} \tag{4.35}$$

The case of the isolated load which is calculated by Eq. (4.35). It is evident that in Eq. (4.33) the equivalent static force $\hat{F}_{es}$ has no appearance. In this case, plotting the curve for $\partial E_p/\partial\hat{u}=0$ in the plane $(\mu,\hat{u})$, this curve presents the equilibrium points, in shaded region where $\partial E_p/\partial\hat{u}$ is positive, out of this region, $\partial E_p/\partial\hat{u}$ is negative as shown in Fig. 4.10(a). It can be seen that the number and stability of the equilibrium positions may be varied with the pressure ratio μ. But its real significance is to display that μ at point A is a bifurcation point of the system and its value is determined by Eq. (4.36). When $\mu \le \mu_{\mathrm{bif}}$, there is only one stable equilibrium position (0,0) (called center point) due to $\partial E_p/\partial\hat{u}$ changing from negative to positive on passing through this equilibrium position. This equilibrium position is taken into account as the desirable static equilibrium position. But the value of μ exceeds μ_{bif} the system has three equilibria including two centers which are on solid curve and an unstable equilibrium position (saddle point) lied on dashed line due to $\partial E_p/\partial\hat{u}$ changing from positive to negative on passing through this equilibrium position.

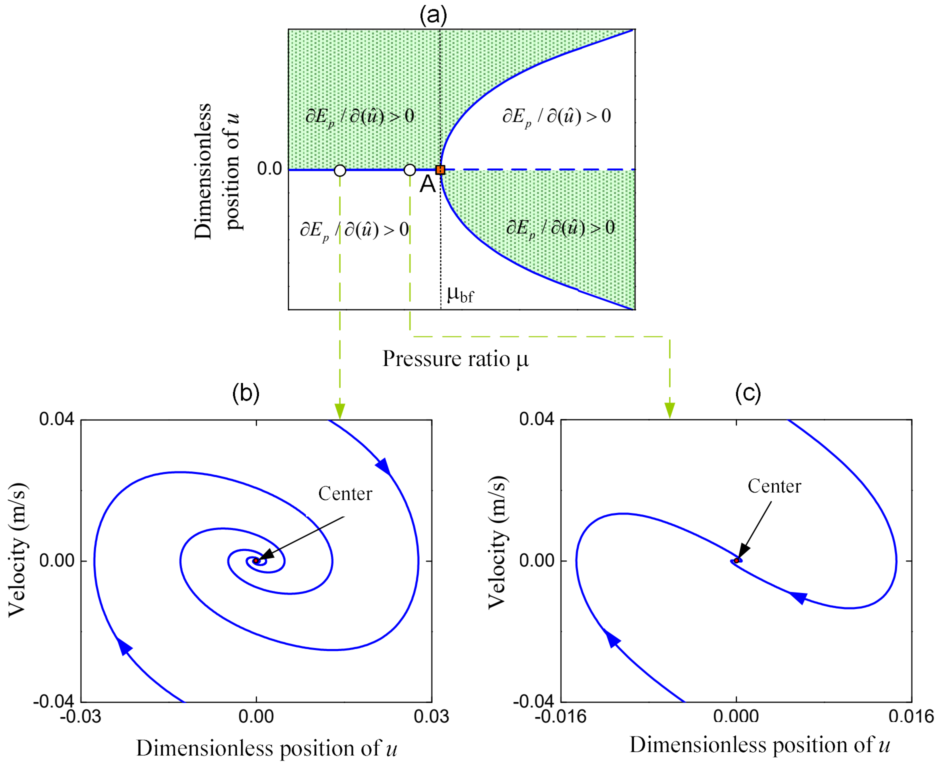

Fig.4.10. (a) Stability curves for equilibrium positions; (b-c) the phase orbits for $\mu \le \mu_{\mathrm{bif}}$

$$\mu_{bif} = \left. \frac{d\hat{f}(\hat{u},\mu)}{d\hat{u}} \right|_{\hat{u}=0} \tag{4.36}$$

If the static equilibrium position of the QSAVIM using RAS is not coincident with the DSEP, the equilibrium point of the system depends on the equivalent static force $\hat{F}_{es}$ and the pressure ratio μ as shown in Fig. 4.11. If $\mu \le \mu_{\mathrm{bif}}$, there is only one equilibrium point (center point) regardless of the equivalent static force as shown in Fig. 4.12(a, b), herein, the equivalent static force is drawn by the black solid line, the blue solid line presents for the force $\hat{F}$ given by Eq. (4.34).

If $\mu > \mu_{\mathrm{bif}}$ the system will occur one or three equilibrium positions depending on the equivalent static force in Fig. 4.12(c). In this case, it can be observed that the system offers two bifurcation points at $\hat{F}^1$ and $\hat{F}^2$. It is derived that a center point denoted by a green filled circle appeared when $\hat{F}_{es} < \hat{F}^2$ or $\hat{F}_{es} > \hat{F}^1$ with the equilibrium static force is denoted by the black solid line. When $\hat{F}^2 < \hat{F}_{es} < \hat{F}^1$, the system has three equilibria including two centers presented by two green filled circles and a saddle point marked with a red filled square. Besides, the system may exist a center as marked by green filled circle and an unstable equilibrium point (center-saddle point) plotted by a black filled diamond when $\hat{F}_{es} = \hat{F}^1$ or $\hat{F}_{es} = \hat{F}^2$ plotted by green dashed-dot lines, where $\hat{F}^1$ and $\hat{F}^2$ are the values of extrema of the restoring force determined by Eq. (4.37).

$$\hat{F}^1 = \hat{F}(\hat{u}_1) \text{ and } \hat{F}^2 = \hat{F}(\hat{u}_2), \text{ where } \hat{u}_1 \text{ and } \hat{u}_2 \text{ are roots of } d\hat{F}/d\hat{u} = 0 \tag{4.37}$$

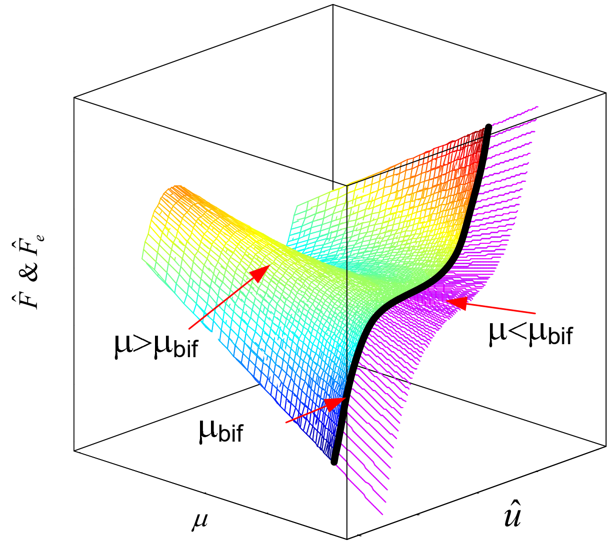

Fig. 4.11. Equilibrium position in space $\left(\hat{u}, \mu, \hat{F}_e\right)$

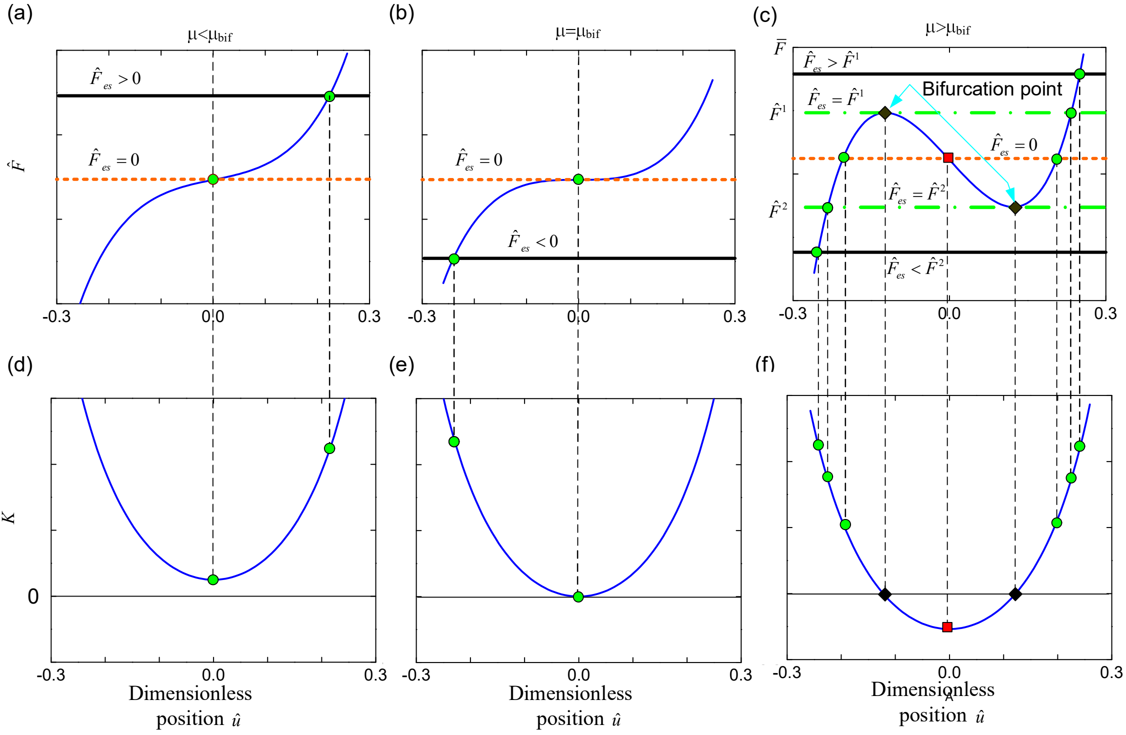

Fig.4.12. Restoring force and stiffness curves for various values of the pressure ratio μ

In addition, Fig. 4.12(d-f) present the dynamic stiffness of the QSAVIM RAS for various values of the pressure ratio. It can be observed that the dynamic stiffness at the center points (denoted by the green filled circles) is positive, conversely, it is negative at the saddle point (plotted by the red filled square). At the bifurcation points (drawn by black filled diamonds), the dynamic stiffness is equal to zero. However, these points are unstable, because the stiffness of the system is changed the sign from negative to positive and reversely from positive to negative as the system goes through these equilibrium positions. Furthermore, if the equilibrium static force equals zero (red dot lines in Fig. 4.12(a-c), the QSAVIM using RAS will achieve the lowest stiffness at the DSEP$\left(\hat{u}=0\right)$.

It is interesting to note that when $\mu \leq \mu_{\text{bif}}$ the dynamic stiffness of the system is always greater than or equal to zero for any equilibrium positions as shown in Fig. 4.12(d, e). Especially, the stiffness can be quasi-zero at the DSEP for $\mu = \mu_{\text{bif}}$. If $\mu > \mu_{\text{bif}}$, it may occur two cases including the dynamic stiffness of the QSAVIM using RAS is always positive for the equivalent static force out of range$\left(\hat{F}^1, \hat{F}^2\right)$, conversely, the QSAVIM using RAS will offer two regions of the dynamic stiffness including the positive and negative stiffness areas which depends on the position of the isolated object.

4.4. Dynamic analysis

A simple model of the proposed isolator is shown in Fig. 4.13 in which M is weight of the isolated object as defined in sub-section 4.3.2, K is the dynamic stiffness of the system given by Eq. (4.30), C_d is the damping coefficient. The case in which the base frame is excited by a signal z_e, the excited energy is transmitted to the isolated object through an air spring system (including the LBM and SCM) and a damper. This can cause the absolute displacement of the isolated object (z)

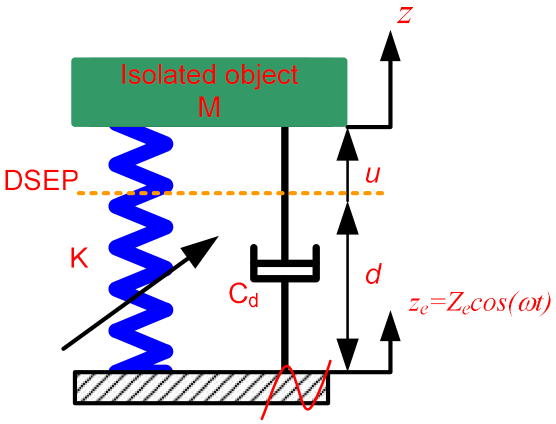

Fig. 4.13. Simple model of QSAVIM

4.4.1. Dynamic Equation

The kinetic energy (E_k) of the isolated object:

$$E_k = \frac{1}{2} M \dot{z}^2 \tag{4.38}$$

where, z is the absolute displacement of the isolated object.

The potential energy (E_p) generated by the F_s given in Eq. (4.24)

$$\begin{aligned} E_p = \int_0^{\Delta L} F_S d\Delta L = \frac{1}{2} K_L \Delta L^2 - 2K_{air2}\left[(H_o - \Delta L) + \sqrt{(\mathrm{R}+\mathrm{r})^2 - H_o{}^2}\sqrt{(\mathrm{R}+\mathrm{r})^2 - (H_o - \Delta L)^2}\right] \\ + F_{SC}\sqrt{(\mathrm{R}+\mathrm{r})^2 - (H_o - \Delta L)^2} + 2K_{air2}\left[H_o + (\mathrm{R}+\mathrm{r})^2 - H_o{}^2\right] \\ - F_{SC}\sqrt{(\mathrm{R}+\mathrm{r})^2 - H_o{}^2} + F_{SL}\tan\alpha\Delta L \end{aligned} \tag{4.39}$$

where *ΔL* is the vertical deformation of the system as shown in Fig. 4.9 (b)

The energy dissipation function:

$$D = \frac{1}{2} C_d (\dot{\mathrm{z}} - \dot{z}_e)^2 \tag{4.40}$$

herein C_d is the damping coefficient

Besides, as shown in Fig. 4.13, we have:

$$z = u + d + z_e \tag{4.41}$$

where *u* is the relative displacement of the center of the semicircular cam referring the DSEP, *d* is the fixed distance between the base and the DSEP.

Combining Eq. (4.27), Eq. (4.41) can be rewritten as following:

$$z = H_o - \Delta L + d + z_e \tag{4.42}$$

By applying Lagrange's equation, we have

$$\frac{d\left(\frac{d(\mathrm{E}_k - E_P)}{d\dot{z}}\right)}{dt} - \frac{d(\mathrm{E}_k - E_P)}{d\Delta L}\frac{d\Delta L}{dz} + \frac{dD}{d\dot{z}} = Q \tag{4.43}$$

where *Q*=-*Mg* is the generalized force in absolute coordinate of *z* and according to Eq. (4.42), dΔL/ d*z*=-1.

$$M\ddot{z} + C_d(\dot{z} - \dot{z}_e) - F_S + Mg = 0 \tag{4.44}$$

Then, using Eq. (4.41), Eq. (4.44) is rewritten respect to the relative displacement (*u*) of the isolated object as below

$$M\ddot{u} + C_d\ \dot{u} - F_S + Mg = -M\ddot{z}_e \tag{4.45}$$

4.4.2. Equation of vibration transmissibility

In order to simplify the dynamic analysis, it is assumed that the isolate object vibrates with small amplitude around the DSEP (*u*=0) at which the working height of the rubber air springs is h_{wh}. By expanding Taylor series, the restoring force given in Eq. (4.28) can be expressed as a fifth-order approximate function as below:

$$F_{ap} = F_o + \sum_{i=1}^{5} a_i u^i + \mathcal{O}(u^6) \tag{4.46}$$

where $a_i = \frac{1}{i!}\frac{d^iF_s}{du^i}\bigg|_{u=0}$ with i=1,2,3,…,5, we have:

$$\hat{F}_o = \hat{H}_o + \hat{F}_{SL}$$
$$a_1 = \mu C - D - (A+\mu B)\left(\sqrt{1-H_o^2}-1\right)-1$$
$$a_2 = 0$$
$$a_3 = \frac{1}{2}\left(\mu C - D - (A+\mu B)\sqrt{1-H_o^2}\right)$$
$$a_4 = 0;$$
$$a_5 = \frac{3}{8}\left(\mu C - D - (A+\mu B)\sqrt{1-H_o^2}\right)$$

Through the specifications of the rubber air spring listed in table 4.1, the result is that the approximate curve (given by Eq. (4.46)) agrees well with the original one (given by Eq. (4.28)) as shown in Fig. 4.14. The notation of the line types is presented in the right-top corner panel.

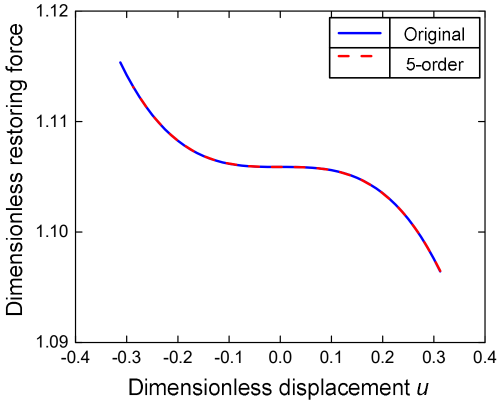

Fig. 4.14. Restoring force curves versus the dimensionless displacement.

Next, supposing the base is excited by a harmonic excitation $z_e = Z_e\cos(\omega t)$ with Z_e is the excitation amplitude in mm and ω is the excitation frequency in rad/s. In the same manner as in the static analysis section, to simplify the dynamic analysis, some dimensionless parameters are introduced as below:

$$\bar{u} = \frac{u}{Z_e};\ \tau\text{=t}\omega_n;\ \omega_n = \sqrt{-2a_1 / M};\ \eta_i = -2\frac{a_i Z_e^{i-1}}{i!a_1}\ \text{(i=2,3,...,5)},\ \xi\text{=}\frac{C_d}{2M\omega_n};\ \Omega = \frac{\omega}{\omega_n}$$

From Eq. (4.45), the vibration equation around the DSEP is rewritten in non-dimension as:

$$\bar{u}'' + 2\xi\ \bar{u}' + \bar{u} + \sum_{i=2}^{5} \eta_i \bar{u}^i = \Omega^2 \cos(\Omega\tau) \tag{4.47}$$

herein, the prime " ′ " is used to denote differentiation with respect to the τ.

A Normal form analysis is employed to find out the fundamental solution of the dynamic equation, the dynamic equation (4.47) is transformed as

$$\bar{u}'' + \bar{u} + \Gamma(\bar{u}, \bar{u}') = pxq \tag{4.48}$$

where $p = \left[\Omega^2 / 2\ \Omega^2 / 2\right]$; q$=\left[e^{i\Omega\tau}\ e^{-i\Omega\tau}\right]^T$; $\Gamma(\bar{u}, \bar{u}') = \varepsilon f(\bar{u}, \bar{u}')$; and ε is a small parameter.

with

$$\begin{gathered} f(\bar{u}, \bar{u}') = \left(2\hat{\xi}'\ \bar{u}' + \sum_{i=2}^{5} \hat{\eta}_i' \bar{u}^i \right) \\ \hat{\xi}' = \frac{\xi}{\varepsilon};\ \hat{\eta}' = \frac{\eta_i}{\varepsilon} \end{gathered} \tag{4.49}$$

By transforming as following:

$$\bar{u} = \bar{w} + \varepsilon h(\bar{w}, \bar{w}');\ \bar{u}' = \bar{w}' + \varepsilon \frac{dh(\bar{w}, \bar{w}')}{dt};\ \bar{u}'' = \bar{w}'' + \varepsilon \frac{d^2 h(\bar{w}, \bar{w}')}{dt^2}; \tag{4.50}$$

The result is that Eq. (4.48) is transmitted as following:

$$\bar{w}'' + \bar{w} + \varepsilon g(\bar{w}, \bar{w}') = p_w xq \tag{4.51}$$

or

$$\bar{w}'' = p_w xq - \bar{w} - \varepsilon g(\bar{w}, \bar{w}') \tag{4.52}$$

Substituting Eq. (4.50) and (4.52) into Eq. (4.48), we obtain:

$$\begin{aligned} & p_w xq - \varepsilon g(\overline{w},\overline{w}') + \varepsilon \frac{d^2 h(\overline{w},\overline{w}')}{dt^2} + \varepsilon h(\overline{w},\overline{w}') \\ & + \varepsilon f\left(\overline{w} + \varepsilon h(\overline{w},\overline{w}');\ \overline{w}' + \varepsilon \frac{dh(\overline{w},\overline{w}')}{dt} \right) = pxq + \mathcal{O}\left(\varepsilon^2\right) \end{aligned} \tag{4.53}$$

The function of $f\left(\overline{w} + \varepsilon h(\overline{w},\overline{w}');\ \overline{w}' + \varepsilon \frac{dh(\overline{w},\overline{w}')}{dt} \right)$ can be approximated by expanding Taylor series and the higher order ε terms can be ignored. We obtain as below:

$$f\left(\overline{w} + \varepsilon h(\overline{w},\overline{w}');\ \overline{w}' + \varepsilon \frac{dh(\overline{w},\overline{w}')}{dt} \right) = f\left(\overline{w};\ \overline{w}'\right) + \mathcal{O}\left(\varepsilon^1\right) \approx f\left(\overline{w};\ \overline{w}'\right) \tag{4.54}$$

Substituting Eq. (4.54) into Eq. (4.53), then the balance of ε^0 and ε^1 is given by:

$$\begin{aligned} & \varepsilon^o \qquad\qquad\qquad p_w xq = pxq \\ & \varepsilon^1 \quad g(\overline{w},\overline{w}') - \frac{d^2 h(\overline{w},\overline{w}')}{dt^2} = h(\overline{w},\overline{w}') + f\left(\overline{w};\ \overline{w}'\right) \end{aligned} \tag{4.55}$$

The state $\overline{w}$ can be split into two components as following:

$$\overline{w} = \overline{w}_p + \overline{w}_m \tag{4.56}$$

in which, $\overline{w}_p$ and $\overline{w}_m$ can be:

$$\overline{w}_p = \frac{\overline{W}_p}{2} e^{i\Omega\tau} \text{ and } \overline{w}_m = \frac{\overline{W}_m}{2} e^{-i\Omega\tau} \tag{4.57}$$

with $\overline{W}_p = \overline{W}(\varepsilon\tau) e^{-i\varphi}$ and $\overline{W}_m = \overline{W}(\varepsilon\tau) e^{i\varphi}$, $\overline{W}(\varepsilon\tau)$ is the peak value and φ is the phase angle.

Taking derivative of $\overline{w}$ versus the scaling time τ:

$$\begin{cases} \overline{w}' = i\Omega\left(\overline{w}_p - \overline{w}_m\right) + \mathcal{O}(\varepsilon^1) \\ \overline{w}'' = -\Omega\left(\overline{w}_p + \overline{w}_m\right) + i\Omega\left(e^{i\Omega\tau} \overline{W}_p'\left(\varepsilon\tau\right) - e^{-i\Omega\tau} \overline{W}_m'\left(\varepsilon\tau\right)\right) + \mathcal{O}(\varepsilon^2) \end{cases} \tag{4.58}$$

In addition, the functions of $f(\bar{w},r)$; $g(\bar{w},\bar{w}')$ and $h(\bar{w},\bar{w}')$ are determined as below:

$$\begin{cases} f(\bar{w},\bar{w}',r)=[f]\bar{w}^*(\bar{w}_p,\bar{w}_m,\mathrm{r}) & \text{(a)} \\ g(\bar{w},\bar{w}',r)=[\mathrm{A}]\bar{w}^*(\bar{w}_p,\bar{w}_m,\mathrm{r}) & \text{(b)} \\ h(\bar{w},\bar{w}',r)=[B]\bar{w}^*(\bar{w}_p,\bar{w}_m,r) & \text{(c)} \end{cases} \tag{4.59}$$

By substituting $\bar{u}=\bar{w}$ and $\bar{u}'=\bar{w}'$, then, combination of Eq. (4.49) and Eq. (4.59a) we obtain:

$$[\mathrm{f}]^T=[-2\xi'\gamma\ 2\xi'\gamma\ \eta_2'\ 2\eta_2'\ \eta_2'\ \eta_3'\ 3\eta_3'\ 3\eta'\ \eta_3'\ \eta'\ 4\eta_4'\ 6\eta_4'\ 4\eta_4'\ \eta_4'\ \eta_5'\ 5\eta_5'\ 10\eta_5'\ 10\eta_5'\ 5\eta_5'\ \eta_5'] \tag{4.60}$$

$$\bar{w}^*=\begin{bmatrix} \bar{w}_m\ \bar{w}_p\ \bar{w}_m^2\ \bar{w}_m\bar{w}_p\ \bar{w}_p^2\ \bar{w}_m^3\ \bar{w}_m^2\bar{w}_p\ \bar{w}_m\bar{w}_p^2\ \bar{w}_p^3\ \bar{w}_m^4\ \bar{w}_m^3\bar{w}_p\ \bar{w}_m^2\bar{w}_p^2\ \bar{w}_m\bar{w}_p^3\ \bar{w}_p^4\ \bar{w}_m^5\ \bar{w}_m^4\bar{w}_p\ \bar{w}_m^3\bar{w}_p^2 \\ \bar{w}_m^2\bar{w}_p^3\ \bar{w}_m\bar{w}_p^4\ \bar{w}_p^5 \end{bmatrix} \tag{4.61}$$

in which $\gamma=i\Omega$

Substituting Eq. (4.59) into the second equation of Eq. (4.55), we have:

$$[\mathrm{A}]\bar{w}^*(\bar{w}_p,\bar{w}_m,r)-[B]\psi\bar{w}^*(\bar{w}_p,\bar{w}_m,r)=[B]\bar{w}^*(\bar{w}_p,\bar{w}_m,r)+[f]\bar{w}^*(\bar{w}_p,\bar{w}_m,\mathrm{r}) \tag{4.62}$$

where Ψ is found from following condition:

$$\frac{d^2\bar{w}^*(\bar{w},\bar{w}',r)}{dt^2}=\Psi\bar{w}^*(\bar{w},\bar{w}',r) \tag{4.63}$$

Considering the non-zero $\bar{w}^*(\bar{w},r)$, the matrices [A] and [B] are determined by

$$[A]-[B]\psi-[B]=[f] \tag{4.64}$$

Finally, the matrices [A] and [B] are expressed as following:

$$[A]=[-2\xi'\gamma\ 2\xi'\gamma\ 0\ 0_2\ 0_2\ 0\ 3\eta_3'\ 3\eta'\ 0\ 0\ 0_4\ 0_4\ 0_4\ 0_4\ 0_5\ 0_5\ 10\eta_5'\ 10\eta_5'\ 0\ 0] \tag{4.65}$$

$$\begin{gathered}[B]=[0\ 0\ \eta_2'/3\Omega^2\ \text{-}2\eta_2'/\Omega^2\ \eta_2'/3\Omega^2\ \eta_3'/8\Omega^2\ 0_3\ 0\ \eta_3'/8\Omega^2\ \eta_4'/15\Omega^2\ 4\eta_4'/3\Omega^2\ \text{-}6\eta_4'/\Omega^2 \\ 4\eta_4'/3\Omega^2\ \eta_4'/15\Omega^2\ \eta_5'/24\Omega^2\ 5\eta_5'/8\Omega^2\ 0\ 0\ 5\eta_5'/\Omega^2\ \eta_5'/24\Omega^2]\end{gathered} \tag{4.66}$$

By substituting Eqs. (4.57-4.59) into Eq. (4.51), then balancing the $e^{i\Omega\tau}$ and $e^{-i\Omega\tau}$ terms, the first-order differential equation in $\bar{W}_p$ and $\bar{W}_m$ can be written as following:

$$\begin{bmatrix} \bar{W}'_p \\ \bar{W}'_m \end{bmatrix} = \frac{1}{2\Omega}\begin{bmatrix} (1-\Omega^2)\,\bar{\mathrm{W}}_p\, i + \frac{3}{4}\eta_3\,\bar{\mathrm{W}}_p^2\bar{\mathrm{W}}_m\, i + \frac{10}{16}\eta_5\,\bar{\mathrm{W}}_p^3\bar{\mathrm{W}}_m^2\, i - 2\xi\Omega\,\bar{\mathrm{W}}_p - i\Omega^2 \\ -(1-\Omega^2)\,\bar{\mathrm{W}}_m\, i - \frac{3}{4}\eta_3\,\bar{\mathrm{W}}_p\bar{\mathrm{W}}_m^2\, i - \frac{10}{16}\eta_5\,\bar{\mathrm{W}}_p^2\bar{\mathrm{W}}_m^3\, i - 2\xi\Omega\,\bar{\mathrm{W}}_m + i\Omega^2 \end{bmatrix} \tag{4.67}$$

In order to find the steady-state amplitude solutions, $\bar{W}'_p$ and $\bar{W}_m$ are set zero, simultaneously using with $\bar{W}_p = \bar{W}(\varepsilon\tau)e^{-i\varphi}$ and $\bar{W}_m = \bar{W}(\varepsilon\tau)e^{i\varphi}$, the result is to obtain:

$$\begin{cases} \Omega^4 = \left((1-\Omega^2)\,\bar{\mathrm{W}} + \frac{3}{4}\eta_3\,\bar{\mathrm{W}}^3 + \frac{10}{16}\eta_5\,\bar{\mathrm{W}}^5 \right) + 2\xi\Omega\,\bar{\mathrm{W}} \\ \tan\varphi = \dfrac{2\xi\Omega\,\bar{\mathrm{W}}}{(1-\Omega^2)\,\bar{\mathrm{W}} + \frac{3}{4}\eta_3\,\bar{\mathrm{W}}^3 + \frac{10}{16}\eta_5\,\bar{\mathrm{W}}^5} \end{cases} \tag{4.68}$$

Thus, using Eqs.(4.56-57), the result of the relative displacement of the load plate at the steady state is obtained as following:

$$\bar{u} = \bar{w} = \bar{W}\cos(\Omega\tau - \varphi) \tag{4.69}$$

In addition, by substituting $\tau = t\omega_n$, the excitation signal can be written in dimensionless form as:

$$\bar{z}_e = \frac{z_e}{Z_e} = \cos(\Omega\tau) \tag{4.70}$$

Inserting Eqs. (4.69) and (4.70) into Eq. (4.41), the dimensionless absolute displacement response of the isolated object being:

$$\bar{z} = \bar{d} + \cos(\Omega\tau) + \bar{W}\cos(\Omega\tau - \varphi) \tag{4.71}$$

where: $\bar{d} = d / Z_e$

By using Euler equation:

$$e^{i\delta} = \cos\left(\delta\right) + i\sin\left(\delta\right)$$
$$\Rightarrow \begin{cases} \cos\left(\delta\right) = \dfrac{1}{2}\left(e^{i\delta} + e^{-i\delta}\right) \\ \sin\left(\delta\right) = -\dfrac{1}{2}i\left(e^{i\delta} - e^{-i\delta}\right) \end{cases} \tag{4.72}$$

Eq. (4.71) can be rewritten as following:

$$\overline{z} = \overline{d} + \frac{1}{2}\left(1 + \hat{W}e^{-i\varphi}\right)e^{i\Omega\tau} + \frac{1}{2}\left(1 + \hat{W}e^{i\varphi}\right)e^{-i\Omega\tau} \tag{4.73}$$

Letting:

$$\begin{aligned} 1 + \overline{W}e^{-i\varphi} &= \overline{Z}e^{-i\Phi} \\ 1 + \overline{W}e^{i\varphi} &= \overline{Z}e^{i\Phi} \end{aligned} \tag{4.74}$$

with $\overline{Z}$ is the absolute vibration amplitude of the isolated object in dimensionless form, Φ is the phase difference between z and z_e, that is:

$$\begin{cases} \overline{Z} = \sqrt{1 + \overline{W}^2 + 2\overline{W}\cos\varphi} \\ \tan\Phi = \left|\dfrac{\overline{\mathrm{W}}\sin\varphi}{1 + \overline{W}\cos\varphi}\right| \end{cases} \tag{4.75}$$

According to Eq. (4.74), Eq. (4.73) is recast as below:

$$\overline{z} = \overline{d} + \frac{1}{2}\overline{Z}e^{-i\Phi}e^{i\Omega\tau} + \frac{1}{2}\overline{Z}e^{+i\Phi}e^{-i\Omega\tau} = \overline{d} + \overline{Z}\cos\left(\Omega\tau - \Phi\right) \tag{4.76}$$

Next, it is meaningful that the isolation effectiveness (vibration transmissibility) of the QSAVIM using RAS which is defined by the ratio of the absolute amplitude (Z) of the load plate to the excitation amplitude (Z_e), can be estimated by following formula:

$$T_a = \frac{|Z|}{|Z_e|} = \overline{Z} = \sqrt{1 + \overline{W}^2 + 2\overline{W}\cos\varphi} \tag{4.77}$$

As seen in Eq. (4.77), the effected vibration isolation is the region in which the value of the vibration transmissibility (T_{a}) is lower than one. This means that the absolute displacement of the isolated load is smaller than the excitation.

Furthermore, to determine the stability of the steady state response solution predicted by the Normal form technique, the amplitude of the response must be allowed to vary slowly with time. It means that a small disturbance is superposed on the steady state solution. The stability is governed by eigenvalue of the Jacobian of the Eq. (4.78). The Jacobian can be written as following:

$$j = \begin{bmatrix} j_{11} & j_{12} \\ j_{21} & j_{22} \end{bmatrix} \tag{4.78}$$

in which j_{11}, j_{12}, j_{21} and j_{22} are given in (4.79)

$$\begin{cases} j_{11} = \dfrac{d\bar{W}_p'}{d\bar{W}_p} = \dfrac{1}{2\Omega}\left((1-\Omega^2)i + \dfrac{3}{2}\eta_3\, \bar{\mathrm{W}}_p \bar{\mathrm{W}}_m\, i + \dfrac{30}{16}\eta_5\, \bar{\mathrm{W}}_p^2 \bar{\mathrm{W}}_m^2\, i - 2\xi\Omega \right) \\ j_{12} = \dfrac{d\bar{W}_p'}{d\bar{W}_m} = \dfrac{1}{2\Omega}\left(\dfrac{3}{4}\eta_3\, \bar{\mathrm{W}}_p^2\, i + \dfrac{10}{8}\eta_5\, \bar{\mathrm{W}}_p^3 \bar{\mathrm{W}}_m\, i \right) \\ j_{21} = \dfrac{d\bar{W}_m'}{d\bar{W}_p} = -\dfrac{1}{2\Omega}\left(\dfrac{3}{4}\eta_3\, \bar{\mathrm{W}}_m^2\, i + \dfrac{10}{8}\eta_5\, \bar{\mathrm{W}}_p \bar{\mathrm{W}}_m^3\, i \right) \\ j_{22} = \dfrac{d\bar{W}_m'}{d\bar{W}_m} = -\dfrac{1}{2\Omega}\left((1-\Omega^2)i + \dfrac{3}{2}\eta_3\, \bar{\mathrm{W}}_p \bar{\mathrm{W}}_m\, i + \dfrac{30}{16}\eta_5\, \bar{\mathrm{W}}_p^2 \bar{\mathrm{W}}_m^2\, i + 2\xi\Omega \right) \end{cases} \tag{4.79}$$

The eigenvalue of the Jacobian is determined as below:

$$\begin{vmatrix} j_{11} - \lambda & j_{12} \\ j_{21} & j_{22} - \lambda \end{vmatrix} = \lambda^2 - (j_{11} + j_{22})\lambda + j_{12} j_{21} = 0 \tag{4.80}$$

By using the Routh criterion, to determine the boundary of the stability of the solution given in Eq. (4.68), it is observed that $(j_{11}+j_{22})$ is negative, it can be deduced that the system can have an eigenvalue with a positive real component if $j_{12}j_{21} \leq 0$, such that $j_{12}j_{21}=0$ is the boundary where the transition from the stable to unstable regions occurs.

4.5. Effects of configurative parameters on vibration transmissibility curve

4.5.1. Influence of pressure ratio on the shape of the amplitude-frequency response curve

Firstly, the influence of the pressure ratio μ defined as the proportion of P_{wh2} to P_{wh1} on the relative amplitude-frequency responses, which are numerical simulations of Eq. (4.68), is shown in Fig. 4.15(a). The pressure ratio is varied from 1.2 to 1.57, but other parameters are kept at the values of $\alpha=37^{o}$, R=60mm, r=20mm, H_o=25.6mm for which the dynamic stiffness around the desirable static equilibrium position is predicted by using Eq. (4.30) as shown in Fig. 4.15(b). It is interesting to observe that the resonant peak amplitude and frequency are decreased according to the growth of the pressure ratio μ. Besides, the boundary of stability of the steady state solution denoted by the red dashed lines is also expanded in accordance with the increase in the resonant peak including the amplitude and frequency. It is evident that when the pressure ratio is upgraded, the dynamic stiffness at the DSEP is reduced as shown in Fig. 4.15(b). As known, the benefit of low stiffness is low resonance frequency.

In addition, as seen in Fig. 4.15(a), the amplitude-frequency curves are bended to the right. It means that there exists the frequency jump phenomenon including the jump-up and jump-down. The level of bending is reduced as the pressure ratio is increased. For each value of the pressure ratio, the system will offer a jump-down and a jump-up point. In region between the jump-up and jump-down points (plotted by the dot lines), there can exist three branches corresponding to three solution of Eq. (4.47) obtained by the Normal form. Among them, the middle branch is unstable solution and unrealizable in any experiment determined by the Routh criterion meanwhile the two remaining cases including upper and low branches are stable solutions. For a given frequency of excitation, the steady response of the system can only be upper branch (called resonant solutions) or low branch (called non-resonant solutions). The initial conditions (position and velocity) will determine which branch will actually occur. This will be explained clearly next section.

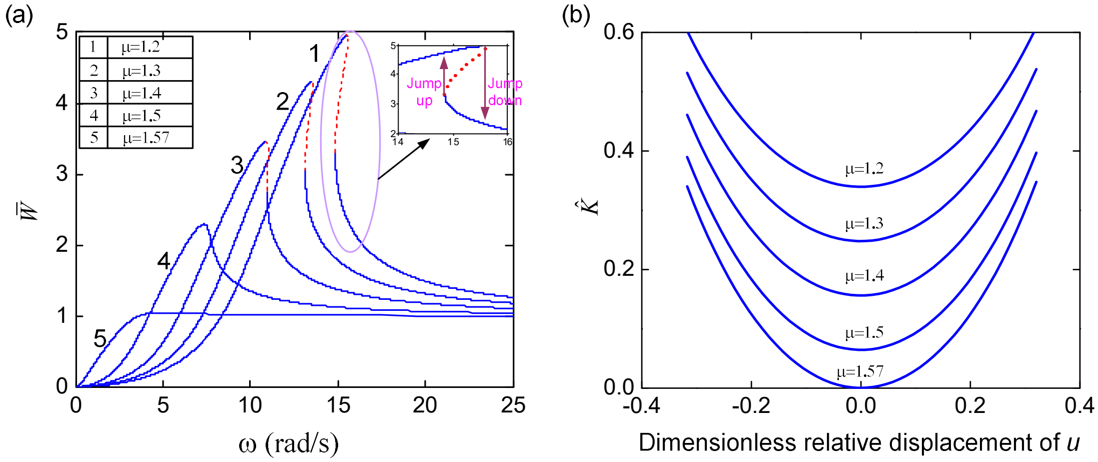

Fig.4.15. (a) The relative amplitude-frequency response of the QSAVIM using RAS with Eq. (4.68) for P_{wh1}=2 bar, ξ=0.06, α=37°, R=60mm, r=20mm, H_o=25.6mm and μ=1.2, 1.3, 1.4, 1.5, 1.57. (b) Dynamic stiffness curves with the same parameters in (a).

The trajectory of these frequency jump points versus the frequency is plotted in Fig. 4.16 (a) for μ=0.47, 0.5, 0.7, 1.0, 1.2, 1.43, the same other parameters as in Fig. 4.15. The point of jump-up frequency is presented by the red solid line, the jump-down one is exhibited by the blue dashed line. It can be noteworthy that, with values of μ=1.43 or 0.47, the jump-down point closely moves to jump-up one. In other words, the effect of the frequency jump phenomena on the dynamic response is reduced. However, it is clear that as shown in Fig. 4.16(b) that if μ=0.47, the non-dimension dynamic stiffness at the DSEP is quasi-unity. In this case, the dynamic stiffness of the proposed system at the DSEP is nearly equal to that of the load bearing mechanism in vertical direction. The result is that in the resonant region the isolation effectiveness of the QSAVIM using RAS (presented by the red solid line) may be lower than that of the ETVIM in which the load plate is supported by the LBM meanwhile the SCM is removed (the blue dashed line) as presented in Fig. 4.17. Oppositely, if μ=1.43 for which the dimensionless dynamic stiffness at the DSEP is smaller than one (approximately 0.12), the isolation effectiveness of the proposed system (exhibited by the pink dot line) is improved remarkably compared with that of the system without the SCM.

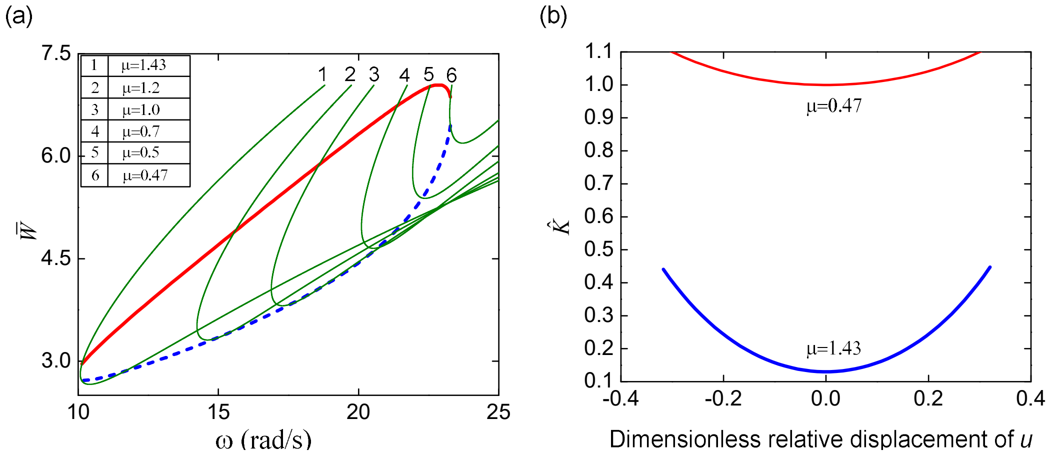

Fig. 4.16. (a) Trajectories of the frequency-jump points for ξ=0.06 and the same other parameters as in Fig. 4.15. Herein, the red solid line is denoted for the jump-up points and the jump-down points are presented by the blue dashed line. (b) Dynamic stiffness curves for μ=1.43 and 0.47 the same other parameters as in (a)

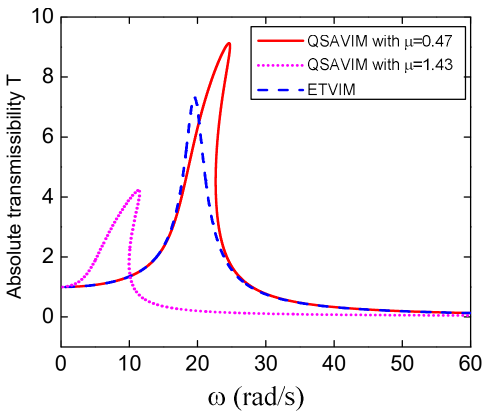

Fig. 4.17. Comparison of isolation effectiveness of the ETVIM and the QSAVIM using RAS having ξ=0.06 and μ=0.47 and 1.43 and the same other parameters as in Fig. 4.15 (a).

Secondly, on the aspect of geometry, to obtain the desirable static equilibrium position, the dependence of the isolated object weight on the wedge angle α and the radius r of roller is shown in Fig. 4.18(a). Among the inclined angle α and the radius r, the isolated load is strongly affected by the inclined angle α. However, in the proposed structure, the load bearing mechanism is only employed to support the isolated object, meanwhile, the dynamic stiffness of the system is corrected by the stiffness corrected mechanism, therefore, with the suitably chosen parameters of r, α and P_{wh1} for the corresponding isolated mass, it is possible to gain the DSEP but not to obtain the desirable low dynamic stiffness at this position. Indeed, in order to satisfy these requirements, there is a relation between the pressure ratio μ and these geometric parameters so that the dynamic stiffness at the DSEP is quasi-zero as shown in Fig. 4.18 (b). It can be seen that the pressure ratio μ is increased according to the growth of the radius r of the roller and the inclined angle α. Specifically, if the angle α is smaller than 45 degrees, the influence of the radius r of the roller on μ is light, after 45 degrees, the pressure ratio is strongly affected by the variation of the radius r. Similarly, the slope of the curve of the pressure ratio with respect to the wedge angle α will be upgraded along with the expansion of this angle.

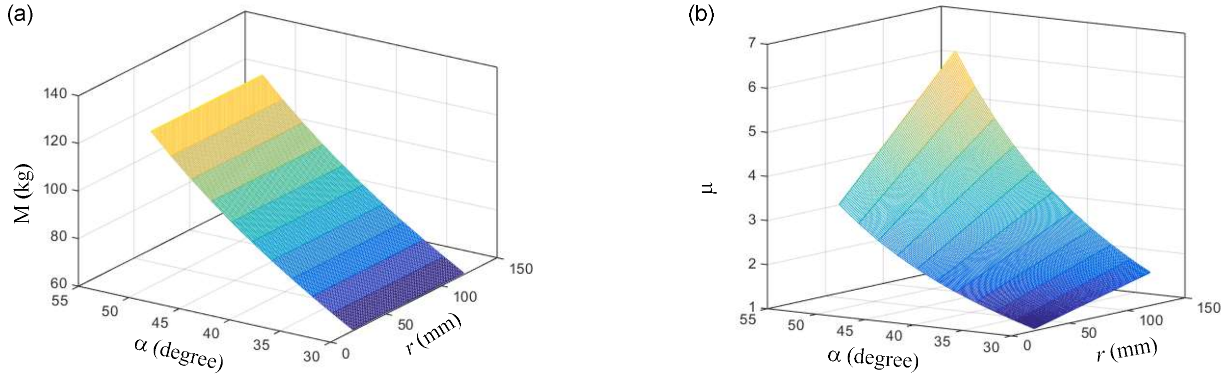

Fig. 4.18. Relationship between the geometric parameters consisting of the wedge angle α, the radius r of the roller and the isolated load M (a) and the pressure ratio μ (b). It is noted that for this relationship the QSAVIM using RAS obtains the quasi-zero stiffness at the DSEP, $P_{wh1} = 2\ bar$

4.5.2. Influence of geometrical parameters on the resonant peak.

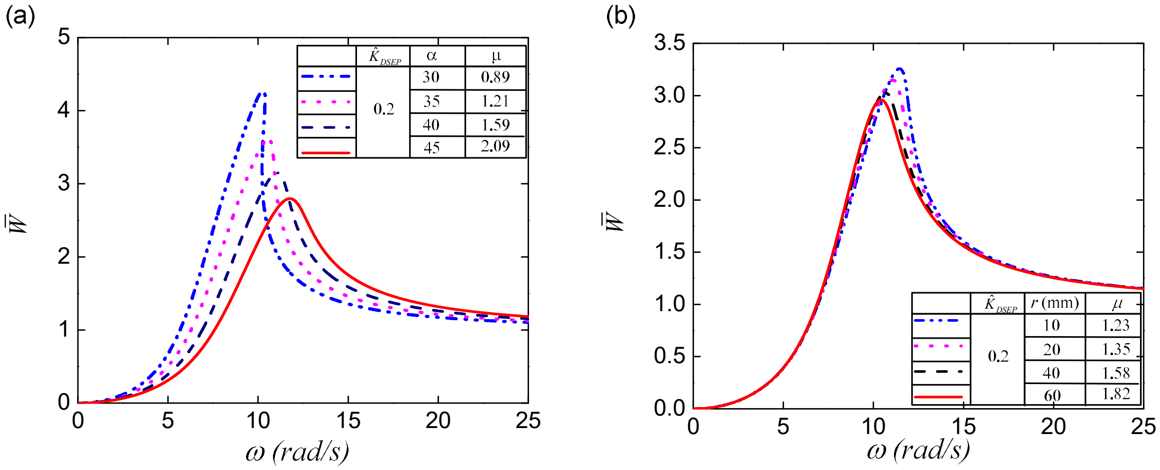

Fig. 4.19. Relative amplitude-frequency curves of the proposed model with Eq. (4.68) for r=20 mm and various values of α (a), for α=37° and various values of r (b), herein, $P_{wh1} = 2$ bar, ξ=0.06, R=60 mm, H_o=25.6mm, other parameters noted in top-right corner panel for (a) and bottom-right corner panel for (b)

Furthermore, the effects of the geometrical parameters including the wedge angle α and the radius r of the roller on the shape of the amplitude-frequency curve are studied when the dimensionless dynamic stiffness value $\hat{K}_{DSEP}$ at the DSEP is always equal to 0.2. Firstly, the influence of varying the wedge angle α is taken into account as shown in Fig. 4.19 (a). As above analyzed, in order to achieve $\hat{K}_{DSEP} = 0.2$, as the values of α=30°, 35°, 40°, 45°, the value of r=20 mm and the same other parameters as in Fig. 4.16, the pressure ratio calculated by using Eq. (4.31) is equal to 0.89, 1.21, 1.59, 2.09. The result confirmed that peak amplitude is reduced in accordance with the increase in value of α, oppositely, the peak frequency is increased lightly. Secondly, the radius r of the roller is varied with a value set of 10, 20, 40 and 60mm, the value of α=37° and other parameters are remained as in the first case. For which, the pressure ratio is determined as following: 1.23, 1.35, 1.58 and 1.82. It can be observed from Fig. 4.19(b) that there is a small reduction in the resonant peak amplitude and frequency when the diameter of the roller is developed. These results are also confirmed in Fig. 4.20 and it may be seen that the effect of the wedge angle α on the resonant peak is stronger than that of the diameter of the roller.

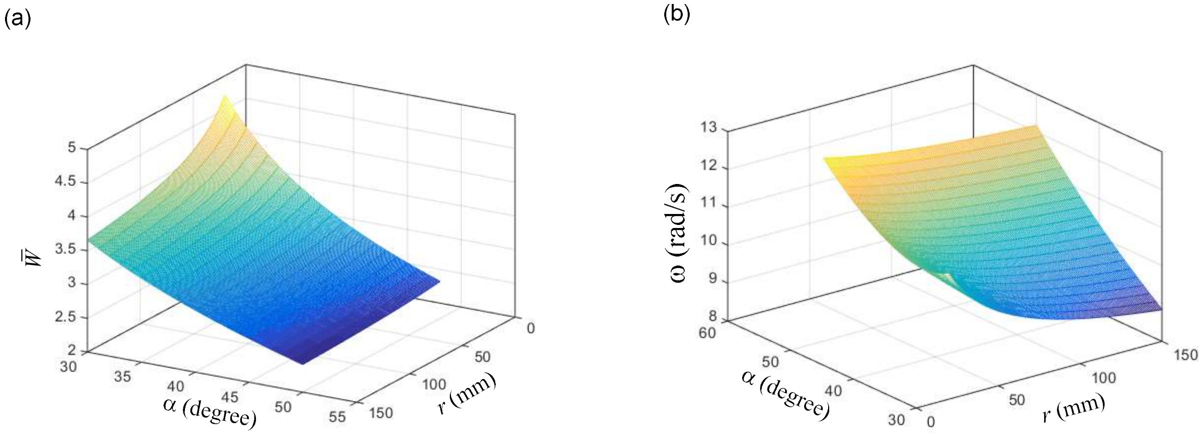

Fig. 4.20. Dependence of the resonant peak on the geometrical parameters of the system given by Eq. (4.68) with the same parameters as in Fig. 4.19 (a) Peak amplitude. (b) Peak frequency

4.5.3. Effects of damping on vibration transmissibility curve

In order to study the effects of the parameter ξ on the shape of the amplitude-frequency curve, the parameters of the QSAVIM using RAS are set as following: $P_{wh1} = 2\,\text{bar}$, α=37°, R=60mm, r=20mm, H_o=25.6mm and the pressure ratio μ=1.35 for which the dimensionless dynamic stiffness $\hat{K}_{DSEP}$ at the DSEP is equal to 0.2. Meanwhile, a set of parameters ξ=0.01, 0.02, 0.04 and 0.07 is employed to investigate these effects. By using Eq. (4.68), the amplitude-frequency curves are predicted as shown in Fig. 4.21, herein, the notations of the response curves are presented in detail in upper-left corner panel. It reveals that the peak amplitude and the resonant frequency are increased as the damping ratio is reduced. Besides, the system with a smaller value of the parameter ξ will have greater bending level of the amplitude-frequency curve.

Especially, in this case, with ξ=0.01, the resonant peak is very far compared with that of ξ>0.01.

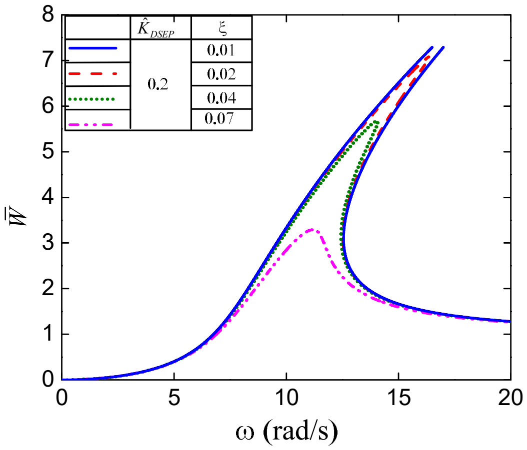

Fig. 4.21. Amplitude-frequency response of the QSAVIM using RAS for P_{wh1}=2 bar, α=37°, R=60mm, r=20mm, H_o=25.6mm and μ=1.35.

4.6. Complex dynamic analysis

As presented above, the effects of the pressure ratio (μ) and geometrical parameters on the dynamic response as the vibration transmissibility curve were disclosed thank to Normal form method. However, this method is considered as one of the approximate analytical methods, which carried out through some assumption in which the load plate vibrates around the equilibrium position with small amplitude as there is a harmonic excitation from the base, simultaneously, the restoring force is mainly contributed by the compressed air and is expressed simply by an approximated polynomial. Nevertheless, the proposed model offers strongly complex and nonlinear characteristic in dynamic response such as the coexistence of multiple solutions, bifurcation, chaotic motions, etc…But these phenomena are not revealed by the simple analytical method in the previous section. This is also one of the limitations of using the analytical method.

Hence, it is necessary to explore more complex dynamic behavior through the numerical integration for Eq. (4.45) by using fourth-order Runge-Kutta algorithm with a fixed time step of 1/100 of the harmonic excitation period. Simultanuosly, the data of maximum amplitude are sampled via using Poincaré sections. Namely, the force of the air spring contributed by three components: compressed air, friction and viscoelastic will be taken into account which means that F_s is calculated by Eq. (4.23) in which F_{air} is replaced by F_{ras} given in Eq. (4.1). Besides, for a more challenging excitation, a random signal excited from the base will be also considered to evaluate the isolation response of the QSAVIM using RAS.

4.6.1. Frequency jump phenomenon

By integrating numerically for Eq. (4.45) in which a harmonic excitation with amplitude of 10 mm and frequency swept from 0 to 3 rad/s (denoted by the dashed line) and vice versa from 3 to 0 rad/s (the dot line) is used, the result is to obtain the amplitude-frequency response curve as shown in Fig. 4.22. Meanwhile, the solid line denotes the amplitude-frequency response curve through Normal form solution. Where, the pressure P_{wh1} of the air spring 1 is set at the value of 2.5 bar, the dimensionless stiffness value at the DSEP is 0.01 and damping ratio (ξ) is 0.1 meanwhile other parameters are the same as the cases mentioned above, obtaining the pressure ratio of 0.7245. It is noteworthy to observe that the Normal form solution with the fifth-order approximate curve of the restoring force gives closer approximation to the time-stepping solution

As observed in Fig. 4.22, the simulation result confirms that the frequency jump phenomenon including the jump up about 1.7 rad/s and jump down 2.2 rad/s is occurred. The frequency jump can appear the resonant or non-resonant solution as the excited frequency is within the up and down frequency range, which means that this phenomenon is dangerous for vibration isolation. Accordingly, what steady-state solution will be obtained depending on the initial state which includes the position and velocity. Namely, each resonant and non-resonant solution is determined by the region of the initial states determined by using Poincaré section. For example, if the frequency is 1.9 rad/s, the region of the initial state for obtaining the resonant response denoted by the yellow filled area whilst the area filled by dark blue color is representative for the non-resonant one as presented in Fig. 4.23(a). Although, the system can occur a resonant or non-resonant response, the solution of which is periodic with a fixed point marked by the filled circles as shown in Fig. 4.23(b).

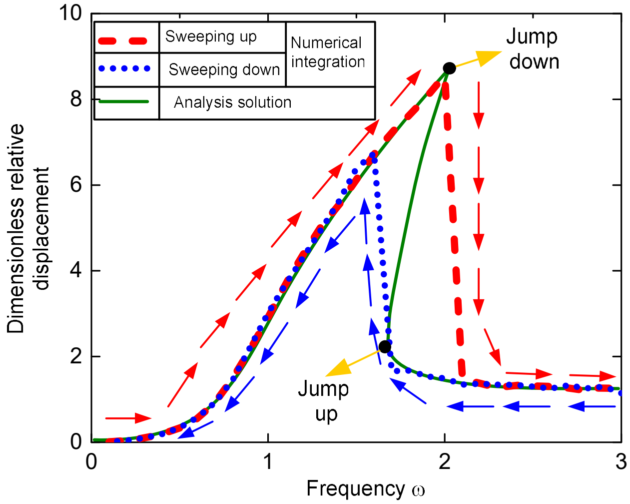

Fig. 4.22. Comparison between the time-stepping and normal form method

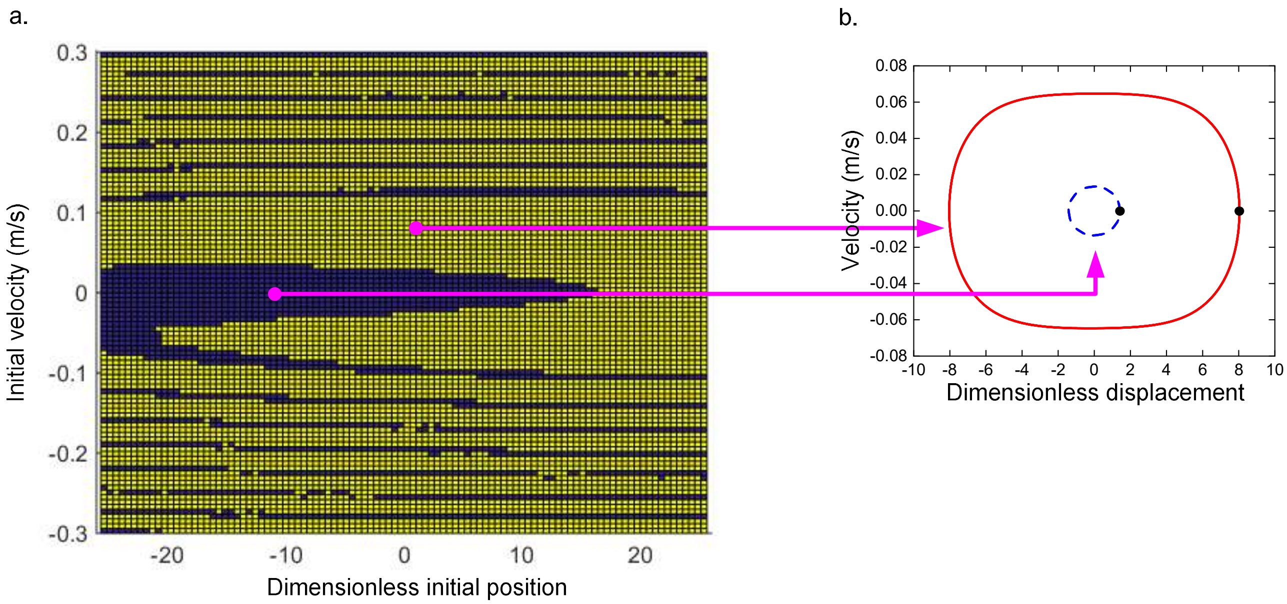

Fig. 4.23.(a) Initial state family of Eq. (4.45) for ξ=0.1, P_{wh1}=2.5 bar, and $\hat{K}_{DSEP} = 0.01$

(b) Phase portray for initial states u=0 mm; v=0 m/s; and u=0 mm, v=0.1 m/s

4.6.2. Bifurcation phenomenon

As mentioned in the analysis solution, the dynamic behavior is only considered as the system attains the desirable static equilibrium position. Therefore, to evaluate comprehensively the complex dynamic behavior of the system in the case in which the equilibrium position will be drifted away from the wanted equilibrium position. This indicates that the air pressure of the load bearing mechanism is not changed but that of the isolated load is changed. Indeed, in the case of P_{wh1}= 2.5 bar, $\mu=0.704$ and $\xi=0.1$, the optimal load to obtain the DSEP is 4.747 kg. Two cases are considered as following:

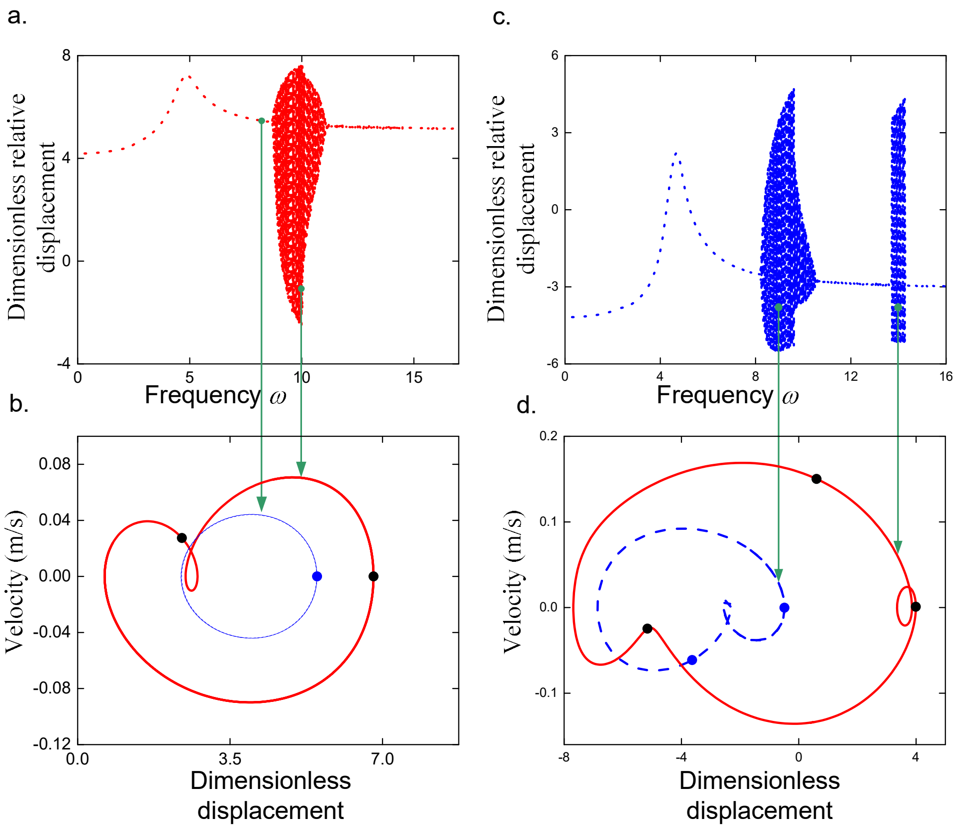

Fig. 4.24. Dimensionless displacement response with respect to frequency for *M*=4.509kg (a), *M*=4.984 kg (c); phase orbit for *M*=4.509 (b), *M*=4.984 kg (d)

1^{st} study case, the isolated load is reduced about 5% comparing with that of the optimal load, remaining 4.509 kg. Its complex dynamic behavior is shown in Fig. 4.24(a). Clearly, there is the appearance of bifurcation of the amplitude-frequency curve from 1-periodic to 2- periodic solution and reversely. The amplitude of the 2-periodic solution may be increased more significantly than that of the 1-periodic solution. For example, if there are two signals of excited frequencies of 8 and 10 rad/s, Fig. 4.24(b) presents the phase trajectory and Poincáre section (denoted by filled circles) indicating that the vibration level of the isolated object subjected to the second excited frequency is higher than the first one.

2^{nd} study case, in the same manner of reducing the isolated load, increasing the isolated load about 5 % (obtaining 4.984 kg) compares with the optimal load. The result is presented in Fig. 4.24(c) and (d). Similar to the aforementioned, there is the appearance of the bifurcation phenomenon in the amplitude-frequency curve. However, in this case, bifurcation occurs in two regions including the frequency from 8 to 10.5 rad/s (2-perriodic solution) and from 13 to 14.5 rad/s (3-perriodic solution) and it is noteworthy that in the bifurcation region, the vibration level of the isolated load may be increased impressively.

4.6.3. Dynamic response under random excitation

In order to see clearly the isolation effectiveness of the QSAVIM using RAS, a random excitation from the base is expressed by Eq. (4.81) described in [60].

$$z_e = \sum_{i=1}^{N} Z_{ei} \sin\left(i\omega t + \phi_i\right) \tag{4.81}$$

in which $Z_{ei} = \sqrt{2P(i\Delta n)\Delta n}$ is the amplitude with i=1,2,3…,N and Δn=2π/90, ω=1.5 rad/s is the fundamental frequency , ϕ_1 is a random variable. P(iΔn) is calculated as following:

$$P(n) = \begin{cases} P(n_o)\left(\dfrac{n}{n_o}\right)^{-w_1} & \text{for } n \le n_\text{o} \\ P(n_o)\left(\dfrac{n}{n_o}\right)^{-w_2} & \text{for } n > n_\text{o} \end{cases} \tag{4.82}$$

with $P(n_\text{o})=16\text{x}10^{-6}$, $w_1=2$, $w_2=1.5$ and $n_\text{o}=1/2\pi$.

Fig. 4.25(a) shows the time history of the random signal with the maximum displacement of 8 mm simultaneously, the power spectrum density of the random excitation is denoted in Fig. 4.25(b). It is noted that the energy of the excitation is distributed mainly within 1.5÷20 rad/s. In this work, the parameters of the QSAVIM using RAS including P_{wh1}, μ, ξ are kept as in Fig. 4.24. Considering three cases of the isolated load include the 4.747, 4.509 and 4.984 Kg. The first load case considered as the optimal load indicates that the system can attain the DSEP but for two remaining cases, the equilibrium position of the QSAVIM using RAS is drifted away from the DSEP. The result is to obtain the isolation response of the system as presented in Fig. 4.26 in which the detailed annotation of the line types is presented in top-right corner panel. It is interesting to see that with M=4.747 kg, the vibration of the isolated object is attenuated strongly. Indeed, the steady state vibration amplitude of the system is approximately 3mm, whilst reducing or increasing the isolation load about 5% indicating M=4.509 kg or 4.984 kg will lead to the increase in the amplitude about 56.25% comparing with the excitation. This is evident because it exists the excited frequency being in the region comprising from 8 to 12 rad/s for the case of M=4.509 kg (seen Fig. 4.24(a)) and from 8 to 14.5 rad/s for M=4.984 kg (seen Fig. 4.24(c)) in which the vibration amplitude of the isolated object can be developed. Furthermore, this simulation result also proved that the isolation effectiveness of the QSAVIM using RAS is the best when the system obtains the desirable equilibrium position as shown in Fig. 4.27. It can be seen that comparing with the excitation, the energy of the QSAVIM using RAS bearing the optimal load is reduced remarkably whilst for two remaining loads, it is developed.

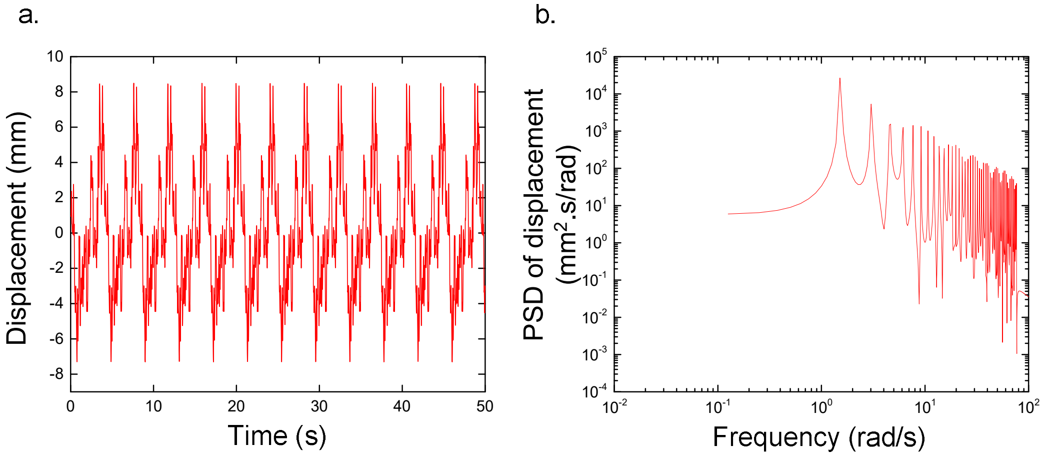

Fig. 4.25.(a) Response with respect to the time of the excitation, (b) Power spectrum density of the excitation.

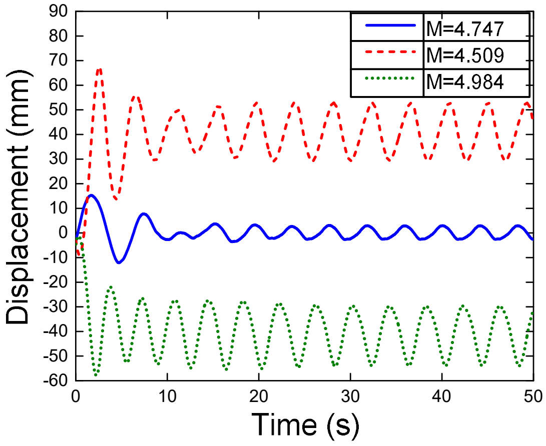

Fig. 4.26. Time history of displacement of the QSAVIM using RAS for three cases including *M*=4.747, 4.509 and 4.984 kg, the same other parameters as in Fig. 4.24

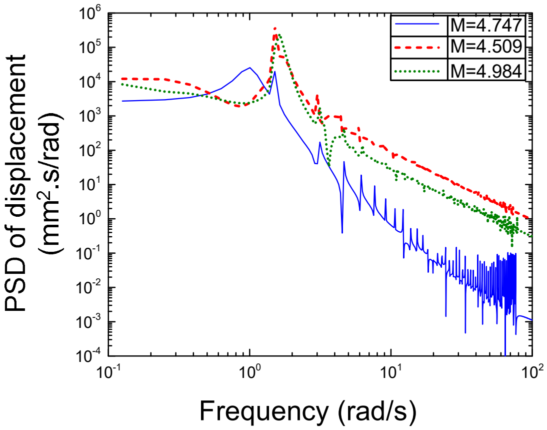

Fig. 4.27. Comparison of power spectrum density of displacement of the QSAVIM using RAS supporting various loads

4.7. Design procedure for obtaining quasi-zero stiffness isolator

The results obtained above indicate that the more reduction in stiffness is, the more the region of effective isolation is broadened and the proposed system still remains the load support capacity. Besides, as the QSAVIM obtains the lowest dynamic stiffness at the desirable static equilibrium position, its isolation effectiveness is much better than that of the case without achieving the DSEP.

Hence, the parameters of the pressure P_{wh1} of the LBM and pressure P_{wh2} of the SCM are very important for design of the QSAVIM. Namely, the pressure P_{wh1} of the LBM should be adjusted according to the isolated load by using Eq. (4.35) so that the system always achieves the DSEP. The low dynamic stiffness $\hat{K}_{DSEP}$ at the DSEP will be then chosen preliminarily. From this selection, the pressure ratio μ will be calculated thank to Eq. (4.31), meaning that the pressure P_{wh2} of the SCM should be determined by $P_{wh2} = \mu P_{wh1}$. Then, the prediction of the isolation region will be realized by numerical simulation of the vibration transmissibility by using Eq. (4.77). If the demanded isolation region is enclosed by the predictable one, the output parameters (R, r, α, P_{wh1},

P_{wh2}) are obtained , whereas, returning the step of preliminary selection of $\hat{K}_{DSEP}$ will be done by reducing the value of $\hat{K}_{DSEP}$ until attaining the demanded isolation region. The design procedure of the proposed model using RAS is shown clearly in Fig. 4.28.

Additionally, the inclined angle α of the wedge is calculated preliminarily by using the Eq. (4.35) to ensure the maximum load and pressure condition. As analyzed, if the inclined angle α is large (more than 45 degree), the deformation of the rubber air spring calculated in the second equation of Eq. (4.18) can exceed the design position region of an air spring given by manufacturers. But if the inclined angle α is too small, this will result in a difficulty for bearing the isolated load. Besides, the radii of the semicircular CAM and roller can be chosen according to the demandable dimension of the QSAVIM using RAS because the effects of these parameters on the vibration transmissibility is unremarkably compared with that of the pressure.

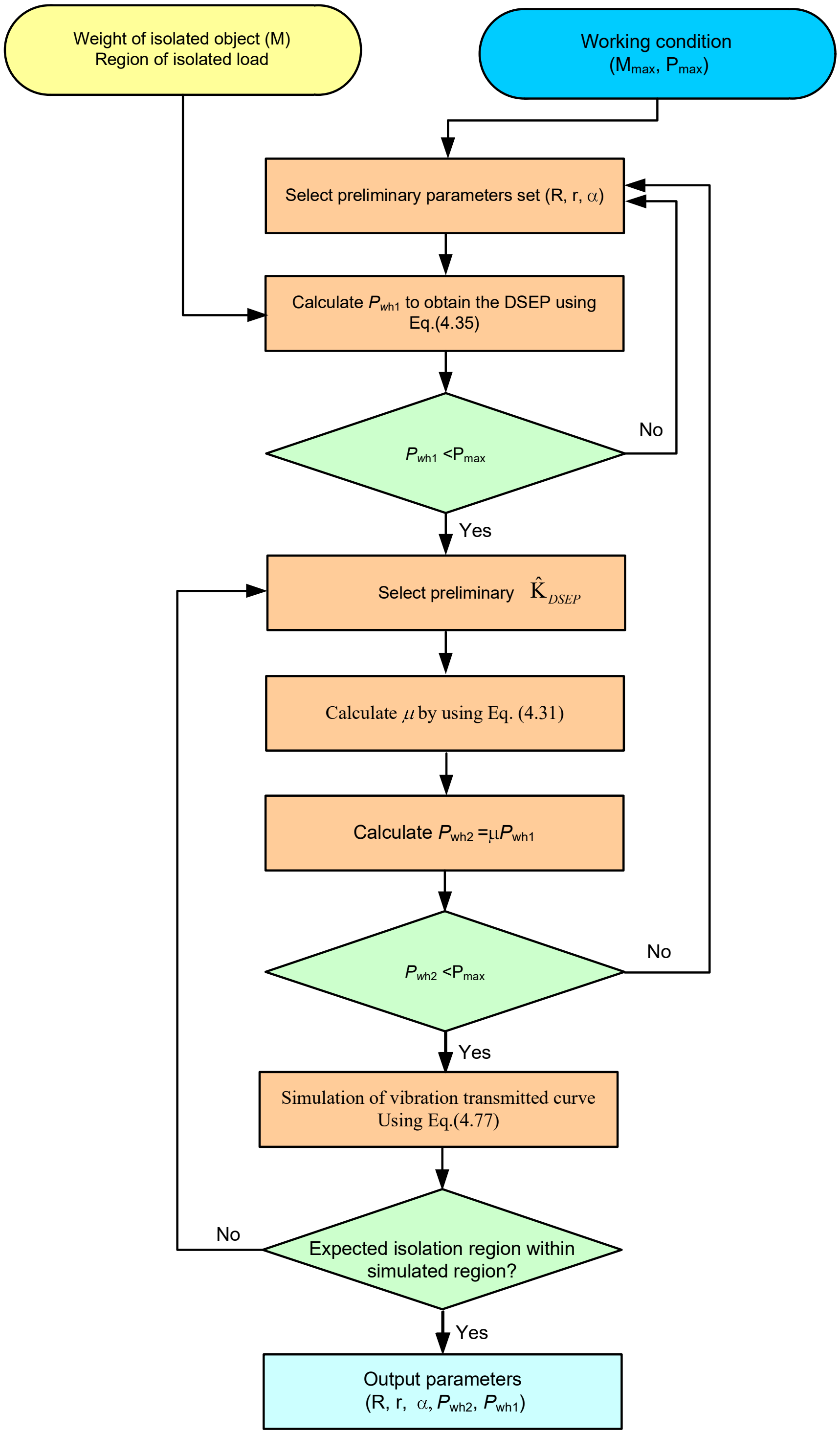

Fig. 4.28. Design procedure of the QSAVIM using RAS with the quasi-zero dynamic stiffness characteristic at the DSEP

4.8. Experimental result and apparatus

As shown in Fig. 4.29, a prototype of the QSAVIM using RAS with the parameters listed in the table 4.2 is built to assess the vibration transmissibility of the theoretical model. For this purpose, the isolation performance of the proposed model is compared with that of the ETVIM in which the load plate is supported by the LBM meanwhile the SCM is removed. In order to realize the works, both QSAVIM and ETVIM will be experimentally done in which the load capacity, the static deformation of the QSAVIM and ETVIM as well as excitation conditions are the same.

Table 4. 2: The parameters of the QSAVIM using a RAS

Parameters	**Original values**
Air pressure of the power supply	6 bar
Atmospheric pressure	1 bar
Radius of cam	60mm
Radius of roller	20 mm
Inclined angle of the leg	37^o
M	70kg

The experimental apparatus is set up as shown in Fig. 4.30(a) and the process of collecting data is described in Fig.4.30(b). Herein, the base frame of the QSAVIM is fixedly placed on the supported plate of the hydraulic shaker manufactured by T.D. Le et al. [61]. The configuration of the exciter is shown in Fig. 4.31(a) in which the motion of the supported plate is realized by a hydraulic cylinder. The position of the supported plate is monitored by a linear sensor with mode RLP50S. In this configuration, the hydraulic cylinder is controlled by a servo valve manufactured by Yuken with mode EHDFG-04 as shown in Fig. 4.31(b). Additionally, controlling the hydraulic circuit is performed through a NI card 6221 which is worked as an A/D converter to connect the computer and peripheral devices (sensor, servo valve…). This shaker can generate the displacement of the supported plate with maximum amplitude of 15mm and maximum frequency of 63 rad/s.

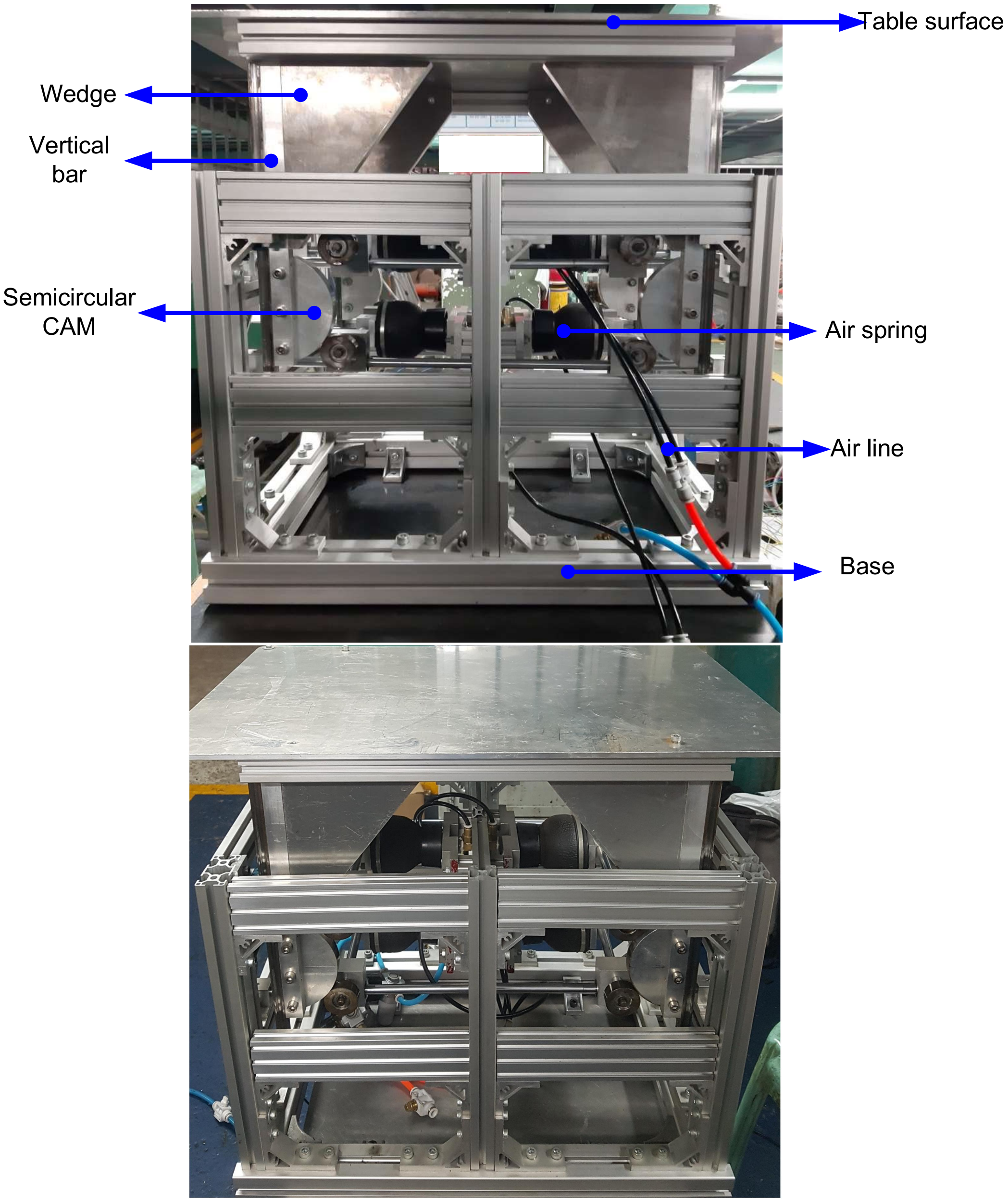

Fig. 4.29. Prototyping of Vibration isolation model

As the supported plate of the shaker is excited with a desirable signal (z_e), this excitation will be transmitted to the load plate of the QSAVIM through the base frame. The relative displacement (u) and absolute acceleration of the load plate (z) are measured by a linear sensor (LZ-19) and an accelerometer ±2g (AS-GB), respectively.

Both data from these two sensors are sent to the PC thank to the NI card 6221. In these experiments, Matlab/Simulink is employed to collect these data. It is noted that the absolute displacement of the load plate is indirectly measured by using Eq. (4.41).

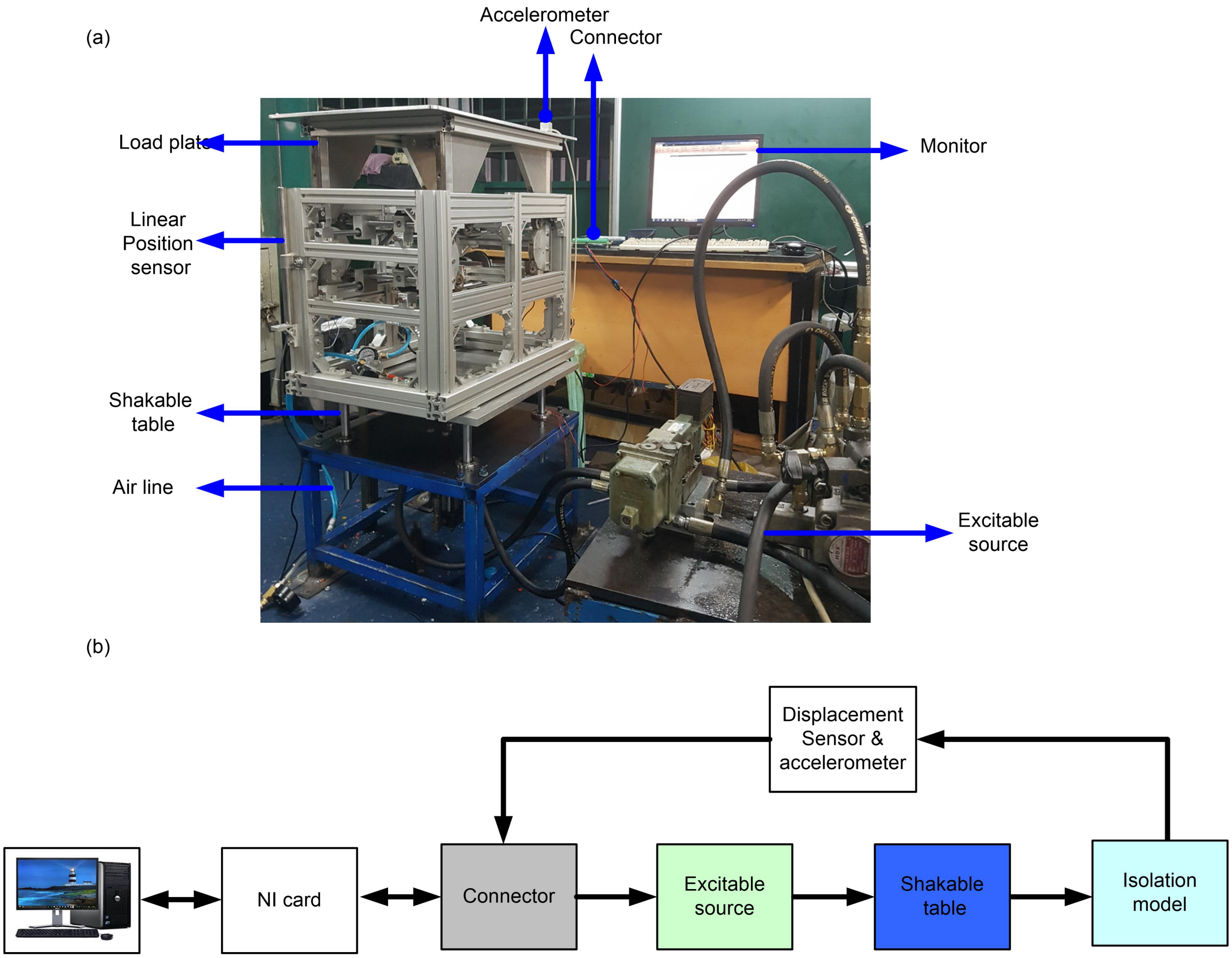

Fig. 4.30. (a) Experimental setup, (b) Schematic Diagram of obtaining data

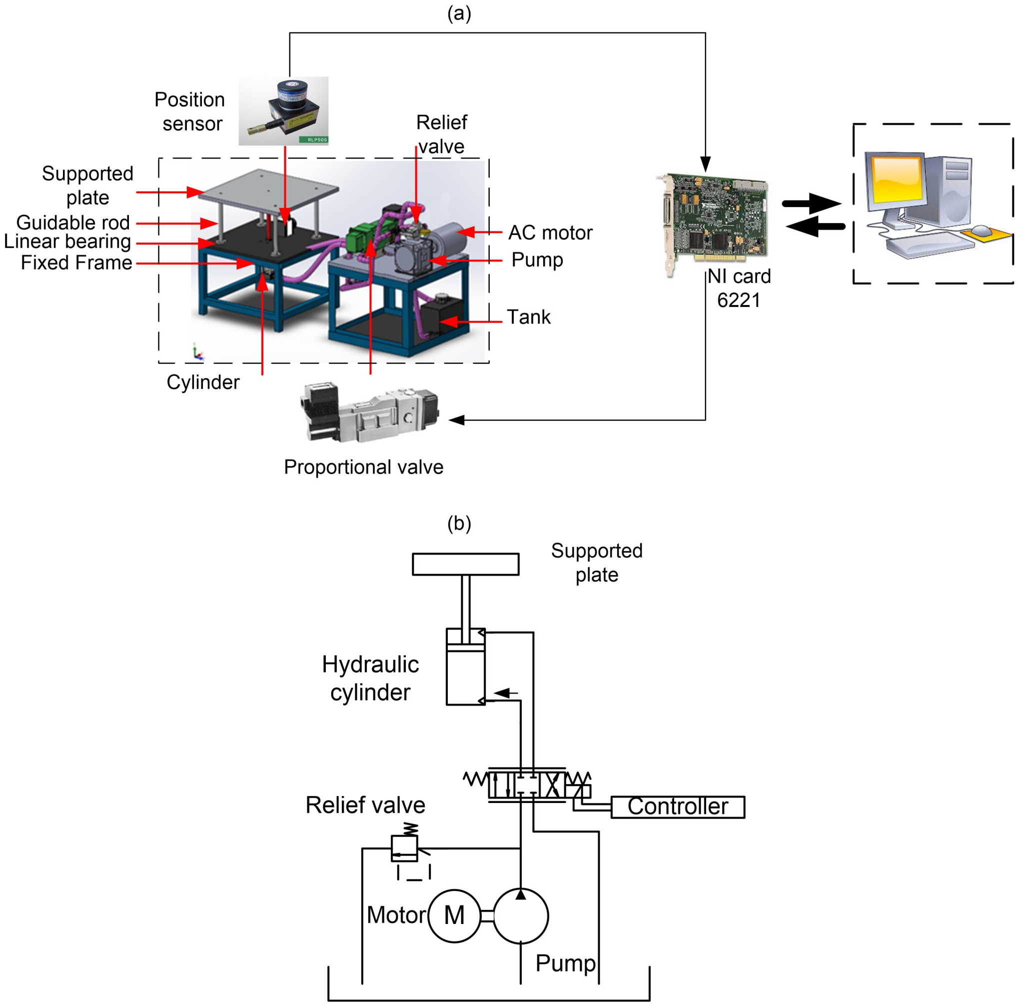

Fig. 4.31. (a) Configuration of the hydraulic shaker; (b) Hydraulic circuit

The 1st study case: To investigate the effects of the SCM on isolation performance, the excitation is the sinusoidal signal with the amplitude of 10 mm and frequency swept from 0 to 50 rad/s. As known, the vibration isolation only occurs when the transmissibility is less than one. The experimental vibration transmissibility of the QSAVIM using RAS and the ETVIM are compared in Fig. 4.32. The latter denoted by the dashed line can not prevent the excitation having frequencies less than 37.7 rad/s, meanwhile, by using the SCM, the former with the pressure ratio μ=1.8 exhibited by the solid line can mitigate the vibration transmissibility from the base to the load plate for excited frequencies larger than 18.8 rad/s. In addition, the proposed model has resonant frequency smaller than that of the ETVIM that is close to 12.5 rad/s for the former and 27 rad/s for the latter. This result means that the isolation region of the proposed model is extended toward the low frequency compared with that of the ETVIM. Furthermore, at the resonant frequency, the vibration transmissibility of the QSAVIM using RAS is smaller than that of the ETVIM. Indeed, as seen in Fig. 4.32, the values of the absolute vibration transmissibility of the isolated model with and without SCM at corresponding resonant frequencies are approximately 1.4 and 3.2, respectively. This experimental investigation proves that the isolation effectiveness of the QSAVIM using RAS is better than the ETVIM.

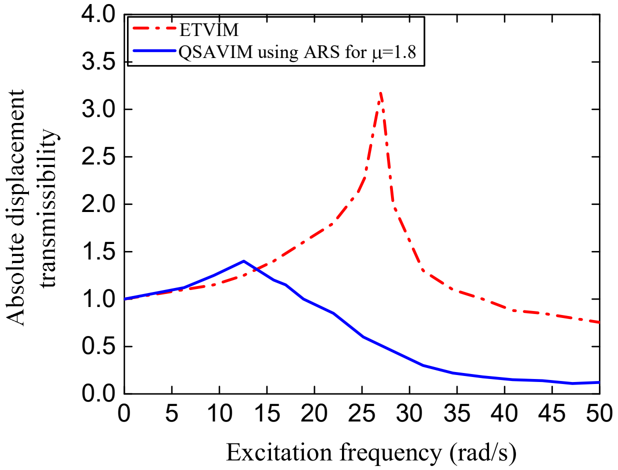

Fig. 4.32. Comparison of the experimental transmissibility between the QSAVIM using RAS for μ=1.8 and ETVIM

The 2nd study case: In this case, the effects of the various values of the pressure ratio μ on the vibration transmissibility curve of the QSAVIM using RAS are experimentally assessed. For this purpose, two values of the pressure ratio including μ=1.1 and μ=1.6 are considered. The experimental result of the vibration transmissibility shown in Fig. 4.33 reveals that when the air pressure in the air spring 2 at the DSEP is 1.6 times the air pressure in the air spring 1, the frequency range in which the vibration isolation takes effect is broadened compared with that in the case of μ=1.1. As observed, the isolation region of the QSAVIM using RAS with μ=1.1 is larger than 25 rad/s, meanwhile with μ=1.6 the proposed model can isolate for input frequencies greater than 21 rad/s. In addition, as numerically simulated in Fig. 4.15, the higher the pressure ratio is, the lower the resonant peak comprising of the frequency and peak value is as well as the frequency jump phenomenon may be vanished. Indeed, this is also proved by the experiment, in the case of μ=1.6, the QSAVIM using RAS obtains the resonant frequency and the peak value are approximately 15.7 rad/s and 1.5 respectively, whereas in the other case, the values are about 23.8 rad/s and 1.9 correspondingly. The phenomenon of frequency jump almost disappeared for the value of μ=1.6 while it appeared around the frequency of 25 rad/s for μ=1.1.

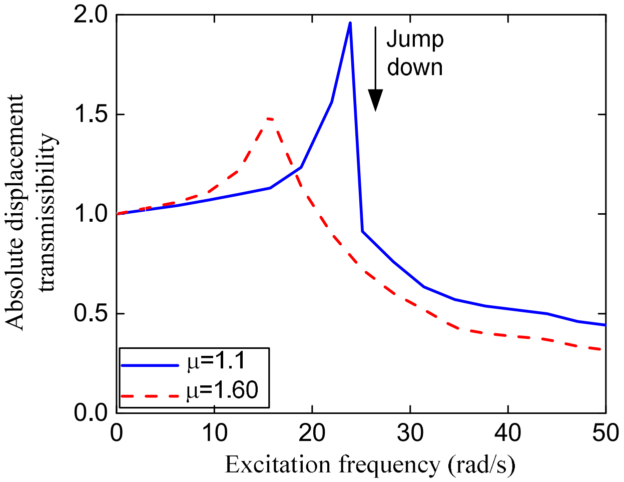

Fig. 4.33. Experimental transmissibility curves of the QSAVIM using a RAS for μ=1.1 and 1.6

The 3rd study case: The pressure ratio μ of the QSAVIM using RAS is set at the value of 1.6, while the other parameters are the same as in the 2nd case. The isolation response of the proposed model and the ETVIM for a multiple frequency excitation which is a linear combination of the harmonic signals including 19, 22 rad/s and 25 rad/s is performed as shown in Fig. 4.34. Firstly, the absolute displacement response of the former and latter are shown in Fig. 4.34(a) and (c), respectively. Comparing between them, the vibration level of the QSAVIM using RAS for μ=1.6 is lower than the excitation as seen Fig. 4.34(a), the detailed notations of the response curves are presented in upper-right corner of the figure, oppositely, as the stiffness corrected mechanism is not setup along with the load bearing mechanism, the displacement of the load plate is increased as observed in Fig. 4.34(c). Secondly, the absolute acceleration response of the QSAVIM using RAS with μ=1.6 and the ETVIM are compared in Fig. 4.34(b) and (d), respectively. The experimental result confirmed that the isolation effectiveness of the QSAVIM using RAS outperforms in comparison with the ETVIM.

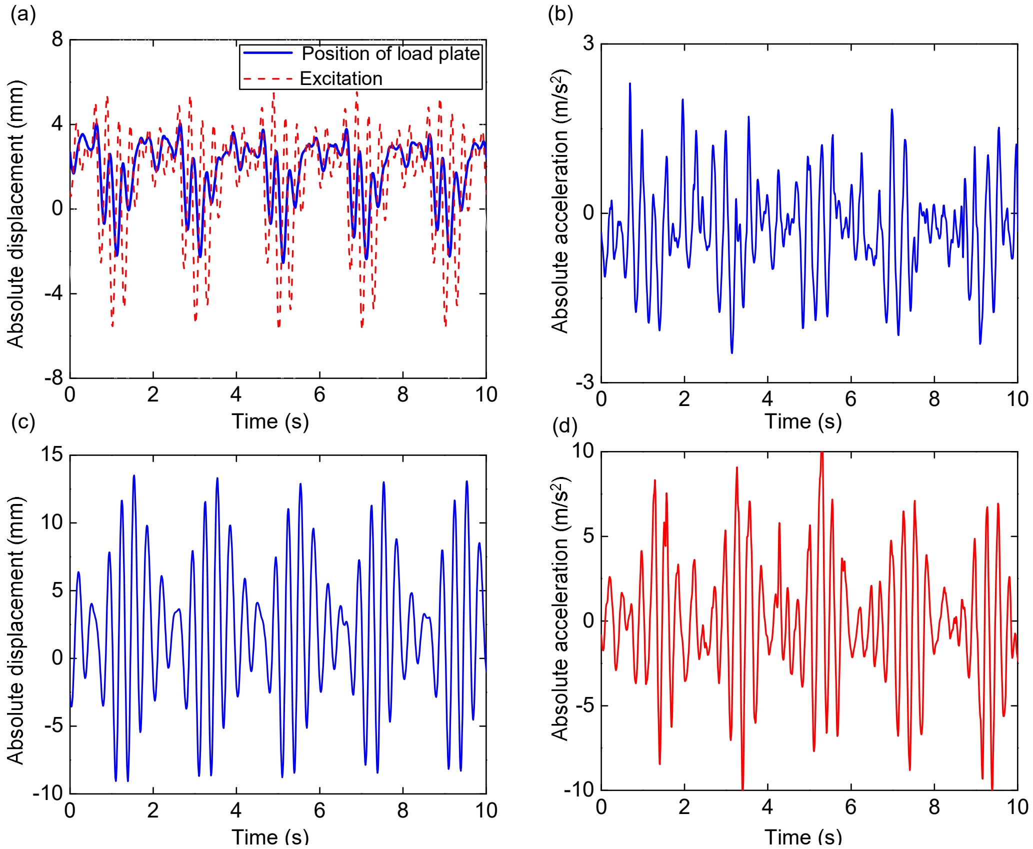

Fig. 4.34. Time history of absolute displacement (a, c) and acceleration (b, d) of the load plate in the case of platform with μ=1.6 and the one without SCM. Noted that the isolated load is the same as in Fig. 4.33.

Fig. 4.35 shows the power spectrum density (PSD) of the absolute displacement of the load plate for the same excitation as in Fig. 4.34. The annotation for the types of the lines is presented in the upper-right corner of the figure. As clearly seen, at the steady state motion, the displacement response of the load plate has the same frequencies as the excitation, while the free vibration term is absent. The decay of the free vibration term is caused by the positive damping, showing that the damping phenomenon exists in the experimental model. In addition, by comparing with the excitation, the vibration level of the load plate is lessened. The result of this experiment also confirms that the vibration attenuation is increased in accordance with the growth of the excitation frequency.

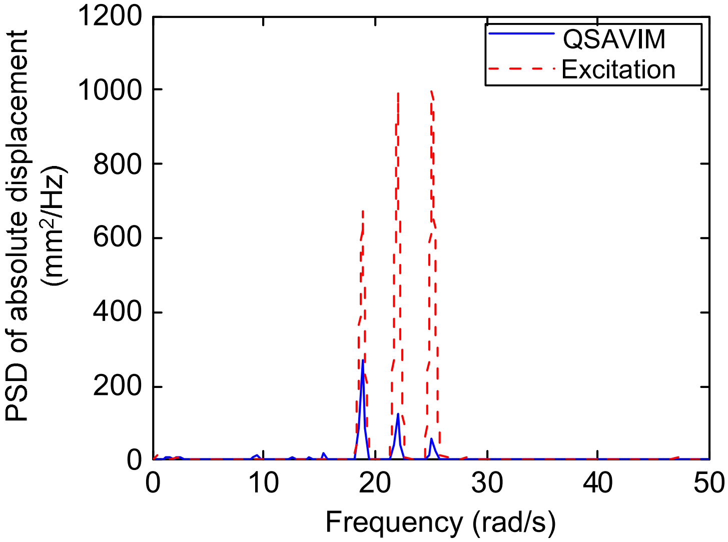

Fig. 4.35. PSD of the absolute displacement of the load plate.

SUMMARY OF CHAPTER 4

Firstly, the mechanical model of an innovated isolator which comprises two opposite stiffness mechanisms was proposed. One is the load bearing mechanism and the other is the corrected stiffness mechanism. The pressure of the LBM can be adjusted to deal with the variation in the isolated load, which indicates that the system always remains the DSEP. The restoring model of a specific commercial rubber air spring was analyzed and experimentally identified, showing the hysteresis response of the air spring. From this identified result, the static analysis and the stability of the equilibrium position of the proposed isolation model were analyzed. It confirmed that the dynamic stiffness curve is concave parabola and obtains the minimum at the DSEP. Regulating the pressure of the LBM can achieve the wanted stiffness even it can attain the quasi-zero stiffness at the DSEP.

Secondly, the dynamic equation of the isolation model subjected by a harmonic vibrating base was established based on the analysis results. The amplitude-frequency relation, vibration transmissibility as well as steady state solution were found via Normal form method. The effects other configurative and working parameters on the frequency response were investigated, proving that the lower stiffness is, the larger the isolation region is, simultaneously the peak and amplitude and frequency is also reduced and unstable branch of the amplitude-frequency curve is narrowed. Specially, the isolated region of the proposed model is larger than that of the ETVIM. Additionally, the investigational results also indicated the drawback of the QZS isolated method as the system doesn't obtain the DSEP. The proposed model can surmount easily this issue by regulating the pressure of the LBM meanwhile the dynamic stiffness of the model can be remained at the desirable low value through regulating the pressure of the SCM.

Finally, a prototype of the QSAVIM using RAS was built to assess the vibration transmissibility of the theoretical model. An experimental apparatus was also set up to collect the data. Again, the experimental results confirmed the isolated effectiveness of the proposed model and the advantages of the proposed against the ETVIM. Finally, design procedure of the proposed model was suggested to obtain the desired isolated response.

CHAPTER 5

A QUASI-ZERO STIFFNESS ADAPTIVE VIBRATION ISOLATION MODEL USING PNEUMATIC CYLINDERS

This chapter will consider an alternative structure of the QSAVIM in which the rubber air springs are replaced by pneumatic cylinders (PC). This model is named QSAVIM using PC. Firstly, the stiffness of a pneumatic cylinder is built and its frictional model is identified by using virtual prototyping technical. Next, the stiffness of the modified model is found and analyzed. Then, the effects of the configuration parameters such as the auxiliary chamber volume as well as the wedge angle on the system stiffness are taken into account. The stability of the modified model is also analyzed. Besides, the frequency-amplitude relation as well as the force transmissibility of the modified model are studied and established. Furthermore, the family of the initial conditions named the attractor-basin phase portrait affecting on the dynamic response will be detected. This chapter is organized as following: section 5.1 describes structure of the QSAVIM using PC. Section 5.2 shows the pneumatic cylinder. Section 5.3 to 5.7 introduce the stiffness analyses. Section 5.8 presents the numerical simulation of the modified model.

5.1. Model of QSAVIM using PC

In the same way of the isolated model introduced in chapter 4, herein the isolated model is modified a few by replacing four rubber air springs by two pneumatic cylinders including cylinders 1 and 2 in which each cylinder is connected with an individual tank (called auxiliary chamber). Indeed, the compressed air can flow from cylinder 1 into the tank 3 and vice versa meanwhile the cylinder 2 is connected to the tank 4. Each end of the cylinder is linked with the connector 8 through the rod 5, the rod 9. A remained end of the rod 5 is fixed on the cylinder but the other of the rod 9 is fixed on the piston sliding on the cylinder. Especially, the cylinders only slide horizontally without frictional phenomenon thank to sliders 6 sliding on fixed guidance bars 7. Thus, the load bearing mechanism comprises the wedges, rollers and pneumatic cylinder 1 with the tank 3. The stiffness correction mechanism includes semicircular cams, rollers 4 and pneumatic cylinder 2 with the tank 4. While the motion of the load plate as well as the semicircular cam and wedge is the same as the isolation model described in chapter 4. The stiffness of the QSAVIM using PC can offer a desirable low value by adjusting the pressure in cylinders 1 and 2.

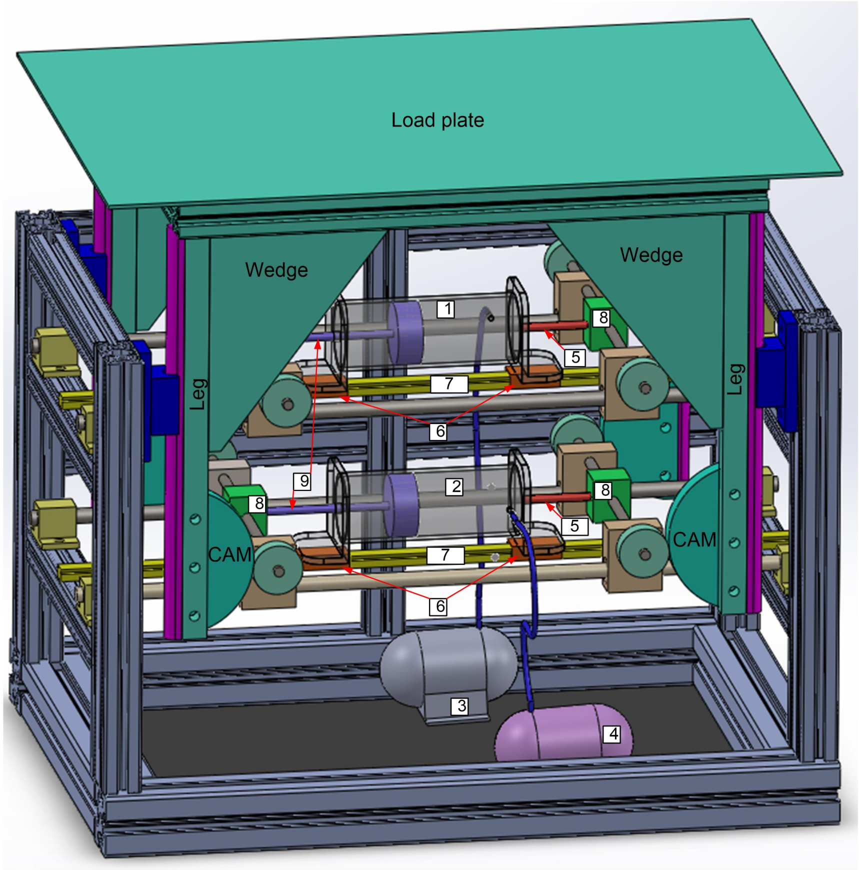

Fig. 5.1. 3D model of the modified isolator: 1 and 2- pneumatic cylinder; 3 and 4-tank; 5 and 9-rod; 6 slider; 7-guidance bar; 8-connector; (*Published by Vo et al. "Static analysis of low frequency Isolation model using pneumatic cylinder with auxiliary chamber", International Journal of Precision Engineering and Manufacturing)*

5.2. Pneumatic cylinder with auxiliary chamber

5.2.1. Pressure change

By applying the first law of thermodynamic and ideal air equation presented in chapter 3, the pressure equation in the pneumatic chamber is expressed as below:

$$\dot{P} = \frac{n}{V}\left(G_{in}R_{air}T_{in} - G_{out}R_{air}T - P\dot{V}\right) \tag{5.1}$$

where: T and P are the temperature and pressure of the air in the pneumatic working chamber, V is the volume of the working chamber. G_{in} and G_{out} are mass low rates at the inlet and outlet, R_{air} is the gas constant (R_{air}=287 J/kg.K), $n=C_{\text{p}}/C_{\text{v}}$ is the ratio of specific heat capacity.

Considering, the pneumatic cylinder with an auxiliary chamber working as an air spring is exhibited in Fig. 5.2. The air flows from the cylinder into the chamber, causing a displacement of the piston an announce x, by applying the first law of thermodynamic and ideal air equation, the pressure changing equations in the pneumatic cylinder (P_{cy}) and the auxiliary chamber (P_{ac}) are expressed as following:

$$\dot{P}_{cy} = \frac{n}{V_{cy}}\left(-G_{out}R_{air}T - P\dot{V}_{cy}\right) \tag{5.2}$$

$$\dot{P}_{ac} = \frac{n}{V_{ac}}G_{in}R_{air}T \tag{5.3}$$

in which V_{cy} and V_{ac} are the volumes of the cylinder and the auxiliary chamber (tank), respectively, h is the height of the cylinder as presented in Fig. 5.2, A is the area of the piston and

$$V_{\text{cy}}=A(h-x) \tag{5.4}$$

The air leakage and pressure drop in the line are neglected, the result is:

$$\begin{aligned} G_{out} &= G_{in} \\ P_{cy} &= P_{ac} = P_s \end{aligned} \tag{5.5}$$

The pressure change process in the air spring is obtained as below:

$$\dot{P}_s = \frac{nP_s}{(h-x)A + V_{ac}} A\dot{x} \tag{5.6}$$

herein, *A* is the effectiveness area of the pneumatic cylinder.

From Eq. (5.6), the air pressure in the cylinder at an arbitrary position is expressed as following

$$P_s = P_{so}\left(\frac{Ah + V_{ac}}{Ah + V_{ac} - Ax}\right)^n \tag{5.7}$$

herein P_{so} is the pressure in the cylinder at the initial position

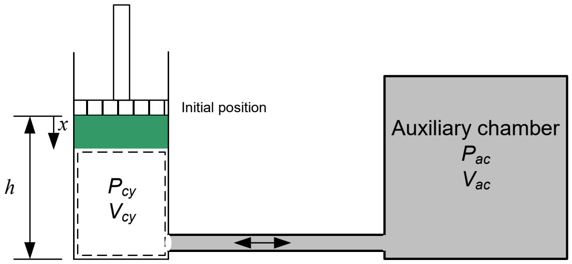

Fig. 5.2. Schematic diagram of the pneumatic spring with an auxiliary chamber

Instead of doing experiment to assess the predicted pressure in Eq. (5.7), a virtual model of the pneumatic cylinder with auxiliary chamber is built by using AMEsim software as shown in Fig. 5.3. In which, the effective area of the cylinder A=0.002m^2, the length of the piston stroke h=150mm, the initial pressure of the cylinder P_{so} is set at the value of 2.5 bar, the volume of the auxiliary chamber V_{ac} is set at the various values of 0.001m^3, 0.01m^3, 0.015m^3 and 0.020m^3. Besides, the dead volumes at the two ends of cylinder and the effect of heat exchange in the air spring are considered in a virtual model. The comparison between the analysis solution and the simulation result from the virtual model is presented in Fig. 5.4. It can be observed that the pressure obtained from virtual model is always smaller than that predicted by Eq. (5.7) excepting the initial position. Because the analysis solution neglects the dead volumes at the ends of the cylinder, the length of the air lines as well as compressibility of the line, etc.

However, the variation trend of pressure in the air spring obtaining from Eq. (5.7) and the virtual model are consistent. Hence, the predictable solution will be employed for static analysis of the proposed isolation model in next section.

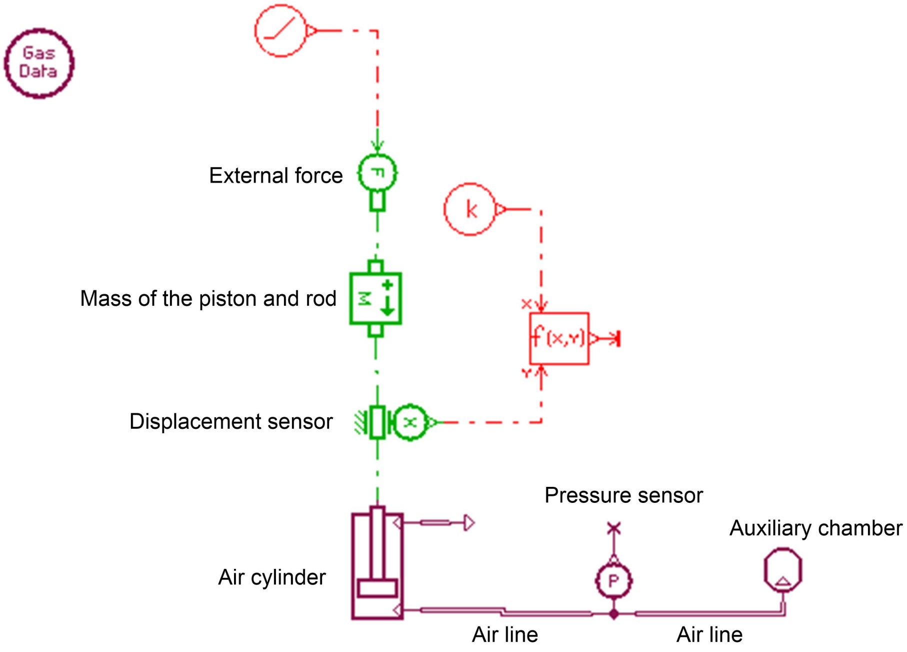

Fig. 5.3. Virtual model of the cylinder with auxiliary chamber built by AMEsim software for A=0.002m^2, h=150mm, P_{S0}=2.5 bar, V_{ac}= 0.001m^3, 0.01m^3, 0.015m^3 and 0.020m^3

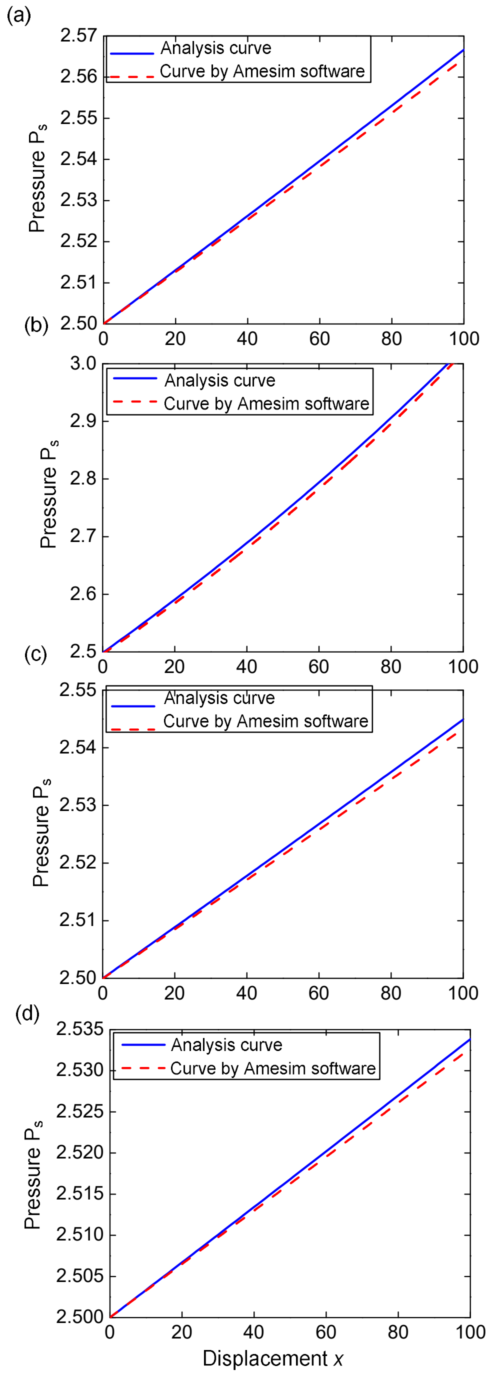

Fig. 5.4. Pressure-changing process in pneumatic spring predicted by Eq. (5.7) and obtained by the virtual model for various volumetric values of the auxiliary chamber: V_{ac}=0.001 m^3 in subplot (a); V_{ac} =0.01 m^3 in subplot (b); V_{ac} =0.015 m^3 in subplot (c); V_{ac} =0.02 m^3 in subplot (d); (Details for the line types are presented in left-top corner panel of each figure)

5.2.2. Frictional model

Because of the nonlinear dynamic characteristic as well as the existing of the relative sliding between the piston and cylinder, it is the need for analyzing the complex behavior of the proposed system. As shown in chapter 3, the sliding friction model (F_{sf}) is presented as following:

$$F_{sf} = F_c + (F_{st} - F_c)e^{-(v_r/v_s)^{n_s}} + \sigma v_r \tag{5.8}$$

in which F_{c} is Coulomb friction force, F_{st} is the static friction force, v_{s} is the Stribeck velocity, v_r is the relative velocity between two contacting surfaces, σ is the viscous friction coefficient and n_{s} is the exponent of the Stribeck curve.

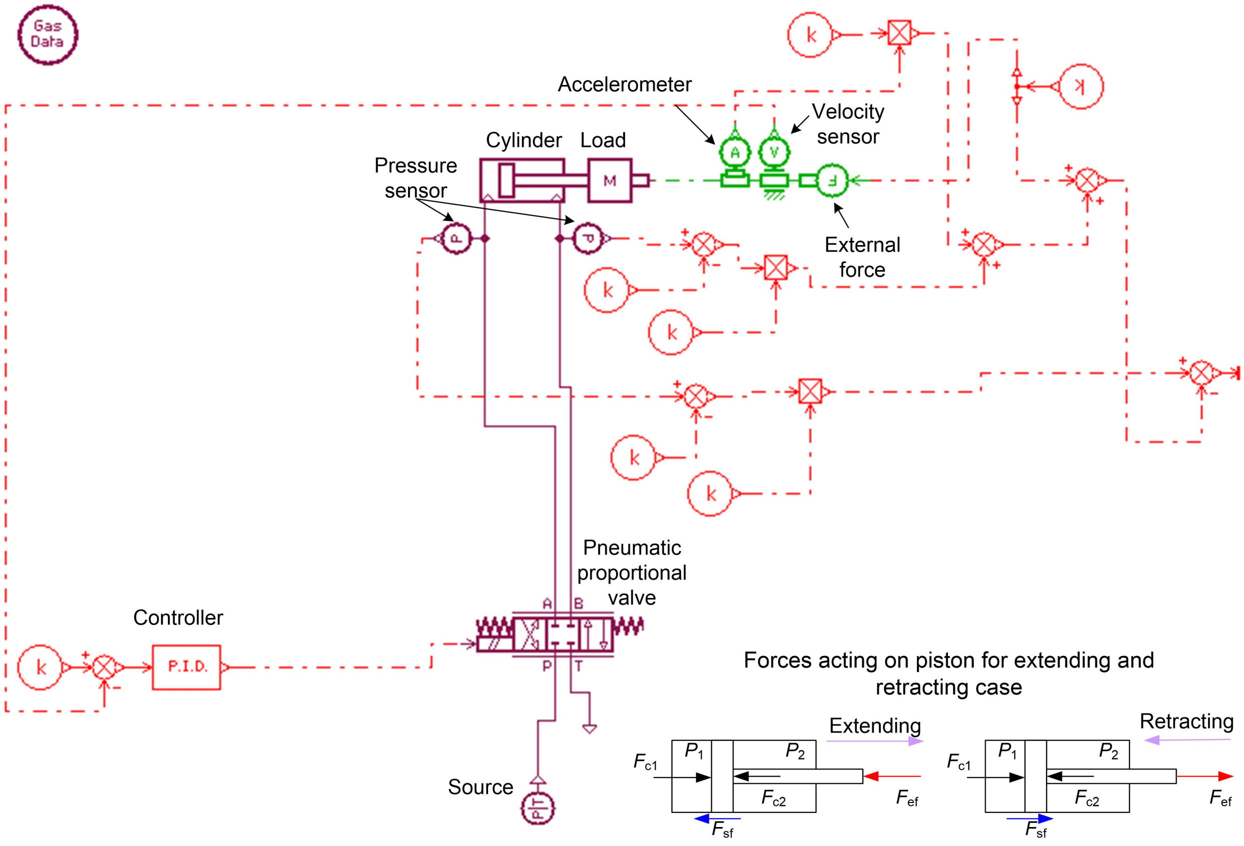

Fig. 5.5. Virtual test-rig of pneumatic cylinder using AMEsim software

In order to identify parameters of the friction model of a cylinder, instead of experiment, a virtual prototype technique shown in Fig. 5.5 is built through AMEsim software. This technique ensures the accuracy and reduces the fabrication time because the environment of a virtual model is similar to an actual environment. For instance, it exists the heat exchange between the air in cylinder and surrounding environment, the dead volume of the cylinder, frictional phenomenon, etc. Herein, the cylinder used for identification has the piston diameter of 80 mm, rod diameter of 32 mm, stroke length of 300 mm and the dead volume at two ends of 50 cm^3 whilst the parameters for simulation is given in table 5.1. During the simulated process, the cylinder is fixed meanwhile the speed of load attached at the end of rod is controlled to track the constant value through introducing a PID controller simultaneously its acceleration is measured by an accelerometer. In this identification, the frictional force between the cylinder and piston is not measured directly that it is calculated as following:

$$F_{sf} = \begin{cases} F_1 - F_2 - F_{ef} & \text{for Extending} \\ F_2 - F_1 - F_{ef} & \text{for Retracting} \end{cases} \tag{5.9}$$

Table 5. 1: Parameters for simulation

Parameter	**Original value**
Atmosphere pressure	1 bar
Specific heat ratio	1.4
Thermal exchange coefficient	500 J/mm^2/K/s
External temperature	293.15K
External force	100N
Source pressure	5 bar
Velocity of load (v_r)	0.003; 0.006; 0.01; 0.015; 0.02; 0.03; 0.05; 0.1; 0.15; 0.2; 0.25 m/s

In this calculation, due to constant velocity, the inertia force is ignored, F_{ef} is the external force, $F_1=P_1A$ and $F_2=P_2(A-a)$ in which A, a are the areas of the piston and rod, P_1 and P_2 are the air pressure in chamber as denoted in Fig. 5.5, which are directly measured by two pressure sensors.

Then, GA including three operations: reproduction, crossover and mutation as shown in Fig. 3.9 in chapter 3, which is employed to determine optimal values of the friction model given in Eq. (5.8). This work aims to minimize the cost function expressed by Eq. (5.10). As observed in Fig. 5.6, after 30 iterations, the cost function converges to zero.

$$J=\frac{1}{2}\sum\left(F_{msf}^{i}-F_{sf}^{i}\right)^{2} \tag{5.10}$$

in which F_{msf} is the friction force measured at i^{th} constant velocity, F_{sf} is the friction force calculated by Eq. (5.9). The best values of the friction model are given in the table 5.2.

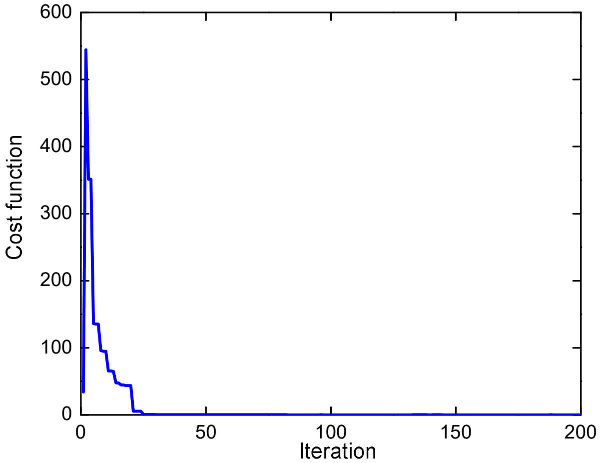

Fig. 5.6. The value of cost function with respect to iteration

Table 5.2: Values of friction force model

Parameters	Extending	Retracting
F_c	4.338	-3.904
F_{st}	11.655	-9.906
v_s	0.4961	-0.372
σ	23.7	23.356
n_s	0.681	0.681

Fig. 5.7 shows the friction force curve of the pneumatic cylinder model in which the solid line denotes the identified curve for extending stroke whilst the reverse stroke, that is the retracting, is exhibited by the dashed line. It is noteworthy to see that the identified results match well with the simulated ones marked by the square and circle points according to the extending and retracting stroke, respectively. The friction force in the extending stroke is larger than in the retracting one. This model will be used to analyze the complex responses in section 5.8.2.

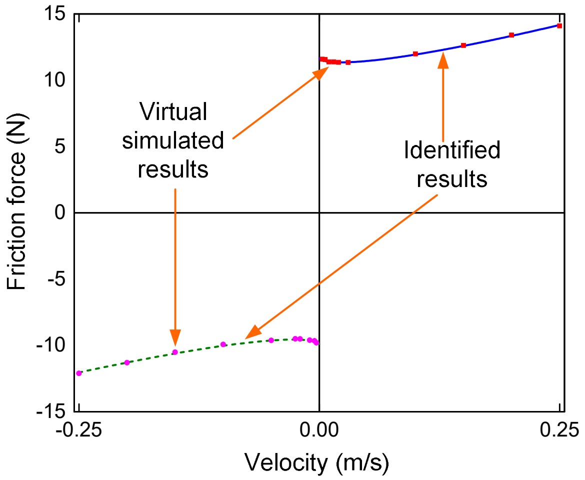

Fig. 5.7 Steady-state friction force characteristic.

5.3. Stiffness of the modified model

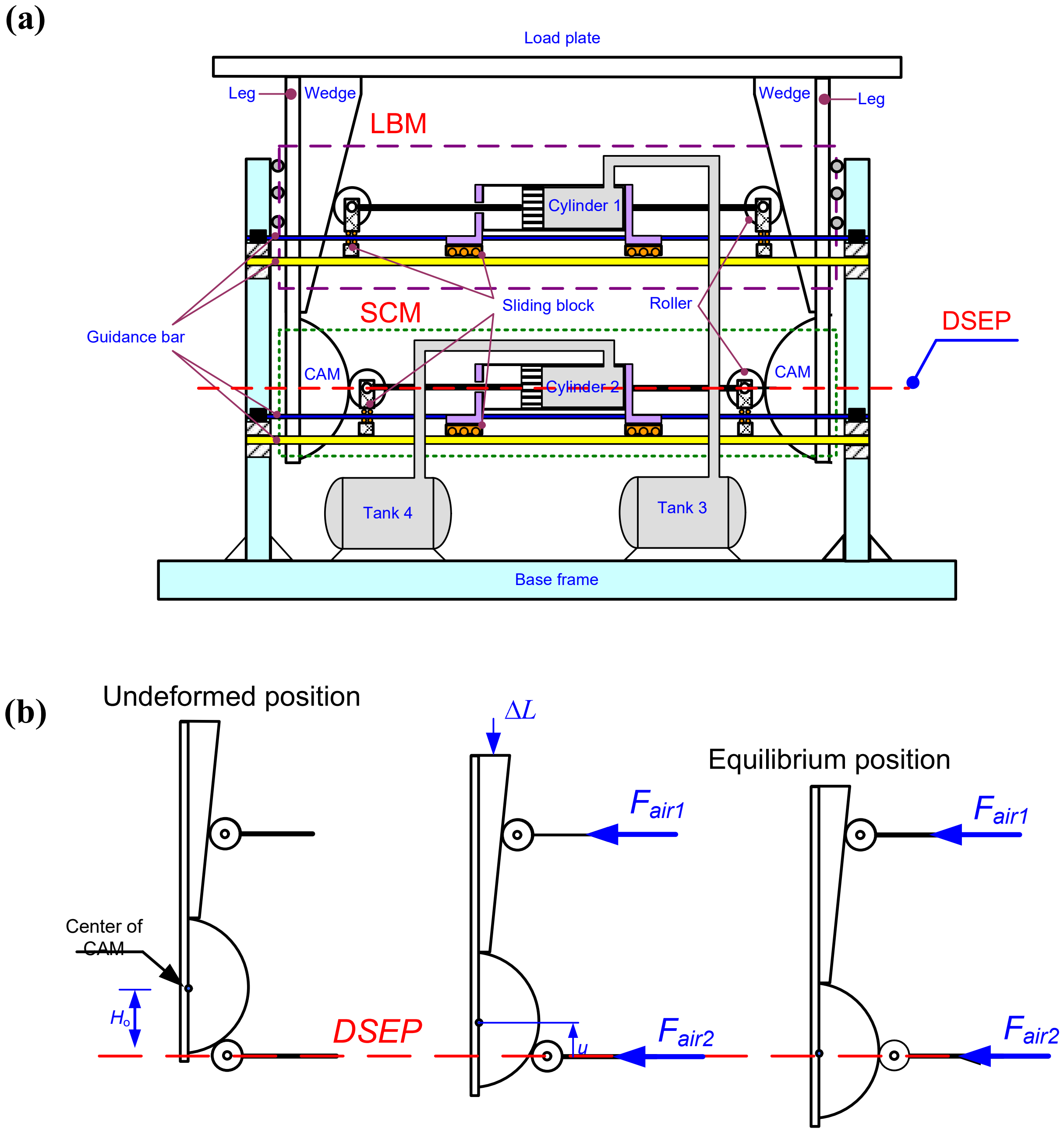

Fig. 5.8. (a) Schematic diagram of the QSAVIM using PC composed by the LBM and SCM; (b) Specific states of the QSAVIM using PC

Based on the 3D model shown in Fig. 5.1, the schematic diagram of the QSAVIM using PC is presented in Fig. 5.8(a). The working principle of this model is the same as that of the model presented in chapter 4. Really, during the operation of the system, it also spends three states as shown in Fig.5.8(b) including the undeformed, desirable equilibrium and arbitrary position. Among them, only at the undeformed state, the air in the cylinders 1 and 2 is not compressed, meaning that no force is generated by the LBM and SCM. The same as in chapter 4, the desirable static equilibrium position (DSEP) is determined as the load plate is loaded until the centers of semicircular cam and roller are on the same horizontal line. At this state, the vertical force which acts on the load plate is only caused by the load bearing structure, whilst the arbitrary state is determined when the load plate moves away from the DSEP a distance *u* (relative coordinate), at this position, the load plate will be acted by two vertical forces generated by both the LBM and SCM. H_o is also called the vertical static deformation.

In the same way of chapter 4, considering the load plate moves down away from the initial position an amount of ΔL as shown in Fig. 4.9 (b), each end of cylinder 1 and cylinder 2 moves horizontally to be x_1 and x_2 given by Eq. (4.18). By applying Eq.(5.4), the volumes (V_{cy}) of the cylinder 1 and 2 are determined by Eq. (5.11). Hereafter, it is noted that subscripts "*1*" and "*2*" present for the pneumatic springs 1 and 2, respectively.

$$\begin{aligned} V_{cy1} &= A_1(h_1 - x_1) \\ V_{cy2} &= A_2(h_2 - x_2) \end{aligned} \tag{5.11}$$

Using Eq.(4.18) and (4.27), Eq.(5.11) can be rewritten as:

$$V_{cy1} = A_1(h_1 - 2(H_0 - u)\tan\alpha) \tag{5.12}$$

$$V_{cy2} = A_2(h_2 - 2(\sqrt{(R+r)^2 - u^2} - \sqrt{(R+r)^2 - H_0^2})) \tag{5.13}$$

Applying Eq. (5.7), the pressure in cylinder 1 and 2 is expressed as below:

$$P_{s1} = P_{so1}\left(\frac{V_{e01}}{V_{e01} - 2A_1H_o\tan\alpha + 2A_1u\tan\alpha}\right)^n \tag{5.14}$$

$$P_{s2} = P_{so2}\left(\frac{V_{e02}}{V_{e02} + 2A_2\sqrt{\left(R+r\right)^2 - H_o^2} - 2A_2\sqrt{\left(R+r\right)^2 - u^2}}\right)^n \tag{5.15}$$

in which $V_{e01} = A_1h_1 + V_{ac1}$; $\mathrm{V}_{e02} = A_2h_2 + V_{ac2}$

The pressure P_{wh} of the pneumatic cylinder at the equilibrium position is determined by substituting u=0 in Eq. (5.14 and 5.15) as following:

$$P_{wh1} = P_{so1}\left(\frac{V_{e01}}{V_{e01} - 2A_1H_o\tan\alpha}\right)^n \tag{5.16}$$

$$P_{wh2} = P_{so2}\left(\frac{V_{e02}}{V_{e02} + 2A_2\sqrt{\left(R+r\right)^2 - H_o^2} - 2A_2\left(R+r\right)}\right)^n \tag{5.17}$$

In addition, the force of the cylinder generated by compressed air (F_{air}) is:

$$F_{air} = \left(P_s - P_{atm}\right)A \tag{5.18}$$

where P_{atm} is absolute ambient pressure in Pa,

Based on Eq. (4.23), the vertical resultant force acting on the load plate can be rewritten shortly as below

$$F_s = F_{LBM} + F_{SCM} \tag{5.19}$$

where F_{LBM} and F_{SCM} are the restoring forces of the load bearing mechanism and the stiffness correcting one, respectively, and defined by Eq. (5.20-5.21)

$$F_{LBM} = 2F_{air1}\tan\left(\alpha\right) \tag{5.20}$$

$$F_{SCM} = 2F_{air2}\frac{(\mathrm{H}_o - \Delta L)}{\sqrt{(\mathrm{R}+\mathrm{r})^2 - (\mathrm{H}_o - \Delta L)^2}} \tag{5.21}$$

Substituting Eq. (5.18) into Eqs. (5.20 & 5.21), we have:

$$F_{LBM} = 2A_1\left[P_{s1} - P_{atm}\right]\tan\alpha \tag{5.22}$$

$$F_{SCM} = 2A_2\left[P_{s2} - P_{atm}\right]\frac{u}{\sqrt{\left(R+r\right)^2 - u^2}} \tag{5.23}$$

By introducing the dimensionless parameters as below:

$$\hat{A} = \frac{A_2}{A_1};\ \hat{H}_o = \frac{H_o}{R+r};\ \hat{P}_{atm} = \frac{P_{atm}}{P_{wh1}};\ \hat{u} = \frac{u}{R+r};\ \hat{V}_{e01} = \frac{V_{e01}}{A_1(R+r)};\ \hat{V}_{e02} = \frac{V_{e02}}{A_1(R+r)};$$
$$\hat{V}_{d1} = \frac{V_{d1}}{V_{e01}};\ \hat{V}_{d2} = \frac{V_{d2}}{V_{e02}};\hat{F}_{LBM} = \frac{F_{LBM}}{A_1P_{wh1}};\ \hat{F}_{SCM} = \frac{F_{SCM}}{A_1P_{wh1}};\ \mu = \frac{P_{wh2}}{P_{wh1}};\ \hat{F}_{\mathrm{s}} = \frac{F_{\mathrm{s}}}{A_1P_{wh1}}$$

in which μ is called the air pressure ratio. u is the relative displacement of the semicircular cam compared with the DSEP given in Eq. (4.27). V_{d} is the volume of the pneumatic cylinder at the desirable static equilibrium position and is determined by:

$$\begin{aligned} V_{d1} &= A_1(h_1 - 2H_0\tan\alpha) \\ V_{d2} &= A_2(h_2 - 2(R + r - \sqrt{(R+r)^2 - H_0{}^2})) \end{aligned} \tag{5.24}$$

Eqs. (5.22-5.23) are recast in dimensionless form as following:

$$\hat{F}_{LBM} = 2\left[\hat{V}_{d1}^n\left(\frac{\hat{V}_{e01}}{\hat{V}_{e01} - 2\hat{H}_o\tan\alpha + 2\hat{u}\tan\alpha}\right)^n - \hat{P}_{atm}\right]\tan\alpha \tag{5.25}$$

$$\hat{F}_{SCM} = 2\hat{A}\left[\begin{array}{l} \mu\hat{V}_{d2}^n\left(\dfrac{\hat{V}_{e02}}{\hat{V}_{e02} + 2\hat{A}\sqrt{1-\hat{H}_o^2} - 2\hat{A}\sqrt{1-\hat{u}^2}}\right)^n \\ -\hat{P}_{atm} \end{array}\right]\frac{\hat{u}}{\sqrt{1-\hat{u}^2}} \tag{5.26}$$

By substituting Eqs. (5.25-5.26) into Eq. (5.19) then taking differentiation of Eq. (5.19) with respect to $\hat{u}$, the dynamic stiffness of the proposed model is explained as below:

$$\hat{K}_s = \frac{d\hat{F}_{LBM}}{d\hat{u}} + \frac{d\hat{F}_{SCM}}{d\hat{u}} = \hat{K}_{LBM} + \hat{K}_{SCM} \tag{5.27}$$

where $\hat{K}_{LBM}$ and $\hat{K}_{SCM}$ are the dimensionless dynamic stiffness of the LBM and SCM, respectively, are determined as following:

$$\hat{K}_{LBM} = 4n \frac{\hat{V}_{d1}^{n}\hat{V}_{e01}^{n}}{\left(\hat{V}_{e01} - 2\hat{H}_{o}\tan\alpha + 2\hat{u}\tan\alpha\right)^{n+1}}\tan^{2}\alpha \tag{5.28}$$

$$\begin{aligned}\hat{K}_{SCM} = {} & \frac{2\hat{A}}{\sqrt{1-\hat{u}^{2}}}\left[\hat{P}_{atm} - \mu\hat{V}_{d2}^{n}\left(\frac{\hat{V}_{e02}}{\hat{V}_{e02} + 2\hat{A}\sqrt{1-\hat{H}_{o}^{2}} - 2\hat{A}\sqrt{1-\hat{u}^{2}}}\right)^{n}\right]\left(1+\frac{\hat{u}^{2}}{1-\hat{u}^{2}}\right) \\ & + 4\hat{A}^{2}\mu\hat{V}_{d2}^{n}n\frac{\hat{u}^{2}}{1-\hat{u}^{2}}\frac{\hat{V}_{e02}^{n}}{\left(\hat{V}_{e02} + 2\hat{A}\sqrt{1-\hat{H}_{o}^{2}} - 2\hat{A}\sqrt{1-\hat{u}^{2}}\right)^{n+1}}\end{aligned} \tag{5.29}$$

This analysis reveals the effects of the volume of the auxiliary chamber and the pressure of the cylinder on the restoring forces of the load bearing and the stiffness corrected mechanisms as expressed by Eqs. (5.25–5.26) and the dynamic stiffness of these mechanisms as calculated by Eqs. (5.28–5.29)

5.4 Stiffness analysis of the LBM and SCM

The dynamic stiffness of the LBM is numerically simulated via using the Eq. (5.28) for the pressure in the cylinder 1, P_{S01}=1.91 bar and the effective area of cylinder 1 A_1=0.0079m^2.

Taking into account the LBM without the auxiliary chamber as shown in Fig. 5.9(a) (see the notations of curves in upper-right corner panel), it can be seen that the LBM has a significant nonlinear characteristic in the stiffness and the stiffness of which is reduced as the relative displacement of the isolated object is increased. However, the smaller the inclined angle α is, the lower the nonlinearity of the stiffness curve is. If the value of α is small enough, the stiffness of the LBM will be nearly unchanged around DSEP (u=0), for instance in this case $\alpha<20^{o}$, but a reduction in the inclined angle results in a decrease in the stiffness as seen in the Fig.5.9(b).

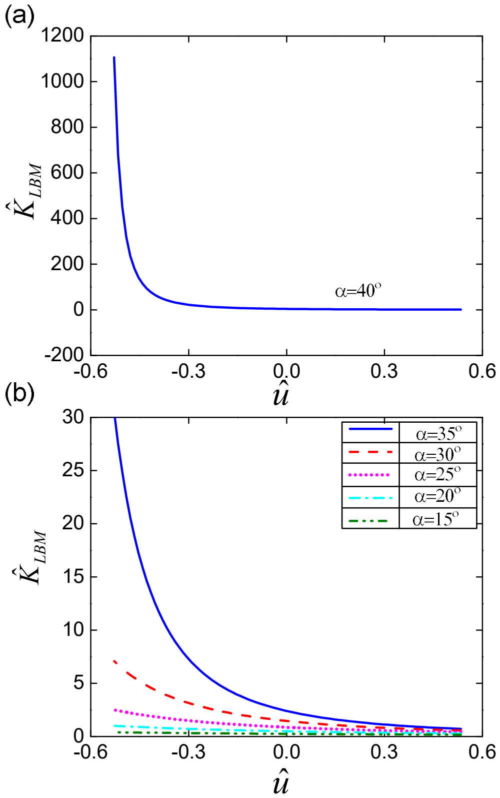

Fig. 5.9. Effect of the inclined angle on the dynamic stiffness of LBM for $\hat{V}_{ac1}=0$: (a) α=40 ^{o}; (b) α=15 ^{o}, 20^{o}, 25 ^{o}, 30^{o} 35^{o} (Detailed annotations of the line types given in right-corner panel)

As with the inclined angle effect, Fig. 5.10 shows us the effects of the volume of the auxiliary chamber on the dynamic stiffness curve of the LBM for α=37^{o}. If $\hat{V}_{ac1}=0$ as shown in Fig. 5.10(a), the LBM obtains the biggest stiffness and the stiffness of which is a strong nonlinear function with respect to the relative displacement $\hat{u}$. In addition, it can be noted that there will be a large variation in the stiffness curve for a change in value of $\hat{V}_{ac1}$ as depicted in Fig. 5.10(b) herein the values of $\hat{V}_{ac1}$ are arranged from small to large value according to stiffness curves from up to down. As observed, increasing the volume of the auxiliary chamber will produce a low dynamic stiffness and a slow change of stiffness around the desirable static equilibrium position. When the value of $\hat{V}_{ac1}$ is larger than 100, the variation of the stiffness of the LBM versus the dimensionless displacement $\hat{u}$ is almost very small, meaning that the stiffness of the LBM is nearly constant around the desirable static equilibrium position. However, if the volume of the auxiliary chamber is increased remarkably for instance $\hat{V}_{ac1} = 159.01$, this will cause a difficulty in the practical application of the proposed model.

If the inclined angle of the wedge is designed with a small value for instance α=5°, the values of $\hat{V}_{ac1} = 0;\ 1.59;\ 7.95;\ 15.9$ for which the curve of the dynamic stiffness of the LBM is shown in Fig. 5.11. Compared with the case of α=37° (showing in Fig. 5.10 (b)), in this case, the dynamic stiffness of the LBM changes more slowly around DSEP and the value and the nonlinearity of the stiffness curve are much lower.

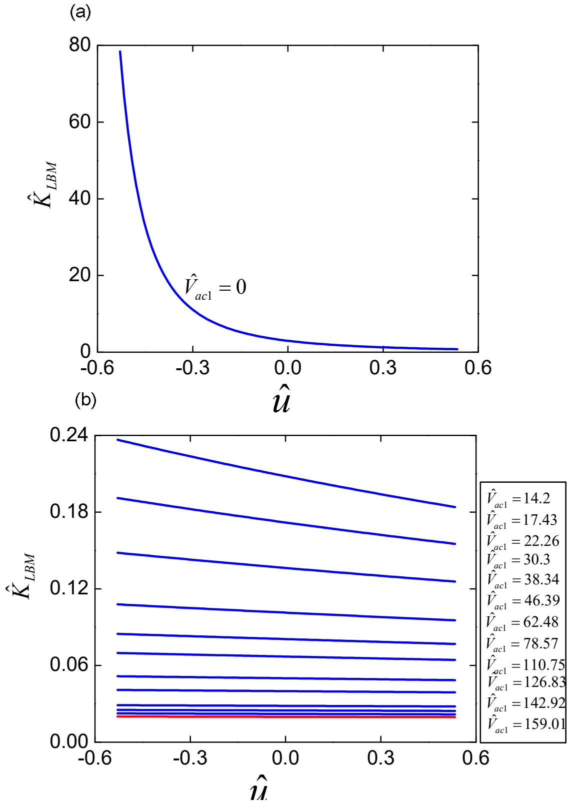

Fig. 5.10. The dynamic stiffness curve of the LBM for α=37°, P_{S01}=1.91 bar: (a) $\hat{V}_{ac1}$=0; (b) various values of $\hat{V}_{ac1}$ given in right-corner panel (Noted that the values of $\hat{V}_{ac1}$ are arranged from small to big according to the stiffness curves from up to down, respectively)

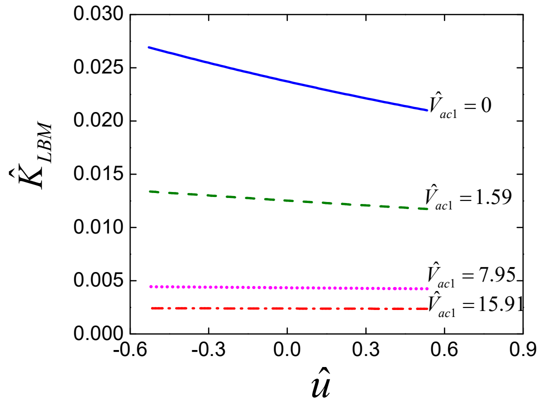

Fig. 5.11. Dynamic stiffness for α=5° and the various values of $\hat{V}_{ac1}$

Indeed, in order to obtain the constant stiffness around the DSEP, the slope (*SL*) of the stiffness curve at the DSEP given by Eq. (5.30) must be equal to zero. The influence of the inclined angle α and volume $\hat{V}_{ac1}$ of the auxiliary chamber on the slope of the dynamic stiffness at the DSEP are shown in Fig. 5.12. Once again, it can be seen that slope of dynamic stiffness curve of the LBM is large for a large value of α and a small value of $\hat{V}_{ac1}$. The slope is fallen as there is a reduction in the value of α or in increase in the value of $\hat{V}_{ac1}$.

$$SL=\left.\frac{d\hat{K}_{LBM}}{d\hat{u}}\right|_{\hat{u}=0}=-4n(n+1)\frac{\hat{V}_{d1}^{n}\hat{V}_{e01}^{n}}{\left(\hat{h}_1+\hat{V}_{ac1}-2\hat{H}_o\tan\alpha\right)^{n+2}}\tan^3\alpha \qquad (5.30)$$

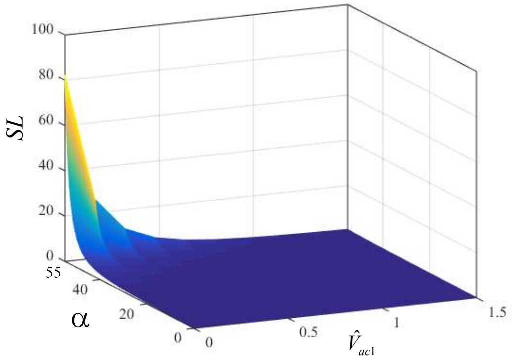

Fig. 5.12. The influence of the inclined angle α and the auxiliary chamber volume $\hat{V}_{ac1}$ of the auxiliary chamber on the slope of the dynamic stiffness curve at the DSEP

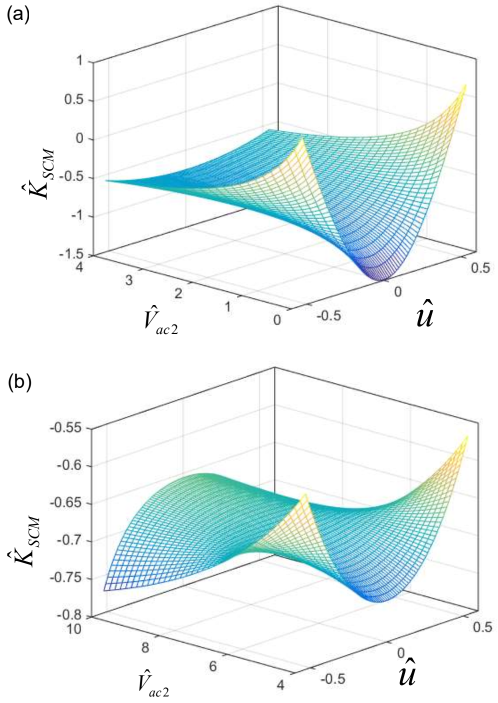

Fig.5.13 Influence of the auxiliary chamber volume $\hat{V}_{ac2}$ of the SCM on the dynamic stiffness $\hat{K}_{SCM}$ for P_{S01}=1.55 bar, P_{S02}=1.45 bar, A_2=0.0079 m^2, $\hat{V}_{e01}=33.7$; (a) $\hat{V}_{ac2}=0\div4$; (b) $\hat{V}_{ac2}=5\div10$

Next, the influences of the auxiliary chamber volume ($\hat{V}_{ac2}$) of the SCM on the stiffness of the stiffness corrected mechanism are investigated by using the Eq. (5.29) for P_{S01}=1.55 bar, P_{S02}=1.45 bar, A_2=0.0079m^2, $\hat{V}_{e01}=33.7$ and $\hat{V}_{ac2}$ changed from 0 to 10. As shown in Fig. 5.13, it can be seen that, the dynamic stiffness of the SCM is symmetric around the DSEP and reaches the extremum at this position. The value of extremum is minimum as $\hat{V}_{ac2}=0$ and is increased according to the growth of the auxiliary chamber volume of the SCM. Besides, around the DSEP, the shape of stiffness curve can be a convex or concave parabola that depends on the value of $\hat{V}_{ac2}$. Indeed, in this case if the value of $\hat{V}_{ac2}$ is smaller than approximately 7, the dynamic stiffness of the SCM will be a concave curve and may obtain the negative value around the DSEP but after 7, it will become a convex parabola.

In order to determine the condition for which the transmission between the concave and convex curve occurs, the Eq. (5.29) can be approximated by expanding the power series around the DSEP$\left(\hat{u}=0\right)$as following:

$$\hat{K}_{SCM}^{ap} = a_o + a_1\hat{u} + a_2\hat{u}^2 + O(\hat{u}) \qquad (5.31)$$

where $\hat{K}_{SCM}^{ap}$ is the approximate stiffness of the SCM

$$\begin{aligned} a_o &= 2\hat{A}\left[\hat{P}_{atm} - \mu\hat{V}_{d2}^{n}\left(\frac{A_2h_2+V_{ac2}}{A_2h_2+V_{ac2}+2\hat{A}\sqrt{1-\hat{H}_o^2}-2\hat{A}}\right)^{n}\right] \\ a_1 &= 0; \\ a_2 &= 6\hat{A}\left[\hat{P}_{atm} - \mu\hat{V}_{d2}^{n}\left(\frac{A_2h_2+V_{ac2}}{A_2h_2+V_{ac2}+2\hat{A}\sqrt{1-\hat{H}_o^2}-2\hat{A}}\right)^{n}\right] + \frac{12n\mu\hat{A}^2\hat{V}_{d2}^{n}\left(A_2h_2+V_{ac2}\right)^2}{\left(A_2h_2+V_{ac2}+2\hat{A}\sqrt{1-\hat{H}_o^2}-2\hat{A}\right)^{n+1}} \end{aligned} \qquad (5.32)$$

This is a second-order equation, with a_1=0, this confirms that the dynamic stiffness curve of the SCM is symmetric around the equilibrium position. In addition, to obtain the concave curve, the coefficient of the order $\hat{u}^2$ must be larger than zero as given by the condition Eq. (5.33)

$$a_2 = 6\hat{A}\left[\hat{P}_{atm} - \mu\hat{V}_{d2}^{n}\left(\frac{A_2h_2+V_{ac2}}{A_2h_2+V_{ac2}+2\hat{A}\sqrt{1-\hat{H}_o^2}-2\hat{A}}\right)^{n}\right] + \frac{12n\mu\hat{A}^2\hat{V}_{d2}^{n}\left(A_2h_2+V_{ac2}\right)^2}{\left(A_2h_2+V_{ac2}+2\hat{A}\sqrt{1-\hat{H}_o^2}-2\hat{A}\right)^{n+1}} > 0 \qquad (5.33)$$

As shown in Fig. 5.14, the coefficient of a_2 will be diminished as the dimensionless volume $\hat{V}_{ac2}$ of the auxiliary chamber of the SCM is increased. To plot this curve, exception of $\hat{V}_{ac2}$ the other parameters of the system are the same as in Fig. 5.13. It is interesting to note that as the value of $\hat{V}_{ac2}$ is in the region from 0 to approximate 7, the value of a_2 is positive. This leads the dynamic stiffness of the SCM to be a concave parabola but out of this region, the stiffness curve is convex due to $a_2<0$. These results are confirmed in Fig. 5.15, seeing the detailed annotation of the types of lines and chosen parameters in upper panel of the figure. It is observed that around the DSEP, the dynamic stiffness curves of the SCM are concave as $\hat{V}_{ac2}=3.18;\,4.77$ and convex one as $\hat{V}_{ac2}=7.48;\,8.05$.

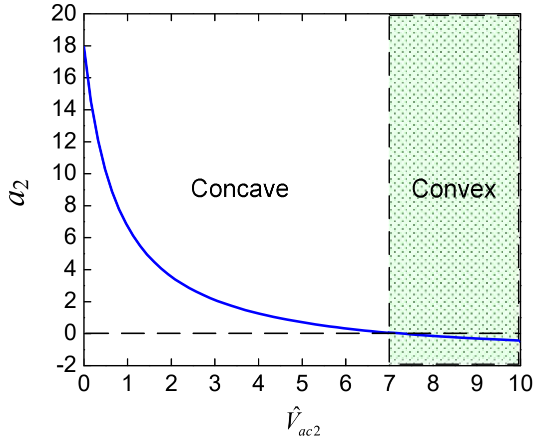

Fig. 5.14. Domain of the concave and convex curve versus $\hat{V}_{ac2}$ and the same other parameters as in Fig. 5.13

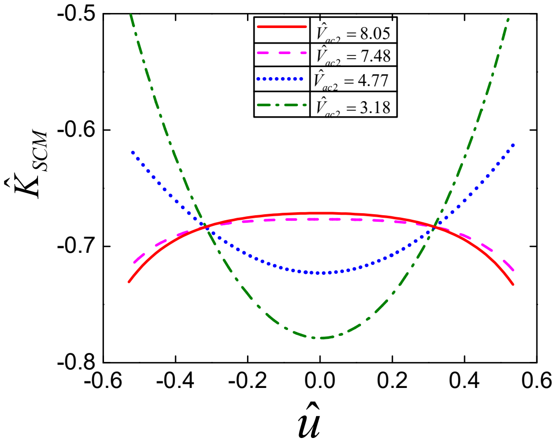

Fig.5.15. Dynamic stiffness curves of the SCM for various values of $\hat{V}_{ac2}$, the same other parameters as in Fig. 5.13 (Detailed annotation of line types and chosen parameters are presented in upper panel).

To further illustrate the effects of $\hat{V}_{ac2}$ and the pressure P_{S02} in the pneumatic spring 2 on the condition Eq. (5.33), the numerical calculation is realized for P_{S02}=1÷5 bar, $\hat{A}$=0÷1.2 and $\hat{V}_{ac2}$=0 as exhibited in Fig. 5.16(a). It can be seen that the value of a_2 is always positive for any value of $P_{s02}\geq 1$, indicating that the SCM achieves the concave stiffness curve. In the case of $\hat{V}_{ac2}\neq 0$, the region of $\hat{V}_{ac2}$ in which the value of a_2 is positive depends on the pressure P_{S02}. This is clearly observed in Fig. 5.16(b-c) that the area of the $\hat{V}_{ac2}$ having $a_2>0$ is reduced for an increase in the pressure P_{S02}.

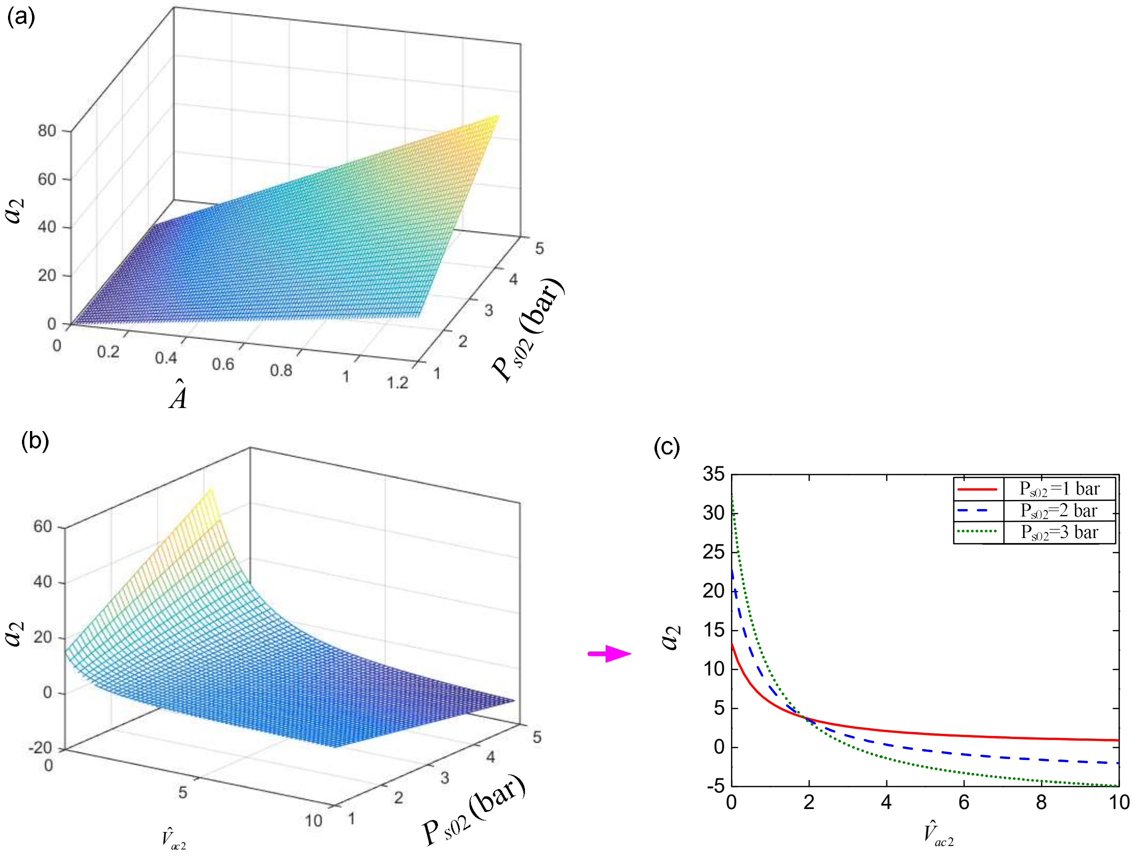

Fig. 5.16. By numerical calculation of Eq. (5.33): (a) surface of coefficient a_2 for P_{S02}=1÷5 bar, $\hat{A}$=0÷1.2 and $\hat{V}_{ac2}$=0; (b) Effect of P_{S02} and $\hat{V}_{ac2}$ on the coefficient of a_2 for P_{S02}=1÷5 bar and $\hat{V}_{ac2}$=0÷10; (c) the sections cut by P_{S02}=1, 2 and 3 bar (the notations of various type of lines are given in sub-panel).

In addition, in order to comprehensively analyze the characteristic of the dynamic stiffness of the SCM, the effects of the effective area and the pressure P_{S02} of the pneumatic cylinder 2 are taken into account. Firstly, the effective area is increased to 0.031m^2, the other parameters are kept as in Fig. 5.13. The shape of the dynamic stiffness curve of the SCM is not changed as shown in Fig. 5.17. However, the comparing between Figs. 5.13 and 5.17, it can be seen that with a large value of the effective area A_2, the dynamic stiffness of the SCM can obtain the lower value. In this case, the SCM offers a minimum stiffness value at the DSEP when the value of $\hat{V}_{ac2}$is smaller than approximately 21.6. The second case is shown in Fig. 5.18 for P_{S02} =1.65 bar but the other parameters are kept as in Fig. 5.17. This result is that the form of the dynamic stiffness surface is also unchanged but the dynamic stiffness of the SCM is reduced in accordance with the increase in the pressure P_{S02}. Besides, to obtain the concave curve, the volume of $\hat{V}_{ac2}$ is shrunk from 21.6 (for P_{S02}=1.45 bar) to 18 (for P_{S02}=1.65 bar) as shown in Fig. 5.19.

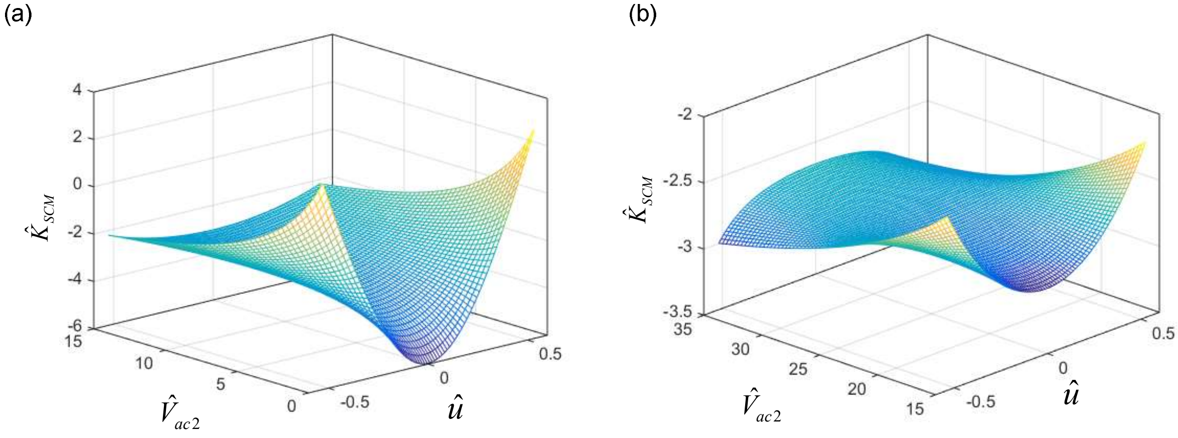

Fig. 5.17. Influence of the auxiliary chamber volume $\hat{V}_{ac2}$ of the SCM on the dynamic stiffness for effective area A_2=0.031 m^2, the same other parameters as in Fig. 5.13: (a) $\hat{V}_{ac2} = 0 \div 15$, (b) $\hat{V}_{ac2} = 16 \div 35$

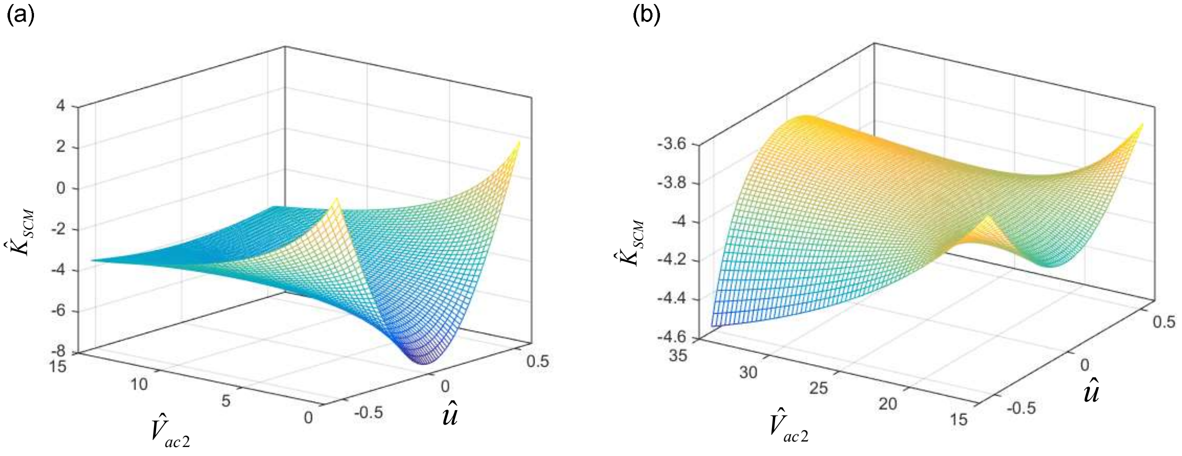

Fig. 5.18. Influence of the auxiliary chamber volume $\hat{V}_{ac2}$ of the SCM on the dynamic stiffness for P_{S02}=1.65 bar, the same other parameters as in Fig. 5.17: (a) $\hat{V}_{ac2}=0\div15$, (b) $\hat{V}_{ac2}=16\div35$

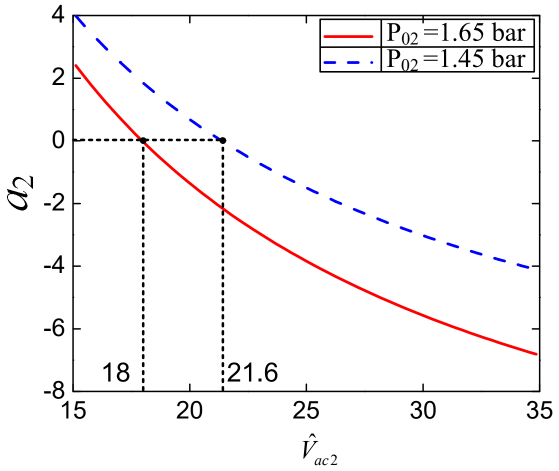

Fig. 5.19. Plot of coefficient a_2 versus $\hat{V}_{ac2}$ for the effective area A_2=0.031m^2 and P_{S02}=1.45 and 1.65 bar

5.5 Stiffness analysis of the modified model

In order to simplify the dynamic analysis in the next section, the restoring force given by Eq. (5.19) can be expressed approximately (F_{ap}) by expanding Taylor series around the DSEP (u=0) as below:

$$F_{ap} = F_o + a_1 u + a_2 u^2 + a_3 u^3 + a_4 u^4 + a_5 u^5 + \mathrm{O}(u^6) \tag{5.34}$$

herein,

$$\begin{aligned} F_o &= 2A_1 \left[P_{so1} \left(\frac{A_1 h_1 + V_{ac1}}{A_1 h_1 + V_{ac1} - 2A_1 H_o \tan\alpha} \right)^n - P_{atm} \right] \tan\alpha \\ a_n &= \frac{1}{n} \left(\frac{dF_{LBM}{}^n}{du^n} + \frac{dF_{SCM}{}^n}{du^n} \right) \Bigg|_{u=0} \qquad n = 1, 2, 3, 4, 5 \end{aligned} \tag{5.35}$$

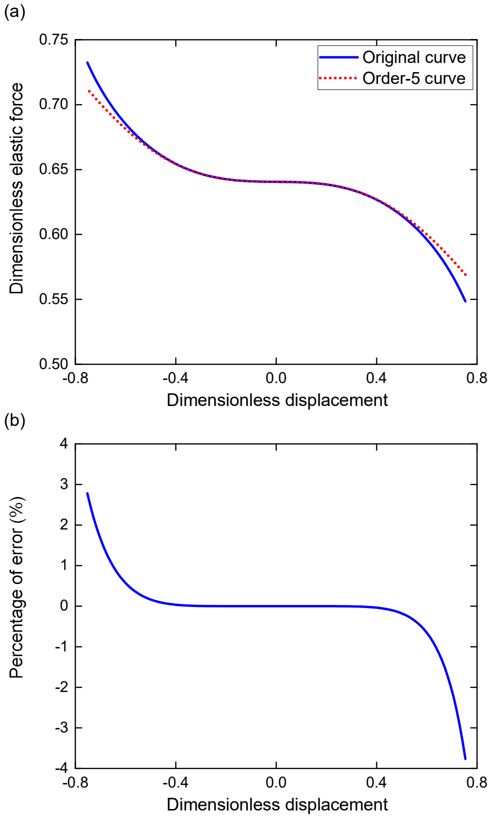

Fig. 5.20. (a) Comparison between of the original (solid line) and 5th - order approximated (dot line) curve of the elastic force; (b) The error percentage between the exact solution and approximation one

The original elastic force given by Eq. (5.19) and its approximated form expressed by Eq. (5.34) are compared as in Fig. 5.20(a). The former is denoted by the solid line while the latter is drawn by the dot line. It is interesting to see that the curve of Eq.

(5.19) approximated to 5^{th} - order through expanding Taylor series is in good agreement with the other. Furthermore, the error percentage of the approximated curve is lower than 4% compared with the exact solution as shown in Fig. 5.20(b). As observed, in the neighborhood of the equilibrium position (u=0), the error is extremely small but it will be grown as it is moved far away from the equilibrium position, meaning that the 5^{th} - order polynomial is suitable for small amplitude oscillation. This approximated solution will be considered to analyze the primary resonance response of the proposed system.

Fig. 5.21 (a) shows the dynamic stiffness surface in the space $\hat{V}_{ac1},\hat{u},\hat{K}_s$ in which the pressure ratio μ is 1.83 while other parameters including $\hat{V}_{cy1}=1.875;\ \hat{V}_{cy2}=0.248$. It revealed that the stiffness of the QSAVIM using PC is strongly affected by the auxiliary chamber volume V_{ac1} of the load bearing mechanism. Reducing the value of V_{ac1} will increase the value of the system stiffness. Simultaneously, the asymmetric level of the stiffness curve around the equilibrium position is also developed. This is seen clearly in Fig.5.21(b) created by cutting sections at $\hat{V}_{ac1}=7.892,\ 13.153, 26.306$ (types of lines are presented in the top-right corner panel). Furthermore, because of the asymmetry of the stiffness curve, the system cannot achieve the lowest stiffness at the equilibrium position (u=0). As observed, for the 1st value of the dimensionless auxiliary chamber volume, the position defined by $\hat{u}_{ls}$ at which the stiffness is to achieve the lowest value is approximated 0.084 and the value of $\hat{u}_{ls}$ can be reduced to 0.034 and 0.009 as the dimensionless volume of the auxiliary chamber is grown to 13.153 and 26.306, respectively.

The lowest stiffness position can be predicted by differentiating Eq. (5.34) to second-order versus the displacement and then equals zero as expressed in Eq. (5.36). It can be seen that this position will be asymptotic to the DSEP as when the auxiliary chamber volume $\hat{V}_{ac1}$ is increased as shown in Fig. 5.22.

$$2a_2 + 6a_3u + 12a_4u^2 + 20a_5u^3 \quad = 0 \tag{5.36}$$

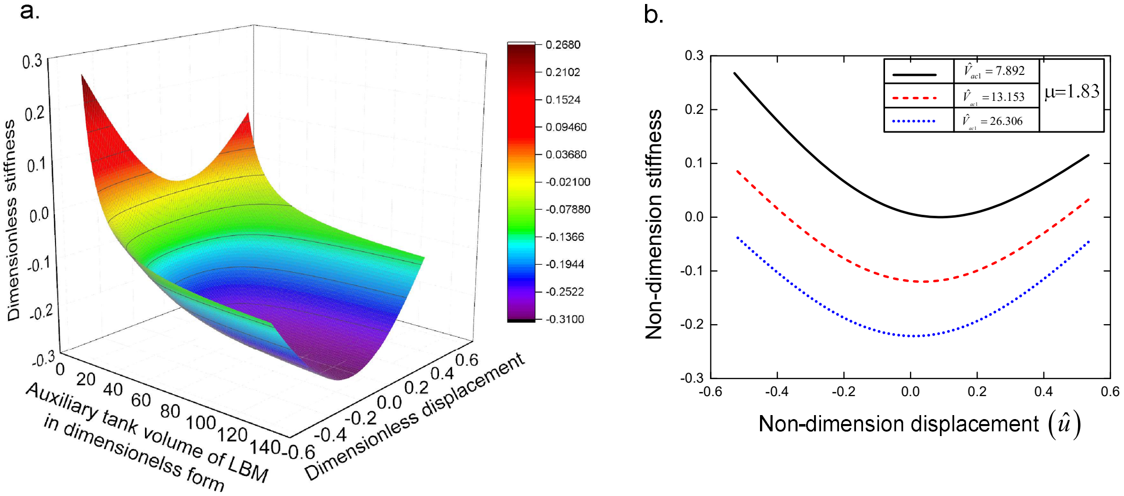

Fig. 5.21. (a) The vertical stiffness surface in the space $(\hat{V}_{ac1}, \hat{u}, \hat{K}_s)$ for pressure ratio μ=1.83; (b) The dynamic stiffness curves for different values of dimensionless auxiliary chamber volume given in right-top corner panel

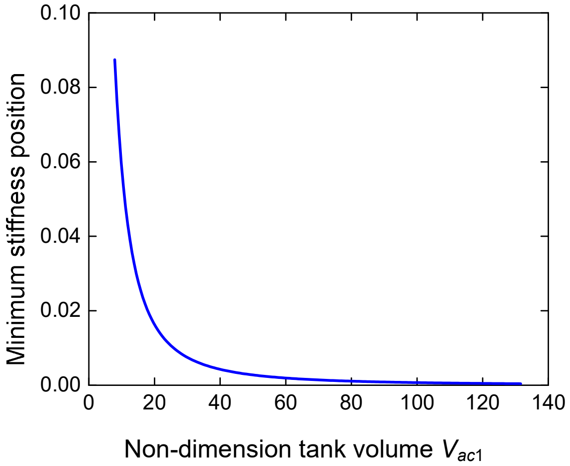

Fig. 5.22. The influence of auxiliary tank volume $\hat{V}_{ac1}$ on the minimum stiffness position.

In addition, from Eq. (5.27) for P_{wh1}=2 bar, by setting K_{s}=0, the relationship between the pressure ratio and the auxiliary chamber volume for which the pressure in cylinder of the SCM will be calculated, is marked in Fig.5.23(a). The pressure ratio curve is formed by cutting sections at the various values of the auxiliary chamber volume $\hat{V}_{ac1}$ as shown in Fig. 5.23(b) in which the values of $\hat{V}_{ac1}$ and the notation for line types are noted in the middle of panel. It can be observed that in the case of $\hat{V}_{ac1} = 34.198$, at the extremum point A corresponding to the pressure ratio μ=0.905, the oscillation system can obtain the quasi-zero stiffness at only one position $\hat{u}_A = 0.008$ but μ>0.905, there may exist two positions at which the stiffness is also nearly equal to zero such as at point A_2 ($\hat{u} = 0.381$) and point A_1($\hat{u} = -0.364$) for μ=1.2. It is shown that as lessening the volume $\hat{V}_{ac1}$ leads to the increase of the pressure ratio. For instance, $\hat{V}_{ac1} = 21.045$, 13.153 and 7.982, the lowest pressure ratios to obtain quasi-zero stiffness are 1.096, 1.379 and 1.834 are marked by the extremum point such as B, C and D, respectively. The slope of the stiffness curve at points A $(\hat{u}_A = 0.008)$, B $(\hat{u}_B = 0.021)$, C $(\hat{u}_C = 0.046)$, D$(\hat{u}_D = 0.083)$, is nearly equal to zero as depicted in Fig. 5.23(c) (all parameters are the same as in Fig. 5.23(b)), meanwhile other positions (A_1, A_2, etc.) the slope is nonzero, indicating that for the value of μ at extreme points of the pressure ratio curve, the dynamic stiffness can be equal to zero and obtains the minimum value in the expected working region. This result is also confirmed in Fig. 5.24 (a), herein the values of μ and annotation of the line types are given in the top-right corner panel of the figure.

As mentioned above, it may exist the points at which the stiffness of the QSAVIM using PC is quasi-zero but the slope of the stiffness curve is nonzero. For example, for μ=1.2, $\hat{V}_{ac1} = 34.198$, the system has quasi-zero stiffness at the position A_2 ($\hat{u} = 0.381$) and A_1 ($\hat{u} = -0.364$) (seen in Fig. 5.23 (b)) but at which the slope of the stiffness curve is larger than zero at A_2 and smaller than zero at A_1 (seen in Fig. 5.23 (c)). The result is in area from the position A_1 to A_2 in which the dynamic stiffness of the QSAVIM using a PC is negative as shown by dot line in Fig. 5.24 (b). On the aspect of isolation, this case is not suitable for designing an isolated model due to its unstableness. Besides, if the pressure ratio is chosen so that its value is smaller than that at the extremum point of the pressure ratio curves, the stiffness of the system is always larger than zero as exhibited in the Fig.5.23 (b) herein, the value of μ is chosen 0.7 (solid line), 0.8 (dashed line) and 0.85 (dash-dot line) while the dimensionless value of the auxiliary chamber volume is 34.198. Furthermore, it is interesting to note that the region *d* in which the dynamic stiffness of the QSAVIM using PC is smaller than that of the ETVIM is increased according to the increase in the pressure ratio.

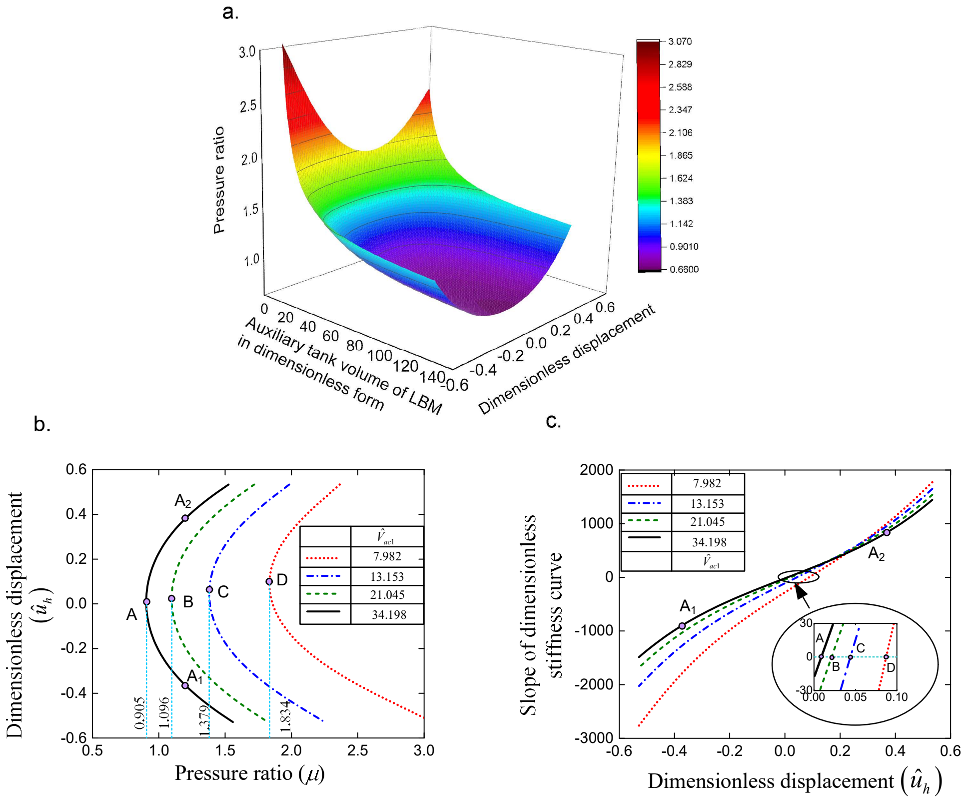

Fig. 5.23. (a). The quasi-zero stiffness surface in the space ($\hat{V}_{ac1},\hat{u},\mu$); (b). The pressure ratio curve for various values of $\hat{V}_{ac1}$;

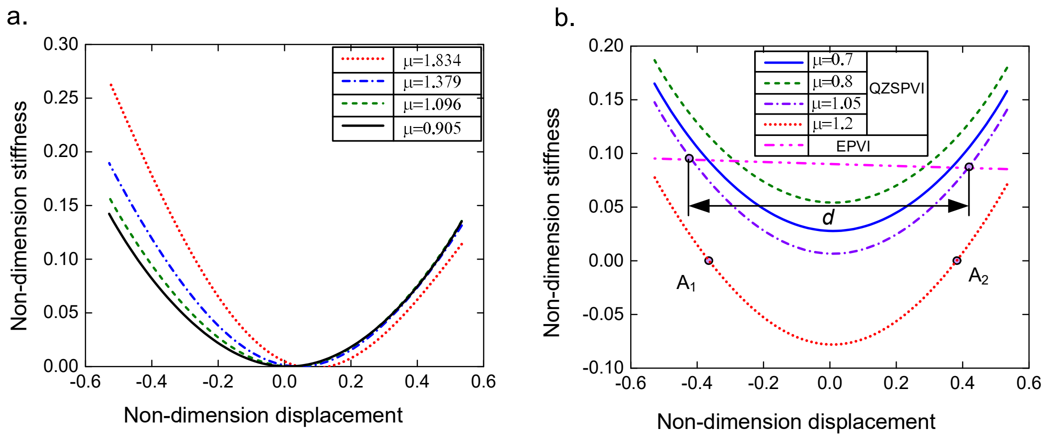

Fig. 5.24. Stiffness curve for different values of μ given in the panel of figure, the same other parameters as in Fig. 5.23: (a) Quasi-zero stiffness at position ($\hat{u}=0.008, 0.021, 0.046, 0.083$); (b) Arbitrary stiffness

5.6 The analysis of equilibrium position

The static equilibrium position was defined in Eq.(4.32), it can be written in dimensionless form as below:

$$\hat{f}\left(u,\mu,P_{wh1}\right)=\hat{F}_s-\hat{F}_g=0 \tag{5.37}$$

in which the dimensionless restoring force $\hat{F}_s=F_s/\left(\mathrm{A}_1 P_{wh1}\right)$ is determined by substituting Eqs. (5.25 - 5.26) into Eq. (5.19), obtaining

$$\begin{aligned}\hat{F}_s&=2\mu\hat{A}\hat{V}_{d2}^n\left(\begin{array}{l}\dfrac{\hat{V}_{e02}}{\hat{V}_{e02}+2\hat{A}\sqrt{1-\hat{H}_o^2}-2\hat{A}\sqrt{1-\hat{u}^2}}\\-\hat{A}\hat{P}_{atm}\end{array}\right)^n\frac{\hat{u}}{\sqrt{1-\hat{u}^2}}\\&\quad+2\hat{V}_{d1}^n\left(\frac{\hat{V}_{e01}}{\hat{V}_{e01}-2\hat{H}_o\tan\alpha+2\hat{u}\tan\alpha}-\hat{P}_{atm}\right)^n\tan\alpha\end{aligned} \tag{5.38}$$

and $\hat{F}_g=\dfrac{Mg}{P_{wh1}A_1}$ (5.39)

To obtain the DSEP, the isolated load (M) is calculated as following:

$$M = \left(P_{wh1} - P_{atm}\right)\frac{2A_1 \tan\alpha}{g} \tag{5.40}$$

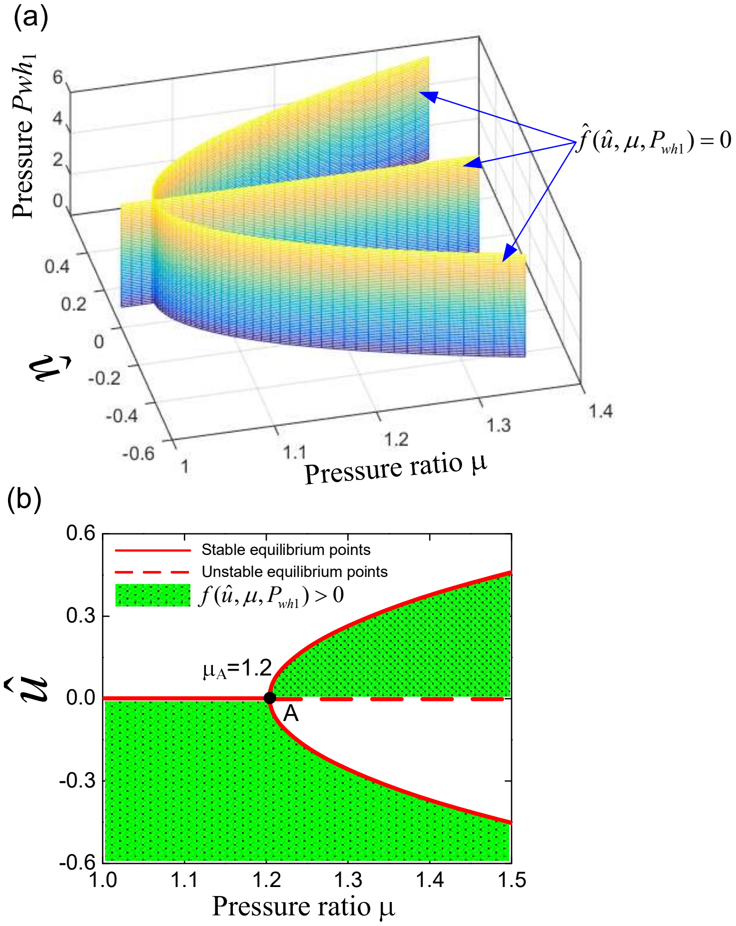

Fig. 5.25. (a) Equilibrium surface in space $(\mu,\hat{u},\hat{V}_{ac1})$ (b) Stability curves for equilibrium positions created by section plane $P_{wh1}=2\,\text{bar}$.

(Herein $\hat{V}_{ac1}=159.01$, $\hat{V}_{ac2}=0$, $A_1=0.0079\,\text{m}^2$, $\hat{A}$=0.01, P_{wh2}=3.6 bar)

The equilibrium surface in space with Eq. (5.41) for $\hat{V}_{ac1}=159.01$, $\hat{V}_{ac2}=0$, $A_1=0.0079m^2$, $\hat{A}=0.01$, P_{wh2}=3.6 bar, is shown in Fig. 5.25(a). It can be seen that depending on the pressure ratio μ and P_{wh1}, the equilibrium points of the QSAVIM using PC may lay on the plane having $\hat{u}=0$ or the curved surface. It indicates that the system may exist three or one equilibrium position. In order to further illustrate the stability of the equilibrium points, a curve for $\hat{f}(\hat{u},\mu,P_{wh1})=0$ in the plane $(\hat{u},\mu)$ as shown in Fig. 5.25 (b) is created by the cutting section having P_{wh1}=2bar. In the shaded region where $\hat{f}(\hat{u},\mu,P_{wh1})$ is positive, out of this region, $\hat{f}(\hat{u},\mu,P_{wh1})$ is negative. It can be seen that the number and stability of the equilibrium positions may be varied in accordance with the pressure ratio μ. But its real significance is to display the fact that μ at point A (called μ_{A}) is a bifurcation point of the system, at this section, the value of μ_{A}=1.2. When the $\mu \leq \mu_{\text{A}}$, then there is only one stable equilibrium position (called center point) at $\hat{u} = 0$ due to the changing of $\hat{f}(\hat{u},\mu,P_{wh1})$ from positive to negative on passing through this equilibrium position. But the value of μ is larger than μ_{A} the system has three equilibria including two centers which are on solid curve and an unstable equilibrium position (saddle point) lied on dashed line ($\hat{u} = 0$). Furthermore, in this case, around the DSEP the QSAVIM using PC can attain the quasi-zero stiffness (solid line) for $\mu=\mu_{\text{A}}$, larger stiffness than zero (dashed line) for $\mu<\mu_{\text{A}}$ and negative stiffness (dot line) for $\mu>\mu_{\text{A}}$ as shown in Fig. 5.26.

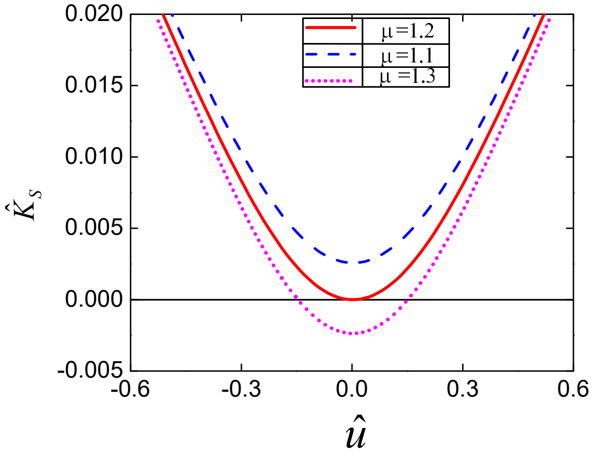

Fig. 5.26. Quasi-zero stiffness around the DSEP for P_{wh1}=2 bar and μ=1.1(dashed line), 1.2 (solid line), 1.3 (dot line)

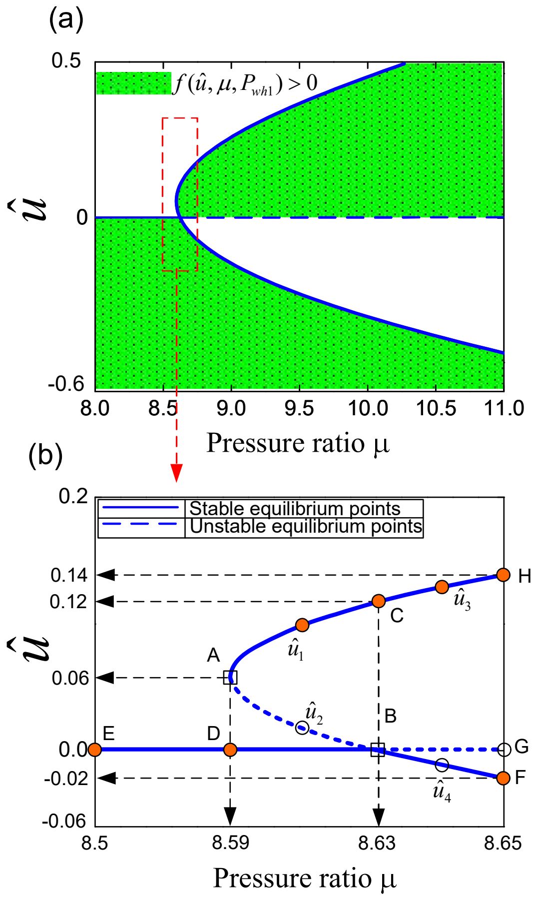

Fig. 5.27. Equilibrium curve of Eq. (5.41) for P_{wh1}=3.7 bar and $\hat{V}_{ac1}=14.21$, the same other parameters as in Fig. 5.25. (b) Equilibrium curve enlarged for $\mu \in [8.5, 8.65]$. (The detailed annotation is presented in the upper-left corner of each figure)

Next, considering the case of P_{wh1}=3.7 bar, $\hat{V}_{ac1}=14.21$, other parameters are the same as in Fig.5.25, the equilibrium curve ($\hat{f}\left(\hat{u}, \mu, P_{wh1}\right) = 0$) is denoted in Fig. 5.27 (a). The region offering $\hat{f}\left(\hat{u},\mu,P_{wh1}\right)>0$ is shaded meanwhile the non-shaded area is representative for $\hat{f}\left(\hat{u},\mu,P_{wh1}\right)<0$. In this case, notes that the stability curve for the equilibrium points is asymmetric around the DSEP and there exists two bifurcation points including μ_{A}=8.59 and μ_{B}=8.63 as revealed in Fig. 5.27 (b), an enlarged equilibrium curve in the dashed rectangle of Fig. 5.27 (a), seeing the details for the notations of the types of lines in the upper-left corner. If the value of μ is lower than μ_{A}

there exists only one stable equilibrium position at $\hat{u} = 0$, and if the value of μ is between μ_A and μ_B that would result in two centers at $\hat{u} = 0$ and $\hat{u} = \hat{u}_1 > 0$ (lying on solid line), and one saddle point at $\hat{u} = \hat{u}_2 > 0$ (lying on dashed line). If after μ_B, the system will offer three equilibrium points including 2 centers at $\hat{u} = \hat{u}_3 > 0$, $\hat{u} = \hat{u}_4 < 0$ (lying on the solid line) and one saddle point at $\hat{u} = 0$ corresponding to the dashed line. With $\mu = \mu_A$, there are two equilibrium positions including one center at $\hat{u} = 0$ marked by the filled circle D, and a center-saddle point at $\hat{u} > 0$ expressed by the non-filled square A. Oppositely, if $\mu = \mu_B$, it will have one center-saddle point at $\hat{u} = 0$ denoted by the non-filled square B and one center at $\hat{u} > 0$ marked by filled circle C.

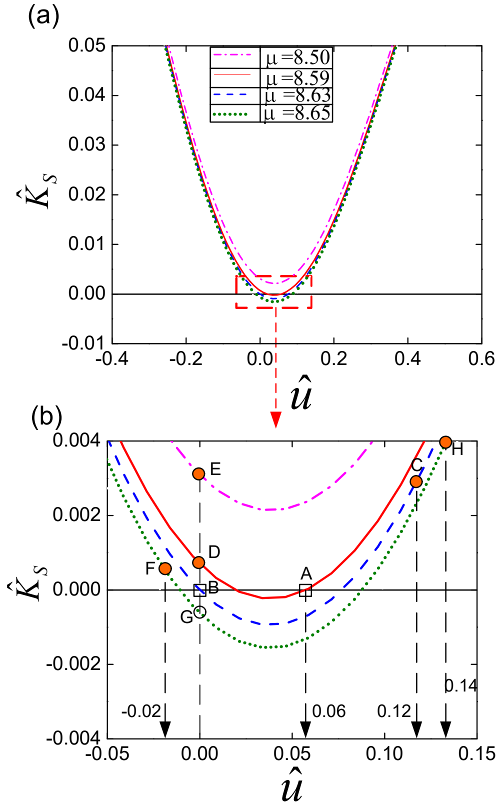

Fig. 5.28. (a) Stiffness curve of Eq. (5.27) for P_{wh1}=3.7 bar, $\hat{V}_{ac1} = 14.21$ and μ=8.50, 8.59, 8.63, 8.65. (b) Stiffness curve enlarged for $\hat{u} \in$[-0.05, 0.15] and $\hat{K}_S \in$[-0.004, 0.004]. (The notation of the various types of lines is presented in the upper panel)

In addition, Fig. 5.28(b) presents the dynamic stiffness of the QSAVIM using PC for given values of μ, seeing the detailed annotation of the types of the lines in upper panel of the figure. It reveals that the stiffness curve of the QSAVIM using PC is asymmetrical around the DSEP and at center points, the dynamic stiffness of the proposed model is positive for instance, at E (μ=8.5), D ($\mu=\mu_A$), C ($\mu=\mu_B$), F, H (μ=8.65). But with the saddle point, for example, the stiffness is negative at G (μ=8.65). Meanwhile, at bifurcation points A and B (center-saddle point), the dynamic stiffness is equal to zero but this equilibrium is unstable because the stiffness may be negative as the isolated object is moved away from the center-saddle point.

5.7. Dynamic analysis

5.7.1. Frequency-amplitude relation

Consider that the absolute displacement of the isolated object (z) due to a harmonic force with the amplitude F_e and frequency ω from the isolated object as shown in Fig. 5.29.

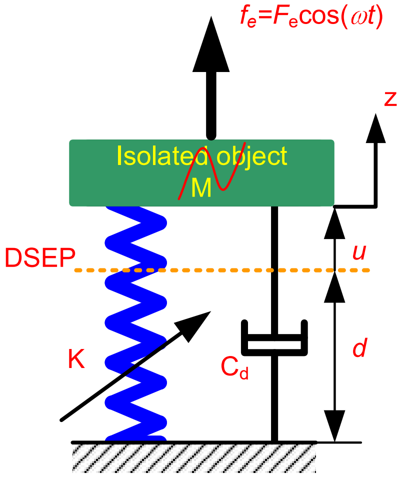

Fig. 5.29. Simple model of QSAVIM using PC

The kinetic energy is given by Eq. (4.38), meanwhile the potential energy (E_p) of the approximate restoring force given in Eq. (5.34) can be expressed as:

$$E_p = \int_0^{\Delta L} F_{ap} d\Delta L = F_o \Delta L + \sum_{i=1}^{5} a_i \frac{H_o^{i+1}}{i+1} - \sum_{i=1}^{5} a_i \frac{\left(H_o - \Delta L\right)^{i+1}}{i+1} \tag{5.41}$$

where the relation between the origin of the relative coordinate *u* and the static deformation H_o is denoted in Eq. (4.27), that is $\Delta L = H_o - u$

The energy dissipation function (*D*):

$$D = \frac{1}{2} C_d \dot{z}^2 \tag{5.42}$$

The generalized force in absolute coordinate of *z:*

$$Q = f_e - Mg \tag{5.43}$$

with f_e is the harmonic external force

The case in which the system attains the DSEP, indicating the weight of the isolated object is determined by Eq. (5.40), by using Eq. (4.43), the motion equation of the load plate is expressed as following:

$$M\ddot{z} + C_d \dot{z} - \left(F_o + \sum_{i=1}^{5} a_i \left(H_o - \Delta L\right)^i \right) + Mg = F_e \cos\left(\omega t\right) \tag{5.44}$$

Utilizing Eq. (4.41) in which z_e is removed and Eq. (4.27), the dynamic equation Eq. (5.44) is rewritten according to the relative coordinate (*u*) in dimensionless form, we obtain:

$$\bar{u}' + 2\xi \bar{u}' + \bar{u} + \sum_{n=2}^{5} \alpha_n \bar{u}^n = c\,\mathrm{os}\left(\Omega \tau\right) \tag{5.45}$$

Herein, some parameters given in this equation are defined as following:

$$\bar{u} = \frac{u}{u_o};\ \omega_n^2 = -\frac{a_1}{M};\ \Omega = \frac{\omega}{\omega_n};\ \tau = \omega_n t;\ \xi = \frac{C_d}{2\omega_n M}; \alpha_n = -\frac{a_n u_o^{n-1}}{M\omega_n^2};\ u_o = \left.\frac{F_e}{-a_1}\right|_{\omega=0; a_i=0(i=2,3,\ldots,5)}$$

where the number of primes denote the order of differentiation with respect to time-scaling τ

In order to find the solution in the neighborhood of the equilibrium position $\hat{u}=0$, we let $\hat{u}=\varepsilon\hat{x}$ with ε is a small detuning term:

$$\overline{x}''+2\varepsilon^4\tilde{\xi}\overline{x}'+\overline{x}+\sum_{n=2}^{5}\alpha_n\varepsilon^{n-1}\overline{x}^n=\varepsilon^4\tilde{k}\cos\left(\Omega\tau\right) \tag{5.46}$$

herein ε<<1, $\xi\hat{x}'=\varepsilon^4\tilde{\xi}\overline{x}'$; $\cos(\Omega\tau)=\varepsilon^5\tilde{k}\cos(\Omega\tau)$ (5.47)

By applying Multi-scale method, the approximated solution of the Eq. (5.46) is obtained as following:

$$\begin{aligned}\overline{x}(\tau,\varepsilon)&=\overline{x}_o(T_o,T_1,T_2,T_3,T_4)+\varepsilon\overline{x}_1(T_o,T_1,T_2,T_3,T_4)+\varepsilon^2\overline{x}_2(T_o,T_1,T_2,T_3,T_4)\\&+\varepsilon^3\overline{x}_3(T_o,T_1,T_2,T_3,T_4)+\varepsilon^4\overline{x}_4(T_o,T_1,T_2,T_3,T_4)+\ldots+O(\varepsilon^5)\end{aligned} \tag{5.48}$$

in which $T_i=\varepsilon^i\tau\ (i=0,1,2,3,4)$. Substituting Eq. (5.48) into Eq. (5.46) and letting $\Omega=1+\varepsilon^2\sigma$ then equating the coefficient of $\varepsilon^o,\varepsilon^1,\varepsilon^2,\varepsilon^3,\varepsilon^4$ on both sides of the equation ..

$$\begin{aligned}&\varepsilon^o\quad \mathrm{D}_o^2\overline{x}_o+\overline{x}_o=0\\&\varepsilon^1\quad \mathrm{D}_o^2\overline{x}_1+\overline{x}_1=-2D_oD_1\overline{x}_o-\alpha_1\overline{x}_o\\&\varepsilon^2\quad \mathrm{D}_o^2\overline{x}_2+\hat{x}_2=-2D_oD_1\overline{x}_1-2D_oD_2\overline{x}_o-\mathrm{D}_1^2\overline{x}_o-\alpha_1\overline{x}_o\overline{x}_1-\alpha_2\overline{x}_o^3\\&\varepsilon^3\quad \mathrm{D}_o^2\overline{x}_3+\overline{x}_3=-2D_oD_1\overline{x}_2-2D_oD_2\overline{x}_1-2D_oD_3\overline{x}_o-2D_1D_2\overline{x}_o-\mathrm{D}_1^2\overline{x}_1-\alpha_1\left(\overline{x}_1^2+2\overline{x}_o\overline{x}_2\right)-3\alpha_2\overline{x}_o^2\overline{x}_1-\alpha_3\overline{x}_o^4\\&\varepsilon^4\quad \mathrm{D}_o^2\overline{x}_4+\overline{x}_4=-2D_oD_1\overline{x}_3-2D_oD_2\overline{x}_2-2D_oD_3\overline{x}_1-2D_oD_4\overline{x}_o-2D_1D_2\overline{x}_1-2D_1D_3\overline{x}_o-2\tilde{\xi}D_o\overline{x}_o-\mathrm{D}_1^2\overline{x}_2-\mathrm{D}_2^2\overline{x}_o\\&\qquad\qquad -\alpha_1\left(2\overline{x}_o\overline{x}_3+2\overline{x}_1\overline{x}_2\right)-3\alpha_2\left(\overline{x}_o^2\overline{x}_2+\overline{x}_o\overline{x}_1^2\right)-4\alpha_3\overline{x}_o^3\overline{x}_1-\alpha_4\overline{x}_o^5+\tilde{k}\cos(T_o+\sigma T_2)\end{aligned} \tag{5.49}$$

where $D_i^n=\dfrac{\partial^n}{dT_i^n}$; i=1,2,3,4; n is the order of the differentiation

The general solution of the first equation in Eq. (5.49) is expressed as below:

$$\overline{x}_o=\overline{A}\left(T_{1,}T_{2,}T_{3,}T_{4,}\right)e^{iT_o}+\overline{\overline{A}}\left(T_{1,}T_{2,}T_{3,}T_{4,}\right)e^{-iT_o} \tag{5.50}$$

with $\overline{A}$ is an unknown complex function and $\overline{\overline{A}}$ is the complex conjugate of $\overline{A}$

Substituting Eq. (5.50) into the second equation in Eq. (5.49), we obtain as following:

$$\mathrm{D}_o^2\bar{x}_1 + \bar{x}_1 = -2D_1\bar{A}e^{iT_o}i - \alpha_1\left(\bar{A}^2e^{2iT_o} + 2\bar{A}\bar{\bar{A}} + \bar{A}^2e^{-2iT_o}\right) + 2D_1\bar{\bar{A}}e^{-iT_o}i \tag{5.51}$$

In order to obtain the periodic solution of Eq. (5.51), imaginary terms in the right side of Eq. (5.51) must be zero. Namely,

$$D_1\bar{A} = 0;\ D_1\bar{\bar{A}} = 0 \Rightarrow \bar{A} \in (T_2, T_3, T_4) \tag{5.52}$$

Hence, the solution of Eq. (5.51) is:

$$\bar{x}_1 = \frac{\alpha_1\bar{A}^2}{3}e^{2iT_o} - 2\alpha_1\bar{A}\bar{\bar{A}} + \frac{\alpha_1\bar{\bar{A}}^2}{3}e^{-2iT_o} \tag{5.53}$$

Substituting $\hat{x}_o$ and $\hat{x}_1$ into the third equation in Eq. (5.49), we obtain:

$$\begin{aligned}\mathrm{D}_o^2\bar{x}_2 + \bar{x}_2 = &\left(-2D_2\bar{A}i + \frac{10\alpha_1^2\bar{A}^2\bar{\bar{A}}}{3} - 3\alpha_2\bar{A}^2\bar{\bar{A}}\right)e^{iT_o} - \left(\frac{2\alpha_1^2}{3} + \alpha_2\right)\bar{A}^3e^{3iT_o} - \left(\frac{2\alpha_1^2}{3} + \alpha_2\right)\bar{\bar{A}}^3e^{-3iT_o} \\ &+ \left(2D_2\bar{\bar{A}}i + \frac{10\alpha_1^2\bar{A}\bar{\bar{A}}^2}{3} - 3\alpha_2\bar{A}\bar{\bar{A}}^2\right)e^{-iT_o}\end{aligned} \tag{5.54}$$

As above, the secular terms in Eq. (5.54) will be ignored if the coefficient of e^{iT_o} or e^{-iT_o} are equal to zero, we have:

$$2D_2\bar{A}i = \frac{10\alpha_1^2\bar{A}^2\bar{\bar{A}}}{3} - 3\alpha_2\bar{A}^2\bar{\bar{A}} \text{ or } 2D_2\bar{\bar{A}}i = -\frac{10\alpha_1^2\bar{A}\bar{\bar{A}}^2}{3} + 3\alpha_2\bar{A}\bar{\bar{A}}^2 \tag{5.55}$$

By letting

$$\bar{A} = \frac{1}{2}\bar{a}e^{i\beta},\ \bar{\bar{A}} = \frac{1}{2}\bar{a}e^{-i\beta} \tag{5.56}$$

with a and β are real, then separating the real and imaginary parts, the differential equation for amplitude and frequency of Eqs. (5.52, 5.55) are expressed as below:

$$
\begin{aligned}
&D_1\bar{a} = 0;\\
&\bar{a}D_1\beta = 0\\
&D_2\bar{a} = 0;\\
&\bar{a}D_2\beta = \frac{3\alpha_2\bar{a}^3}{8} - \frac{10\alpha_1^2\bar{a}^3}{24}
\end{aligned}
\tag{5.57}
$$

The solution of Eq. (5.54) as following:

$$
\bar{x}_2 = \left(\frac{2\alpha_1^2}{24} + \frac{2\alpha_2}{8}\right)\bar{A}^3 e^{3iT_o} + \left(\frac{2\alpha_1^2}{24} + \frac{2\alpha_2}{8}\right)\bar{\bar{A}}^3 e^{-3iT_o}
\tag{5.58}
$$

Next, substituting Eqs. (5.50, 5.53, 5.58) into the 4th order equation in Eq.(5.49) is rewritten as following:

$$
\begin{aligned}
\mathrm{D}_o^2\bar{x}_3 + \bar{x}_3 = {} & -2D_3\hat{A}ie^{iT_o} - \left(\frac{8\alpha_1\bar{A}D_2\bar{A}}{3}i + \alpha_1\left(\frac{2\alpha_2\bar{A}^3\bar{\bar{A}}}{8} - \frac{30\alpha_1^2\bar{A}^3\bar{\bar{A}}}{24}\right) - 5\alpha_1\alpha_2\bar{A}^3\bar{\bar{A}} + 4\alpha_3\bar{A}^3\bar{\bar{A}}\right)e^{2iT_o}\\
& - \left(\frac{14\alpha_1^3}{72} + \frac{9\alpha_1\alpha_2}{8} + \alpha_3\right)\bar{A}^4 e^{4iT_o} + \left(4\alpha_2\alpha_1 - 6\alpha_3 - \frac{38\alpha_1^3}{9}\right)\bar{A}^2\bar{\bar{A}}^2\\
& + 2D_3\bar{\bar{A}}ie^{iT_o} - \left(-\frac{8\alpha_1\bar{\bar{A}}D_2\bar{\bar{A}}}{3}i + \alpha_1\left(\frac{2\alpha_2\bar{A}\bar{\bar{A}}^3}{8} - \frac{30\alpha_1^2\bar{A}\bar{\bar{A}}^3}{24}\right) - 5\alpha_1\alpha_2\bar{A}\bar{\bar{A}}^3 + 4\alpha_3\bar{A}\bar{\bar{A}}^3\right)e^{-2iT_o}\\
& - \left(\frac{14\alpha_1^3}{72} + \frac{9\alpha_1\alpha_2}{8} + \alpha_3\right)\bar{\bar{A}}^4 e^{4iT_o}
\end{aligned}
\tag{5.59}
$$

The periodic solution of Eq. (5.59) can be achieved by:

$$
D_3\bar{A} = 0; \Rightarrow D_3\bar{a} = 0 \;\&\; \bar{a}D_3\beta = 0
\tag{5.60}
$$

Eqs. (5.52, 5.60) reveal that the parameter $\bar{A}$ is independent on the scale time T_1 and T_3. The solution $\bar{x}_3$ is expressed as following:

$$\begin{aligned}\bar{x}_3 = {} & \frac{1}{3}\left(\frac{8\alpha_1\bar{A}D_2\bar{A}}{3}i+\alpha_1\left(\frac{2\alpha_2\bar{A}^3\bar{\bar{A}}}{8}-\frac{30\alpha_1^2\bar{A}^3\bar{\bar{A}}}{24}\right)-5\alpha_1\alpha_2\bar{A}^3\bar{\bar{A}}+4\alpha_3\bar{A}^3\bar{\bar{A}}\right)e^{2iT_o} \\ & +\frac{1}{15}\left(\frac{14\alpha_1^3}{72}+\frac{9\alpha_1\alpha_2}{8}+\alpha_3\right)\bar{\bar{A}}^4e^{4iT_o}+\left(4\alpha_2\alpha_1-6\alpha_3-\frac{38\alpha_1^3}{9}\right)\bar{A}^2\bar{\bar{A}}^2 \\ & +\frac{1}{3}\left(-\frac{8\alpha_1\bar{\bar{A}}D_2\bar{\bar{A}}}{3}i+\alpha_1\left(\frac{2\alpha_2\bar{A}\bar{\bar{A}}^3}{8}-\frac{30\alpha_1^2\bar{A}\bar{\bar{A}}^3}{24}\right)-5\alpha_1\alpha_2\bar{A}\bar{\bar{A}}^3+4\alpha_3\bar{A}\bar{\bar{A}}^3\right)e^{-2iT_o} \\ & +\frac{1}{15}\left(\frac{14\alpha_1^3}{72}+\frac{9\alpha_1\alpha_2}{8}+\alpha_3\right)\bar{\bar{A}}^4e^{4iT_o}\end{aligned} \tag{5.61}$$

Similarly, substituting Eqs. (5.53, 5.58, 5.61) in the last equation in Eq. (5.49), then the coefficient of e^{iT_o} is set to zero as following:

$$\begin{aligned}2D_4\bar{A}i = {} & -2\tilde{\xi}\bar{A}i+\left(\frac{10\alpha_1^2}{6}-\frac{3\alpha_2}{2}\right)^2\bar{A}^3\bar{\bar{A}}^2-\alpha_1\left(\frac{26\alpha_1\alpha_2}{12}-\frac{1172\alpha_1^3}{216}-\frac{28\alpha_3}{3}\right)\bar{A}^3\bar{\bar{A}}^2 \\ & -\alpha_2\left(\frac{1926\alpha_1^2}{216}+\frac{3\alpha_2}{8}\right)\bar{A}^3\bar{\bar{A}}^2-\frac{56\alpha_1\alpha_3}{3}\bar{A}^3\bar{\bar{A}}^2-10\alpha_4\bar{A}^3\bar{\bar{A}}^2+\frac{\tilde{k}}{2}e^{i\sigma T_2}\end{aligned} \tag{5.62}$$

By taking differentiation of $\bar{A}=\frac{1}{2}\bar{a}e^{i\beta}$ versus scale time T_4, the real and imaginary parts of Eq. (5.62) are obtained as following:

$$\begin{aligned}D_4\bar{a} = {} & -\tilde{\xi}\bar{a}+\frac{1}{2}\tilde{K}\sin\left(\sigma T_2-\beta\right) \\ -\bar{a}D_4\beta = {} & -\left(\frac{10\alpha_1^2}{6}-\frac{3\alpha_2}{2}\right)^2\frac{1}{2^5}\bar{a}^5-\alpha_1\left(\frac{26\alpha_1\alpha_2}{12}-\frac{1172\alpha_1^3}{216}-\frac{28\alpha_3}{3}\right)\frac{1}{2^5}\bar{a}^5 \\ & -\alpha_2\left(\frac{1926\alpha_1^2}{216}+\frac{3\alpha_2}{8}\right)\frac{1}{2^5}\bar{a}^5-\frac{56\alpha_1\alpha_3}{3}\frac{1}{2^5}\bar{a}^5-\frac{10\alpha_4}{2^5}\bar{a}^5+\frac{1}{2}\tilde{k}\cos\left(\sigma T_2-\beta\right)\end{aligned} \tag{5.63}$$

In addition, the differentiation of *a* and *β* with respect to dimensionless time *τ is* presented as below:

$$\begin{aligned} \overline{a}' &= \frac{da}{d\tau} = \varepsilon D_1\overline{a} + \varepsilon^2 D_2\overline{a} + \varepsilon^3 D_3\overline{a} + \varepsilon^4 D_4\overline{a} \\ \beta' &= \frac{d\beta}{d\tau} = \varepsilon D_1\beta + \varepsilon^2 D_2\beta + \varepsilon^3 D_3\beta + \varepsilon^4 D_4\beta \end{aligned} \tag{5.64}$$

From Eqs. (5.57, 5.60, 5.63), Eq. (5.64) is rewritten as following:

$$\begin{aligned} \overline{a}' &= -\tilde{\xi}\varepsilon^4\overline{a} + \frac{1}{2}\varepsilon^4\tilde{k}\sin\left(\sigma T_2 - \beta\right) \\ \overline{a}\beta' &= \frac{3\alpha_2}{8}\varepsilon^2\overline{a}^3 - \frac{10\alpha_1^2}{24}\varepsilon^2\overline{a}^3 + \left(\frac{10\alpha_1^2}{6} - \frac{3\alpha_2}{2}\right)^2 \frac{1}{2^5}\varepsilon^4\overline{a}^5 + \alpha_1\left(\begin{array}{c}\dfrac{26\alpha_1\alpha_2}{12} \\ -\dfrac{1172\alpha_1^3}{216} - \dfrac{28\alpha_3}{3}\end{array}\right)\frac{1}{2^5}\varepsilon^4\overline{a}^5 \\ &\quad + \alpha_2\left(\frac{1926\alpha_1^2}{216} + \frac{3\alpha_2}{8}\right)\frac{1}{2^5}\varepsilon^4\overline{a}^5 + \frac{56\alpha_1\alpha_3}{3}\frac{1}{2^5}\varepsilon^4\overline{a}^5 + \frac{10\alpha_4}{2^5}\varepsilon^4\overline{a}^5 - \varepsilon^4\frac{\tilde{k}}{2}\cos\left(\sigma T_2 - \beta\right) \end{aligned} \tag{5.64}$$

Substituting Eq. (5.56) into (5.50) and then, the obtained result is substituted into Eq. (5.48), the primary solution of Eq. (5.46) is expressed as following:

$$\overline{x} = \overline{a}\cos(\tau + \beta) + \mathcal{O}(\varepsilon) \tag{5.65}$$

Recalling $\hat{u} = \varepsilon\hat{x}$, the general solution of Eq. (5.45)

$$\hat{u} = \overline{a}_u\cos(\tau + \beta) + \mathcal{O}(\varepsilon) \tag{5.66}$$

in which $\overline{a}_u = \varepsilon\overline{a}$

Letting $\gamma = \sigma T_2 - \beta$, and combining Eq. (5.47), Eq. (5.64) is expressed with respect to $\overline{a}_u$ as below:

$$\begin{cases} \overline{a}_u' = -\xi\overline{a}_u + \dfrac{1}{2}\sin\gamma \\ \overline{a}_u\gamma' = \overline{a}_u\sigma - G(\alpha_1,\alpha_2)\overline{a}_u^3 - F(\alpha_1,\alpha_2)\overline{a}_u^5 + \dfrac{1}{2}\cos\gamma \end{cases} \tag{5.67}$$

with

$$
\begin{aligned}
&G(\alpha_1,\alpha_2)=\left(\frac{3\alpha_2}{8}-\frac{10\alpha_1^2}{24}\right);\\
&F(\alpha_1,\alpha_2)=\left(\begin{array}{l}\left(\dfrac{10\alpha_1^2}{6}-\dfrac{3\alpha_2}{2}\right)^2\dfrac{1}{2^5}+\varepsilon^4\alpha_1\left(\dfrac{26\alpha_1\alpha_2}{12}-\dfrac{1172\alpha_1^3}{216}-\dfrac{28\alpha_3}{3}\right)\dfrac{1}{2^5}\\ +\alpha_2\left(\dfrac{1926\alpha_1^2}{216}+\dfrac{3\alpha_2}{8}\right)\dfrac{1}{2^5}+\dfrac{56\alpha_1\alpha_3}{3}\dfrac{1}{2^5}+\dfrac{10\alpha_4}{2^5}\end{array}\right)
\end{aligned}
\tag{5.68}
$$

As the amplitude and phase are unchanged versus time, the steady state motion will occur, meaning that

$$
\begin{cases}
\dfrac{\sin\gamma}{2}=\xi\overline{a}_u\\
\dfrac{\cos\gamma}{2}=G(\alpha_1,\alpha_2)\overline{a}_u^3+F(\alpha_1,\alpha_2)\overline{a}_u^5-\overline{a}_u\sigma
\end{cases}
\tag{5.69}
$$

Through $\sin^2(\gamma)+\cos^2(\gamma)=1$, the sum of two sides of Eq. (5.69), the frequency-response relationship of Eq. (5.45) is obtained as following:

$$
\left(\xi\overline{a}_u\right)^2+\left(G(\alpha_1,\alpha_2)\overline{a}_u^3+F(\alpha_1,\alpha_2)\overline{a}_u^5-\overline{a}_u\sigma\right)^2=\frac{1}{4}
\tag{5.70}
$$

From Eq. (5.70), we have:

$$
\sigma_{1,2}=\frac{G(\alpha_1,\alpha_2)\overline{a}_u^3+F(\alpha_1,\alpha_2)\overline{a}_u^3\pm\sqrt{\dfrac{1}{4}-\left(\xi\overline{a}_u\right)^2}}{\overline{a}_u}
\tag{5.71}
$$

The peak amplitude ($\hat{a}_{up}$) and frequency (σ_p) are calculated as below:

$$
\begin{cases}
\overline{a}_{up}=\dfrac{1}{2\xi}\\
\sigma_p=\dfrac{G(\alpha_1,\alpha_2)\overline{a}_{up}^3+F(\alpha_1,\alpha_2)\overline{a}_{up}^5}{\overline{a}_{up}}
\end{cases}
\tag{5.72}
$$

5.7.2. Stability of the steady state solution

Considering $\bar{a}_{uo}$ & γ_{uo} along with a set of steady state solutions and its neighborhood are determined by introducing small variations $\bar{a}_{u1}$ & γ_{u1} as following:

$$\begin{cases} \bar{a}_u = \bar{a}_{uo} + \bar{a}_{u1} \\ \gamma = \gamma_{uo} + \gamma_{u1} \end{cases} \tag{5.73}$$

To accomplish the stable analysis, Eq. (5.67) is rewritten as

$$\begin{cases} \bar{a}'_{uo} = -\xi\left(\bar{a}_{uo} + \bar{a}_{u1}\right) + \frac{1}{2}\sin\left(\gamma_{uo} + \gamma_{u1}\right) \\ \gamma' = \sigma - G(\alpha_1,\alpha_2)\left(\bar{a}_{uo} + \bar{a}_{u1}\right)^2 - F(\alpha_1,\alpha_2)\left(\bar{a}_{uo} + \bar{a}_{u1}\right)^4 + \frac{1}{2\left(\bar{a}_{uo} + \bar{a}_{u1}\right)}\cos\left(\gamma_{uo} + \gamma_{u1}\right) \end{cases} \quad 5.74)$$

Based on Routh-Hurwitz Criterion for nonlinear system, the stability of the steady state solution depending on the eigenvalues λ is determined as below:

$$\begin{vmatrix} -\xi - \lambda & G(\alpha_1,\alpha_2)\bar{a}_u^3 + F(\alpha_1,\alpha_2)\bar{a}_u^5 - \bar{a}_u\sigma \\ -2G(\alpha_1,\alpha_2)\bar{a}_{uo} - 4F(\alpha_1,\alpha_2)\bar{a}_{uo}^3 - \frac{1}{2\bar{a}_{uo}^2}\cos\gamma_{uo} & -\xi - \lambda \end{vmatrix} = 0 \tag{5.75}$$

The unstable region of the steady state motion above is obtained as following

$$\xi^2 + \begin{pmatrix} 2G(\alpha_1,\alpha_2)\bar{a}_{uo} \\ +4F(\alpha_1,\alpha_2)\bar{a}_{uo}^3 + \frac{1}{2\hat{a}_{uo}^2}\cos\gamma_{uo} \end{pmatrix}\left(G(\alpha_1,\alpha_2)\bar{a}_u^3 + F(\alpha_1,\alpha_2)\bar{a}_u^5 - \bar{a}_u\sigma\right) < 0 \tag{5.76}$$

5.7.3. Transmissibility for force excitation

The case of the QSAVIM using PC is subjected to a harmonic forcing excitation *$f_e = F_e\cos(\omega t)$,* through the LBM, SCM and an air damping, the force is transmitted to the base can be written in dimensionless form as below:

$$\bar{F}_t = 2\xi\bar{u}' + \bar{u} + \sum_{n=2}^{5}\alpha_n\bar{a}^n \tag{5.77}$$

It reveals that the transmitted force depends on the velocity and position of the load plate given in Eq. (5.66). This force may be rewritten as:

$$\bar{F}_t = -2\xi\bar{a}_u\Omega\sin(\Omega\tau-\gamma)+\left(a_u+\frac{3\alpha_3\bar{a}_u^3}{4}+\frac{7\alpha_5\bar{a}_u^5}{8}\right)\cos(\Omega\tau-\gamma) \tag{5.78}$$

Applying Eq. (4.72), Eq. (5.78) can be rewritten as following:

$$\bar{F}_t = -2\xi\bar{a}_u\Omega\frac{\left(ie^{-i(\Omega\tau-\gamma)}-ie^{\mathrm{i}(\Omega\tau-\gamma)}\right)}{2}+\left(a_u+\frac{3\alpha_3\bar{a}_u^3}{4}+\frac{7\alpha_5\bar{a}_u^5}{8}\right)\frac{\left(e^{\mathrm{i}(\Omega\tau-\gamma)}+e^{-i(\Omega\tau-\gamma)}\right)}{2} \tag{5.79}$$

or

$$\begin{aligned}\bar{F}_t &= \frac{1}{2}\sqrt{\left(a_u+\frac{3\alpha_3\bar{a}_u^3}{4}+\frac{7\alpha_5\bar{a}_u^5}{8}\right)^2+\left(2\xi\bar{a}_u\Omega\right)^2}\,e^{i((\Omega\tau-\gamma)+\theta)}\\ &\quad+\frac{1}{2}\sqrt{\left(a_u+\frac{3\alpha_3\bar{a}_u^3}{4}+\frac{7\alpha_5\bar{a}_u^5}{8}\right)^2+\left(2\xi\bar{a}_u\Omega\right)^2}\,e^{-i((\Omega\tau-\gamma)+\theta)}\\ &=\sqrt{\left(a_u+\frac{3\alpha_3\bar{a}_u^3}{4}+\frac{7\alpha_5\bar{a}_u^5}{8}\right)^2+\left(2\xi\bar{a}_u\Omega\right)^2}\cos\left((\Omega\tau-\gamma)+\theta\right)\end{aligned} \tag{5.80}$$

where

$$\tan(\theta)=\frac{\left|2\xi\bar{a}_u\Omega\right|}{\left|a_u+\frac{3\alpha_3\bar{a}_u^3}{4}+\frac{7\alpha_5\bar{a}_u^5}{8}\right|}$$

The maximum force is transmitted to the base being:

$$\bar{F}_{t\max}=\sqrt{\left(2\xi\bar{a}_u\Omega\right)^2+\left(\bar{a}_u+\frac{3\alpha_3\bar{a}_u^3}{4}+\frac{7\alpha_5\bar{a}_u^5}{8}\right)^2} \tag{5.81}$$

The transmissibility for forcing excitation is defined as below:

$$|\,T_F\,|=\left|\frac{\bar{F}_{t\max}}{\bar{F}_e}\right| \tag{5.82}$$

herein from Eq. (5.45) the non-dimensional magnitude of the excited force $\bar{F}_e = 1$

5.8. Numerical simulation

5.8.1. Influence of parameters on the force transmitted curve

In this section, the effects of the pressure ratio and volume of auxiliary chamber on the force transmissibility of the QSAVIM using PC are investigated. Firstly, the pressure ratio will be studied meanwhile a set of parameters of the isolation system comprising of $\xi = 0.1$; $\hat{A} = 0.16$; $\hat{V}_{ac1} = 13.153$; $\hat{H}_o = 0.53$ is given, simultaneously at the equilibrium position, the pressure P_{wh1} of the LBM is set at the value of 1.85 bar for which the weight of the isolated load is 122.41 kg. As observed in Fig. 5.30 the dynamic stiffness (denoted by the solid line) of the QSAVIM using a PC for various values of μ within 1.350 to 1.377 is always smaller than that of the ETVIM (exhibited by the dashed line) when the position of the load plate is in the working region ($|\hat{u}| < \hat{H}_o$). Especially, μ=1.379, the minimum stiffness of the QSAVIM using PC is nearly equal to zero and it will be increased according to reduction in the pressure ratio. The result is the force transmitted curves shown in Fig. 5.31 (the detailed annotation of the type of lines and the chosen values of µ are presented in the left-upper corner panel of the figure). It can be argued that the nonlinearity of the proposed model bends the force transmitted curves to the left or the right depending on the pressure ratio. In the case of μ=1.379, the curve is bended to the left, indicating that this is the case of the soft nonlinear system. Reducing the pressure ratio will lead to reduce the soft nonlinearity even to become the hard nonlinearity. As observed, the amplitude-frequency curve is bended to the right for μ=1.360. However, the bending level of the response curve to the right may be lessened as there is a lessening in the pressure ratio such as μ=1.360, μ=1.350 and even trends no bending for μ=0 as seen in Fig. 5.31. This is evident because the pressure of the stiffness corrected mechanism will be reduced according to the reduction in the value of μ, meaning that the effects of this mechanism on the dynamic stiffness of the QSAVIM using PC become lightly and hence, the peak amplitude is increased. Furthermore, the increase of the pressure ratio will broaden the isolation region of the hardening system toward the low frequency as plotted in Fig. 5.32. On the other hand, the comparison between the proposed system and the ETVIM in which the SCM is removed, it is noteworthy to observe that the suppression of the force transmissibility from the load plate to the base of the QSAVIM using PC is better than the ETVIM, meaning that isolation region and vibration attenuated ratio of the former is larger than those of latter.

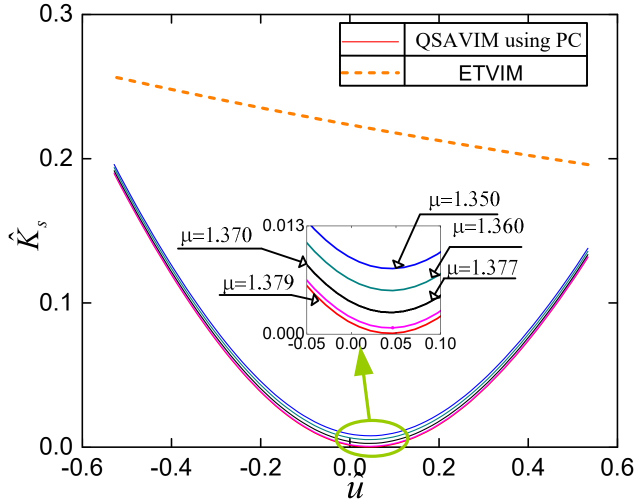

Fig. 5.30. The dynamic stiffness curve of the QSAVIM using PC for $\xi = 0.1$; $\hat{A} = 0.16$; $\hat{V}_{ac1} = 13.153$; $\hat{H}_o = 0.53, P_{\mathrm{wh1}} = 1.85$ bar and different values of μ

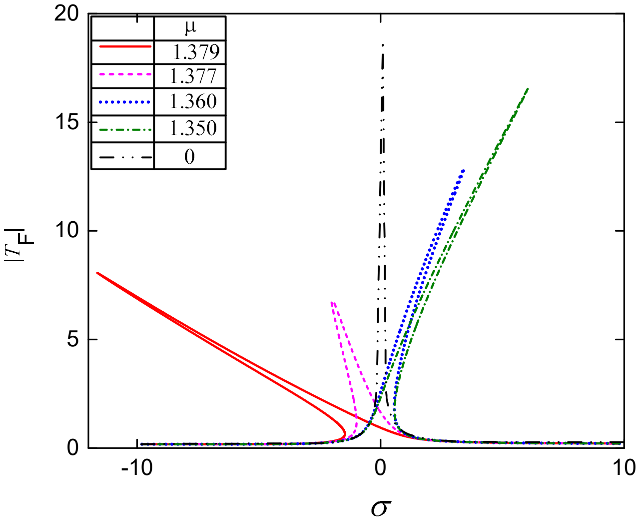

Fig. 5.31. Force transmissibility of the QSAVIM using PC for various values of μ and the same other parameters as in Fig. 5.30

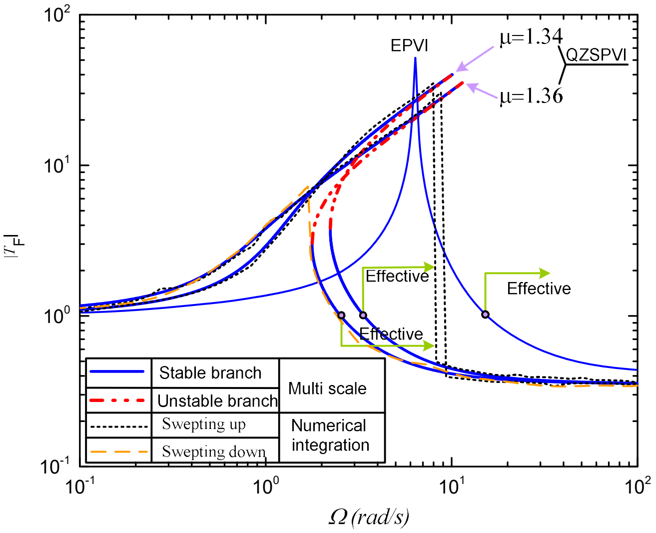

Fig.5.32. Comparing force transmissibility of the QSAVIM using PC and ETVIM for various values of μ and the same other parameters as in Fig. 5.30 (the details of types of lines are presented in panel)

As analyzed above, the amplitude-frequency response of the proposed system can be soft or hard depending on the peak frequency σ_p. Indeed, this value is negative corresponding to the response curve bending to the left. Oppositely, the bending to the right is appeared for the positive value of σ_p. Fig. 5.33 shows the influence of the pressure ratio on the peak frequency of the QSAVIM using PC for the same parameters as in Fig. 5.30. It is interesting to see that if the pressure ratio is larger than 1.376, the value of σ_p is negative, indicating that the response curve is bended to the left as confirmed in Fig. 5.31 meanwhile the bending of the curve to the right is occurred for $\mu<1.376$ due to $\sigma_p>0$.

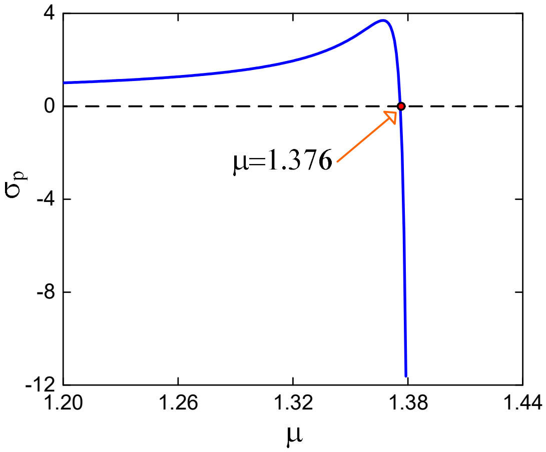

Fig.5.33. Effect of the pressure ratio on the peak frequency σ_p of the QSAVIM using PC for the same parameters as in Fig.5.30

The relation of the pressure ratio and volume of the auxiliary chamber of the load bearing mechanism for which the minimum stiffness of the QSAVIM using PC will be nearly equal to zero in the working region is determined by setting $\hat{K}_s$=0 in Eq. (5.27) while the other parameters are the same as in the first case. The result is depicted in Fig. 5.34, it can be seen that the pressure ratio is reduced in accordance with the increase in the volume. Namely, if the dimensionless volume of the auxiliary chamber of the load bearing mechanism is set at the values 7.892; 14.460; 18.814; 24.992; 39.453; 47.358, the dynamic stiffness curve is plotted in Fig. 5.35. It is noteworthy to see that the asymmetry of the system around the equilibrium position is reduced according to the increase in the volume of the auxiliary tank, indicating that the position at which the dynamic stiffness is quasi-zero moves towards the equilibrium position.

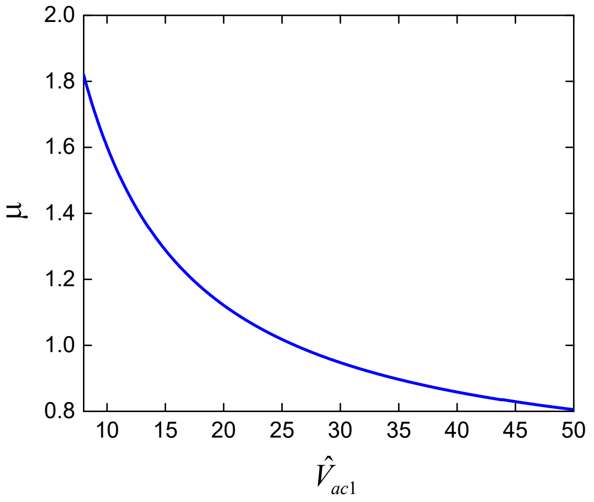

Fig.5.34. The relation of pressure ratio versus the auxiliary chamber volume, the same other parameters as in the first case

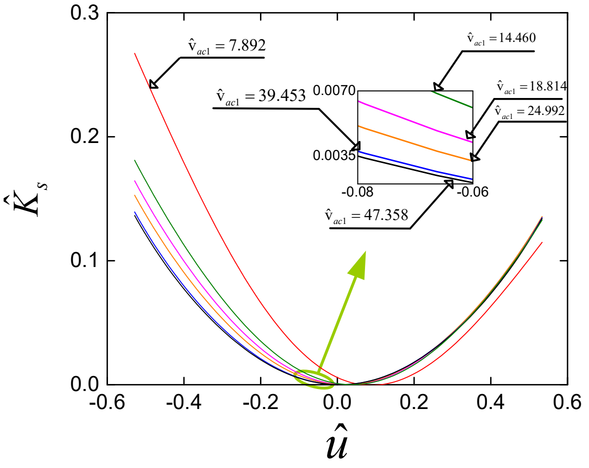

Fig.5.35. The dynamic stiffness curve of the QSAVIM using PC for the different values of the auxiliary chamber volume as annotated in figure meanwhile the pressure ratio is calculated as in Fig.5.30.

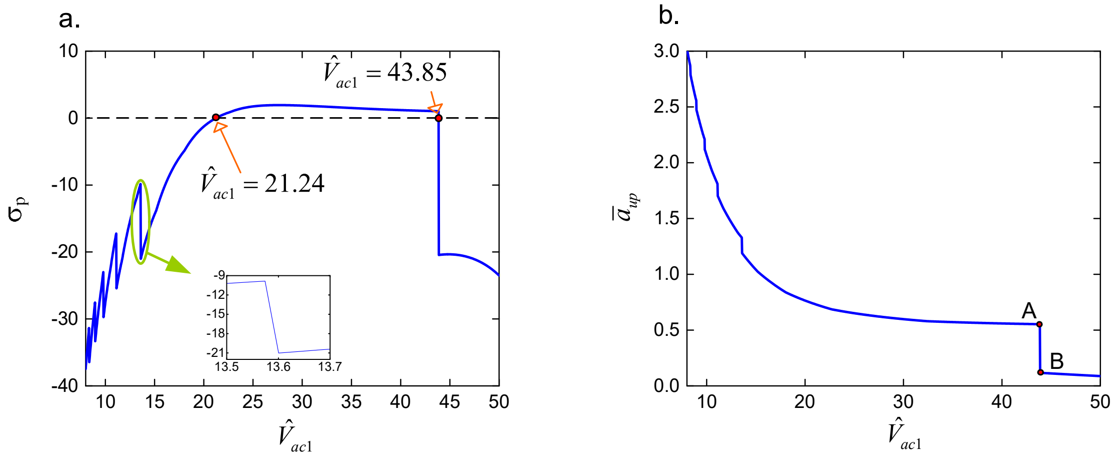

Fig.5.36. The peak frequency curve (a) and peak amplitude curve (b) of the QSAVIM using PC for the same parameters as in Fig.5.35

In this case, the peak frequency and amplitude curves with respect to the auxiliary chamber volume of the QSAVIM using PC having the dynamic stiffness curves shown in Fig.5.35 are presented in Fig.5.36. It can be seen that if the dimensionless volume of the auxiliary chamber is larger than 21.24 and smaller than 43.85 the value of σ_p is positive but this value is negative for the volume of auxiliary chamber is out of this range as shown in Fig.5.36(a). Besides, increasing the auxiliary chamber volume will lead to a lessening in the peak amplitude as observed in Fig.5.36(b) while this may be no appearance of the peak frequency. For instance, with $\hat{V}_{ac1} = 13.5$ the value of σ_p is around -10.5 but if $\hat{V}_{ac1} = 13.6$ this value is nearly equal to -21. Furthermore, as the dimensionless volume of the auxiliary chamber is changed from 43.83 (at point A) to 43.88 (at point B) the value of σ_p is changed suddenly from positive to negative, simultaneously, the peak amplitude is decreased remarkably. In addition, it is essential to note that increasing the auxiliary chamber volume will extend the region isolation toward low frequency as shown in Fig. 5.37. This result proves that improving the symmetric of the stiffness curve will increase the effectiveness of suppressing the force transmissibility from the load plate to the base.

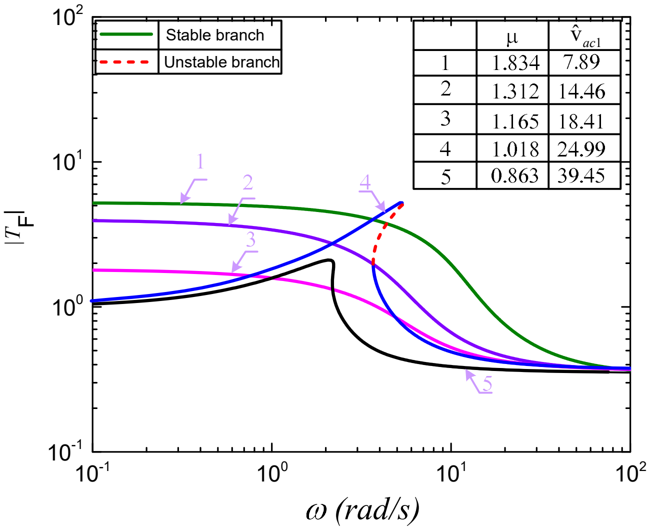

Fig. 5.37. Force transmissibility of the QSAVIM using PC for various values of $\hat{V}_{ac1}$ including 7.89; 14.46, 18.41 and 24.99; 39.45; the same other parameters as in Fig.5.36.

The effect of nonlinearity in dynamic characteristic, the amplitude-frequency curve can be bended as analyzed above, which indicates the appearance of the down (J_D) and up (J_U) jump frequency as expressed in Fig.5.38. Herein, the values of μ and $\hat{V}_{ac1}$ are given in left-top corner panel, the other parameters are the same as in Fig.5.35. The points on the response curve lying between J_D and J_U are unstable solutions because these points are in the unstable region calculated by Eq. (5.76**).** When the down jump frequency which is also the peak frequency σ_p moves closely to zero, the phenomenon of the frequency jump may be neglected, meaning that all points on the amplitude-frequency curve are stable as numerically simulated by the dashed line in Fig.5.39. Likewise, the stable branches of the proposed model with various values of μ and $\hat{V}_{ac1}$ are denoted in Figs. 5.32 and 5.37. The detailed annotation for line types is presented in the lower-left and upper-left corner of these figures.

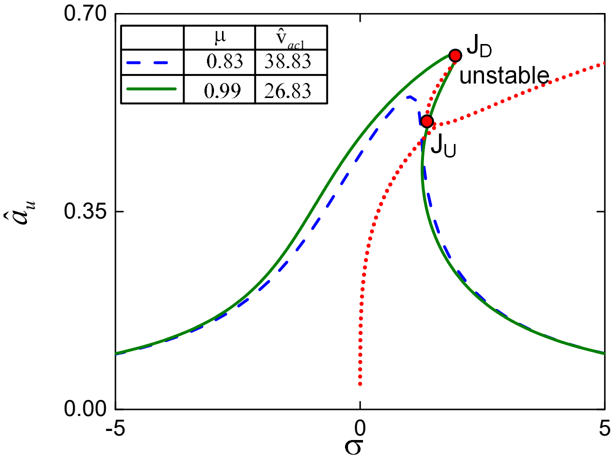

Fig.5.38. The stability of the response curve

5.8.2. Complex dynamic analysis.

Because of the nonlinear dynamic characteristic as well as the existing of the relative sliding between the piston and cylinder, thus it is necessary to analyze the complex behavior of the proposed system.

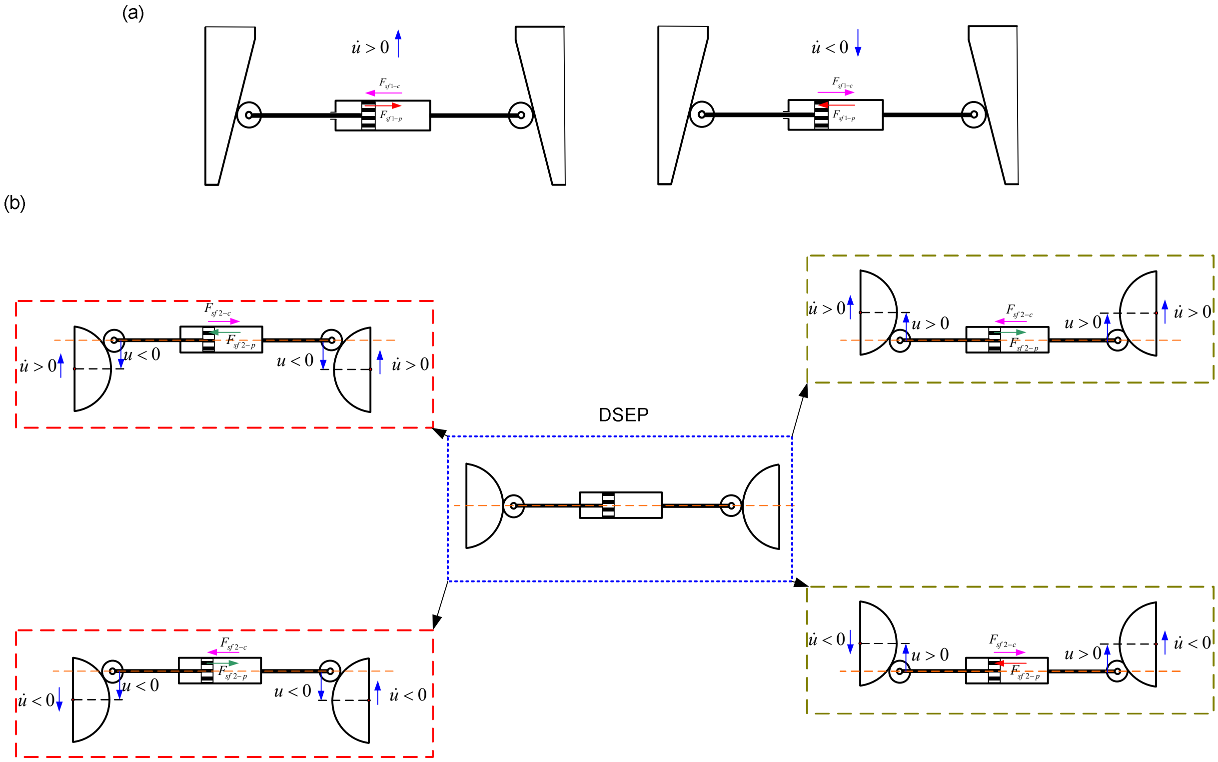

Fig. 5.39. Sliding friction under various states

As known, as there is a relative sliding between piston and cylinder, it will occur the sliding friction as shown in Fig. 5.39. Herein, it is noteworthy that $F_{\text{sf-c}}$ and $F_{\text{sf-p}}$ are the frictional forces inserting the cylinder and piston and the denotation of "1" and "2" are representation of the cylinders 1 and 2, respectively. We have:

$$\begin{aligned} F_{sf1-c} &= F_{sf1-p} = \left|F_{sf1}\right| sign(\dot{u}) \\ F_{sf2-c} &= F_{sf2-p} = \left|F_{sf2}\right| sign(\dot{u}u) \end{aligned} \tag{5.83}$$

in which F_{sf} is calculated by Eq. (5.8)

From this analysis, Fig. 5.40 shows the free body diagram of the system which is subjected to the sliding friction and excited force $f_e = F_e\cos(\omega t)$ with the force amplitude of F_e and frequency of ω.

Consider virtual displacement δu, the virtual works done by these forces become

$$\sum \delta W = \left(F_{sf1-p} + F_{sf1-p}\right)\delta x_1 + \left(F_{sf2-p} + F_{sf2-p}\right)\delta x_2 - Mg\delta u + f_e\delta u \tag{5.84}$$

herein, δx_1 and δx_2 are the corresponding virtual displacements of the piston 1 and 2. These are the same as the virtual displacements of the center of the rollers 2 and 3 as defined in Fig. 4.9(b).

Applying Eq. (4.22), (4.27) and (5.83), Eq. (5.84) can be recast, by

$$\sum \delta W = -\left(2\left|F_{sf2}\right| \mathrm{s}i\,\mathrm{gn}(u\dot{u}) \frac{u}{\sqrt{\left(R+r\right)^2 - u^2}} + 2\left|F_{sf1}\right| \mathrm{s}i\,\mathrm{gn}(\dot{u}) \tan\alpha + Mg - f_e \right)\delta u \tag{5.85}$$

Accordingly, the generalized force in the direction of the relative coordinate u is obtained as below:

$$Q = f_e - \left(2\left|F_{sf2}\right| \mathrm{s}i\,\mathrm{gn}(u\dot{u}) \frac{u}{\sqrt{\left(R+r\right)^2 - u^2}} + 2\left|F_{sf1}\right| \mathrm{s}i\,\mathrm{gn}(\dot{u}) \tan\alpha + Mg \right) \tag{5.86}$$

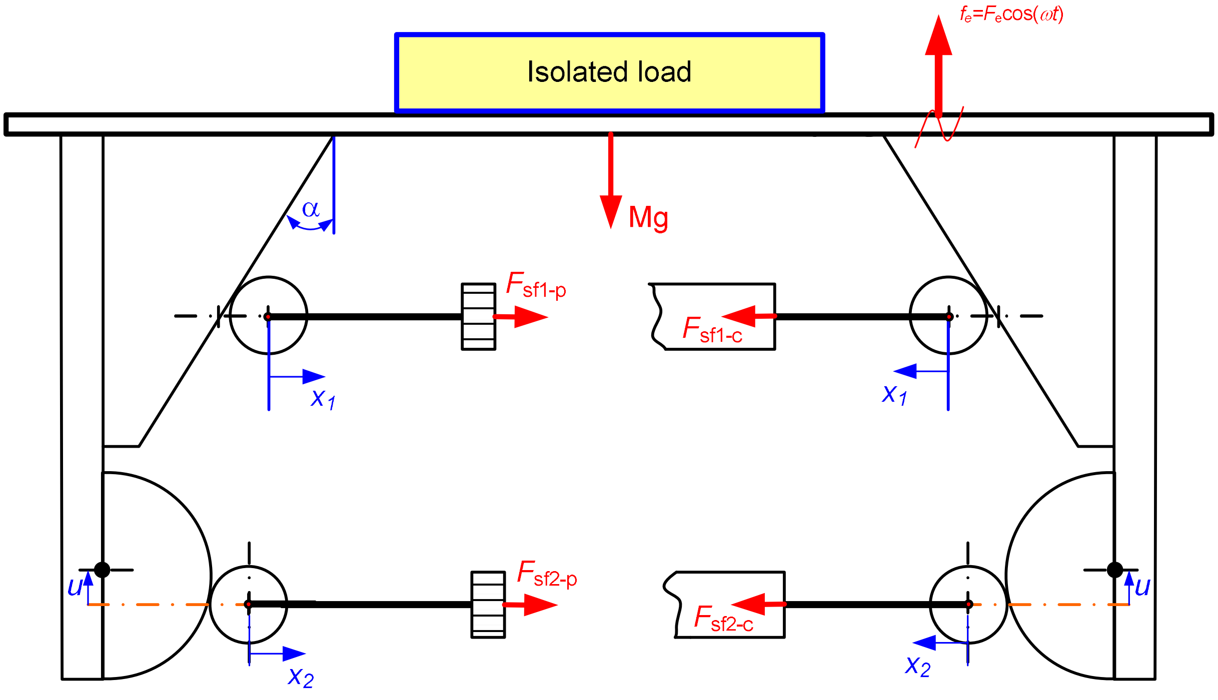

Fig. 5.40. External forces acting on the system

The potential energy: $P_e = \int_0^{\Delta L} F_S d\Delta L$ (5.87)

with F_s is determined by Eq. (5.19)

The kinetic energy and dissipation function are the same as in Eq. (4.38) and (5.42), respectively.

Now, substituting Eqs. (4.38, 5.42, 5.86, 5.87) into Eq. (4.43), we obtain the dynamic equation, by

$$M\ddot{z}+c\dot{z}-F_s+2F_{sf1}\,\mathrm{sign}(\dot{u})\tan\alpha+2F_{sf2}\,\mathrm{sign}(u\dot{u})\frac{u}{\sqrt{(R+r)^2-u^2}}+Mg=F_e\cos(\omega t)$$

(5.88)

Or through Eq. (4.41) that z_e is deleted, the dynamic equation is written in relative coordinate u as:

$$M\ddot{u}+c\dot{u}-F_s+2F_{sf1}\,\mathrm{sign}(\dot{u})\tan\alpha+2F_{sf2}\,\mathrm{sign}(u\dot{u})\frac{u}{\sqrt{(R+r)^2-u^2}}+Mg=F_e\cos(\omega t) \quad (5.89)$$

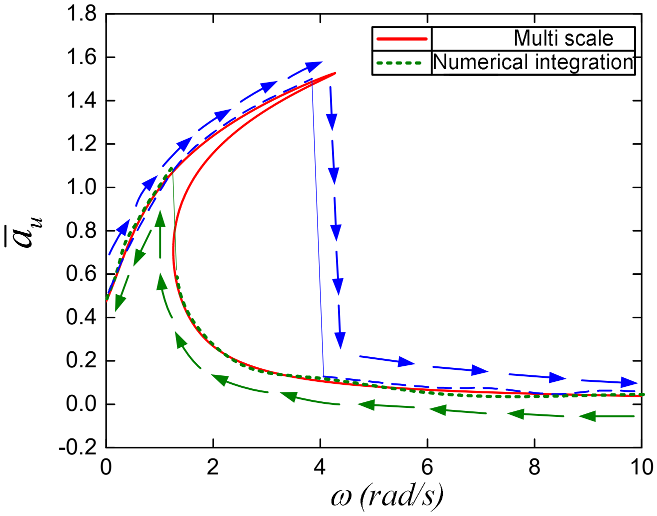

Fig. 5.41. Multi-scale method compared with numerical integration

First of all, the amplitude-frequency curves obtained by Multi-scale method and fourth-order Runge-Kutta algorithm are compared as shown in Fig. 5.41. Herein, the frequency of the excited force is swept up slowly from 0 to 10 rad/s (denoted by the dashed line). In contract to reducing slowly frequency 10 rad/s to 0, the amplitude-frequency curve is exhibited by the dot line. It can be seen that although at the down jump point, there is a difference between two methods due to approximate error and exiting sliding friction between the piston and cylinder, two curves are still in good agreement.

Next, the complex behavior of the proposed system will be investigated through the numerical integration for Eq. (5.89) using a fourth-order Runge-Kutta algorithm with the various initial conditions including velocity and position. The bifurcation diagram of Eq. (5.89) for $\hat{V}_{ac1}=7.89$, μ=1.834, ω changed from 1 to 10 rad/s and the same other parameters as in Fig.5.30. The value of u is determined by using Poincare map with the period T=2π/ω. The simulated result is plotted in Fig. 5.42. It can be seen that if the initial condition is zero for both of the position and velocity, the dynamic response of the system (denoted by filled circles) will be period-2 oscillation as the excited frequency is within 2.2-2.6 rad/s but out of this range the solution is period-1 periodic. Meanwhile, the response marked by squares is realized by sweeping the parameter ω from 1 to 10 rad/s, for which the initial position and velocity are set at zero only for the first parameter ω and the final state of the system will be considered as the initial condition for the next value of ω. In this case, the oscillation transformed from period-1 to period-3 periodic is occurred with ω around of 4 and 8 rad/s. Hence, it revealed from this figure that depending on the initial condition the dynamic response of the system can be bifurcated at A (1.9 rad/s), B (2.8 rad/s) and C (4 rad/s), meaning that the parameter ω<1.9, there only exists a period-1 solution, but 1.9<ω<2.8 two cases for two period-1 or period-2 solutions may be appeared. But if the parameter is within B and C, there are two cases for period-1 periodic oscillation, after C the dynamic behavior of the system can be period-1 or period-3 solution.

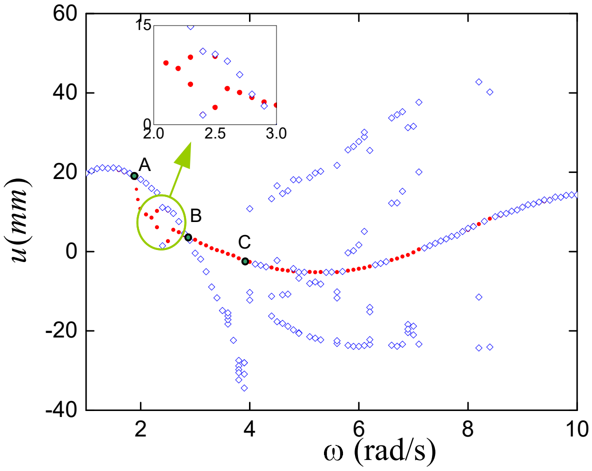

Fig.5.42. Bifurcation diagram of Eq. (5.89) for $\hat{V}_{ac1} = 7.89$, μ=1.834, ω changed from 1 to 10 rad/s

Furthermore, in order to obtain the solution of the dynamic response, the family of the initial conditions named the attractor-basin phase portrait affecting on the dynamic response will be detected in three cases following. In the 1st study case, the parameter ω is taken account into at value of 2.4 rad/s, simultaneously other parameters are set as in Fig.5.42. As shown in Fig.5.42, it can be seen that it may exist the period-1 or period-2 solution depending on the initial condition. It is interesting to see that in the attraction basin depicted in Fig.5.43, the attractor region of the period-1 oscillation is greater than that of the period-2 one. This means that the ability to obtain period-1 steady dynamic response is higher. Additionally, the vibration ability of the period-1 oscillation plotted in Fig. 5.44 (b) is higher than that of period-2 one depicted in Fig.5.44 (a) in which the initial position and velocity of the first solution is zero but the second one is obtained for $u_o = 20$ mm and $\dot{u}_o = 0.2$ m/s, meanwhile the fixed points calculated by Poincare section are annotated by filled circles.

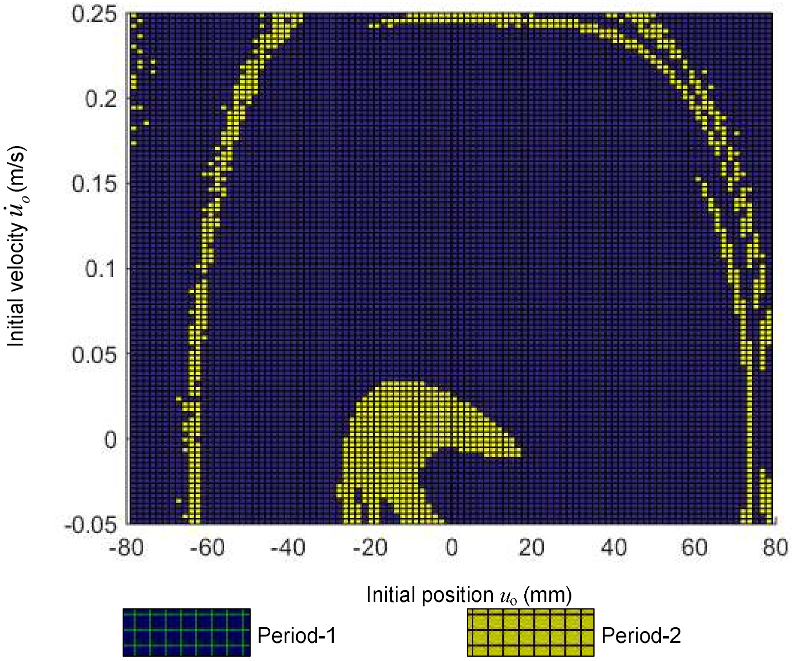

Fig.5.43. Attractor-basin phase portrait for ω=2.4 rad/s, other parameters set as in Fig.5.42

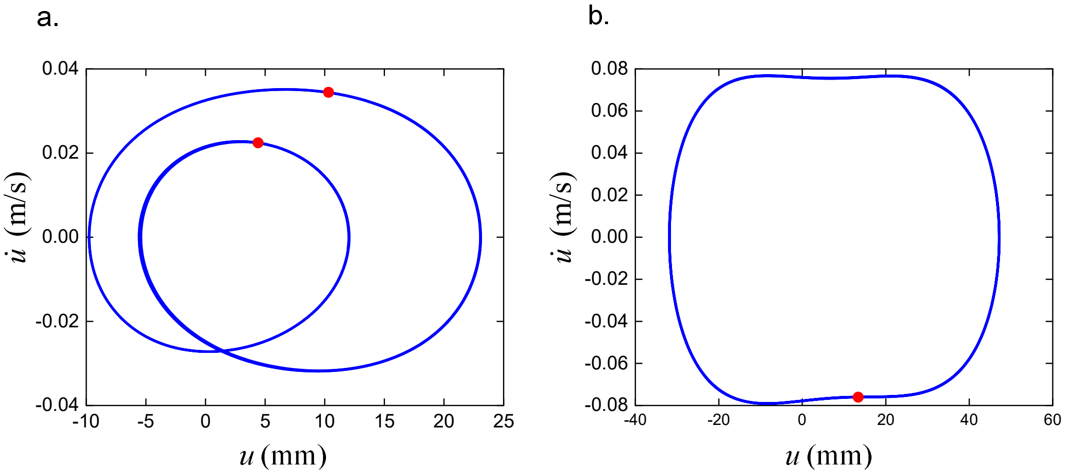

Fig.5.44. Phase orbit of Eq. (5.89) for ω=2.4 rad/s and $u_o = 0$ and $\dot{u}_o = 0$ (a)

$u_o = 20$ mm and $\dot{u}_o = 0.2$ m/s (b)

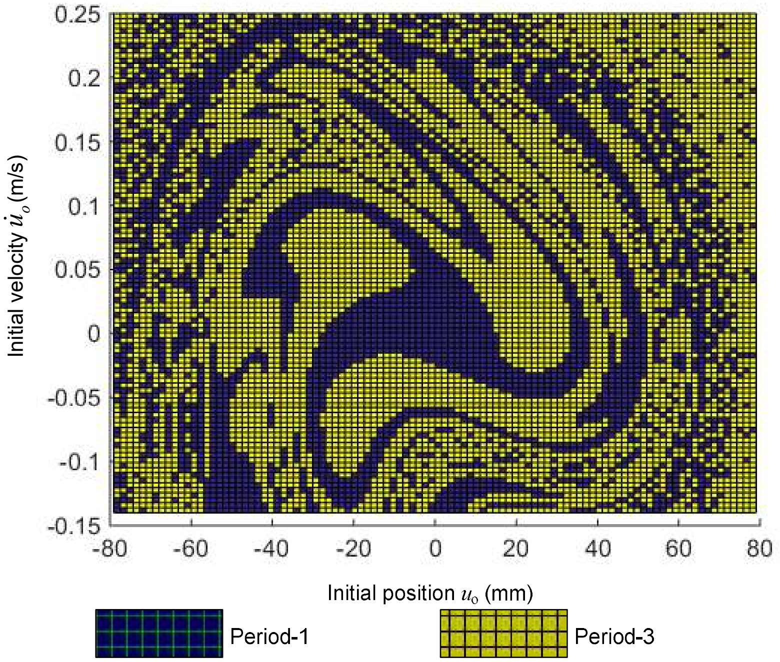

Fig. 5.45. Attraction basin for *ω*=6rad/s and the same other parameters as in Fig. 5.42

In the 2nd study case, suppose that ω=6rad/s and other parameters are not changed. In this case, the dynamic response of the QSAVIM using PC can be period-1 or period-3 solution. As depicted in Fig.5.45, the possibility of appearing the period-1 steady response is reduced because the region of attractors for which the period-1 solution is occurred is narrower than that in the 1st case. Furthermore, in this case as shown in Fig.5.46 (the detailed annotation of line types is presented in right-top corner panel of each figure), the vibration level of the period-1 solution (Fig. 5.46(b)) is lower than that of period-3 one (Fig. 5.46(a)). Both solutions also revealed that the vibration of the system occurs at a position which is drifted away from the equilibrium position (*u*=0).

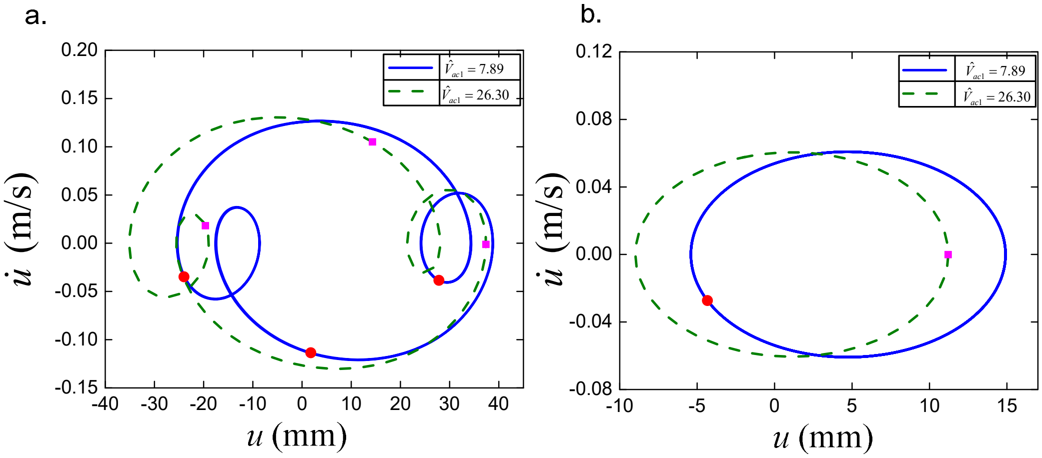

Fig. 5.46. The phase orbits of the system for $\hat{V}_{ac1} = 7.89;\ 26.30$ and

$u_o = -20$ mm and $\dot{u}_o = -0.05$ m/s (a); $u_o = 0$ and $\dot{u}_o = 0$ (b)

In the 3rd study case, the dimensionless volume of the auxiliary chamber is increased to the value of 26.30 but other parameters and frequency are the same as in the 2nd case. To guarantee that the minimum stiffness is nearly zero, the pressure ratio is calculated at value of 0.997. The result is that the area of the period-1 solution is expanded compared with the second case as shown in Fig.5.47. Similar to the 2nd case, the amplitude and velocity of the period-1 solution are reduced compared with the period-3 oscillation as shown in Fig.5.46 in which the phase orbits are drawn by the dashed line meanwhile the fixed point is annotated by square. This case confirms that the position at which the load plate oscillates around was moved to the equilibrium position.

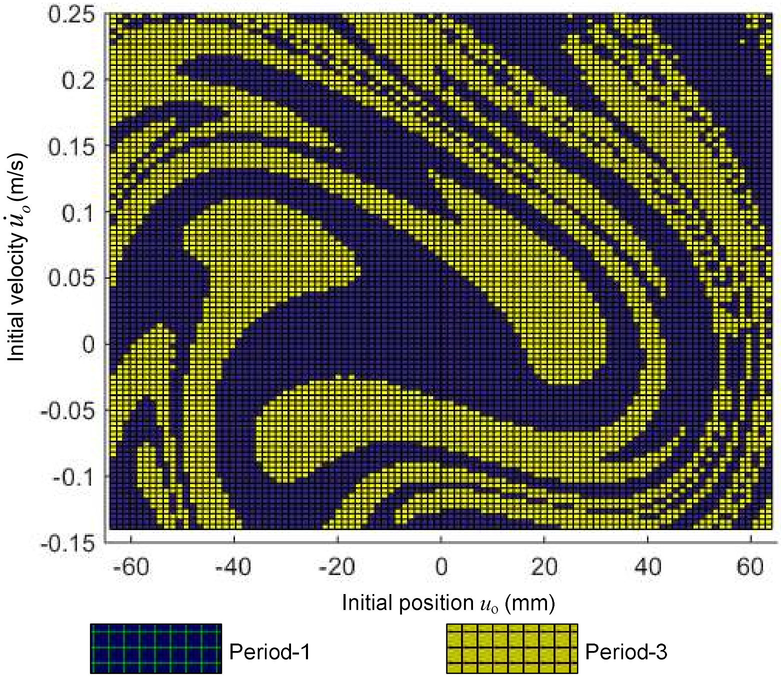

Fig.5.47. Attraction basin for ω=6rad/s, μ=0.997 and $\hat{V}_{ac1} = 26.30$ the same other parameters as in Fig.5.42

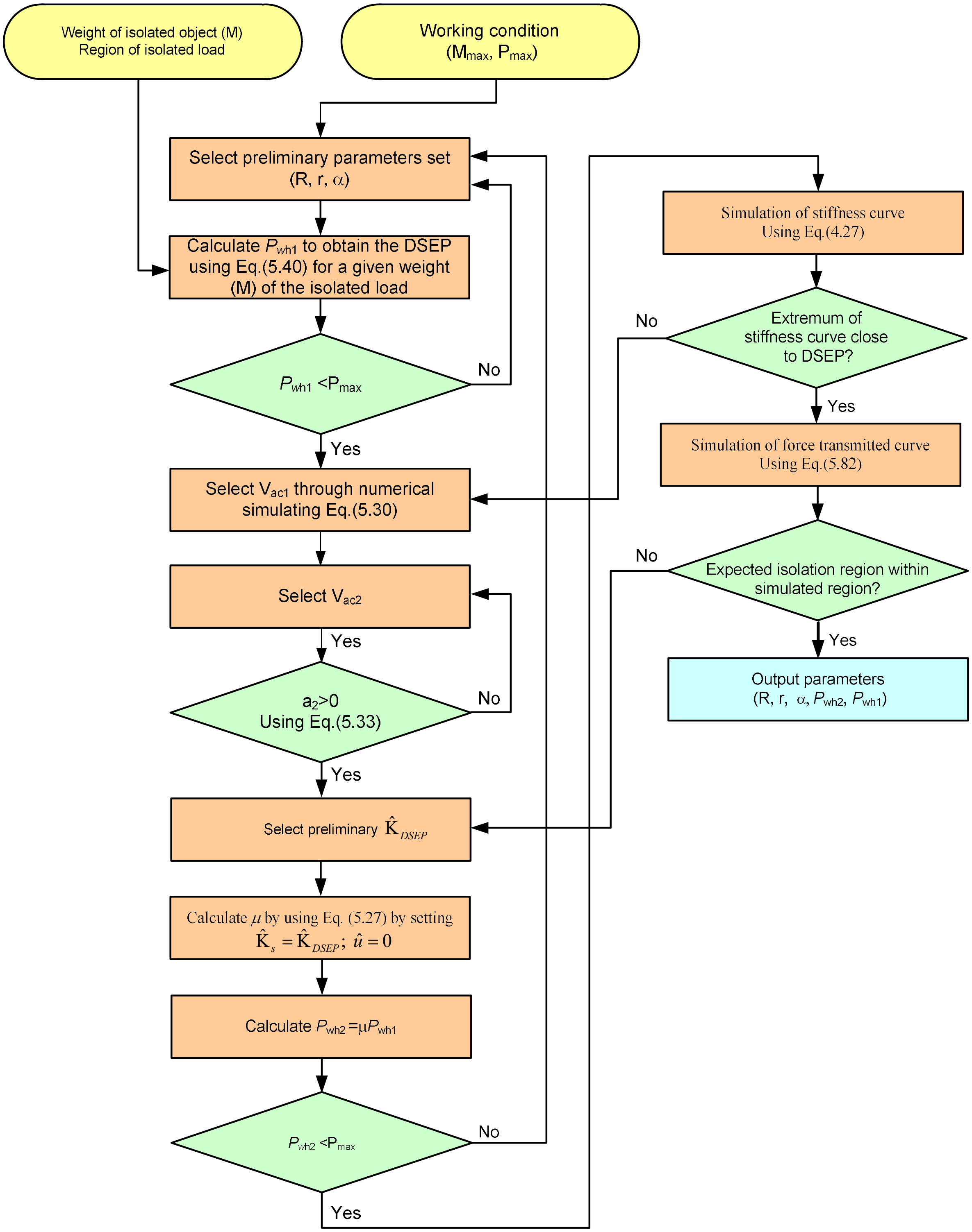

Fig. 5. 48. Flow chart for designing the QSAVIM using PC

In summary, from these analysis results, it indicates that the stiffness curve of the system is asymmetrical around the DSEP, meaning that the extremum of the stiffness curve is not at DSEP. The level of the asymmetry depends on the auxiliary tank volume of the LBM. The symmetry of the stiffness curve will be improved according to increasing this volume. In addition, the QSAVIM using PC having asymmetrical stiffness curve will give the lower isolation effectiveness than the one with symmetrical stiffness curve. Thus, as the QSAVIM using PC is designed, the volume of the LBM should be selected so that the extremum of the stiffness curve is closed to the DSEP. The design procedure is shown in detail in Fig. 5.48

SUMMARY OF CHAPTER 5

This chapter introduced a modified model of QSAVIM in which the pneumatic cylinder connecting with an auxiliary tank is introduced as a non-steel elastic element. The stiffness of the pneumatic cylinder and sliding frictional force generated by relative motion between the cylinder and piston were built and verified through the virtual prototyping technology. Following this analysis, the dynamic stiffness of the LBM, SCM and QSAVIM using PC was analyzed and numerically simulated. The results revealed that the stiffness of the load bearing mechanism is an asymmetrical curve around the DSEP, whose asymmetrical level will be reduced according to the increase in the volume of the auxiliary chamber. Oppositely, the stiffness curve of the stiffness corrected mechanism always has parabolic form with the vertex at the DSEP regardless of the volume of the auxiliary tank. However, concave or convex form depends on the pressure and volume of air inside the cylinder and auxiliary chamber. On the aspect of vibration isolation, the parameters of the system should be calculated so that the stiffness curve of the SCM is a concave parabola. Due to connecting between LBM and SCM in parallel, resultant stiffness of the QSAVIM using PC is also an asymmetrical curve around the DSEP, meaning that the QSAVIM using a PC cannot attain the lowest stiffness value at the DSEP. Similar to the LBM, the asymmetry of the stiffness curve will be reduced along with growing the volume of the auxiliary chamber. Then, the analysis of equilibrium position and the procedure for designing the QSAVIM using PC having the lowest stiffness value around the DSEP investigated and suggested.

The fundamental resonance response and force transmissibility of the QSAVIM using PC subjected to the externally harmonic force is analyzed through Multi-Scale method and the numerical simulations are verified. The simulation indicated that because of the effect of asymmetrical stiffness curve, the QSAVIM using PC can be a soft or hard system depending on the auxiliary chamber volume and pressure. It also confirmed that the lower the dynamic stiffness is, the larger the effective isolation region is and the better the isolation effectiveness is. Especially, the lower the asymmetry level of the stiffness curve is, the more the effectiveness of suppressing the force transmissibility from the load plate to the base is improved. Additionally, parameter bifurcation analysis of the QSAVIM using PC had been realized through numerical integration from the original dynamic equation. Simultaneously, fixed points had been also calculated by using Poincare map. The result proved that the system can occur period-1, period-2 or period-3 oscillation depending on the initial conditions.

CHAPTER 6

CONCLUSIONS AND FUTURE WORKS

6.1 Conclusion

This thesis gives a comprehensive understanding as well as a guidance of designing a QZS isolator using rubber air springs or pneumatic cylinders to prevent the unwanted effects of low frequency vibrations (≥32 rad/s) to the isolated object. This is frequency region in which it can be a challenge for the traditional isolation method. The proposed model offers a potential application and effectiveness in vibration isolation fields, especially low frequency domain. Indeed, the proposed model can be supposed including the suspension for vehicles, isolation seats to improve the comfort as well as to guarantee healthy and working efficient when the divers or passengers sit or work on the ground moving vehicles which are subjected to low excitation frequencies, mounts for machineries or equipment sensitizing vibration.

The advantage of the QZS vibration isolation method motivates development of an innovative QZS vibration isolation structure employing the conceptual design of the wedge and cam mechanism. Different from other studies relating quasi-zero stiffness isolation system, in this thesis, the non-steel elastic elements including rubber air springs or pneumatic cylinders were employed to replace steel or magnetic elastic elements. A key merit of the innovative model is that the stiffness of the load bearing and the stiffness corrected mechanism can be easily adjusted according to the change of the isolated load so that the system can always remain the wanted low stiffness value at the DSEP. Hence, the proposed model can overcome the conflict between the stiffness and the load bearing capacity, meaning that although having low stiffness, the load ability and static deformation of the proposed model are still maintained. Meanwhile, it is not easy for the traditional isolation method to surmount this contradiction. Especially, the proposed model can be fabricated and applied certainly in Viet Nam. The study result proved that the adjustment of the stiffness of both mechanisms is realized easily through controlling the air pressure in the air spring. In addition, the operation of the proposed model can be easily transferred from passive into active state to obtain the wanted isolation response. Whilst, it is very difficult for the quasi-zero stiffness vibration isolator using mechanical springs to realize this mission.

Specifically, the result of this study obtained as following:

1. A QZS vibration isolation model using rubber air springs

The physical parameters such as effective area and volume of a commercial rubber air spring were built and identified experimental. Then, the restoring force model as well as stiffness of the air spring due to compressed air was obtained. Moreover, because of inheritance of the rubber material which includes the friction between reinforce fiber and rubber, and viscoelasticity, the hysteresis curve of the rubber air spring was also identified experimentally through Berg's model and fractional Kelvin-Voigt's model. The result confirmed that model of the rubber air spring contributed by compressed air, friction, and viscoelasticity follows well the experimental data.

Based on the result obtained from rubber air spring model, the stiffness equation of the QSAVIM was established. Then numerical simulation of the stiffness curve was realized meaning that the stiffness curves is a symmetrical concave parabola around the DSEP. Over expected working range, the dynamic stiffness of the QSAVIM is lower than that of the ETVIM. The pressure ratio, that is the pressure ratio of the load bearing mechanism to the stiffness corrected one, is obtained, indicating that the dynamic stiffness of the QSAVIM is increased according to the growth of the pressure ratio. Thank to this relation, the pressure of both mechanisms can be easily adjusted so that the quasi-zero dynamics stiffness of the proposed system is always remained at the

DSEP as there is a change of the isolated weight. From that, a procedure for designing QSAVIM was set up.

The dynamic equation of the QSAVIM subjected to a harmonic excitation from the base frame was analyzed and built. Based on the approximate analytical method, the amplitude-frequency relation was then drawn. Simultaneously, an important index, which is used to assess the isolated effectiveness, was also defined and attained that is the vibration transmissibility. The numerical simulation revealed that the curve of vibration transmissibility as well as the amplitude-frequency is bended to the right, appearing the frequency of down and up jump and within this frequency, it can exist multiple solutions including resonant and non-resonant one. The frequency region of down and up jump can be narrowed according to increasing the pressure ratio simultaneously the isolated range is broadened toward low frequency, which is meaningful that resonance peak including frequency and amplitude will be reduced. Furthermore, the complex dynamic response of the QSAVIM was discovered, indicating that within frequency occurring multiple solutions, the initial condition comprising the position and velocity will decide which solution can be existed in the steady state. Additionally, the bifurcation phenomenon from period-1 to multi period solution and vice versa is seen as the isolated weight is larger or smaller than the optimal one for which the system can attain the DSEP. This thesis proved the isolated effectiveness of the QSAVIM much better than that of the ETVIM.

In order to assess the theoretical model of the QSAVIM as well as compare isolation effectiveness of the proposed model and ETVIM. The prototype of the QSAVIM and ETVIM was fabricated. The experimental apparatus was then set up. The experimental results confirm the good effect of the stiffness corrected mechanism on the isolation response as well as prove the analysis model of the QSAVIM that is the expansion of the isolation frequency region according to the increase of the pressure ratio. The experiment asserted again the advantage of the QSAVIM against the ETVIM. Indeed, the obtained result is that the proposed model can presented the attenuation of vibration transmission from the source to the isolated object in frequency region larger than 31.5 rad/s (5Hz)

2. A QZS vibration isolation model using pneumatic cylinders

To show comprehensively the quasi-zero stiffness vibration isolation model using air springs, in this thesis, the pneumatic cylinders connecting auxiliary tanks were also considered as elastic elements. First of all, the stiffness model of the pneumatic cylinder was obtained by the analysis solution based on thermodynamic equation and ideal gas. The sliding friction between the piston and cylinder was then taken into account. Instead of experiment, this thesis utilized the development of software technology and virtual prototyping technique. Particularly, a virtual model of the pneumatic cylinder adding an auxiliary tank was built to evaluate the analysis model of the pneumatic cylinder and identify the sliding frictional model. The result of the virtual simulation confirmed the accepted accuracy of the analysis model.

Next, the stiffness model of the load bearing mechanism (LBM) using the pneumatic cylinder adding the auxiliary tank was drawn and analyzed. The simulation result shown clearly that the stiffness of this mechanism is not a constant value that it will be changed with respect to the position of the load plate. Moreover, it is a nonlinear and asymmetric curve around the DSEP. The asymmetry and nonlinearity will be reduced in accordance with the increase in the volume of the cylinder adding auxiliary tank. This means that when this volume is large enough, the slope of the stiffness curve is very small. Then, stiffness model of the stiffness corrected mechanism (SCM) using the pneumatic cylinders adding auxiliary tanks was also obtained. Unlike stiffness curve form of the LBM, the stiffness curve of the SCM is always a symmetric parabola round the DSEP. This parabola can be concave or convex depending on the volume of the cylinder connecting tank. The analysis result indicated that when the auxiliary volume is increased from zero to a critical value, the stiffness curve of the SCM is changed from concave parabola into convex one. In terms of isolation, the stiffness curve of the SCM should be concave form. From these analyses, the resultant stiffness of the QSAVIM was simulated, showing that the asymmetry of the stiffness curve around the DSEP will be reduced according to the increase in the auxiliary tank volume of the LBM. This implies that the position at which the QSAVIM has the smallest stiffness value will be asymptotic to the DSEP as the auxiliary chamber volume is increased

Dynamic response of the QSAVIM was analyzed in the case in which the load plate is excited by a harmonic force. By approximated analytical method, the force transmissibility around the primary resonance of the system was attained and simulated numerically. The result confirmed that the curve of the force transmissibility may be bended to left or right corresponding to soft or hard system, respectively. The bending depends on the pressure ratio. Addition, this study revealed that the same lowest stiffness value, the more the stiffness curve is symmetrical, the more the vibration isolation region is enlarged. Furthermore, the effects of the sliding friction between the piston and cylinder on the complex dynamic response of the system were taken into account. The simulated result confirmed that this effect is unremarkable. Simultaneously, these study results proved the significant effectiveness of the QSAVIM to prevent the force transmissibility from the load plate to the base frame.

6.2 Future works:

Although the proposed model can improve the isolation effectiveness in low frequency region, the isolation performance of the system is still limited. Because

1. Resonance peak is still high
2. Due to passive isolation model, the isolation capacity is still lower than the desirable response.

The next studies will be realized contents as following:

- Studying the damping methods to reduce peak frequency
- Studying control algorithms to improve the isolation performance

Published papers

International Journal

1. **N.Y.P Vo** and T.D. Le**,** “Adaptive pneumatic vibration isolation platform”, *Mechanical Systems and Signal processing*, 133,106258, 2019. (ISI, Q1, IF=6.832, H-index=167).
   https://doi.org/10.1016/j.ymssp.2019.106258
2. **Ngoc Yen Phuong Vo** and Thanh Danh Le, “Static analysis of low frequency Isolation model using pneumatic cylinder with auxiliary chamber,” *International Journal of Precision Engineering and Manufacturing,* 21, pp. 681-697, 2020. (ISI, Q2, IF=2.106, H-index=50).
   DOI: 10.1007/s12541-019-00301-y
3. **N. Y. P. Vo**, T. D. Le, “Analytical study of a pneumatic vibration isolation platform featuring adjustable stiffness”, *Journal of Commun Nonlinear Sci Numer Simulat*, 98, 105775, 2021 (ISI, Q1, IF=4.26, H-index=113).
   https://doi.org/10.1016/j.cnsns.2021.105775
4. **Ngoc Yen Phuong Vo** and Thanh Danh Le**, “**Dynamic analysis of quasi-zero stiffness pneumatic vibration isolator”, *Applied Science, 12, 2378, 2022,* (ISI, Q2, IF=2.679, H-index=52).
   https://doi.org/10.3390/app12052719
5. **N.Y.P Vo,** M.K. Nguyen and T.D. Le, “Dynamic Stiffness Analysis of a Nonlinear Vibration Isolation Model with Asymmetrical and Quasi-Zero Stiffness Characteristics”, *Journal of Polimesin*, 19, pp. 7-15, 2021. (IF=0.65).
   http://e-jurnal.pnl.ac.id/polimesin/article/view/1956.

6. **N. Y. P. Vo,** T. D. Le, "Analysis model of restoring force of a rubber air spring" *Journal of Vibroengineering*, 23, pp. 1138-1147, 2021 (ESCI-Scopus, IF=0.83, H-index=26).
   https://doi.org/10.21595/jve.2021.21889

International Conference

7. **N.Y.P Vo** and T.D. Le**, "**Modeling and Simulation of low frequency vibration isolation table," *Proceeding of the First Conference on Material, Machines and Methods of sustainable Development*, 2018.
8. **N.Y.P Vo** and T.D. Le**, "**Effects of configuration parameters on the dynamic stiffness and stability of pneumatic vibration isolation model,"*International Conference on Fluid Machinery and Automation System*,2018
9. **N.Y.P Vo**, M.K. Nguyen and T.D. Le**,"**Study on Vibration Transmissibility Characteristic of a novel asymmetric nonlinear model using pneumatic spring,"*IEEE International Conference on System Science and Engineering*, 2019.
10. **N.Y.P Vo**, M.K. Nguyen and T.D. Le**,** "Identification of friction force model of a pneumatic cylinder" *IEEE International Conference on System Science and Engineering*, August 27-28,2021.

National Journal

11. **N.Y.P Vo**,M.K. Nguyen, T.D. Le, "Dynamic stiffness analysis and isolation effectiveness of vibration isolation platform using pneumatic spring with auxiliary chamber,"*Journal of Technical education science*, 2019.

Research project

12. **Vo Ngoc Yen Phuong (Principal investigator),** Nguyen Minh Ky, Le Thanh Danh, "Dynamic analysis of nonlinear asymmetric vibration isolator,"*The*

project grant No: T2020-05NCS funded by Ho Chi Minh City University of Technology and Education, (Completed:2021)

Reference

[1] O. Thuong and M.J. Griffin. The vibration discomfort of standing persons: the effect of body supports. *Journal of Rail and Rapid Transit*, 225 (2), 228-235, 2011.

[2] O. Thuong and M.J. Griffin. The vibration discomfort of standing persons: 0.5-16-Hz fore-and-aft, lateral, and vertical vibration. *Journal of Sound and Vibration*. 330 (4), 816-826, 2011.

[3] O. Thuong and M.J. Griffin. The vibration discomfort of standing people: Relative importance of fore-and-aft, lateral, and vertical vibration. *Journal of Applied Ergonomics*, 43, 902-908, 2012

[4] D. Thorby. Structural dynamics and vibration in practice. *Elsever*, 2008.

[5] L.N. Virgin, S.T. Santillan and R.H. Plaut. Vibration isolation using extreme geometric nonlinearity. *Journal of Sound and Vibration,* 315, (3), 721-731, 2008.

[6] E.J. Chin, K.T. Lee, J. Winterflood, L. Ju and D.G. Blair. Low frequency vertical geometric anti-spring vibration isolators. *Journal of Physics letters A,* 336 (2-3), 97 - 105, 2005.

[7] J. Winterflood, D.G. Blair and B. Slagmolen. High performance vibration isolation using springs in Euler column buckling mode. *Journal of Physics Letters A,* 300, 122-130, 2002.

[8] A. Carella, M.J. Brennan and T.P. Waters. Static analysis of a passive vibration isolator with quasi-zero-stiffness characteristic. *Journal of Sound and vibration*, 301, 678-689, 2006.

[9] Z. Hao and Q. Cao. A novel dynamical model for GVT nonlinear supporting system with stable-quasi-zero-stiffness. *Journal of Theoretical and Applied Mechanics,* 52, 199-213, 2014.

[10] G. Dong, X. Zhang, Y. Luo, Y. Zhang and S. Xie. Analytical study of the low frequency multi-direction isolator with high-static-low-dynamic stiffness struts and spatial pendulum. *Journal of Mechanical Systems and Signal Processing,* 110, 521-539, 2018.

[11] A. Carrella, M.J. Brennan, T.P. Waters and V. Lopes. Force and displacement transmissibility of a nonlinear isolator with high-static-low-dynamic-stiffness. *International Journal of Mechanical Sciences*, 55, 22–29, 2012.

[12] X. Wang, H. Liu, Y. Chen and P. Gao. Beneficial stiffness design of a high-static-low-dynamic-stiffness vibration isolator based on static and dynamic analysis. *International Journal of Mechanical Sciences,* 142–143, 235–244, 2018.

[13] Z. Hu, X. Wang, H. Yao, G. Wang and G. Zheng. Theoretical analysis and experimental identification of a vibration isolator with widely-variable stiffness. *Journal of Vibration and Acoustics,* 140, 051-114, 2018.

[14] A. O. Oyelade. Vibration isolation using a bar and an Euler beam as negative stiffness for vehicle seat comfort. *Journal of Advances in Mechanical Engineering*, 11(7), 1-10, 2019.

[15] X. Liu and X. Huang. On the characteristics of a quasi-zero stiffness isolator using Euler buckled beam as negative stiffness corrector. *Journal of Sound and Vibration*, 3359-3376, 2013.

[16] C. Liu and K. Yu. Design and experimental study of a quasi-zero-stiffness vibration isolator incorporating transverse groove springs. *Journal of Archives of Civil and Mechanical Engineering*, 20-67, 2020.

[17] K. Ye, J.C. Ji and T. Brown. A novel integrated quasi-zero stiffness vibration isolator for coupled translational and rotational vibrations. *Journal of Mechanical Systems and Signal Processing,* 149, 107340, 2021.

[18] Q. Meng, X. Yang, W. Li, E. Lu and L. Sheng. Research and Analysis of Quasi-Zero-Stiffness Isolator with Geometric Nonlinear Damping. *Journal of Shock and Vibration*, 9 pages, 2017.

[19] T. D. Le and K. K. Ahn. A vibration isolation system in low frequency excitation region using negative stiffness structure for vehicle seat. *Journal of Sound and Vibration* 330 (26), 6311-6335, 2011.

[20] T. D. Le and K. K. Ahn. Experimental investigation of a vibration isolation system using negative stiffness structure. *International Journal of Mechanical science,* 70 99-112, 2013.

[21] X. Sun, J. Xu, X. Jing and L. Cheng. Beneficial performance of a quasi-zero stiffness vibration isolator with time-delay active control. *International Journal of Mechanical Sciences*, 82, 32-40, 2014.

[22] D. Chen, H. Zi, Y. Li and X. Li. Low frequency ship vibration isolation using the band gap concept of sandwich plate-type elastic metastructures. *Journal of Ocean Engineering*, 235, 2021.

[23] G. Yan, H. X. Zou, S. Wang, L. C. Zhao, Z. Y. Wu and W. M. Zhang. Bio-inspired toe-like structure for low-frequency vibration isolation. *Journal of Mechanical Systems and Signal Processing*, 162, 2022.

[24] R. Chen, X. Li, Z. Yang, J. Xu a and H. Yang. A variable positive-negative stiffness joint with low frequency vibration isolation performance. *Journal of Measurement*, 185, 2021.

[25] L. Yan, S. Xuan and X. Gong. Shock isolation performance of a geometric anti-spring Isolator. *Journal of Sound and Vibration,* 413, 120-143, 2018.

[26] Y. Zheng, Q. Li, B. Yan, Y. Luo and X. Zhang. A Stewart isolator with high-static-low-dynamic stiffness struts based on negative stiffness magnetic springs. *Journal of Sound and Vibration*, 422, 390-408, 2014.

[27] Y. Zheng and X. Zhang, Y. Luo, B. Yan and C.Ma. Design and experiment of a high-static-low-dynamic stiffness isolator using a negative stiffness magnetic spring. *Journal of Sound and Vibration*, 31-52, 2016.

[28] F. Zhang, S. Shao, Z. Tian, M. Xu and M. Xie. Active passive hybrid vibration isolation with magnetic negative stiffness isolator based on Maxwell normal stress. *Journal of Mechanical system and Signal Processing,* 123, 244-263, 2019.

[29] Q. Li, Y. Zhu, D. Xu, J. Hu, W. Min and L. Pang. A negative stiffness vibration isolator using magnetic spring combined with rubber membrane. *Journal of Mechanical Sciences and Technology,* 27(3),813-824, 2013.

[30] G. Dong, X. Zhang, Y. Luo, Y. Zhang and S. Xie. Analytical study of the low frequency multi-direction isolator with high-static-low-dynamic stiffness struts and spatial pendulum. *Journal of Mechanical Systems and Signal Processing*, 110, 521-539, 2018.

[31] C. Liu, R. Zhao, K. Yu and B. Liao. In-plane quasi-zero-stiffness vibration isolator using magnetic interaction and cables: Theoretical and experimental study. *Applied Mathematical Modelling*, 96, 497-522, 2021.

[32] C. Li, T. Jiang, Q. He and Z. Peng. Stiffness-mass-coding metamaterial with broadband tunability for low-frequency vibration isolation. *Journal of Sound and Vibration*, 22, 115685, 2020.

[33] S. Yuan, Y. Sun, J. Zhao, K. Meng, M. Wang, H. Pu, Y. Peng, J. Luo and S. Xie. A tunable quasi-zero stiffness isolator based on a linear electromagnetic spring. *Journal of Sound and Vibration*, 482, 115449, 2020.

[34] M. W. Holtz and J. Niekerk. Modeling and design of a novel air-spring for a suspension seat. *Journal of Sound and vibration*, 329,4354-4366, 2010.

[35] C. H. Nguyen, C. M. Ho and K. K. Ahn. An Air Spring Vibration Isolator Based on a Negative-Stiffness Structure for Vehicle Seat. *Journal of Applied Science*, 11, 11-23, 2021.

[36] A. Facchinetti, L. Mazzola and S. Bruni. Mathematical modelling of the secondary air spring suspension in railway vehicles and its effect on safety and ride comfort. *Journal of Vehicle System Dynamic*, 48, 429-449, 2010.

[37] L. Mazzola and M. Berg. Secondary suspension of railway vehicles-Air spring modelling: performances and critical issues. *Processing Inst. Mechanical engineering, Part F:J, Rail Rapid Transit*, 228, 225-241, 2014.

[38] C. Erin, B. Wilso and J. Zapfe. An improved model of a pneumatic vibration isolator: theory and experiment. *Journal of Sound and vibration*, 218, 81-101, 1998.

[39] J.H. Lee and K. J. Kim. Modeling of nonlinear complex stiffness of dual-chamber pneumatic spring for precision vibration isolators. *Journal of Sound and vibration*, 301, 909-926, 2007.

[40] T. Mankovits and T. Szabó. Finite Element Analysis of Rubber Bumper Used in Air-springs. *Journal of Procedia Engineering*, 48, 388-395, 2012.

[41] H. Pu, X. Luo and X. Chen. Modeling and analysis of dual-chamber pneumatic spring with adjustable damping for precision vibration isolation. *Journal of Sound and vibration*, 330, 3578-3590, 2011.

[42] H. Zhu, J. Yang, Y. Zhang and X. Feng. A novel air spring dynamic model with pneumatic thermodynamics, effective friction and viscoelastic damping. *Journal of Sound and vibration,* 408, 87-104, 2017.

[43] G. Quaglia and M. Sorli. Air suspension dimensionless analysis and design procedure. *Journal of Vehicle System Dynamics*, 35, 443-475, 2001.

[44] S.J. Lee. Development and analysis of an air spring model. *International Journal of Automotive Technology*, 11, 471-479, 2010.

[45] E. Palomares, A. L. Morales, A. J. Nieto, J. M. Chicharro and P.Pintado. Improvement of Comfort in Suspension Seats with a Pneumatic Negative Stiffness System. *Journal of Actuators*, *9*, 126, 2020

[46] C. H. Nguyen, C. M. Ho and K. K. Ahn**.** An Air Spring Vibration Isolator Based on a Negative-Stiffness Structure for Vehicle Seat. *Journal of Applied Science, 11*, 2021.

[47] Y. Jiang, C. Song, C. Ding and B. Xu. Design of magnetic-air hybrid quasi-zero stiffness vibration isolation system. *Journal of Sound and Vibration*, 477, 2020.

[48] M. Wang, X. Chen, and X. Li. An Ultra-Low Frequency Two DOFs' Vibration Isolator Using Positive and Negative Stiffness in Parallel. *Hindawi Publishing Corporation Mathematical Problems in Engineering*, 15 pages, 2016.

[49] Y. Zhao, J. Cui, J. Zhao, X. Bian and L. Zou. Improving Low Frequency Isolation Performance of Optical Platforms Using Electromagnetic Active-Negative-Sti**ff**ness Method. *Journal of Applied Science*, *10*, 2020

[50] *www.firestoneip.com*

[51] P. Beater. Pneumatic Drives, System Design, Modelling and Control. *Springer*, 2007

[52] X.B. Tran, V.L. Nguyen and K.D. Tran. Effects of friction models on simulation of pneumatic cylinder. *Journal of Mechanical Science*, 10, 517–528, 2019.

[53] M. Berg. A non-linear rubber spring model for rail vehicle dynamics analysis. *International Journal of Vehicle Mechanical Mobile*, 30, 197-212, 1998.

[54] Y.A. Rossikhin and M.V. Shitikova. The fractional derivative Kelvin-Voigt model of viscoelasticity with and without volumetric relaxation. *Journal of Physics*, 991, 2018.

[55] I. Podlubny. Fractional differential equations. *Academic Press*,1999.

[56] A.H. Nayfeh and D.T. Mook. Nonlinear oscillations. *John Willey & Sons, INC*, 1995

[57] J.C. Butcher. Numerical methods for ordinary differential equations. *2nd Edition, John Willey & Sons*, 2008

[58]. P.W. Jordan and P. Smith. Nonlinear ordinary differential equations. *4th Edition, Oxford*, 2007.

[59] M. Mitchell. An introduction to genetic algorithms. *Cambridge*, 5th printing, 1999.

[60] Y. Liu, H. Matsuhisa and H. Utsuno. Semi-active vibration isolation system with variable stiffness and damping control. *Journal of Sound and Vibration*, 312, 16-28, 2008.

[61] T.D. Le and V.N. Ho. Design and experimental evaluation of an electrohydraulic vibration shaker. *Journal of Mechanical Engineering Research and Development*, 43, 60-67, 2020.